Imperial College of Science, Technology and Medicine
Department of Materials

Room-Temperature Quantum Devices: Innovations in Active Pre-Cooling Protocol, Spin-Phonon Coupling Devices, and Stable Molecular Spins

Kuan-Cheng Chen

Department of Materials
Imperial College London

Supervised by
Prof. Mark Oxborrow

Co-Supervised by
Prof. Sandrine Heutz

Submitted in part fulfilment of the requirements for the degree of
Doctor of Philosophy in Materials Research of Imperial College London and
the Diploma of Imperial College, October 2024

Abstract

The feasibility of active pre-cooling (APC) by temporarily over-coupling microwave cavity modes to a low-noise amplifier acting as an active cold load was demonstrated, offering an effective method to reduce thermal photon occupancy without cryogenic cooling. The potential of the organic radical BDPA as a tunable qubit medium with remarkably long spin-lattice and spin coherence relaxation times was assessed, comparing favorably with state-of-the-art molecular qubit media. A high-quality surface acoustic wave device integrated with pentacene-deposited molecular thin films was developed to achieve heterogeneous optically-detected spin-acoustic resonance (HODSAR), enabling efficient zero-field spin control at room temperature via spin-phonon coupling. Through the construction of specialized experimental setups, the effectiveness of these techniques was demonstrated, facilitating pre-cooling of cavity modes, enhancing coherence times in qubit media, and achieving precise spin manipulation. While APC offers advantages over methods like masers and anti-masers, challenges such as the need for fast, low-loss microwave switches remain. The BDPA radicals showed significant promise for spin ensemble, and the SAW-based HODSAR device provides a scalable platform for spin manipulation in quantum technologies.

Acknowledgements

First and foremost, I would like to express my sincere gratitude to everyone who has supported me throughout my doctoral journey. Without the assistance, guidance, and encouragement from numerous individuals, completing this thesis would not have been possible.

I am deeply grateful to my PhD supervisor, Prof. Mark Oxborrow, for his invaluable mentorship over the past five years. Prof. Oxborrow has imparted extensive knowledge in both microwave engineering (including properly tightening SMA cables) and quantum physics. His unwavering commitment to conducting rigorous, traceable research and his meticulous attention to detail have profoundly influenced my approach to scientific inquiry. Moreover, his encouragement to pursue my own research interests enabled me to engage in diverse and fulfilling activities.

I would also like to extend my heartfelt thanks to all my colleagues in the Maser group. Xiaotian (Felix) Xu and Dr. Wern Ng provided substantial assistance and insightful suggestions in tr-EPR experiments, as well as companionship (lunch, dinner, and hotpot parties) that made campus life memorable. Dr. Max Attwood was instrumental in helping me with thin-film deposition, radical synthesis and pulse-EPR measurements, and his unwavering support during challenging times was greatly appreciated. Our road trip from Chicago to Buffalo remains one of my fondest memories. Michael Newns engaged in meaningful discussions with me regarding noise temperature measurements and benchmarking in the laser lab, while Dr. Yongqiang Wen offered significant support with ODMR measurements. I am also thankful to Prof. Neil Alford for facilitating access to equipment resources at the Henry Royce Institute, and to Prof. Hao (Eric) Wu, now an assistant professor at Beijing Institute of Technology, for his academic advice and warm hospitality during my visits to Beijing. Being part of this group has not only enriched my knowledge of quantum science but also allowed me to forge lifelong friendships.

I would like to extend special thanks to Dr. Irena Nevjestic at Spin-LAB for her assistance with measuring CW-EPR signals, and to Dr. Alberto Collauto at PERP Lab for his support with pulsed EPR measurements. I am also grateful to Dr. Sami Ramadan and Prof. Chen Fu for their help in fabricating high-Q SAW devices. Your expertise and support have been invaluable to my research. Additionally, I would like to honour the memory of Professor Norbert Klein, who served as an assessor for my early-stage assessment and provided valuable insights at the beginning of this thesis.

At Imperial College, I am thankful to Dr. Po-Heng (Henry) Lee for being my academic mentor, guiding me to become a better scholar, and providing invaluable life advice. I also appreciate Prof. Peter Haynes for providing me the opportunity to work as a Quantum Policy-Making Assistant at Imperial QuEST and for collaborating with the Regulatory Horizons Council on quantum technology policies. Additionally, I extend my gratitude to my co-supervisor, Prof. Sandrine Heutz, for granting me access to her group's OMDB equipment. I would also like to thank Dr. Shang Yu and the Distributed Quantum Computing Group (especially Felix Burt and Prof. Kin K. Leung) at Imperial College for their collaboration on the distributed quantum computing project. Lastly, I am deeply grateful to Dr. Annalisa Neri, our Postgraduate Research Coordinator, for her continuous support and assistance throughout my PhD studies.

I would also like to express my gratitude to our industry partners: NVIDIA, IBM Quantum and TSMC. Additionally, I am thankful to the Taiwanese government for their generous scholarship support, which has been crucial in facilitating my studies. I would like to extend my thanks to the Turing Scheme for supporting my Imperial-TUM Global Fellow Programme, allowing me to be supervised by Prof. Robert Wille at the Chair of Design Automation, Technical University Munich.

On a personal note, I would like to thank my parents, my grandmothers, and my younger sister for their unwavering support and encouragement throughout my studies. A special thank you to my girlfriend, Yumeng, for her constant encouragement and for always being there for me. Lastly, I would like to acknowledge my Cyprusian ginger cat, Cheese, whose companionship has provided comfort and joy during these challenging three years, especially throughout the pandemic.

Thank you all for your contributions to my academic and personal growth.

Dedication

I declare that all the work presented here is my own, and any other sources are properly referenced.

Copyright

The copyright of this thesis rests with the author. Unless otherwise indicated, its contents are licensed under a Creative Commons Attribution-NonCommercial 4.0 International Licence (CC BY-NC).

Under this licence, you may copy and redistribute the material in any medium or format. You may also create and distribute modified versions of the work. This is on the condition that: you credit the author and do not use it, or any derivative works, for a commercial purpose.

When reusing or sharing this work, ensure you make the licence terms clear to others by naming the licence and linking to the licence text. Where a work has been adapted, you should indicate that the work has been changed and describe those changes.

Please seek permission from the copyright holder for uses of this work that are not included in this licence or permitted under UK Copyright Law.

— Kuan-Cheng Chen (陳冠丞)

London, United Kingdom

Jan. 2025

Room-Temperature Quantum Devices: Innovations in Active Pre-Cooling Protocol, Spin-Phonon Coupling Devices, and Stable Molecular Spins © 2025 by Kuan-Cheng Chen

is licensed under Creative Commons Attribution-NonCommercial 4.0 International

"The important thing is not to stop questioning. Curiosity has its own reason for existing. One cannot help but be in awe when he contemplates the mysteries of eternity, of life, of the marvelous structure of reality. It is enough if one tries merely to comprehend a little of this mystery every day."

— *Albert Einstein, Life magazine, May 2, 1955*

Contents

Abstract **i**

Acknowledgements **iii**

1 Introduction **1**

1.1 Motivation 1

1.2 Outline of the Thesis 4

1.3 Statement of Originality 7

1.4 Publications List 8

2 Background Theory **13**

2.1 Theory I: Electron Paramagnetic Resonance 14

2.1.1 Introduction of Electron Paramagnetic Resonance 14

2.1.2 Anisotropic of the Electronic g-Value 16

2.1.3 Zero-Field Splitting 18

2.1.4 Type of EPR Spectroscopy 20

2.1.5 Sensitivity of EPR Spectrometers 28

2.2 Theory II. Overcoming Thermal-Noise Limits in Microwave Measurements . . . 41

2.2.1 Number of photons inside a microwave cavity 41

2.2.2 Mode temperature inside the cavity 42

2.2.3 Cavity cooling via a lossy transmission line 43

2.2.4 Multiple cooling ports to a microwave cavity 45

2.2.5 Multiple cooling ports to a microwave cavity with lossy transmission lines 46

2.2.6 Theoretical Noise Analysis of APC 47

2.3 Theory III. Pulse EPR Methods and Their Applications 50

2.3.1 Using Pulse EPR Measurement to Study Quantum Coherence in Electron Spin Systems 50

2.4 Theory IV. Quality Factor Definitions in Microwave Systems 55

2.4.1 How to Measure Q-factor? 55

3 Overcoming the Thermal-Noise Limit by APC Protocol 66

3.1 Introduction of APC with Active Cold Loads 67

3.2 Experimental Setup of a Active-Pre-Cooled tr-EPR Spectrometer 70

3.3 A Low-Noise Amplifier as an Active Cold Load 73

3.4 The Practical Active Pre-Cooling Protocol 76

3.5 Switchover followed by Interrogation 83

3.6 Results and Analysis 87

3.7 Conclusion 93

4 Stable and Processable Photoexcited Molecular Electron Spins 95

4.1 Introduction of Photoexcited Molecular Electron Spins 96

4.2 Experimental Setup 98

4.3 Experimental Results 99

4.3.1 Investigation of spin coherence by pulsed EPR spectroscopy 99

4.3.2 Probing two-level quantum dynamics at room temperature 102

4.3.3 Generation of radical spin polarisation using photoexcited triplets 105

4.4 Discussion 107

4.5 Conclusion 110

5 HODSAR: Heterogeneous Optically-Detected Spin-Acoustic Resonance 112

5.1 Introduction of HODSAR 113

5.2 Experimental Setup of the HODSAR Spectrometer 115

5.2.1 HODSAR Device Fabrication 116

5.2.2 HODSAR System Setup 118

5.2.3 High-Q MMSAR Electro-Mechanical Characteristics 120

5.2.4 Pentacene Thin-Film Characterization 121

5.3 Coherent Acoustic Control of Molecular Thin Film 123

5.3.1 CW-HODSAR Measurement 123

5.3.2 Pulsed HODSAR Measurement (Rabi Oscillation) 125

5.4 Conclusions 126

6 Conclusion 127

6.1 Summary 127

6.2 Future Work 129

A Derivation of the SNR in EPR Spectroscopy **132**

A.1 Signal-to-Noise Ratio 132

A.2 Sensitivity: Minimum Detectable Number of Spins 134

B Noise Analysis and Noise-Figure Characterization of LNAs **137**

B.1 Noise Temperature in Devices and Thermal Noise Analysis of Circuits 137

B.1.1 Noise Parameters of HEMT Ultra-Low-Noise Amplifiers: Why HEMTs Can Achieve Such Low Noise Temperatures 137

B.2 Wave-Approach Noise Analysis and Noise Parameter Measurement 142

B.2.1 OSL Y-Factor Method for Measuring Noise Parameters 144

B.2.2 Setup of Heterodyne Detection for Noise Parameter Measurement and Calibration 146

B.2.3 Markov Chain Monte Carlo for Noise Parameter Model Fitting 148

C Pulse EPR Data Fitting for BDPA in OTP in Different Conditions **151**

C.1 Fitting of Rabi Oscillation in Different Conditions 151

D Quantum Metrology with Single-Strain Coupling in D2h Group **155**

D.1 Single-Strain Coupling in D2h Group 155

E Simulation for Electromagnetic Effect in the System **160**

Bibliography **161**

List of Tables

2.1 Values of parameters -entering the noise-reduction equation 2.53 48

2.2 Symbols in Kajfez's Equivalent Circuit for the Microwave Cavity 61

3.1 Modeled and experimentally-inferred depth of cooling 93

4.1 EasySpin fitting parameters for BDPA in OTP, modeled as an $S = \frac{1}{2}$ spin system. 99

B.1 Symbols in the Small-Signal Equivalent Circuit for HEMTs 139

B.2 Results of the Noise Parameter Characterization for QPL9547 150

List of Figures

1.1 The schematic diagram depicts the quantum information processing platform, encompassing quantum sensing, memory, and computing. Development is organized into three primary components: (1) measurement apparatus and protocols (Chapter 3); (2) signal generation, conditioning, and materials (Chapter 4); and (3) quantum device development and integration (Chapter 5). Additionally, signal processing is integrated with algorithm design, synchronization, and calibration, as detailed in the experimental setups of each respective chapter. . . 6

2.1 Zeeman splitting diagram depicting the energy levels of an isolated electron in the presence of an external magnetic field. The spin-up state has a higher energy level, while the spin-down state corresponds to a lower energy level. The blue trace illustrates the response EPR signal generated as the electron transitions between these spin states[1]. 15

2.2 Schematic representation of the magnetic moment states of a paramagnetic center, depicting the associated g-factor anisotropy and corresponding EPR spectrometer lineshapes. The top row illustrates varying molecular symmetries leading to isotropic (a), axial (b), and rhombic (c) g-tensor components. The middle and bottom rows display the absorption spectra (blue) and their first derivative signals (red), highlighting characteristic g-values such as $g_{\parallel}$, $g_{\perp}$, g_x, g_y, and g_z for different symmetries. Vertical dashed lines indicate peak positions corresponding to different g-factors[2]. 17

2.3 Diagram of degenerate triplet sublevel splitting energy: (a) In a spherically symmetric model, electron distribution leads to degenerate triplet states in three dimensions. (b) In a symmetric planar model (flattened along Z), the molecule is symmetric in the x–y plane with a nondegenerate sublevel T_z. (c) In an asymmetric planar model (flattened along Z and elongated along X), the molecule has three split states T_x, T_y, and T_z [3]. 20

2.4 Principle of lock-in detection. The input signal $V_s(t)$, potentially obscured by noise, is extracted by the lock-in amplifier through mixing with a reference signal $V_r(t)$, enabling phase-sensitive detection [4]. 22

2.5 Time sequence scheme of a tr-EPR experiment with direct detection [5]. The transient signal is recorded post laser excitation without magnetic field modulation, operating on a timescale from nanoseconds to milliseconds. 23

2.6 Schematics of three EPR spectrometer configurations for CW, time-resolved, and advanced pulsed EPR techniques. (a) CW-EPR with lock-in amplifier [6]. The sample is placed in a microwave cavity situated between the poles of the magnet. The microwave source feeds the microwave into the cavity through a circulator, and the microwave reflected from the cavity is directed toward the detector. For enhancing the SNR, additional modulation coils connected with the lock-in amplifier are introduced to the system. With respect to this external modulation, the CW-EPR signal is detected phase-sensitive. However, typically the modulation frequencies are in the range of 10-100 kHz, thus the time-resolution is limited by these modulation frequencies. (b) Time-Resolved EPR Spectrometer[6]: This setup modifies the CW approach by introducing a pulsed light source synchronized with pulsed MW fields directed at the sample. This configuration enables time-resolved detection of transient magnetic resonance signals, allowing the measurement of spin relaxation times and other dynamic processes. The detector and recorder capture the time-dependent response of the sample, providing insights into fast spin dynamics. (c) Pulsed EPR Spectrometer[7]: This configuration incorporates an AWG for custom pulse shaping and frequency modulation, along with components such as a mixer, PIN diode, attenuator, and phase shifter. These elements provide precise control over MW pulse sequences and their phases, enhancing sensitivity and specificity for advanced EPR experiments. This setup supports detailed exploration of spin dynamics and coherence, enabling pulse sequences and phase manipulations suitable for studies of quantum coherence and spin control. 26

2.7 Qualitative noise spectrum of a typical experiment [4]. To achieve a high SNR, the measurement frequency should be in a region that avoids flicker noise, for example, the f_2 frequency. With the same filter bandwidth, f_2 yields a better result than f_1. 32

2.8 The source outputs a signal S_i and noise power N_i. Both signal and noise from the source are amplified by the LNA with a gain, G. Additionally, the LNA adds noise to its output, N_a. 33

2.9 Relationship between frequency and effective noise temperature (K) for different types of devices. Masers and HEMT LNAs can operate at high frequencies with very low noise temperatures [8]. 34

2.10 Friis's formula for cascaded amplifiers. 35

2.11 First-derivative EPR spectra of Mn^{2+} in H_2O at the output of the pulse height analyser. (a) 100 traverses, 5×10^{14} spins; (b) 1 traverse, 5×10^{14} spins; (c) 500 traverses, 5×10^{13} spins; (d) 1 traverse, 5×10^{13} spins [9]. 38

2.12 Configurations enhancing sensitivity in EPR spectrometers through maser techniques [10]. (a) Spectrometer incorporating maser material within the cavity. (b) Reflection-type maser cavity utilized for noise analysis. 39

2.13 The active pre-cooling technique involves electromagnetically coupling a resonator, that is physically heat-sunk to a room-temperature environment (here referred to as the "hot bath"), to an active cold noise source or "load", here functioning as a "cold bath". 41

2.14 Modeled equivalent temperature of an electromagnetic mode inside the cavity as a function of the coupling factor κ (horizontal coordinate) and the noise temperature of the cold load T_{cold} coupled to this mode (vertical coordinate). . 42

2.15 Calculating how the cooling LNA's noise temperature is degraded by transport along a length of (warm) lossy transmission line. 44

2.16 Cavity cooling with two separate cold baths. 46

2.17 How, according to Eq. 2.50, the forward noise power (in units of absolute temperature T) at the far end of a lossy cable depends on the cable's insertion loss L_{dB}. Here the cable is uniformly maintained at a temperature of $T_0 = 290$ K throughout its length and the near end of the cable is terminated and cooled by the ACL whose noise temperature is $T_{\mathrm{cold}} = 29.1$ K (dashed cornflower-blue baseline)– corresponding to the input noise temperature of the Qorvo QPL9547EVB-01 LNA used experimentally. The zoomed-in area details how, when the insertion loss is less than 0.5 dB, equation Eq. 2.44 (red dashed line -"Linear Approx."), *i.e.* the linear approximation provided by equation (8-2-5) in Siegman's book [11], compares against the exact formula Eq. 2.50 (blue solid line). 47

2.18 Anatomy of the signal path at the front end of the homodyne receiver, displaying the forward and backward noise powers between the LNA and microwave cavity. 48

2.19 Hahn echo sequence illustrating the spin echo relaxation mechanism. The process begins with a $\pi/2$ pulse that rotates the initial magnetization vector M_0 from the z-axis to the transverse plane (xy-plane), initiating FID. Over the interval τ, dephasing due to inhomogeneities in the magnetic field causes the spins to diverge. A subsequent π pulse inverts the spin vectors, effectively reversing their positions. This inversion enables the spins to rephase, culminating in the formation of a coherent spin echo at time 2τ. The amplitude of the echo, shown as progressively decaying echoes, reflects the T_{m} (phase memory time) relaxation and provides insights into spin coherence and dephasing effects[12, 13]. 51

2.20 Pulse sequence diagram illustrating the inversion recovery method for measuring spin-lattice relaxation time (T_1). The sequence begins with an initial π pulse that inverts the magnetization along the z-axis, followed by a variable delay time T during which longitudinal relaxation occurs. A subsequent $\pi/2$ pulse rotates the partially recovered magnetization into the transverse plane, initiating FID. The signal intensity as a function of the recovery time T allows for the determination of T_1 by fitting the resulting curve to an exponential recovery model[14, 13]. . . 52

2.21 Pulse sequence diagram of the CPMG experiment, used for measuring the spin-spin relaxation time (T_{m}). The sequence begins with an initial $\pi/2$ pulse that rotates the magnetization into the transverse plane, followed by a time interval τ. A train of π pulses is applied at intervals of 2τ to refocus the dephasing spins and produce successive echo signals. This process is repeated n times to create a series of echoes, each separated by 2τ. The decay of the echo amplitudes provides valuable information for determining T_{m}, revealing spin dephasing and coherence properties[15, 13]. 53

2.22 Pulse sequence diagram illustrating the Rabi oscillation experiment, which measures the coherent oscillations of spin populations under a resonant driving field. The sequence begins with a preparation pulse of duration t_p to set the initial state, followed by a variable waiting period T. A $\pi/2$ pulse rotates the magnetization into the transverse plane, initiating FID. After a time interval τ, a π pulse is applied to refocus the spins and generate an echo signal at the end of another τ interval. The observed echo amplitude as a function of t_p reveals the Rabi oscillations, providing insights into the coherence and interaction strength of the spins[16, 13]. 54

2.23 An illustration of the device-under-test (DUT) showing the incident, reflected, and transmitted waves. 56

2.24 The Q-circle in polar coordinates used for transmission-line analysis. 57

2.25 Kajfez's equivalent circuit model for transmission-line analysis [17]. 60

2.26 Left: Five-point measurement method on the Smith chart [18]. Right: Measured data of the designed cavity resonator. 63

3.1 The left image presents the 3D CAD assembly of the microwave cavity (without microwave walls), featuring a movable "ceiling" (= plunger), raised and lowered by a rotating a helical screw (to which the ceiling is mechanically attached) seated in a matching helical thread tapped into the cavity's "roof" along the cavity's cylindrical axis. The photo to the right of the drawing shows the cavity's innards with the ceiling and roof removed. The cavity includes two ports: an over-coupling loop (at 12 o'clock in the photo) and a smaller critical-coupling loop (at 9 o'clock) just poking out of the cavity's internally-silver-plated wall. The right figure displays the microwave cavity in 2D cross-section. Here, the high-Q sapphire ring is located concentrically on top of a cross-linked polystyrene stand (not shown); its on-axis bore hole, 10 mm in diameter, is filled with the EPR sample (a 0.1% PC:PTP crystal). 71

3.2 The experimental rig (here emphasizing its electrical synchronization and light path) encompassing, from right to left: the OPO's power supply unit (PSU), the OPO laser head itself, the resonator and it surrounding microwave "plumbing", and the tr-EPR spectrometer's support electronics. 72

3.3 Paradigm of a cavity that is externally coupled to an ACL in the form of the input of an LNA whose output in terminated. 75

3.4 (a) Conceptual mechanism of active pre-cooling (APC): A microwave resonator is physically maintained at a temperature T_{hot} (in this article, T_{hot} equals room temperature, denoted as T_0) and supports an electromagnetic mode whose photon occupation number is $\bar{n}_{\text{mode}}$. This mode is coupled to a cold load maintained at a lower temperature T_{cold} with a coupling factor of κ_{over} between the load and the mode. (b) Simplified equivalent electrical circuit: The resonator, here drawn as an LCR tank circuit, is over-coupled (right) through a (SPDT) switch to either a cold load (in the form of the input of an LNA) or an open circuit –depending on the position of the switch. The mode's field amplitude (as generates a voltage across the tank circuit) can be measured by a second LNA through its own coupling port (left –this port's coupling is usually adjusted to be at critical coupling when the cooling LNA is switched out) whose output is recorded on a digital oscilloscope. 77

3.5 The cavity's dissipators, their temperatures, and the resultant noise power outputted. 78

3.6 (a) Photograph of the experimental resonator's interior: a sapphire ring holding a 0.1% Pc:PTP crystal, surrounded by the silver-plated walls of a cylindrical brass enclosure. (b) CAD diagram of the same resonator with a two-dimensional axisymmetric simulation of the magnetic flux (white arrows) and magnetic energy density of the $TE_{01\delta}$ microwave mode[19] that this resonator supports. (c) Signal-path anatomy of the experimental time-resolved EPR spectrometer used to demonstrate active pre-cooling. This circuit incorporates homodyne detection of the transient EPR signal. The firing of the optical-parametric oscillator (OPO) laser system and the closing/opening of the two microwave switches are scheduled via transistor–transistor logic (TTL) control pulses (generated by two cascaded pulse generators –both a Thandar TG105) as explained in Fig. 3.7. . . 80

3.7 Active pre-cooling as applied to time-resolved (tr-) EPR: In Step 1, an LNA connected to an over-coupled cooling port extracts thermal noise (energy) from the microwave cavity (represented here as an LCR circuit); this also pulls the cavity mode's resonance frequency away from f_0 –slightly. Next (Step 2), a switch disconnects the cooling LNA, bringing the mode back on resonance (*i.e.*, its frequency coincident with the EPR transition's line center at 1.45 GHz). Instantaneously with this microwave switching, a q-switched optical pulse (around 7 nanoseconds in duration) of 532-nm pump light is shone on the EPR sample within the cavity. Step 3: a continuous-wave (CW) interrogating microwave tone is thereupon applied via a circulator to the cavity's monitoring port, as shown in Fig. 3.6 (c), which, upon re-emerging from the cavity through the circulator's third arm, provides a tr-EPR signal characterizing the EPR sample. 82

3.8 Active pre-cooling in the frequency domain. The vertical axis is the power spectral density (PSD) of the noise signal extracted by a (small) monitoring probe inserted into the cavity (like what is shown at the bottom right of Fig. 3.5). Here, the linewidth of the thermal noise associated with a mode is inversely proportional to the mode's loaded Q. The area under the curve for curves of the same color is the same. 84

3.9 Increase in measured noise over time as the experimental cavity's monitored microwave mode warms up from "pre-cooled" to ambient conditions. The two red dashed lines track the envelope of the voltage noise. Upon curve-fitting to this envelope (see Fig. 3.12), the characteristic time of the warming up is determined to be $\tau^{\text{exp.}}_{\text{warm up}} \approx 9 \pm 1\mu$s. 88

3.10 (a) Zero-field (ZF) tr-EPR signal of Pc:PTP's $T_{\text{x}} - T_{\text{z}}$ transition[20] without (red) and with (blue) pre-cooling. (b) Thermal noise (in the time domain) extracted from each of these ZF tr-EPR signals and, below, their corresponding spectral densities; as before, blue and red correspond to the pre-cooled (with) and ambient (without) conditions, respectively. (c) Simplified Jablonski (= energy-level) diagram of the ZF sublevels (T_{x}, T_{y}, T_{z}) of pentacene's triplet ground state, where D and E denote the ZF splitting (ZFS) parameters. (d) Modeled noise power reduction (ΔP) at the homodyne receiver's input as a function of the noise temperature of the EPR cavity's operational mode, T_{mode}. Since its uncertainty is lower, the estimated depth of cooling presented here ($\Delta P_{\text{exp-Cool}}$) corresponds to that achieved by active pre-cooling alone (see Table 3.1). The depth's standard error is indicated by dashed cornflower-blue lines. 89

3.11 Modeled average number of thermal photons occupying the cavity's $\text{TE}_{01\delta}$ mode and the mode's corresponding temperature (T_{mode}) as a function of the cold load's own noise temperature (T_{cold}) and its coupling factor (κ) to the mode. In my experimental demonstration, this mode's temperature is reduced from 184.0 K to 85.0 K (modeled), the latter temperature corresponding to an average occupancy of 1221 photons. 91

3.12 Error analysis and fitting of the experimental warming-up signal as presented in Fig. 3.9. The grey area at shorts times (after switching off the cooling LNA) on the far left represents the period when the double-throw switch is still transitioning to connect the over-coupled port to an "open" load, disconnecting the ACL from the resonator; this takes around $t_{\text{switch}} = 2\ \mu$s. Each blue dot plots $\Delta P_{\text{exp}} = 10\log_{10}(< V^2_{\text{cold}} > / < V^2_{\text{ambient}} >)$ in units of dB[21], where $< V^2_{\text{cold}} >$ is the mean-squared received noise voltage averaged over ten consecutive data points, spaced 100 ns apart, spanning one microsecond; $< V^2_{\text{ambient}} >$ is the equivalent mean-squared noise voltage under ambient conditions (based on an adjoining sample spanning several hundred microseconds). The solid red line, along with its surrounding salmon pink standard error band, was obtained by least-squares fitting a bi-exponential to the evolution of ΔP_{exp} excluding the initial switching period. The longer of the two decay constants was determined to be $\tau^{\text{exp.}}_{\text{warm up}} \approx 9 \pm 1\mu$s. 92

4.1 Conceptual diagram of molecular spin ensembles for microwave storage and quantum memory. 97

4.2 (a) Steady-state EPR signal at RT for BDPA in OTP, with S=1/2 fit shown by the grey dashed line; (b) Pulsed EPR measurements of the Hahn echo decay for 0.1%BDPA in OTP; (c) Summary plot showing the variation of T_1 and T_m over different temperatures and spin concentrations; (d) Carr-Purcell-Meiboom-Gill (CPMG) pulsed sequence with an interpulse delay of 410 ns, overlaid a monoexponential fit. 101

4.3 Rabi Oscillation Experiment for 0.1% BDPA over variable temperatures. (a) Nutation curves with normalized Rabi intensities as a function of nutation pulse length at various microwave attenuation levels measured at RT. The data points represent experimental measurements, while the grey dashed lines indicate the fits to a damped sinusoidal function, providing a precise determination of the Rabi frequencies. Insets illustrate the corresponding spin rotations on the Bloch sphere. (b) Shows the Rabi frequency shifts across a spectrum of microwave powers, reflecting the system's resonance characteristics. (c) and (d) plot the Rabi frequency shift against normalized microwave attenuation (arbitrary units), categorized by temperature (5K, 70K, 150K, 200K, and 300K from light to dark) and phase (liquid and solid state), respectively. The fitting curves illustrate the model's alignment with the experimental data, accentuating the temperature's role in modulating electron spin coherence. All fitting results are shown in the Appendix C. 104

4.4 Photoexcited time-resolved EPR spectra for a mixture of 0.1% H_2TPP and BDPA in OTP, showing (a) triplet-radical pair spin polarisation oscillations over 6 ms; (b) field swept transient of the centrefield radical 160 μs after the laser flash; (c) spin polarisation decay of the absolute signal intensity and; (d) powder phase photoexcited EPR spectrum of H_2TPP 440 ns after laser flash. 106

4.5 Comparison of (a) T_1 and (b) T_m for cutting-edge spin-qubit systems for QIP. The data for each spin system are sourced from 1Cu 0.001%[22], $[V(C_8S_8)_3]^{2-}$[23], NV center[24], 0.1% CuPc:H_2Pc, SiC[25], N@C_{60}[26], Fe_8[27], NV center in ^{12}C-enriched diamond[28], Pn-MOF[29], ^{28}Si:P[30], mPTM radical[31], DPyDAT-MOF [32], polydopamine radicals [33], pTEMPO, pBDPA, pTrityl [34], graphenoid in OTP [35], PTM, mPTM, bPTM [36], PDI-TEMPO [37], BDPA in toluene [38], OX63D [39]. It is important to note that the data included in this comparison were not all collected under identical magnetic field conditions, and for instances where a bi-exponential decay was reported, the slow decay constant has been used when available. 108

5.1 (a) Jablonski diagram illustrating the electronic state cycle in pentacene, responsible for spin-polarized triplet-state sublevels in pentacene:p-terphenyl. Optical excitation by a 532 nm laser promotes pentacene molecules from the ground state S_0 to the first singlet state S_1. Spin-orbit coupling mediates spin-selective intersystem crossing from the excited singlet state into the T_2 triplet manifold. The T_2 triplet states then decay non-radiatively to the T_1 triplet state, preserving the spin-polarized populations. Spin-lattice relaxation can occur between the triplet sublevels with rates γ_{XZ}, γ_{XY}, and γ_{YZ}, representing the $T_{X\to Z}$, $T_{X\to Y}$, and $T_{Y\to Z}$ transitions, respectively. The triplet sublevels ultimately decay back to the S_0 ground state with rates k_X, k_Y, k_Z, thus completing the cycle. My ESR readout targets the T_x-T_y transition near 105 MHz under zero applied magnetic field, leveraging the distinct resonance frequencies of the triplet sublevels for enhanced detection sensitivity. (b) Structural depiction of a pentacene thin film deposited on a $LiNbO_3$ substrate, indicating the molecular arrangement and orientation. (c) Schematic of the HODSAR device, featuring a high-Q multimode resonator that enables efficient laser pumping and photon readout for triplet state detection. (d) Alternative schematic of the device architecture, illustrating the integration of an acoustic transducer and RF input for resonance excitation. 116

5.2 Fabrication process for a pentacene thin-film-based High-Q Organic Dielectric Surface Acoustic Resonator (HODSAR) device with gold electrodes. The procedure starts with wafer cleaning, followed by photoresist spin-coating. Photoresist exposure and development define the electrode pattern, followed by gold deposition and lift-off to establish the electrode structure. A shadow mask is then applied to enable selective deposition of the pentacene thin film on targeted areas. 117

5.3 The schematic diagram of the CW and pulsed ODMR setup for the HODSAR device. (a) The HODSAR device is exited by a 532 nm laser that is modulated by a double-passed AOM. (b) The excitation laser is reflected towards the HODSAR device and the fluorescence is filted by a 600 nm long-pass dihroic mirror and transmitted to the SPAD. (c) The Pulse Streamer is used to generate the pulse sequences for the MW switch, the SPAD and the AOM, the Time Tagger counts the singals from the SPAD and the synchronisation signal from the Pulse Streamer. The RF signal generator generates a MW signal and it is modulated by the switched and delivered to the MMSAR device. 119

5.4 Two-port electrical measurements of the HODSAR device are presented. Panels (a) and (b) show the transmission (S_{21}) and reflection (S_{11}) spectra, respectively, over a wide frequency range, highlighting the region of interest for sensing the $T_x - T_y$ transition of photoexcited pentacene thin films. The blue-shaded region indicates the spectral range where these transitions occur. Panels (c), (d), and (e) display the highest Q-factor responses observed within the blue-shaded region, with corresponding Q-factors (calculated using the Q-circle method[40]) of 5,500, 7,800, and 8,500. These measurements demonstrate the exceptional performance of the HODSAR in the selected frequency range. 120

5.5 The HP8753C vector network analyzer (VNA) measurement illustrates the method used to determine the Q-factor values in Fig. 5.4, with a representative Q-factor of 8,505.2 at a frequency centered at 104.8MHz. 121

5.6 (a) SEM cross-sectional image of the MMSAR device, showing the 1% Pc:PTP thin film layer on a $LiNbO_3$ substrate with a 1 μm scale bar. (b) Optical microscope top view of the HODSAR device, highlighting the pentacene thin-film region and IDTs with a 200 μm scale bar. (c) XRD pattern comparison of the 1% Pc:PTP thin film on $LiNbO_3$ (solid blue line) and SiO_2 (dashed red line) substrates, demonstrating structural differences with expanded views of peak regions around 32.67° and 19.54°. 122

5.7 (a) Continuous-wave (CW) HODSAR measurements of the pentacene-deposited MMSAR device with 60 repetitions. The fluorescence data are presented with error bars indicating the standard deviation, with a resolution of 100 kHz. The dashed black box highlights a high-Q mode centered around 105 MHz. (b) S_{21} transmission measurements of the MMSAR device, focusing on the region within the black dashed box in (a). Four distinct high-Q resonant modes are observed, facilitating the coupling to the T_x-T_y transition of the pentacene triplet state. (c) HODSAR readout of the spin-acoustic coupling, shown in comparison with CW-EPR spectroscopy measurements of the hyperfine-coupled ESR. Notably, both readouts exhibit a similar bandwidth, although the line shape in (c) may be influenced by the limited high-Q multimode response of the MMSAR device across the 100-110 MHz range. The electro-mechanical properties of the MMSAR device are detailed in the Appendix. 124

5.8 Characterization of Rabi oscillations in the pentacene thin-film-based HODSAR device. (a) Time-domain measurement of the HODSAR signal, showing normalized signal intensity as a function of time, with the fitted Rabi oscillation overlaid in red. (b) Rabi frequency plotted as a function of the square root of applied power, with experimental data points and a linear fit illustrating power dependence. (c) Schematic of the experimental setup for Rabi oscillation measurements, indicating the timing of laser polarization, acoustic pulse length, and photon counting readout. This characterization validates the coherence and control of Rabi oscillations in the device. 125

B.1 Cross-section of a HEMT semiconductor device [41]. The 2DEG is formed in the undoped GaAs buffer layer near the interface with the undoped AlGaAs spacer. Carriers are supplied by the doped AlGaAs layer. 138

B.2 Small-signal equivalent circuit for HEMTs [42]. Each component is summarized in Table B.1. 139

B.3 Small-signal equivalent circuit for HEMT noise analysis [43]. 140

B.4 Noise analysis using the wave-approach method to characterize the LNA's noise parameters with heterodyne detection [44]. 143

B.5 Block diagram of the heterodyne detection setup for LNA characterization. The characterized LNA is connected to a heterodyne receiver and analyzed using a voltmeter with a logarithmic detector. Using the OSL Y-factor method, the LNA is connected among open, short, 50 Ω load, and cold 50 Ω load to collect data under four different conditions to solve the non-linear equations. 147

B.6 Setup of the heterodyne detection for LNA characterization. Left: The heterodyne detection setup. Right: The cold 50 Ω load soaked in a cup of liquid nitrogen. 147

B.7 Flow chart of the MCMC method for noise parameter model fitting. 149

B.8 Raw data measurement with phase shifter from 0 to 650° and initial curve fitting using the Levenberg–Marquardt method. 149

B.9 The fitting process of the MCMC method. 149

B.10 Corner plot showing the relationships between noise parameters obtained using the MCMC method. 150

C.1 Rabi oscillation experiments conducted at 300 K on 0.1% BDPA doped o-terphenyl in the solid phase. (a) Normalized Rabi intensity as a function of nutation pulse length for various attenuation levels (0 dB to -12 dB). The grey dashed lines represent the fitting curves. (b) Linear relationship between Rabi frequency shift and normalized attenuation, highlighting the proportional increase in Rabi frequency with decreasing attenuation. 152

C.2 Rabi oscillation experiments conducted at 200 K on 0.1% BDPA doped o-terphenyl in the solid phase. (a) Normalized Rabi intensity as a function of nutation pulse length for various attenuation levels (0 dB to -12 dB). The grey dashed lines represent the fitting curves. (b) Linear relationship between Rabi frequency shift and normalized attenuation, highlighting the proportional increase in Rabi frequency with decreasing attenuation. 152

C.3 Rabi oscillation experiments conducted at 150 K on 0.1% BDPA doped o-terphenyl in the solid phase. (a) Normalized Rabi intensity as a function of nutation pulse length for various attenuation levels (0 dB to -12 dB). The grey dashed lines represent the fitting curves. (b) Linear relationship between Rabi frequency shift and normalized attenuation, highlighting the proportional increase in Rabi frequency with decreasing attenuation. 153

C.4 Rabi oscillation experiments conducted at 70 K on 0.1% BDPA doped o-terphenyl in the solid phase. (a) Normalized Rabi intensity as a function of nutation pulse length for various attenuation levels (0 dB to -12 dB). The grey dashed lines represent the fitting curves. (b) Linear relationship between Rabi frequency shift and normalized attenuation, highlighting the proportional increase in Rabi frequency with decreasing attenuation. 153

C.5 Rabi oscillation experiments conducted at 5 K on 0.1% BDPA doped o-terphenyl in the solid phase. (a) Normalized Rabi intensity as a function of nutation pulse length for various attenuation levels (0 dB to -12 dB). The grey dashed lines represent the fitting curves. (b) Linear relationship between Rabi frequency shift and normalized attenuation, highlighting the proportional increase in Rabi frequency with decreasing attenuation. 153

C.6 Rabi oscillation experiments conducted at 300 K on 0.1% BDPA doped o-terphenyl in the solid phase. (a) Normalized Rabi intensity as a function of nutation pulse length for various attenuation levels (0 dB to -12 dB). The grey dashed lines represent the fitting curves. (b) Linear relationship between Rabi frequency shift and normalized attenuation, highlighting the proportional increase in Rabi frequency with decreasing attenuation. 154

C.7 Rabi oscillation experiments conducted at 300 K on 0.1% BDPA doped o-terphenyl in the liquid phase. (a) Normalized Rabi intensity as a function of nutation pulse length for various attenuation levels (0 dB to -12 dB). The grey dashed lines represent the fitting curves. (b) Linear relationship between Rabi frequency shift and normalized attenuation, highlighting the proportional increase in Rabi frequency with decreasing attenuation. 154

E.1 (a) Schematic illustration of the simulation geometry with the used mesh showing the pentacene sample on the lithium niobate substrate. The corresponding simulation results are depicted in the subsequent three figures: (a) the displacement field, (b) the electric field, and (c) the magnetic field around the pentacene sample. Deformation is added to the displacement field for visualization purposes. [The simulation and calculation in the Appendix E are done by Xiaotian Xu.] 161

Chapter 1

Introduction

1.1 Motivation

Over the past century, quantum mechanics has evolved from a theoretical construct into the cornerstone of transformative technologies reshaping modern engineering and scientific research. Currently, quantum technology is advancing in several key areas: (1) quantum computing[45, 46, 47] (including quantum memory[48, 49]), (2) quantum sensing[50], and (3) quantum networks[51, 52]. These technologies exploit quantum entanglement and superposition to transcend the limitations of classical systems[53].

In quantum computing, the design of quantum logic gates enables exponential or quadratic speedups compared to traditional transistor-based computing (such as CPUs or GPUs)[54, 55, 47, 56]. Computational accuracy is enhanced through data encoding in Hilbert space[57], enabling higher precision and better characterization of high-dimensional features while also providing quantum speedup[58]. Quantum sensing achieves superior precision and accuracy over conventional methods[59, 60], while quantum networks offer enhanced information security compared to classical networks[61].

Despite significant experimental achievements, the widespread adoption of quantum technologies in everyday applications remains constrained by major challenges. Chief among these,

particularly in microwave-based signal processing, is the reliance on cryogenic temperatures to maintain quantum coherence and suppress thermal noise[62, 63, 64], which is critical for the operation of most current quantum devices. This necessity for extreme cooling increases the complexity and cost of quantum systems[65], hindering their scalability and portability, and limiting their practical utility and accessibility.

Innovation in materials is also crucial[66, 67]. Quantum materials require long coherence times to ensure the fidelity of quantum information processing[68, 69]. Furthermore, the integration of quantum components or systems, and the effective miniaturization and modular integration of these systems[70] (analogous to the integration achieved with the invention of the transistor), will greatly impact the applicability of quantum technologies.

This thesis aims to address these formidable challenges by pioneering advancements in three critical areas under room-temperature environments: (1) Development of a Quantum Error-Mitigation Protocol for Readout Measurement, (2) Synthesis of Processable Solid-State Quantum Materials and (3) Design of Novel Spin-Phonon Coupling Devices with Molecular Thin Films for Heterogeneous Integration and Miniaturization.

By exploring the intricate interplay between thermal dynamics, material properties, and novel coherent control techniques, this research aspires to lay the foundational groundwork for next-generation quantum devices that are both high-performing and operationally viable in everyday environments.

The significance of realizing room-temperature quantum devices extends beyond convenience; it represents a paradigm shift that can amplify the impact and applicability of quantum technologies. From achieving ubiquitous quantum-enhanced sensing in diverse environments to fostering the development of scalable and energy-efficient quantum computers, the successful realization of room-temperature quantum systems is expected to unleash unprecedented technological capabilities. This thesis is dedicated to making significant contributions to the transformative journey of bridging the gap between the theoretical potential of quantum mechanics and its practical applications, as already demonstrated by the room-temperature solid-state maser[71, 72, 73, 74].

This thesis addresses the challenge of room-temperature operation by introducing innovations in three key areas:

1. **Development of a Practical Protocol for Microwave Active Pre-Cooling to Overcome Thermal Noise Limits:**

   Thermal photons within microwave cavities at room temperature significantly contribute to noise, degrading the signal-to-noise ratio (SNR) of quantum measurement systems. This research develops a practical protocol to reduce the thermal photon population in microwave cavities without resorting to cryogenic cooling. By effectively "pre-cooling" the cavity, the protocol aims to enhance the SNR, thereby improving the performance of quantum sensing and quantum computing applications operating under ambient conditions.

2. **Synthesis and Characterization of Processable Solid-State Quantum Materials:**

   The advancement of quantum information processing (and quantum memory) relies heavily on materials that can sustain quantum coherence at room temperature and are compatible with device fabrication processes. This thesis examines the creation of processable solid-state quantum materials that have long coherence times, making them suitable for applications in quantum memory and quantum sensing. By synthesizing and thoroughly characterizing these materials, the research aims to identify candidates that exhibit long coherence times and can be integrated into practical quantum devices.

3. **Design and Implementation of a Novel Spin-Phonon Coupling Quantum Device with Molecular Thin Films:**

   Spin-phonon interactions offer a promising mechanism for coherently controlling quantum states and facilitating information transfer in quantum systems. This work designs and implements a novel quantum device that exploits spin-phonon coupling within molecular thin films. The device serves as a new platform for quantum sensing, potentially miniaturizing or integrating current quantum sensing systems and providing an alternative paradigm for quantum computing or quantum networking.

By systematically addressing these areas, the thesis aims to make significant contributions to the development of practical, room-temperature quantum devices. The innovations presented have the potential to overcome one of the primary barriers to the widespread adoption of quantum technologies. Success in these endeavors could lead to transformative impacts across various sectors, enabling the integration of quantum devices into everyday technologies and fostering advancements in fields such as secure communication, high-precision sensing, and powerful computation.

1.2 Outline of the Thesis

Chapter 2 presents the background theory across four main sections. Section 2.1, Theory I: Electron Paramagnetic Resonance, begins with an introduction to EPR (2.1.1), outlining the fundamental principles of how unpaired electron spins interact with external magnetic fields. It then addresses the anisotropy of the electronic g-value (2.1.2) and zero-field splitting (2.1.3), both of which are essential for interpreting EPR spectra. Section 2.1.4 reviews various EPR spectroscopy techniques—continuous-wave, time-resolved, and pulsed—while Section 2.1.5 examines EPR spectrometer sensitivity and the constraints imposed by noise. Section 2.2, Theory II: Overcoming Thermal-Noise Limits in Microwave Measurements, explores strategies for mitigating thermal noise in microwave cavities. It introduces the concept of photon number inside a cavity (2.2.1) and mode temperature (2.2.2), followed by cavity cooling via a lossy transmission line (2.2.3), and an expansion on multiple cooling ports (2.2.4 and 2.2.5). Concluding this part, Section 2.2.6 discusses the theoretical noise analysis of active pre-cooling (APC) to enhance sensitivity in quantum measurements. Section 2.3, Theory III: Pulse EPR Methods and Their Applications, investigates how pulse EPR measurements (2.3.1) are utilized to study quantum coherence in electron spin systems, focusing on pulse sequence design, analysis techniques, and the potential for maintaining coherence at room temperature. Finally, Section 2.4, Theory IV: Quality Factor Definitions in Microwave Systems, details how to measure Q-factors (2.4.1) by reviewing the theoretical background and experimental methods required for accurate Q-factor determination, which is key to the integration and miniaturization of quantum devices.

Chapter 3, Overcoming the Thermal-Noise Limit by APC Protocol, details the proposed strategy for suppressing thermal background and enhancing spectrometer sensitivity through the Active Pre-Cooling (APC) approach. Section 3.1 introduces the concept of APC with active cold loads, emphasizing their critical role in noise reduction. Section 3.2 describes the experimental setup of an active-pre-cooled TR-EPR spectrometer, followed by Section 3.3, which explores the use of a low-noise amplifier as an active cold load for further noise mitigation. Section 3.4 discusses the practical implementation of the APC protocol, and Section 3.5 explains the switchover phase preceding the interrogation step under optimized low-noise conditions. Section 3.6 then presents the results and analysis that validate the effectiveness of APC, and Section 3.7 concludes the chapter by summarizing key findings and suggesting avenues for future investigation.

Chapter 4 focuses on the exploration of photoexcited molecular electron spins as potential candidates for room-temperature quantum memory. Section 4.1 introduces the fundamental properties of photoexcited molecular electron spins and their relevance to quantum technologies, and Section 4.2 describes the experimental setup of this study. The experimental investigations are detailed in Section 4.3, which includes the study of spin coherence using pulsed EPR spectroscopy (4.3.1), probing of two-level quantum dynamics at room temperature (4.3.2), and the generation of radical spin polarization through photoexcited triplets (4.3.3). These results are critically discussed in Section 4.4, providing insights into the coherence properties and interaction mechanisms of the electron spins. The chapter discusses and concludes with key findings summarized in Section 4.5.

In Chapter 5, I introduce the novel technique of Heterogeneous Optically-Detected Spin-Acoustic Resonance (HODSAR) for the coherent control of molecular thin films. Section 5.1 provides an overview of HODSAR, explaining its principles and potential applications in quantum control. The experimental setup of the HODSAR spectrometer is detailed in Section 5.2, including the design considerations and operational parameters. The methods employed in device fabrication and system setup are thoroughly explained also in Section 5.2, encompassing 5.2.1 for device fabrication techniques and 5.2.2 for the HODSAR system configuration. The characterization of devices and thin films used in this study is discussed in Sections 5.2.3

and 5.2.4, respectively. Section 5.3 presents the experimental results demonstrating coherent acoustic control, with Section 5.3.1 focusing on continuous-wave HODSAR measurements and Section 5.3.2 on pulsed HODSAR measurements exhibiting Rabi oscillations. The chapter concludes with a discussion of the implications of these findings in Section 5.4.

Chapter 6 concludes the thesis by summarizing the significant achievements of the research and proposing future directions for advancing room-temperature technology. Section 6.1 encapsulates the key contributions, including the successful demonstration of the APC protocol to overcome thermal noise limitations and the development of HODSAR for coherent spin control. Section 6.2 outlines prospective future work, such as optimizing the APC technique for broader applications, further exploration of molecular electron spins, and the integration of these technologies into miniaturized quantum devices to facilitate practical and scalable quantum device solutions.

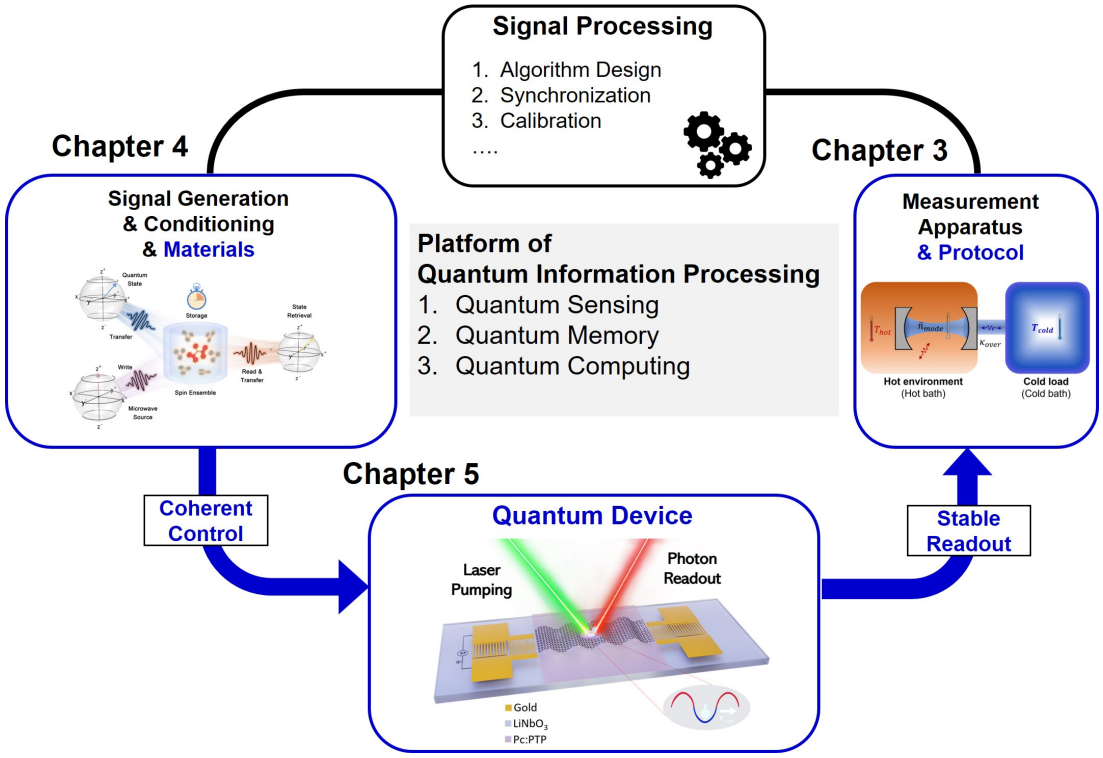

Figure 1.1: The schematic diagram depicts the quantum information processing platform, encompassing quantum sensing, memory, and computing. Development is organized into three primary components: (1) measurement apparatus and protocols (Chapter 3); (2) signal generation, conditioning, and materials (Chapter 4); and (3) quantum device development and integration (Chapter 5). Additionally, signal processing is integrated with algorithm design, synchronization, and calibration, as detailed in the experimental setups of each respective chapter.

1.3 Statement of Originality

This thesis is the culmination of my original research conducted at Imperial College London, under the supervision of Prof. Mark Oxborrow. The work presented herein contributes novel advancements to the field of room-temperature quantum devices, specifically in the following areas:

1. **First Demonstration of a Practical Protocol for Microwave Active Pre-Cooling:**

   Developed and implemented a novel protocol to reduce the thermal photon population in microwave cavities using a low-noise amplifier at room temperature. This method enhances the SNR of quantum measurement systems without the need for cryogenic cooling, thereby improving the performance of quantum sensing and quantum computing applications operating under ambient conditions.

2. **Development of Processable Solid-State Radical Materials for Quantum Information Storage:**

   Synthesized and characterized new solid-state, processable radical materials suitable for quantum information storage at room temperature. These materials exhibit long coherence times and are compatible with existing device fabrication processes, representing a significant advancement in quantum memory technologies.

3. **Design and Implementation of a Heterogeneously Integrated Spin-Phonon Coupling Device with Molecular Thin Films:**

   Designed and fabricated a novel quantum device that heterogeneously integrates spin-phonon coupling mechanisms within molecular thin films. This device serves as a new platform for quantum memory and quantum sensing at room temperature, potentially overcoming the integration and miniaturization problems that the platform of quantum information process face.

1.4 Publications List

Publications Associated with the Thesis

1. **Overcoming the Thermal-Noise Limit of Microwave Measurements by Precooling with an Active Cold Load**

   K. C. Chen, M. Oxborrow. *Physical Review Applied (Accepted).*

   Available at: arXiv:2408.053712. Patent Filed: WO/2024/042,336.

2. **Unlocking the Potential of Photoexcited Molecular Electron Spins for Room Temperature Quantum Information Processing**

   K. C. Chen, A. Collauto, C. J. Rogers, S. Yu, M. Oxborrow, M. Attwood.

   Materials for Quantum Technology 4 (4), 045901.

   Available at: arXiv:2408.16743.

3. **Heterogeneous Optically-Detected Spin-Phonon Coupling in Spin Molecular Thin-film**

   K. C. Chen, Y. Wen, X. Xu, M. Attwood, J. Xu, C. Fu, S. Ramadan, S. Yu, S. Heutz, M. Oxborrow

   (in Preparation).

Other Publication Associated with Quantum Computing

4. **Shedding Light on the Future: Exploring Quantum Neural Networks through Optics**

   S. Yu, Z. Jia, A. Zhang, E. Mer, Z. Li, V. Crescimanna, ***K. C. Chen***, R. B. Patel, *Advanced Quantum Technologies* (2024): 2400074.

   Available at: arXiv:2409.025332.

5. **Validating Large-Scale Quantum Machine Learning: Efficient Simulation of Quantum Support Vector Machines Using Tensor Networks**

   K. C. Chen, T. Y. Li, Y. Y. Wang, S. See, C. C. Wang, R. Wille, N. Y. Chen, A. C. Yang, *Machine Learning: Science and Technology (IOP Publishing) (Accepted)*. Available at: arXiv:2405.02630.

Conference Papers

6. **Short-Depth Circuits and Error Mitigation for Large-Scale GHZ-State Preparation, and Benchmarking on IBM's 127-Qubit System**

   K. C. Chen. Presented at the *2023 IEEE International Conference on Quantum Computing and Engineering (QCE)*, September. 2023, pp. 1–20.

7. **Quantum-Classical-Quantum Workflow in Quantum-HPC Middleware with GPU Acceleration**

   K. C. Chen, X. Li, X. Xu, Y. Y. Wang, C. Y. Liu. Presented at the *2024 International Conference on Quantum Communications, Networking, and Computing (QCNC)*, September 2024.

8. **Quantum-enhanced Support Vector Machine for Large-Scale Multi-class Stellar Classification**

   K. C. Chen, X. Xu, H. Makhanov, H. H. Chung, C. Y. Liu. Presented at the *International Conference on Intelligent Computing (ICIC)*, pp. 155–168, June 2024.

9. **CompressedMediQ: Hybrid Quantum Machine Learning Pipeline for High-Dimensional Neuroimaging Data**

   K. C. Chen, Y. T. Li, T. Y. Li, C. Y. Liu, P. H. Lee, C. Y. Chen. Accepted by the *2025 IEEE International Conference on Acoustics, Speech, and Signal Processing (ICASSP)*, April 2025.

10. **Consensus-based Distributed Quantum Kernel Learning for Speech Recognition**

    K. C. Chen, W. Ma, X. Xu. Accepted by the *2025 IEEE International Conference on Acoustics, Speech, and Signal Processing (ICASSP)*, April 2025.

11. **Quantum-Trained Convolutional Neural Network for Deepfake Audio Detection**

    C. H. A. Lin, C. Y. Liu, S. Y. C. Chen, ***K. C. Chen*** Accepted by the *2025 IEEE International Conference on Acoustics, Speech, and Signal Processing (ICASSP)*, April 2025.

12. **Quantum-Train with Tensor Network Mapping Model and Distributed Circuit Ansatz**

    C. Y. Liu, C. H. A. Lin, ***K. C. Chen***. Accepted by the *2025 IEEE International Conference on Acoustics, Speech, and Signal Processing (ICASSP)*, April 2025.

13. **HamilToniQ: An Open-Source Benchmark Toolkit for Quantum Computers**

    X. Xu, ***K. C. Chen***, R. Wille. Presented at the *2024 IEEE International Conference on Quantum Computing and Engineering (QCE)*, September 2024.

14. **Quantum Computing for Climate Resilience and Sustainability Challenges**

    K. T. M. Ho, ***K. C. Chen***, L. Lee, F. Burt, S. Yu, P. H. Lee. Presented at the *2024 IEEE International Conference on Quantum Computing and Engineering (QCE)*, September 2024.

15. **Learning Quantum Phase Estimation by Variational Quantum Circuits**

    C. Y. Liu, C. H. A. Lin, ***K. C. Chen***. Presented at the *2024 IEEE International Joint Conference on Neural Networks (IJCNN)*, June 2024.

16. **QTRL: Toward Practical Quantum Reinforcement Learning via Quantum-Train**

C. Y. Liu, C. H. A. Lin, C. H. H. Yang, ***K. C. Chen***, M. H. Hsieh. Presented at the *2024 IEEE International Conference on Quantum Computing and Engineering (QCE)*, September 2024.

17. **Generalised Circuit Partitioning for Distributed Quantum Computing**

F. Burt, ***K. C. Chen***, K. Leung. Presented at the *2024 IEEE International Conference on Quantum Computing and Engineering (QCE)*, September 2024.

18. **Quantum-Train Long Short-Term Memory: Application on Flood Prediction Problem**

C. H. A. Lin, C. Y. Liu, ***K. C. Chen***. Presented at the *2024 IEEE International Conference on Quantum Computing and Engineering (QCE)*, September 2024.

19. **Noise-Aware Detectable Byzantine Agreement for Consensus-based Distributed Quantum Computing**

K. C. Chen, M. Prest, F. Burt, S. Yu. Accepted by the *2025 International Conference on Quantum Communications, Networking, and Computing (QCNC)*, March 2025.

20. **Quantum Kernel-Based Long Short-term Memory for Climate Time-Series Forecasting**

Y. C. Hsu, N. Y. Chen, T. Y. Li, P. H. Lee, ***K. C. Chen***. Accepted by the *2025 International Conference on Quantum Communications, Networking, and Computing (QCNC)*, March 2025.

21. **Resource-Efficient Compilation of Distributed Quantum Circuits for Solving Large-Scale Wireless Communication Network Problems**

K. C. Chen, F. Burt, S. Yu, C. Y. Liu,M. H. Hsieh, K. Leung . Accepted by *2025 IEEE International Symposium on Circuits and Systems (ISCAS)*, May 2025.

Official Government Publications

1. **Regulating Quantum Technology Applications**
   Department for Science, Innovation and Technology and Regulatory Horizons Council. *Independent report*. Published 28 February 2024. Available at: GOV.UK.

Patent

1. **Method and Apparatus for Reducing the Noise Temperature of Systems Comprising Samples which Interact with Oscillating Electromagnetic Fields Supported by Electromagnetic Resonators**
   K. C. Chen, M. Oxborrow. *WO Patent WO/2024/042,336*, 2024.

Contributed Talks

1. Quantum Transfer Learning for Digital Image Processing: Application to Biosensing and Medical Image Processing. *31st International Materials Research Congress*, 13-18 August 2023, Cancun, Mexico

2. Short-Depth Circuits and Error Mitigation for Large-Scale GHZ-State Preparation, and Benchmarking on IBM's 127-Qubit System, *4th IEEE International Conference on Quantum Computing and Engineering*, 17-22 September 2023, Washington, USA

3. Quantum-Classical-Quantum Workflow in Quantum-HPC Middleware with GPU Acceleration, *1st International Conference on Quantum Communications, Networking, and Computing*, 1-3 July, 2024 · Kanazawa, Japan

4. Quantum Support Vector Machine for Large-Scale Multi-Class Stellar Classification, *20th International Conference on Intelligent Computing*, 5-8 August 2024, Tianjin, China

5. Noise-Aware Distributed Quantum Approximate Optimization Algorithm on Near-term Quantum Hardware, *5th IEEE International Conference on Quantum Computing and Engineering*, 15-20 September 2024, Montreal, Canada

Chapter 2

Background Theory

In this chapter, I first review the principles of electron paramagnetic resonance (EPR) spectroscopy and the various types of EPR techniques. I then discuss the measurement sensitivity and examine how thermal noise affects EPR measurements. In Section 2.2, I use a wave-based approach to derive/model a method for using an active cold load to remove thermal photons from the microwave cavity, thereby improving the sensitivity of quantum metrology. This theoretical framework underpins the analysis in Chapter 3, where I explore how implementing an active cold load enhances the signal-to-noise ratio (SNR) in a quantum sensing scenario.

Subsequently, I review different pulsed EPR protocols, which will serve as critical background material in Chapter 4. There, I will apply these protocols to characterize the quantum properties of my candidate material, including coherence time and phase memory time, in the context of quantum memory. Finally, I explain how to accurately determine and calibrate the quality factor of the microwave cavity, completing the foundational groundwork for the experimental and theoretical investigations presented in Chapter 3 and 5.

2.1 Theory I: Electron Paramagnetic Resonance, Spectrometer Sensitivity, and Thermal-Noise Limits in Microwave Measurements

2.1.1 Introduction of Electron Paramagnetic Resonance

EPR spectroscopy, also known as Electron Spin Resonance (ESR) spectroscopy[75], is a pivotal tool for studying materials with unpaired electrons providing insights into their electronic structure and dynamics. The fundamental principle involves the resonant absorption of microwave radiation by electron spins in an external magnetic field. When a sample containing paramagnetic species is subjected to a static magnetic field, the energy levels of the electron spins split due to the Zeeman effect[1]. By irradiating the sample with microwaves at frequencies corresponding to these energy transitions, transitions between spin states can be induced, which are then detected and analyzed.

Fundamental Principles of EPR

At the core of EPR spectroscopy lies the behavior of electron spins in a magnetic field. Consider an isolated electron with a spin quantum number $S = \frac{1}{2}$. In the absence of an external magnetic field, the two possible spin states—spin-up ($m_S = +\frac{1}{2}$) and spin-down ($m_S = -\frac{1}{2}$)—are degenerate, possessing identical energies. However, when an external magnetic field $\mathbf{B}_0$ is applied, this degeneracy is lifted due to the Zeeman effect, resulting in two distinct energy levels. The energy difference between these levels, ΔE, shown in Fig. 2.1, is directly proportional to the magnetic field strength and is expressed as[1]:

$$\Delta E = g_e \mu_B B_0 \tag{2.1}$$

In this context, g_e refers to the electron g-factor, which is approximately 2.0023 for a free

electron (more details will be provided in the next part). The symbol μ_B represents the Bohr magneton, valued at 9.274×10^{-24} J·T^{-1}, while B_0 indicates the strength of the applied magnetic field. The magnetic moment of the electron, $\boldsymbol{\mu}_e$, is defined by the relation[76]:

$$\boldsymbol{\mu}_e = -g_e\mu_B\hat{\mathbf{S}} \tag{2.2}$$

An EPR transition occurs when the energy of the microwave radiation, $h\nu$, matches the energy gap between the spin states, satisfying the resonance condition[76]:

$$h\nu = \Delta E = g_e\mu_B B_0 \tag{2.3}$$

This resonance condition enables the absorption of microwave photons, thereby inducing transitions between the spin states. Through this mechanism, EPR spectroscopy effectively probes the magnetic properties of materials by detecting the transitions of electron spins under varying magnetic fields.

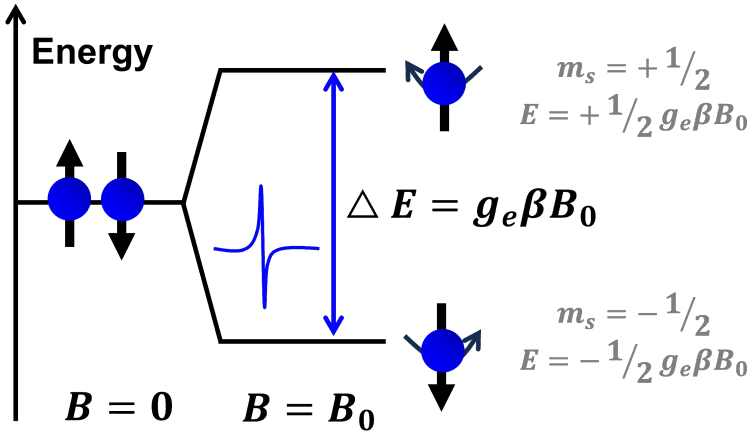

Figure 2.1: Zeeman splitting diagram depicting the energy levels of an isolated electron in the presence of an external magnetic field. The spin-up state has a higher energy level, while the spin-down state corresponds to a lower energy level. The blue trace illustrates the response EPR signal generated as the electron transitions between these spin states[1].

2.1.2 Anisotropic of the Electronic g-Value

The electronic g-value is a dimensionless parameter that characterizes the position of the resonance field in EPR spectroscopy. It reflects the magnetic interactions experienced by an unpaired electron within a specific chemical environment. For a free electron, where spin is the sole contributor to its magnetic moment, the g-value (g_e) is approximately 2.0023. Deviations from this value indicate the influence of the local environment on the electron's magnetic properties.

The g-value can be determined using the fundamental equation[76]:

$$g_e = \frac{h\nu_{\text{res}}}{\mu_B B_0}, \tag{2.4}$$

where h is Planck's constant ($6.626 \times 10^{-34}\,\text{J} \cdot \text{s}$) and ν_{res} is the resonance frequency. In a common X-band EPR spectrometer operating at a resonance frequency of $\nu_{\text{res}} = 9.8\,\text{GHz}$, the corresponding magnetic field B_0 is approximately 350 mT.

In isotropic systems, shown in Fig 2.2(a), the g-value is identical in all spatial directions, denoted as $g_{\text{iso}} = g_{xx} = g_{yy} = g_{zz}$. This isotropy indicates that the EPR signal is independent of the molecular orientation relative to the applied magnetic field, a scenario often observed in solutions where rapid molecular motion averages out anisotropic interactions.

Conversely, in anisotropic systems, shown in Fig. 2.2(b) and (c), the g-value depends on the orientation of the molecule relative to the magnetic field. This anisotropy arises from interactions such as spin-orbit coupling, which are significant in systems containing heavy atoms like paramagnetic metal ions, particularly trivalent lanthanides. In these cases, the g-factor is described by a second-rank tensor, represented as a 3×3 matrix:

$$\mathbf{g} = \begin{pmatrix} g_{xx} & g_{xy} & g_{xz} \\ g_{yx} & g_{yy} & g_{yz} \\ g_{zx} & g_{zy} & g_{zz} \end{pmatrix}. \tag{2.5}$$

When the principal axes of the system coincide with the coordinate axes (thereby diagonalizing the g-tensor), the off-diagonal terms become zero, simplifying the tensor to its principal components g_x, g_y, and g_z:

$$\mathbf{g} = \begin{pmatrix} g_x & 0 & 0 \\ 0 & g_y & 0 \\ 0 & 0 & g_z \end{pmatrix}. \tag{2.6}$$

For systems with axial symmetry, shown in Fig. 2.2(b), two of the principal components are equal, leading to $g_{\parallel} = g_z$ and $g_{\perp} = g_x = g_y$. The effective g-value as a function of the orientation

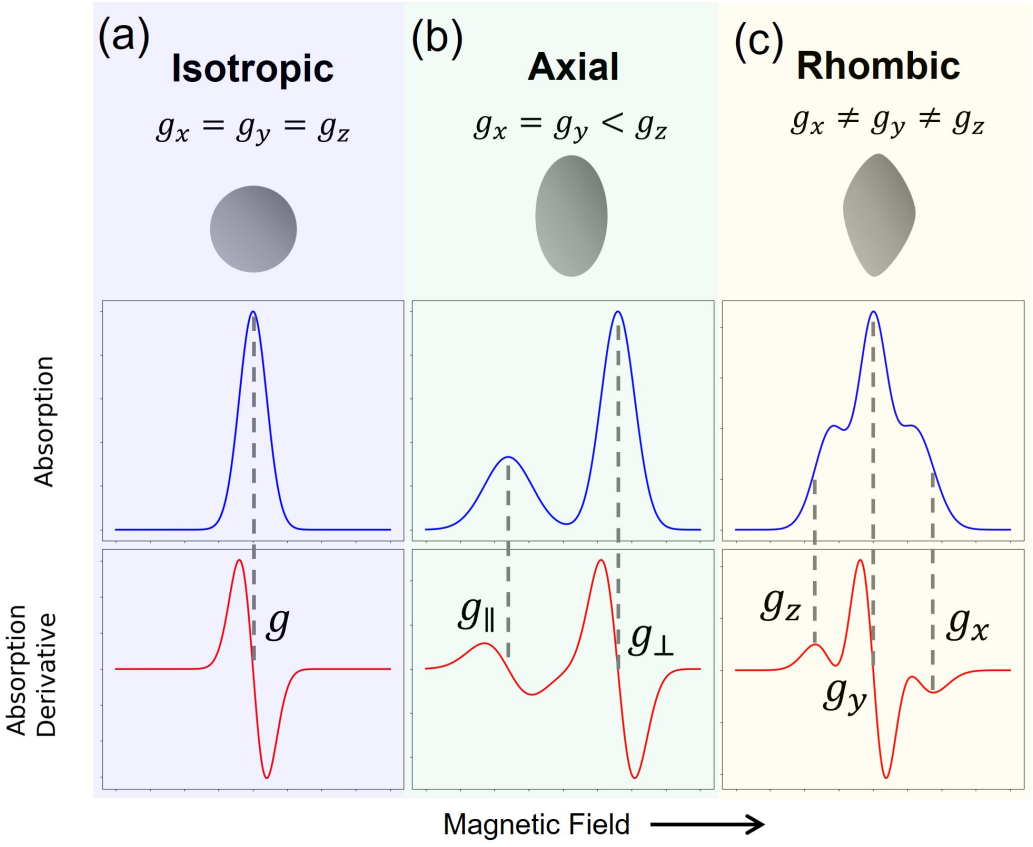

Figure 2.2: Schematic representation of the magnetic moment states of a paramagnetic center, depicting the associated g-factor anisotropy and corresponding EPR spectrometer lineshapes. The top row illustrates varying molecular symmetries leading to isotropic (a), axial (b), and rhombic (c) g-tensor components. The middle and bottom rows display the absorption spectra (blue) and their first derivative signals (red), highlighting characteristic g-values such as $g_{\parallel}$, $g_{\perp}$, g_x, g_y, and g_z for different symmetries. Vertical dashed lines indicate peak positions corresponding to different g-factors[2].

angle θ with respect to the principal z-axis is given by[76]:

$$g_\theta^2 = g_\parallel^2 \cos^2\theta + g_\perp^2 \sin^2\theta, \tag{2.7}$$

where θ is the angle between the magnetic field direction and the z-axis. This equation illustrates how the observed g-value varies with molecular orientation in anisotropic systems.

In situations involving rhombic symmetry, as illustrated in Fig 2.2(c), all three principal components differ from one another ($g_x \neq g_y \neq g_z$). This leads to a complex relationship with molecular orientation. However, since this thesis primarily focuses on isotropic systems, I will not discuss this case further.

2.1.3 Zero-Field Splitting

In systems with spin $S \geq 1$, such as triplet states ($S = 1$) discussed in Chapter 5, the degeneracy of the spin sublevels is lifted even in the absence of an external magnetic field due to dipole–dipole interactions between unpaired electrons. This phenomenon, known as zero-field splitting (ZFS), is described by the Hamiltonian[5, 77]:

$$H_{\mathrm{ZFS}} = \mathbf{S} \cdot \mathbf{D} \cdot \mathbf{S} = -XS_x^2 - YS_y^2 - ZS_z^2, \tag{2.8}$$

where $-X$, $-Y$, and $-Z$ are the principal values of the ZFS tensor $\mathbf{D}$, and due to its traceless nature, $X + Y + Z = 0$.

In organic semiconductors, particularly within conjugated systems, ZFS is often described using the spin Hamiltonian[5, 77]:

$$H = D\left(S_z^2 - \frac{1}{3}S(S+1)\right) + E\left(S_x^2 - S_y^2\right), \tag{2.9}$$

where S_x, S_y, and S_z are the spin operators, and D and E are the axial and rhombic ZFS

parameters representing the axial and transverse components of the magnetic dipole–dipole interaction, respectively.

The ZFS parameters are related to the principal values of the tensor by:

$$\begin{aligned} D &= -\frac{1}{2}(X+Y) - Z = -\frac{3}{2}Z, \\ E &= -\frac{1}{2}(X-Y). \end{aligned} \tag{2.10}$$

Consequently, the energy levels of the triplet sublevels T_X, T_Y, and T_Z correspond to the axes of the ZFS tensor, with energies:

$$\begin{aligned} E_x &= X = \frac{1}{3}D - E, \\ E_y &= Y = \frac{1}{3}D + E, \\ E_z &= Z = -\frac{2}{3}D. \end{aligned} \tag{2.11}$$

As illustrated in Figure 2.3, the ordering of the triplet state sublevels depends on the signs of the ZFS parameters and the molecular symmetry.

The signs of D and E are directly related to molecular symmetry and spin density distribution.[78] In organic compounds, especially aromatic ones where unpaired electron distribution is localized on atoms, ZFS is dominated by spin–spin interactions. The parameters D and E can be expressed as averages over the electronic wave functions:

$$\begin{aligned} D &= \frac{3}{4}\frac{\mu_0}{4\pi\hbar}(g_e\beta_e)^2 \left\langle \frac{1-3\cos^2\theta}{r^3} \right\rangle, \\ E &= \frac{3}{4}\frac{\mu_0}{4\pi\hbar}(g_e\beta_e)^2 \left\langle \frac{y^2-x^2}{r^5} \right\rangle, \end{aligned} \tag{2.12}$$

where r is the distance between unpaired spins, μ_0 is the vacuum permeability, θ is the angle between the interspin vector and the quantization axis, g_e is the electron g-factor, and β_e is the Bohr magneton.

These expressions highlight the relationship between molecular geometry and spin distribution.

A positive D corresponds to an oblate (disk-like) spin distribution with an angle of 90°, whereas a negative D indicates a prolate (cigar-like) distribution with an angle of 0°. The parameter E is associated with rhombic symmetry; for systems with axial symmetry, $E = 0$, while for lower symmetry systems, $E \neq 0$. In extreme cases like isolated atoms, both ZFS parameters are zero, resulting in degenerate triplet sublevels and a spherical spin distribution.

2.1.4 Type of EPR Spectroscopy

There are three primary EPR detection methods utilizing microwave irradiation: **continuous-wave (CW) EPR with lock-in detection**[79], **time-resolved EPR (tr-EPR) with direct detection using photon excitation**[80], and **pulsed EPR**[81]. Each method offers distinct

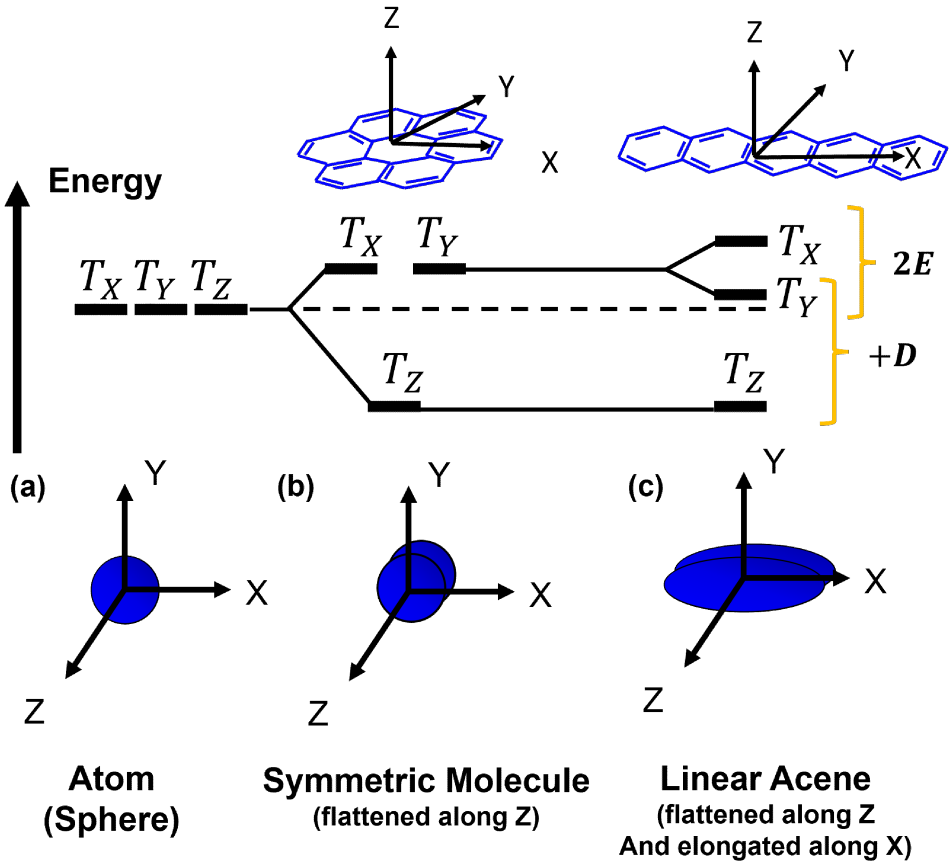

Figure 2.3: Diagram of degenerate triplet sublevel splitting energy: (a) In a spherically symmetric model, electron distribution leads to degenerate triplet states in three dimensions. (b) In a symmetric planar model (flattened along Z), the molecule is symmetric in the x–y plane with a nondegenerate sublevel T_z. (c) In an asymmetric planar model (flattened along Z and elongated along X), the molecule has three split states T_x, T_y, and T_z [3].

advantages and trade-offs in terms of signal-to-noise ratio (SNR), time resolution, and spectral information. Understanding the mechanisms and limitations of these methods is essential for optimizing EPR experiments and interpreting the resulting spectra.

Continuous-Wave EPR Methods

CW-EPR is significant due to the high SNR achieved through lock-in detection (discussed below). Therefore, CW-EPR can distinguish minute differences in the energy levels of electron spin systems. Furthermore, lock-in detection produces the first derivative of a transition's line shape, whereas pulsed detection produces the line shape directly. Recording EPR spectra in the presence of a continuous microwave field, as in a CW-EPR spectrometer, results in a much narrower excitation bandwidth than pulsed detection schemes [6].

The concept of CW-EPR involves the following steps:

1. **Continuous microwave irradiation** at a frequency identical to the transition frequency between each triplet sub-level.
2. **Excitation of the sample** through illumination, introducing polarized triplet states.
3. **Detection of the population difference** between specific sub-levels or the spin magnetization under a specific orientation by a microwave resonator, which is then read out by the receiver and converted into EPR signals [82].

Typically, in commercial EPR spectrometers (e.g., Bruker CW-EPR), measurements are carried out with a critically coupled microwave resonator, as shown in Figure 2.4. The quality factor (Q-factor) of the resonator determines its bandwidth and response time. There are two detection modes: one is **a.c. modulation with lock-in detection**, and the other is **direct detection**.

CW-EPR with Lock-in Detection For the operation of CW-EPR, as shown in Figure 2.6(a), modulation coils generate an alternating magnetic field that is superimposed on

the slowly ramping DC magnetic field produced by the spectrometer's electromagnet. These modulation coils (depicted in blue) are driven (generally through a voltage-to-current converting drive) by the "reference" output of the lock-in amplifier[83]. The output signal received by the detector is connected to a lock-in amplifier, referenced to the modulation frequency for phase-sensitive detection. Because of the magnetic field modulation introduced by the modulation coils, the detector records the CW-EPR spectra as the first derivative of the absorption signal.

The advantage of using lock-in detection is the significant enhancement in SNR. As illustrated in Figure 2.4, even if the signal is completely buried in noise, lock-in amplifiers can measure the amplitude and phase of a signal relative to a defined reference signal. With a typical magnetic field modulation frequency of 100 kHz, the lock-in detection technique achieves a time resolution of approximately 20 microseconds while maintaining a high SNR [84]. However, there is a trade-off between SNR and time resolution. By using a higher modulation frequency of 200 kHz and replacing the low-pass filter with signal averaging, De Jager et al. achieved a time resolution of less than one microsecond [85]. Although this method improved time resolution, detecting short-lived signals on the microsecond scale can still be challenging due to decreased SNR.

tr-EPR with Direct Detection tr-EPR, as shown in Figure 2.6(b) and also known as transient EPR, is a powerful technique for characterizing various short-lived excited species

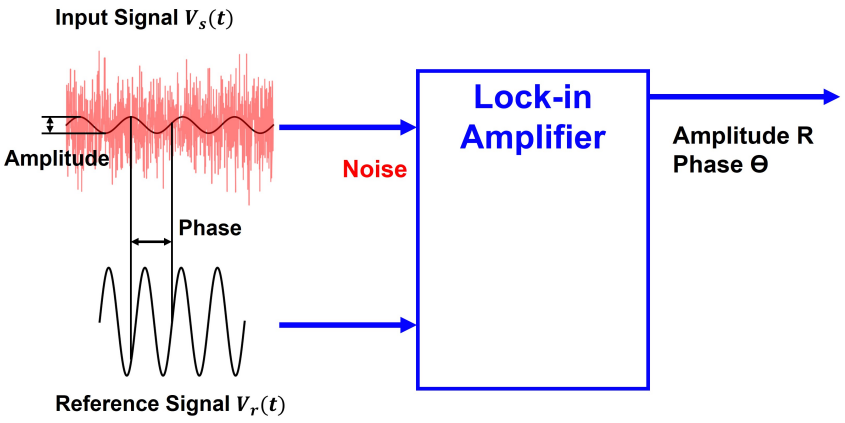

Figure 2.4: Principle of lock-in detection. The input signal $V_s(t)$, potentially obscured by noise, is extracted by the lock-in amplifier through mixing with a reference signal $V_r(t)$, enabling phase-sensitive detection [4].

created after light excitation of organic molecules. Developed in the late 1970s, tr-EPR allows the investigation of transient polarization of paramagnetic species [86]. The lifetimes accessible by tr-EPR range from a few nanoseconds to hundreds of microseconds, enabling the study of radical pairs and photo-excited triplet states. Triplet excitons reveal quantum information on various aspects, such as triplet routes and electronic structure.

Figure 2.5 illustrates the block diagram of a tr-EPR spectrometer in which the pulsed light source is synchronized with the detection system. In Figure 1.3, the time sequence scheme shows an EPR experiment where the transient signal is recorded after a laser flash without magnetic field modulation. tr-EPR signals can be detected directly, resulting in high time resolution due to the non-Boltzmann population of energy levels in spin-polarized paramagnetic states [6].

These EPR signals are detected in absorption or emission mode. The general principle involves using continuous microwaves to monitor the direct-detection EPR signal induced by a short laser pulse (on the nanosecond scale). The physical limit of the EPR's time resolution is given by the precession frequency of the magnetization vector about the external magnetic field, which is directly related to the frequency of the incident microwave. However, the slowest component in the signal path determines the actual time resolution, whether it is the detection bandwidth or the resonator.

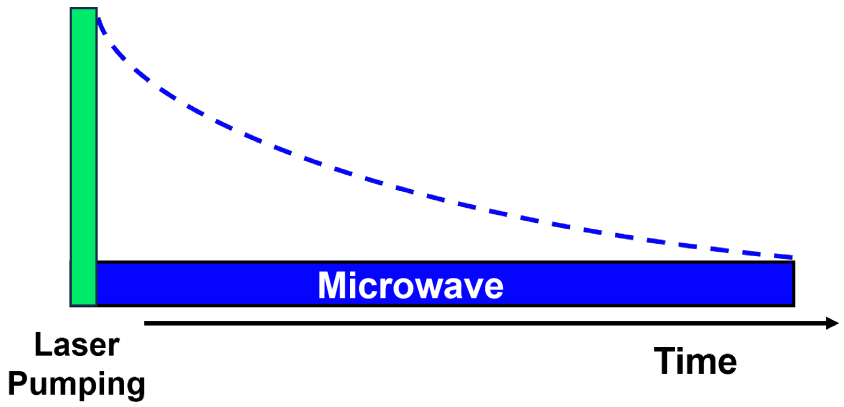

Figure 2.5: Time sequence scheme of a tr-EPR experiment with direct detection [5]. The transient signal is recorded post laser excitation without magnetic field modulation, operating on a timescale from nanoseconds to milliseconds.

The Q-factor of the resonator determines its time resolution. While a high Q-factor resonator enhances sensitivity in CW-EPR, it limits time resolution in tr-EPR due to its longer photon lifetime. The photon lifetime (cavity response time), τ_{cavity}, is defined by [87]:

$$\tau_{\text{cavity}} = \frac{Q_{\text{load}}}{2\pi f_0} \tag{2.13}$$

where Q_{load} is the loaded Q-factor and f_0 is the resonant frequency of the microwave cavity.

Pulsed EPR Methods

Pulsed EPR, as shown in Figure 2.6(c), extends the capabilities of EPR spectroscopy by utilizing sequences of microwave pulses to manipulate spin states and measure their coherent evolution over time[88]. Unlike CW-EPR, which provides steady-state information, pulsed EPR allows for the direct measurement of spin relaxation times and distances between spins through techniques such as Electron Spin Echo (ESE)[89] and Electron Spin Echo Envelope Modulation (ESEEM)[89].

Key features and advantages of pulsed EPR include:

1. **Spin Manipulation with Microwave Pulses**: Pulsed EPR employs short, intense microwave pulses to induce coherent rotations of the spin magnetization vector. By adjusting the duration and phase of these pulses, precise manipulations analogous to those in Nuclear Magnetic Resonance (NMR) spectroscopy can be performed [13].

2. **Measurement of Relaxation Times**: Pulsed EPR enables direct measurement of spin-lattice relaxation time (T_1) and spin-spin relaxation time (T_2) by monitoring the decay of spin echoes following specific pulse sequences.

3. **Distance Measurements**: Techniques such as Double Electron-Electron Resonance (DEER)[90] and Pulsed Electron Double Resonance (PELDOR)[91] allow determination of distances between unpaired electrons, valuable in studying the structures of biomolecules and complex materials [92].

4. **Suppression of Inhomogeneous Broadening**: Pulsed EPR can refocus dephasing caused by inhomogeneous magnetic fields, enhancing spectral resolution and sensitivity[93].

A typical pulsed EPR experiment employs sequences such as the two-pulse echo sequence (also known as Hahn Echo), where a $\pi/2$ pulse is followed by a delay τ, then a π pulse, and the echo signal is detected after an additional delay τ. The echo intensity as a function of τ provides information about spin relaxation processes. Details of pulsed EPR protocols are discussed in the next section. By varying delays and pulse parameters, experiments can probe specific interactions and dynamics within the spin system. Pulsed EPR techniques require instrumentation capable of generating precise microwave pulses and detecting weak echo signals. Advances in microwave technology and signal processing have expanded the applications of pulsed EPR to fields such as structural biology, materials science, and the characterization of quantum processing units.

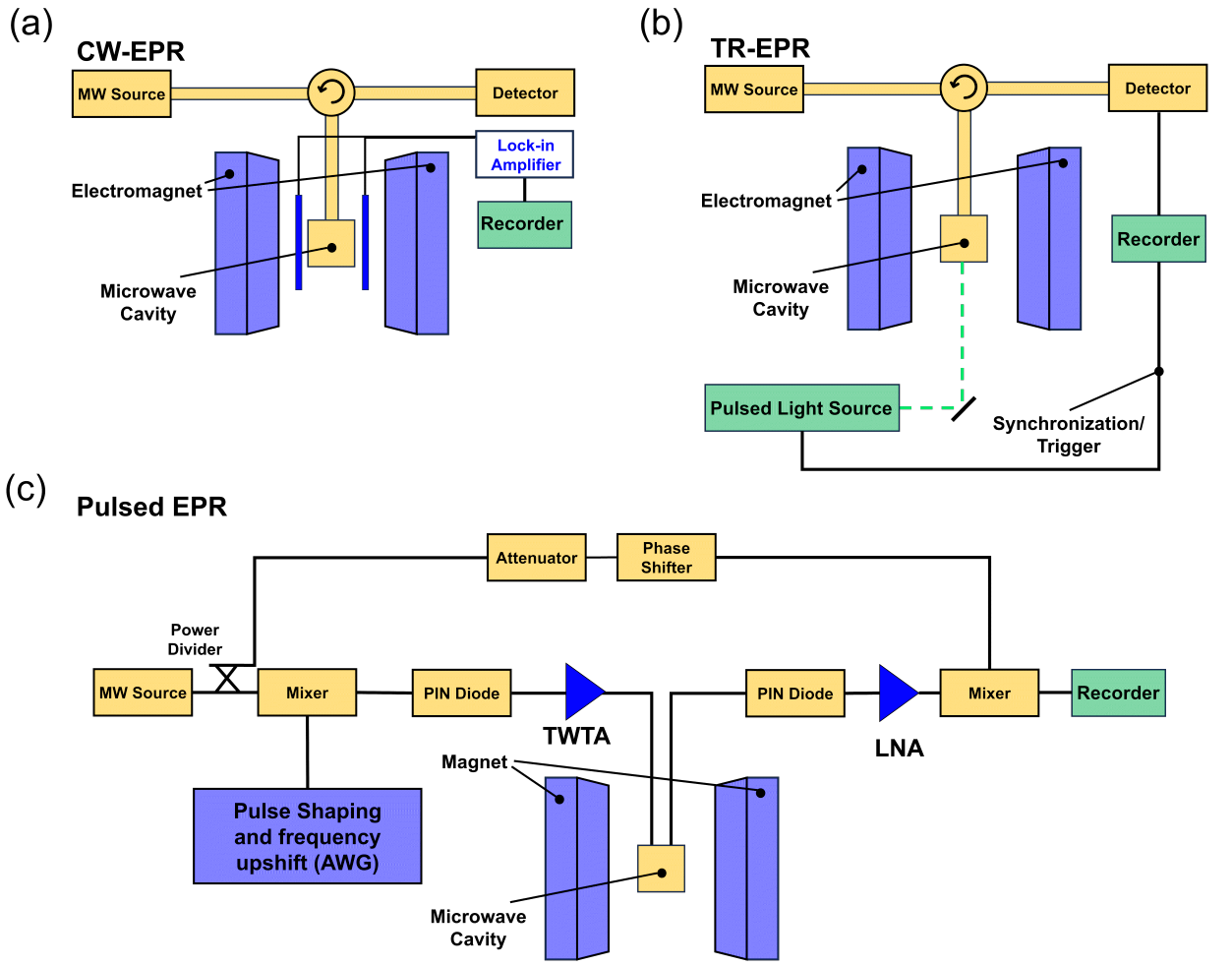

Figure 2.6: Schematics of three EPR spectrometer configurations for CW, time-resolved, and advanced pulsed EPR techniques. (a) CW-EPR with lock-in amplifier [6]. The sample is placed in a microwave cavity situated between the poles of the magnet. The microwave source feeds the microwave into the cavity through a circulator, and the microwave reflected from the cavity is directed toward the detector. For enhancing the SNR, additional modulation coils connected with the lock-in amplifier are introduced to the system. With respect to this external modulation, the CW-EPR signal is detected phase-sensitive. However, typically the modulation frequencies are in the range of 10-100 kHz, thus the time-resolution is limited by these modulation frequencies. (b) Time-Resolved EPR Spectrometer[6]: This setup modifies the CW approach by introducing a pulsed light source synchronized with pulsed MW fields directed at the sample. This configuration enables time-resolved detection of transient magnetic resonance signals, allowing the measurement of spin relaxation times and other dynamic processes. The detector and recorder capture the time-dependent response of the sample, providing insights into fast spin dynamics. (c) Pulsed EPR Spectrometer[7]: This configuration incorporates an AWG for custom pulse shaping and frequency modulation, along with components such as a mixer, PIN diode, attenuator, and phase shifter. These elements provide precise control over MW pulse sequences and their phases, enhancing sensitivity and specificity for advanced EPR experiments. This setup supports detailed exploration of spin dynamics and coherence, enabling pulse sequences and phase manipulations suitable for studies of quantum coherence and spin control.

Comparison and Considerations

When choosing between CW-EPR, tr-EPR, and pulsed EPR, researchers must consider the specific requirements of their study:

- **tr-EPR**: Suited for investigating fast transient phenomena, offering high temporal resolution necessary to capture rapid spin dynamics. It requires fast detection electronics and may suffer from lower SNR.
- **CW-EPR**: Ideal for high-sensitivity measurements of stable or slowly varying spin systems, providing detailed spectral information with excellent SNR. Lock-in detection enhances sensitivity but limits time resolution.
- **Pulsed EPR**: Offers the ability to manipulate spin states and measure relaxation times and distances between spins. It provides high spectral resolution and can suppress inhomogeneous broadening but requires complex instrumentation and precise control of microwave pulses.

The choice of detection method depends on the balance between temporal resolution, spectral resolution, and the specific information desired from the spin system.

2.1.5 Sensitivity of EPR Spectrometers

In this part, I discuss the sensitivity of EPR spectrometers by following Feher's classical analysis [94] and introduce ideas for improving their sensitivity. The detailed derivations are presented in Poole's book on Electron Spin Resonance (pp. 381–409) [95].

Design of Reflection-Type Microwave Cavities for EPR Spectroscopy

The resonance condition for a paramagnetic sample placed in a resonant microwave cavity is given by:

$$\hbar\omega_0 = g\beta H_0, \tag{2.14}$$

where $\hbar$ is the reduced Planck constant, g is the dimensionless g-factor (approximately 2.0023 for free electrons), β is the Bohr magneton, ω_0 is the angular frequency of the microwave cavity ($\omega_0 = 2\pi f_0$), and H_0 is the resonant magnetic field.

The average power absorbed per unit volume due to resonant absorption is defined as:

$$P = \frac{1}{2}\omega_0 H_1^2 \chi'', \tag{2.15}$$

where H_1 is the microwave magnetic field at the sample location, and χ'' is the imaginary part of the magnetic susceptibility.

To derive the change in the Q-factor Q of the cavity due to the sample's absorption, I start with the expression for the loaded Q-factor:

$$\frac{1}{Q} = \frac{1}{Q_u} + \frac{1}{Q_\chi}, \tag{2.16}$$

where Q_u is the unloaded Q-factor of the microwave cavity in the absence of resonant absorption,

and Q_χ represents the contribution from the sample's susceptibility. Assuming that $Q_\chi \gg Q_u$, the change in the Q-factor ΔQ can be expressed as [95]:

$$\Delta Q = -Q^2 \Delta \left(\frac{1}{Q}\right) = -\frac{Q_u^2}{Q_\chi} = \chi'' \eta Q_u^2, \tag{2.17}$$

where η is the filling factor, defined as the fraction of the cavity volume occupied by the sample, and $Q_\chi = \frac{1}{\chi'' \eta}$ because χ'' is assumed to be homogeneous over the sample volume (see Sec. 5-H in Poole's book [95]).

In a reflection-type microwave cavity, the reflected voltage E_r is given by:

$$E_r = E\Gamma = -E\left(1 - \frac{2\,\mathrm{VSWR}}{1 + \mathrm{VSWR}}\right), \tag{2.18}$$

where E is the incident voltage and Γ is the reflection coefficient. The voltage standing wave ratio (VSWR) for a reflection cavity is defined as:

$$\mathrm{VSWR} = \left(\frac{R_g n^2}{R_c}\right)^{\pm 1}, \tag{2.19}$$

with R_g being the internal resistance of the signal generator, R_c the resistance of the resonant cavity, and n the turns ratio of the equivalent circuit transformer. The positive exponent corresponds to the over-coupled case, and the negative exponent corresponds to the under-coupled case.

The change in reflected voltage ΔE_r due to a change ΔR_c in the cavity resistance at resonance is given by [95]:

$$\frac{\Delta E_r}{E} = \frac{1}{E}\frac{\partial E_r}{\partial R_c}\Delta R_c = \pm \Delta R_c \frac{R_g n^2}{(R_g n^2 + R_c)^2}. \tag{2.20}$$

To determine the condition for optimum coupling, I set the derivative $\frac{\partial(\Delta E_r)}{\partial(R_g n^2)} = 0$, which leads

to the matching condition $R_g n^2 = R_c$. Under this matched condition, the expression simplifies to [95]:

$$\frac{\Delta E_r}{E} = \pm\frac{\Delta R_c}{2R_c} = \mp\frac{\Delta Q}{2Q} = \mp\frac{\chi''\eta Q_u}{2}. \tag{2.21}$$

This result indicates that maximum sensitivity is achieved near the matched condition. Furthermore, during resonant absorption, the reflected voltage E_r decreases for an over-coupled cavity and increases for an under-coupled cavity. Therefore, the observed sign of the signal provides information about the type of coupling, as indicated in Equation (8).

In conclusion, the design of the reflection-type microwave cavity and the coupling conditions significantly affect the sensitivity of EPR spectrometers. By operating near the matched condition and optimizing the cavity parameters, the sensitivity can be enhanced, allowing for more precise detection of paramagnetic resonance signals.

Noise Sources in EPR Spectroscopy

Johnson Noise

Johnson noise is the electronic noise generated by the thermal agitation of charge carriers within an electrical conductor at equilibrium. It represents one of the most significant noise sources in an EPR system. The noise power of Johnson noise, N, is defined as [96]:

$$N = k_B T \Delta f \tag{2.22}$$

where k_B is Boltzmann's constant and Δf is the bandwidth in cycles per second.

Eq. 2.22 provides the standard expression for Johnson noise, indicating the noise power at the terminals of any resistor. Additionally, the root-mean-square (RMS) noise voltage between the terminals of the resistor is described by the Johnson-noise formula [96]:

$$V = \sqrt{4k_B T R \Delta f} \tag{2.23}$$

where R is the resistance of the noisy resistor.

Shot Noise

In electronic circuits, shot noise arises from the random fluctuations of the direct current due to the discrete nature of charge carriers (electrons). Typically, shot noise is negligible because electrons carry relatively small charges. Furthermore, compared to Johnson noise and flicker noise, the energy level of shot noise is usually lower. Unlike Johnson noise, which is temperature-dependent, and flicker noise, which is frequency-dependent (discussed later), shot noise is independent of both frequency and temperature. Shot noise exhibits a constant power spectral density (PSD) and is defined by the variance ΔI^2 [97]:

$$\Delta I^2 = 2eI\Delta f \tag{2.24}$$

where I is the current flowing into a node, and Δf is the bandwidth.

Shot noise becomes significant only at high frequencies (terahertz range) and low temperatures (a few Kelvin). Consequently, shot noise is not considered in my noise analysis model for this work.

Flicker Noise (Pink Noise)

In physical systems with a large number of degrees of freedom (DOF), flicker noise, also known as $1/f$ noise, is a fundamental noise source characterized by its PSD, $P(f)$:

$$P(f) \propto f^{-1} \tag{2.25}$$

At sufficiently low frequencies, flicker noise dominates over Johnson noise and shot noise (white noise).

The typical model for the power of flicker noise (P_{pink}) is described as:

$$P_{\text{pink}}(f) = \frac{k_B T f_c}{f} \tag{2.26}$$

where f_c is the corner frequency at which the PSD of flicker noise equals that of white noise.

Noise is inherently present in analog signals and originates from various sources. To achieve a high SNR, it is essential to carefully consider the primary noise sources: Johnson noise, shot noise, and flicker noise. Fig. 2.7 from Zurich Instruments summarizes the qualitative noise spectrum for an EPR spectrometer. In addition to the main three noise types, other technical noise origins include ground loops, cross-talk, 50-60 Hz noise, electromagnetic pick-up, and interference [4]. The qualitative noise spectrum illustrates that (1) flicker noise exhibits a $1/f$ frequency dependence, and (2) Johnson noise maintains a flat spectrum across all observed frequencies. The total noise within a filter is depicted by the grey and blue filled areas in Fig. 2.7. Thus, for the same filter bandwidth, the SNR at a higher frequency f_2 is superior to that at a lower frequency f_1.

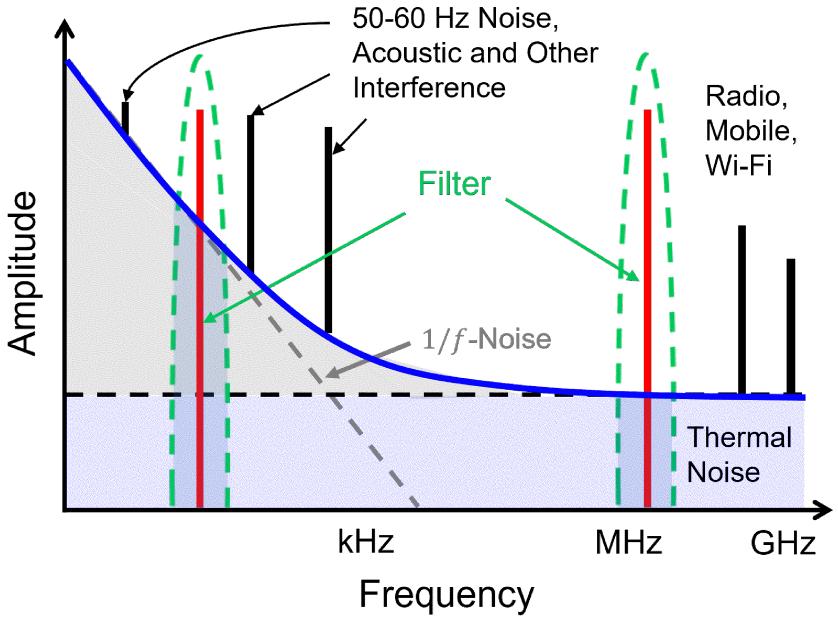

Figure 2.7: Qualitative noise spectrum of a typical experiment [4]. To achieve a high SNR, the measurement frequency should be in a region that avoids flicker noise, for example, the f_2 frequency. With the same filter bandwidth, f_2 yields a better result than f_1.

Added Noise, Noise Figure, and Noise Temperature

Amplifiers, being active devices, inherently generate noise internally. To evaluate the excess noise contributed by an amplifier, the concept of the noise figure, F, is employed. Fig. 2.8 illustrates the noise factor, defined as:

$$F = \frac{\mathrm{SNR}_i}{\mathrm{SNR}_o} \tag{2.27}$$

where SNR_i is the input SNR and SNR_o is the output SNR. The output SNR is defined as:

$$\mathrm{SNR}_o = \frac{S_o}{N_o} = \frac{GS_i}{GN_i + N_a} \tag{2.28}$$

where S_o and N_o are the output signal and noise power, S_i and N_i are the input signal and noise power, G is the power gain, and N_a is the output noise power of the amplifier.

Using the concept of output SNR, SNR_o, the noise factor F can be expressed as:

$$F = 1 + \frac{N_a}{GN_i} = 1 + \frac{T_N}{T_0} \tag{2.29}$$

where T_N is the noise temperature of the amplifier. According to Johnson noise, the input reference noise is $N_i = k_B T_0$ and the output noise power added by the amplifier is $N_a = Gk_B T_{\min}$.

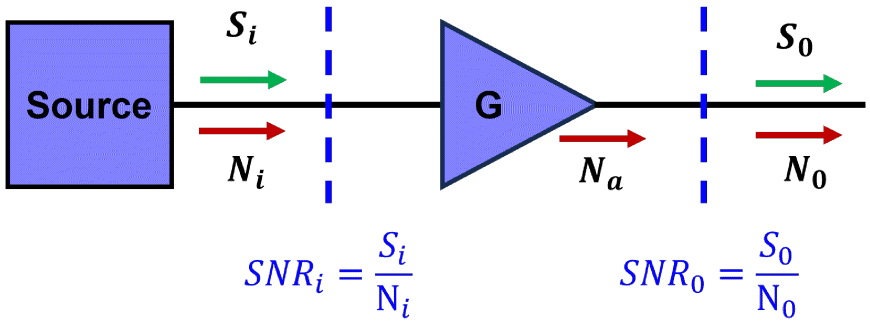

Figure 2.8: The source outputs a signal S_i and noise power N_i. Both signal and noise from the source are amplified by the LNA with a gain, G. Additionally, the LNA adds noise to its output, N_a.

Fig. 2.9 shows that high-electron-mobility transistor (HEMT) low-noise amplifiers (LNAs) and masers exhibit low effective noise temperatures at high frequencies [8]. The noise measurement details for the HEMT LNA are discussed in Appendix B.

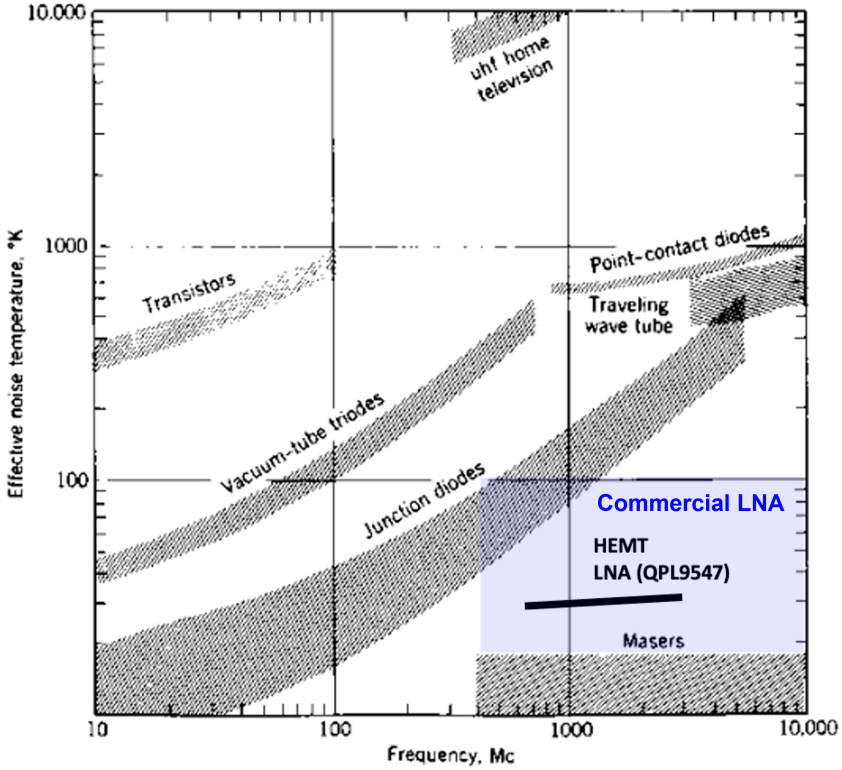

Figure 2.9: Relationship between frequency and effective noise temperature (K) for different types of devices. Masers and HEMT LNAs can operate at high frequencies with very low noise temperatures [8].

The Friis Cascade Formula for a Collection of Amplifiers

In my system, amplifiers act as receivers that amplify the incoming signal along with its accompanying noise and add their own intrinsic noise. To quantify the total noise contributed by a series of amplifiers, Friis's formula is applied. Fig. 2.10 illustrates Friis's formula for cascaded amplifiers.

Friis's formula allows us to calculate the total noise figure (or noise temperature) for a system of cascaded amplifiers as shown in Fig. 2.10 [98]:

$$\begin{aligned} F_{\text{total}} = \frac{\text{SNR}_i}{\text{SNR}_o} &= \frac{\frac{S_i}{N_i}}{\frac{S_i G_1 G_2 G_3}{N_i G_1 G_2 G_3 + N_{a1} G_2 G_3 + N_{a2} G_3 + N_{a3}}} \\ &= 1 + \frac{N_{a1}}{N_i G_1} + \frac{N_{a2}}{N_i G_1 G_2} + \frac{N_{a3}}{N_i G_1 G_2 G_3} \\ &= \underbrace{1 + \frac{N_{a1}}{N_i G_1}}_{=F_1} + \underbrace{\frac{N_{a2}}{N_i G_1 G_2}}_{=\frac{F_2-1}{G_1}} + \underbrace{\frac{N_{a3}}{N_i G_1 G_2 G_3}}_{\frac{F_3-1}{G_1 G_2}} \\ &= F_1 + \frac{F_2 - 1}{G_1} + \frac{F_3 - 1}{G_1 G_2} \end{aligned} \tag{2.30}$$

where G_1, G_2, and G_3 are the power gains of each amplifier, and N_{a1}, N_{a2}, and N_{a3} are the corresponding noise powers added by each amplifier, as shown in Fig. 2.8. The source has a signal power S_i and noise power N_i, while the output has a signal power S_o and noise power N_o.

Additionally, Friis's formula can be expressed in terms of noise temperatures:

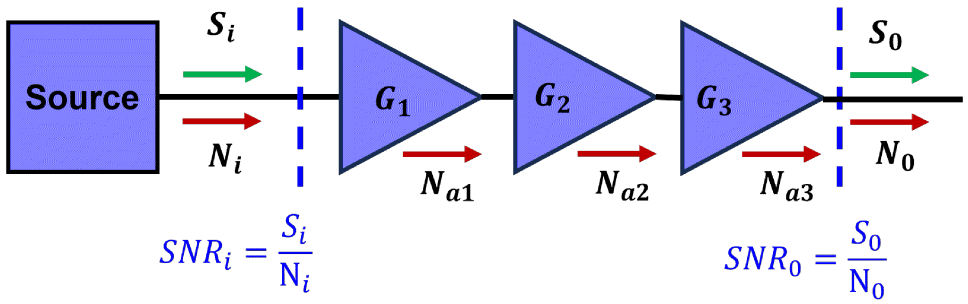

Figure 2.10: Friis's formula for cascaded amplifiers.

$$T_{\text{eq}} = T_1 + \frac{T_2}{G_1} + \frac{T_3}{G_1 G_2} + \dots \tag{2.31}$$

where T_1, T_2, and T_3 are the noise temperatures of each amplifier, respectively.

The SNR of EPR Spectrometer and the Minimum Detectable Number of Spins

To quantify the sensitivity of an EPR spectrometer, it is essential to define the minimum detectable number of spins within an EPR system, denoted as N_{min}. In Appendix A, I follow Poole's derivation to establish the expression for N_{min} [95]:

$$N_{min} = \underbrace{\frac{6V_s k_B T_s}{Q_u \eta g^2 \beta^2 S(S+1)}}_{\text{Term from Curie's Law}} \times \left(\frac{\Delta\omega_{pp}}{\omega_0}\right) \times \underbrace{\left[\frac{F_k - 1 + (G_d F_d + F_{amp} - 1)L}{P_w}(3k_B T_d \Delta f)\right]}_{\text{Noise Term of EPR Spectrometer}}, \tag{2.32}$$

where the term derived from Curie's Law includes V_s (sample volume), S (spin), η (filling factor), Q_u (unloaded Q-factor), T_s (sample temperature), and $\Delta\omega_{pp}$ (equivalent reciprocal linewidth). The noise term encompasses T_d (detection/amplification temperature), Δf (bandwidth), P_w (incident power), L (insertion loss), F_k (noise factor of the network), G_d (gain of the detector), F_d (noise factor of the detector), and F_{amp} (noise factor of the pre-amplifier).

In Equation (1.20), achieving maximum sensitivity of the EPR spectrometer requires minimizing N_{min}. The number of spins in the sample, N_{spin}, is defined by:

$$N_{spin} = y_m^{'} N_{min}, \tag{2.33}$$

where $y_m^{'}$ represents the SNR. To enhance the SNR of the EPR spectrometer, several approaches can be employed:

- increasing the unloaded Q-factor of microwave cavity (Q_u),

- increasing the filling factor (η),
- increasing the incident power (P_w),
- decreasing the temperature of sample and/or detector (T_s and/or T_d),
- decreasing the noise factor of pre-amplifier and/or detector (F_{amp} and/or F_d),
- decreasing the bandwidth (Δf).

Specifically, increasing the unloaded Q-factor Q_u of the microwave cavity, enhancing the filling factor η, and boosting the incident power P_w contribute positively to the SNR. Conversely, reducing the temperatures of the sample and/or detector (T_s and T_d), lowering the noise factors of the pre-amplifier and/or detector (F_{amp} and F_d), and decreasing the bandwidth Δf are effective strategies for improving the SNR.

However, optimizing the SNR involves balancing various trade-offs. In practical scenarios, the number of spins in a sample is determined by comparing the studied sample with standard samples. If both types of spins are compared within the same sample tube (keeping η and V_s constant) and assuming negligible changes in the Q-factor Q_u, at constant power P_w and modulation amplitude H_{mod}, the comparison can be described as [95]:

$$\frac{N^A_{spin}}{N^B_{spin}} = \left(\frac{D^A}{D^B}\right)\left(\frac{g^B}{g^A}\right)^2\left[\frac{S^B(S^B+1)}{S^A(S^A+1)}\right]\left(\frac{\Delta H^A_{pp}}{\Delta H^B_{pp}}\right)^2\left(\frac{\Lambda'^A}{\Lambda'^B}\right)\left(\frac{H^B_{mod}}{H^A_{mod}}\right)\left(\frac{y'^A_m}{y'^B_m}\right), \tag{2.34}$$

where superscripts A and B refer to the two types of spins, D is the multiplicity factor, Λ' characterizes the lineshape, and ΔH_{pp} represents the magnetic field equivalent to the reciprocal linewidth.

In Fig. 2.11, the first-derivative EPR spectra of Mn^{2+} in H_2O illustrate the enhancement achieved through EPR spectroscopy. The experiment demonstrated in Fig. 2.11 shows an improvement in SNR by one to two orders of magnitude by averaging the EPR signal hundreds of times without sacrificing bandwidth [9]. However, signal averaging is time-consuming. There-

fore, this work aims to enhance the SNR of EPR spectrometers more efficiently and swiftly by introducing a novel technique.

The Limit of the EPR Spectroscopy's Sensitivity

In 1973, Mollier et al. analyzed the sensitivities of various EPR spectrometers incorporating masers in their circuitry, as illustrated in Fig. 2.12. They investigated three different modes of operation: (1) classical spectrometer, (2) spectrometer with a maser pre-amplifier, and (3) "Q-multiplier" spectrometer [10].

Mollier et al. defined the sensitivity of EPR spectrometers under optimal conditions as the product of the filling factor η and the minimum detectability limit χ''_{min} (see Appendix A Eq. A.3) [10]:

$$\eta\chi''_{min} = 2\left(\frac{k_B T\Delta f}{\omega W Q_0}\right)^{1/2}\left[1+\frac{Q_u}{Q_{ex}}\frac{F-1}{(1+G^{1/2})^{1/2}}+\frac{Q_u}{Q_{ex}}\frac{G}{(1+G^{1/2})^2}\right]^{1/2}, \tag{2.35}$$

where Q_u is the unloaded Q-factor of the cavity, Q_{ex} is the external coupling Q-factor, T is temperature, η is the filling factor, F is the noise figure of the receiver, Δf is the bandwidth,

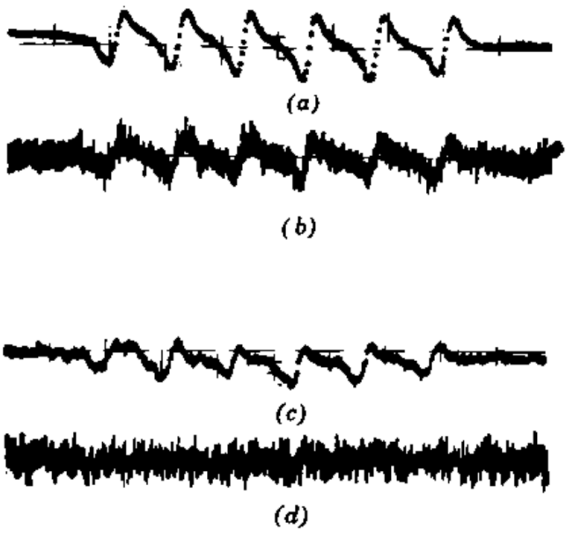

Figure 2.11: First-derivative EPR spectra of Mn^{2+} in H_2O at the output of the pulse height analyser. (a) 100 traverses, 5×10^{14} spins; (b) 1 traverse, 5×10^{14} spins; (c) 500 traverses, 5×10^{13} spins; (d) 1 traverse, 5×10^{13} spins [9].

W is the stored energy in the cavity, ω is the angular resonance frequency of the cavity, and G is the power gain of the amplifier.

Classical Spectrometer In a classical spectrometer, no maser material is placed inside the cavity, resulting in $1/Q_m = 0$. For a perfectly matched cavity where $Q_0/Q_{ex} = 1$ and $G = 0$, the sensitivity is given by [10]:

$$\eta\chi''_{min} = 2\left(\frac{Fk_BT\Delta f}{\omega W Q_u}\right)^{1/2}. \tag{2.36}$$

Spectrometer with Maser Pre-amplifier (Ultra-low Noise) Incorporating a maser pre-amplifier allows the receiver's noise figure to reach its lowest limit, $F = 1$. Consequently, the sensitivity of the EPR spectrometer is determined by [10]:

$$\eta\chi''_{min} = 2\left(\frac{k_BT\Delta f}{\omega W Q_u}\right)^{1/2}. \tag{2.37}$$

This represents the thermodynamic limit for enhancing sensitivity using a pre-amplifier.

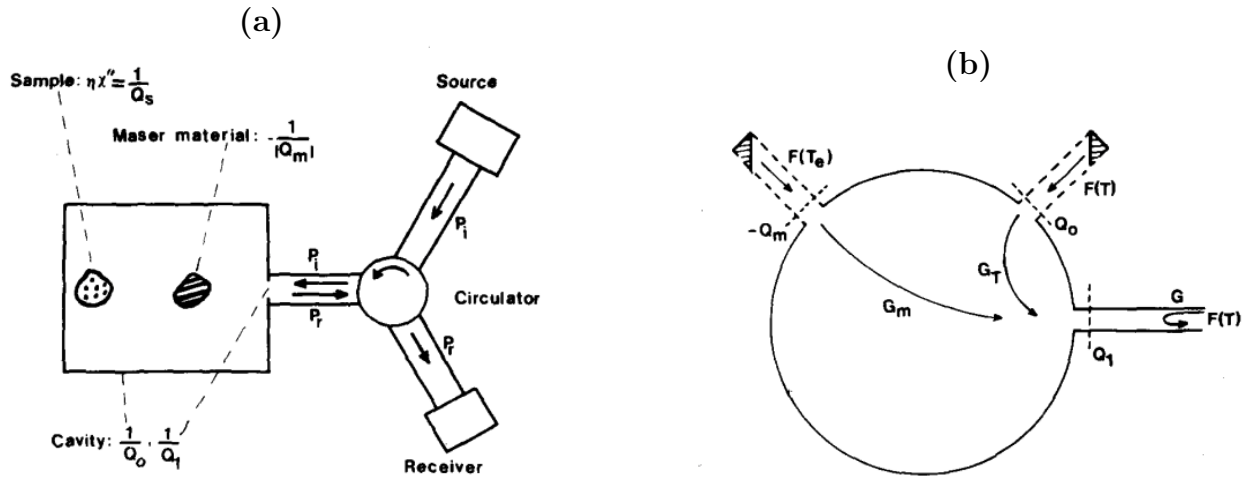

Figure 2.12: Configurations enhancing sensitivity in EPR spectrometers through maser techniques [10]. (a) Spectrometer incorporating maser material within the cavity. (b) Reflection-type maser cavity utilized for noise analysis.

Q-Multiplier Spectrometer In systems utilizing a maser amplifier, the system achieves high gain, making the amplified thermal noise surpass the receiver noise. Under these conditions, the sensitivity is described by [10]:

$$\begin{aligned}\eta\chi''_{min} &= 2\left(\frac{k_B T\Delta f}{\omega W Q_0}\right)^{1/2}(1+\alpha)^{1/2} \\ &= 2\left(\frac{k_B T\Delta f}{\omega W_{sat} Q_u}\right)^{1/2},\end{aligned} \tag{2.38}$$

where $\alpha = Q_u/Q_{ex}$. The optimal sensitivity, achieved when W is on the order of W_{sat} and $\alpha \approx 1$, is obtained by optimizing W_{sat}.

In all the aforementioned cases, the ultimate sensitivity of the EPR spectrometer is governed solely by the thermal noise within the microwave cavity. Even with an ultra-low noise amplifier as a receiver that reaches the thermodynamic sensitivity limit, the inherent thermal noise in the cavity remains a fundamental constraint.

Two primary factors determine the sensitivity of an EPR spectrometer: the photoexcited triplet state and its paramagnetic properties. Time-resolved EPR (tr-EPR) is crucial in determining the kinetic properties of the sample. However, weak signals pose an SNR challenge when measuring samples at room temperature. Therefore, developing a more sensitive tr-EPR technique with a higher SNR is imperative. Building on the understanding that the ultimate sensitivity is limited by thermal noise in the microwave cavity [10], this thesis introduces a novel approach using a HEMT ultra-low noise amplifier to reduce the noise power within an electromagnetic cavity. This approach aims to significantly enhance the sensitivity of tr-EPR beyond the capabilities of commercial instruments.

2.2 Theory II. Overcoming Thermal-Noise Limits in Microwave Measurements

2.2.1 Number of photons inside a microwave cavity

Obeying Bose-Einstein statistics, the average number of photons, $\bar{n}$, occupying an electromagnetic mode of frequency $f_{\text{mode}} = \omega_{\text{mode}}/(2\pi)$ inside an isolated (zero ports) cavity maintained at a physical temperature of T_0, is given by $\bar{n} = \left[\exp\left(\frac{hf_{\text{mode}}}{k_{\text{B}}T_0}\right) - 1\right]^{-1}$, where k_{B} and h are Boltzmann's and Planck's constants, respectively.

Semiclassically, for a microwave cavity with a single port coupling it to an external cold load, as depicted schematically in Fig. 2.13, the number of photons q occupying the mode as a function of time t will obey

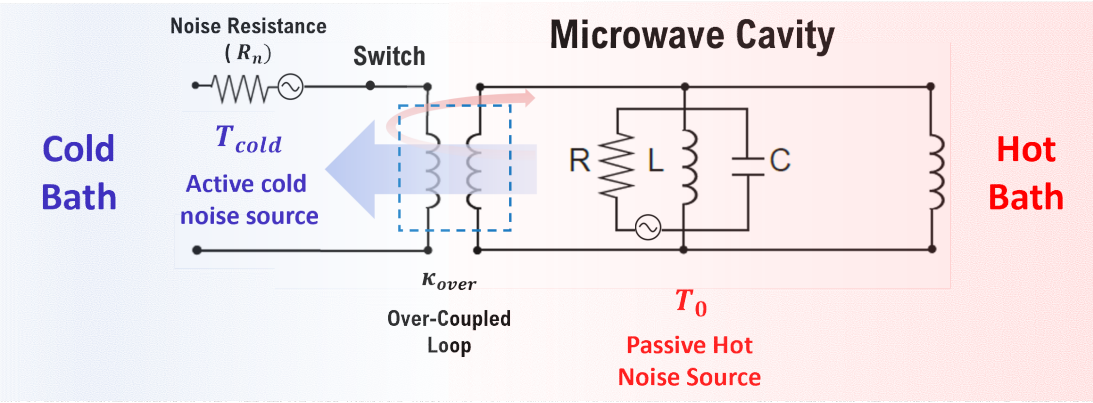

Figure 2.13: The active pre-cooling technique involves electromagnetically coupling a resonator, that is physically heat-sunk to a room-temperature environment (here referred to as the "hot bath"), to an active cold noise source or "load", here functioning as a "cold bath".

$$\frac{\mathrm{d}q}{\mathrm{d}t} \equiv \dot{q} = \underbrace{-\omega_{\mathrm{mode}} Q_0^{-1}(q - \epsilon T_0)}_{\text{interaction with intrinsic “hot” heat bath}} - \underbrace{\omega_{\mathrm{mode}} \kappa Q_0^{-1}(q - \epsilon T_{\mathrm{cold}})}_{\text{interaction with external “cold” heat bath}} , \tag{2.39}$$

where the value of the constant $\epsilon = \frac{k_{\mathrm{B}}}{h f_{\mathrm{mode}}}$ respects Maxwell-Boltzmann equipartition of energy[44]. T_{cold} is the noise temperature of the ACL used in the experiment; Q_0 and Q_{loaded} are the intrinsic and loaded quality factors of the microwave cavity, where $Q_{\mathrm{loaded}} = \frac{Q_0}{1+\kappa}$; κ is the port's coupling factor. This formula can be trivially extended to include additional ports coupling the microwave mode at different couplings strengths κ_i to additional loads at different temperatures T_i:

$$\dot{q} = -\underbrace{\omega_{\mathrm{mode}} Q_0^{-1}(q - \epsilon T_0)}_{\text{intrinsic bath}} - \sum_{i=1} \underbrace{\omega_{\mathrm{mode}} \kappa_i Q_0^{-1}(q - \epsilon T_i)}_{\text{external bath(s)}} . \tag{2.40}$$

2.2.2 Mode temperature inside the cavity

Upon achieving dynamic equilibrium, $\dot{q} = 0$, the rate equation in Eq. 2.39 can thereupon be

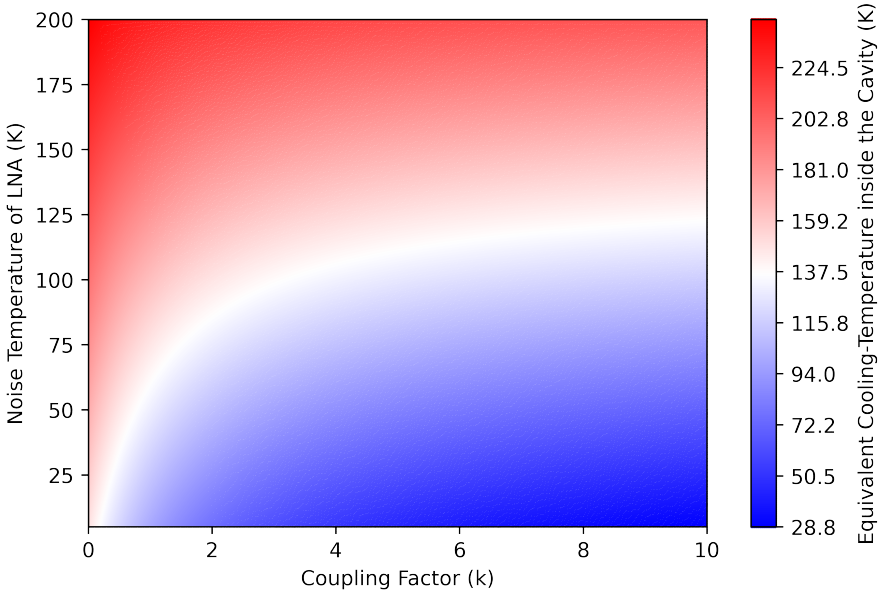

Figure 2.14: Modeled equivalent temperature of an electromagnetic mode inside the cavity as a function of the coupling factor κ (horizontal coordinate) and the noise temperature of the cold load T_{cold} coupled to this mode (vertical coordinate).

used to calculate the expected photon number. Defining the mode's equivalent temperature as $T_{\text{mode}} = \frac{q}{\epsilon} = \frac{qhf_{\text{mode}}}{k_{\text{B}}}$, we obtain, for a single coupling port:

$$T_{\text{mode}} = \frac{T_0 + \kappa T_{\text{cold}}}{1 + \kappa}. \tag{2.41}$$

Note that this steady-state solution of the photon-number dynamics is consistent with the application of Siegman's "useful noise theorem" (see chapter 8 of Ref. [11]). *In words*: the mode's expected temperature is the **weighted average** temperature of the two baths with which the mode interacts, the weighting of each bath being proportional to its interaction strength with the mode, *i.e.* its "coupling". Here, the coupling of the mode to the cavity's own intrinsic heat bath is (by definition/convention) unity. Fig. 2.14 displays the mode temperature predicted by Eq. 2.41. When the coupling factor of the over-coupling loop κ is large, the mode temperature T_{mode} will approach that of the cold load T_{cold}.

2.2.3 Cavity cooling via a lossy transmission line

The input of an LNA can serve as an ACL for reducing the thermal noise inside a cavity that is coupled to it. Here I analyse the additional thermal noise generated by a lossy transmission line, such as a length of coaxial cable, or any other lossy component inserted between the cold load and the cavity, as shown generically in Fig. 2.15. Again, see chapter 8 of Ref. [11] for the conceptual foundations and mathematics of the "wave approach"[99] used here. For initial simplicity, let's assume that the transmission line is uniform and held at a constant physical temperature T_0 along its length. The power P_{sig} of a signal flowing down such a line will decrease exponentially with distance obeying $dP_{\text{sig}}/dz = -2\alpha P_{\text{sig}}$, where α is the line's voltage attenuation coefficient. Not only is the signal attenuated, but thermal noise is generated along the lossy line's length. At a distance $z = l$ from the cold load, the forward-traveling noise power P_l will equal

$$P_l = LP_{\text{cold}} + (1 - L)P_{\text{line}}, \tag{2.42}$$

where P_{cold} and P_{line} are the available noise powers from a cold load at temperature T_{cold} and the end of an infinite length of the lossy transmission line at temperature T_0, respectively; L is the insertion loss of the line between the cold load and the observation point at $z = l$, where $L = e^{-2\alpha l}$ and $L \leq 1$. Across a given frequency band of width B, $P_{\text{line}} = k_{\text{B}} T_{\text{line}} B$ (for $hf/kT \ll 1$).

In the case of a short transmission line (or any other 2-port component) with minimal insertion loss, such that $L \approx (1 - 2\alpha l)$ to good approximation, the equivalent noise power P at the end of the transmission line can be approximated (expressing the line's attenuation in decibels) as:

$$P_l = (1 - \frac{L_{\text{dB}}}{4.34}) P_{\text{cold}} + \frac{L_{\text{dB}}}{4.34} P_{\text{line}}. \tag{2.43}$$

Note that this (slightly more complicated) approximation is more accurate than equation (8-2-5) in Siegman's book [11]. Based on the relation between noise power and noise temperature, namely $P = k_{\text{B}} T B$, the effective noise temperature of the cold load, upon including the additional noise from a lossy transmission line connected to it, can thereupon be approximated as:

$$T_l = (1 - \frac{L_{\text{dB}}}{4.34}) T_{\text{cold}} + \frac{L_{\text{dB}}}{4.34} T_0, \tag{2.44}$$

where T_{cold} the temperature of the cold load itself and $T_0 = T_{\text{line}}$ is the (here assumed to be room) temperature of the transmission line. Combining Eq. 2.41 and Eq. 2.44, the mode's

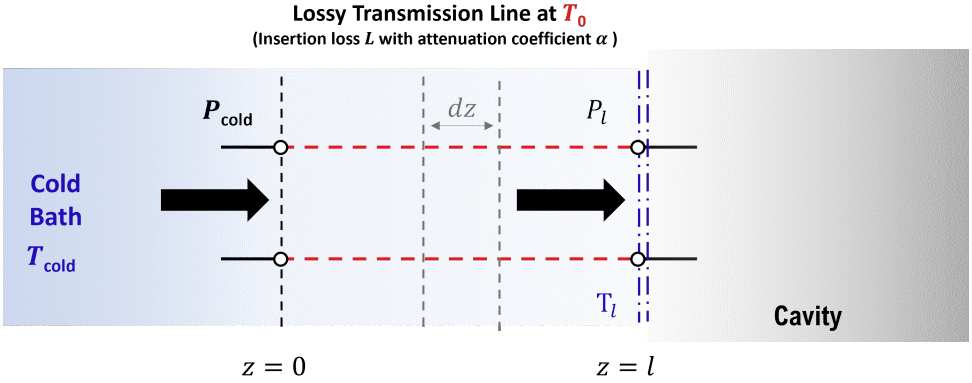

Figure 2.15: Calculating how the cooling LNA's noise temperature is degraded by transport along a length of (warm) lossy transmission line.

noise temperature inside the microwave cavity is now given by:

$$T'_{\text{mode}} = \frac{T_0 + \kappa[(1 - \frac{L_{\text{dB}}}{4.34})T_{\text{cold}} + \frac{L_{\text{dB}}}{4.34}T_0]}{1+\kappa} = T^{\text{orig.}}_{\text{mode}} + \Delta T_{\text{link}}, \tag{2.45}$$

where $T^{\text{orig.}}_{\text{mode}}$ is the original mode temperature as given by Eq. 2.41 above and $\Delta T_{\text{link}} = \frac{L_{\text{dB}}}{4.34}\kappa(T_0 - T_{\text{cold}})/(1+\kappa)$ is the added noise temperature caused by the lossy transmission line.

2.2.4 Multiple cooling ports to a microwave cavity

I now consider a microwave cavity with two ports, one for cooling, the other for read-out, connected to separate LNAs functioning as cold loads. With the setup depicted in Fig. 2.16 and applying Eq. 2.40, the rate equation governing the microwave cavity's photon number is:

$$\dot{q} = -\underbrace{\omega_{\text{mode}}Q_0^{-1}(q - \epsilon T_0)}_{\text{Hot bath}} - \underbrace{\omega_{\text{mode}}(Q_0/\kappa_{\text{over}})^{-1}(q - \epsilon T_{\text{cold}})}_{\text{Cold bath of cooling port}} - \underbrace{\omega_{\text{mode}}(Q_0/\kappa_{\text{crit.}})^{-1}(q - \epsilon T_{\text{cold}})}_{\text{Cold bath of monitoring port}}, \tag{2.46}$$

where κ_{over} and $\kappa_{crit.}$ ($\kappa_{crit.} \equiv 1$) are the coupling factors of the over-coupled and critically-coupled loops, respectively. As in the previous analysis for a single port, the depth of cavity cooling upon reaching dynamic equilibrium (*i.e.* "steady state" conditions) is deduced by solving $\dot{q} = 0$. The mode temperature T_{mode} achieved, as appears in Fig. 2.16, is given by:

$$T_{\text{mode}} = \frac{T_0 + (\kappa_{\text{over}} + \kappa_{\text{crit.}})T_{\text{cold}}}{1 + \kappa_{\text{over}} + \kappa_{\text{crit.}}} = \frac{T_0 + (1 + \kappa_{\text{over}})T_{\text{cold}}}{2 + \kappa_{\text{over}}}. \tag{2.47}$$

In general, the temperature of a mode of a cavity with multiple cooling ports can be expressed as a weighted average:

$$T_{\text{mode}} = \frac{T_0 + \sum_{i=1}^{n}\kappa_i T_i}{1 + \sum_{i=1}^{n}\kappa_i}, \tag{2.48}$$

where κ_i and T_i represent the coupling factor and noise temperature of the i-th cooling (or warming) element coupled to the mode, respectively.

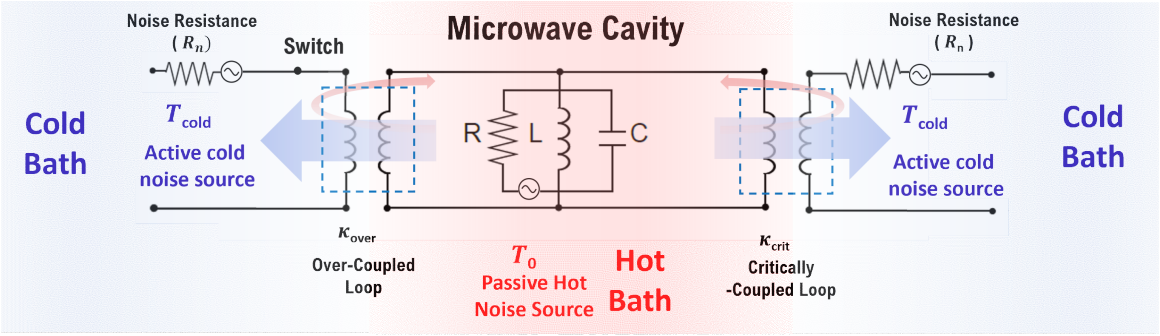

Figure 2.16: Cavity cooling with two separate cold baths.

2.2.5 Multiple cooling ports to a microwave cavity with lossy transmission lines

In this section, I consider a microwave cavity with multiple cooling ports and lossy transmission lines, integrating concepts from sections 2.2.3 and 2.2.4. Combining equations Eq. 2.44 and Eq. 2.48, yields

$$T_{\text{mode}} = \frac{T_0 + \kappa_1[(1 - \frac{L_{\text{dB},1}}{4.34})T_{\text{cold}} + \frac{L_{\text{dB},1}}{4.34}T_0] + \kappa_2[(1 - \frac{L_{\text{dB},2}}{4.34})T_{\text{cold}} + \frac{L_{\text{dB},2}}{4.34}T_0]}{1 + \kappa_1 + \kappa_2}, \tag{2.49}$$

where κ_1 and κ_2 represent the coupling coefficients of the first and second cold baths, respectively. I here assume the insertion losses of the transmission lines associated with the cold baths ($L_{\text{dB},1}$, $L_{\text{dB},2}$) are small. If however the insertion loss of a connecting cable/device is not small, one needs to revert back to Eq. 2.42, equivalent to equation in (8-2-4) in Siegman's book [11]. Based on the relation between noise power and noise temperature, $P = k_B T B$, the equivalent noise temperature of a cold load at temperature T_{cold}, observed through a length of transmission line at temperature T_0 and of significant linear insertion loss $L = 10^{-L_{\text{dB}/10}}$, can be quantified as:

$$\begin{aligned} T_l &= LT_{\text{cold}} + (1 - L)T_0 \\ &= 10^{-\frac{L_{\text{dB}}}{10}}T_{\text{cold}} + \left(1 - 10^{-\frac{L_{\text{dB}}}{10}}\right)T_0. \end{aligned} \tag{2.50}$$

My experimental set-up includes two cold baths: one of them, namely the input of the cooling LNA, is connected to the cavity (when selected by the SPDT switch) via a small insertion loss,

whereas the other heat bath, namely the monitoring LNA's input, is connected to the cavity via a large insertion loss. The most appropriate formula for calculating the temperature of the cavity's operational mode is thus: (These approximations are analyzed in Fig. 2.17.)

$$T_{\text{mode}} = \frac{T_0 + \kappa_1[(1 - \frac{L_{\text{dB},1}}{4.34})T_{\text{cold}} + \frac{L_{\text{dB},1}}{4.34}T_0] + \kappa_2[10^{-\frac{L_{\text{dB},2}}{10}}T_{\text{cold}} + (1 - 10^{-\frac{L_{\text{dB},2}}{10}})T_0]}{1 + \kappa_1 + \kappa_2}. \tag{2.51}$$

2.2.6 Theoretical Noise Analysis of APC

Similar to the previous work by Wu et al. [44], I also adopt the "wave approach" (see Chapter 8 of Siegman [11]) to analyze the flow of noise power from the cavity into my homodyne receiver,

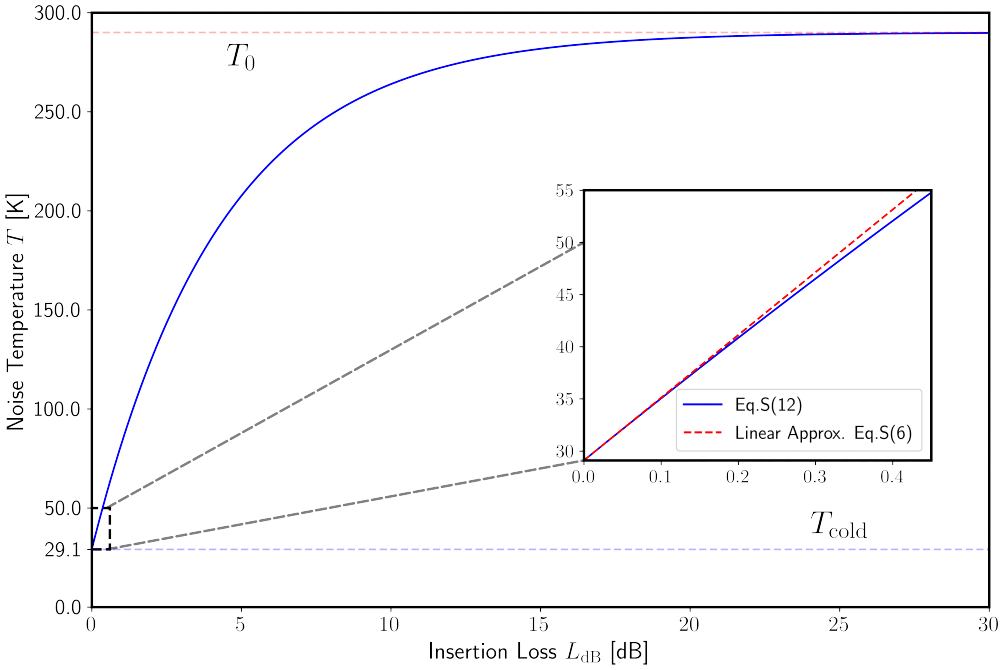

Figure 2.17: How, according to Eq. 2.50, the forward noise power (in units of absolute temperature T) at the far end of a lossy cable depends on the cable's insertion loss L_{dB}. Here the cable is uniformly maintained at a temperature of $T_0 = 290$ K throughout its length and the near end of the cable is terminated and cooled by the ACL whose noise temperature is $T_{\text{cold}} = 29.1$ K (dashed cornflower-blue baseline)–corresponding to the input noise temperature of the Qorvo QPL9547EVB-01 LNA used experimentally. The zoomed-in area details how, when the insertion loss is less than 0.5 dB, equation Eq. 2.44 (red dashed line -"Linear Approx."), *i.e.* the linear approximation provided by equation (8-2-5) in Siegman's book [11], compares against the exact formula Eq. 2.50 (blue solid line).

Table 2.1: Values of parameters -entering the noise-reduction equation 2.53

Description of the Receiver	Symbol	Value (@ 1.4495 GHz)
Linear power gain of first LNA	G_{LNA}	166.0 ±3.3
Minimum noise figure of first LNA	NF_{min}	0.17*
Minimum noise temperature of first LNA	T_{min}	11.6 K*
Optimum source reflection coefficient	Γ_{opt}	(0.073+0.125i)*
Noise resistance of first LNA	R_{n}	2.00 Ω*
Reflection looking into input of first LNA	S_{11}	-(0.107+0.234i)*
Noise temperature of the rest of the receiver	T_{REC}	36.1 K†

* interpolated from published datasheet [100]
† calculated using Friis formula[101]

as shown in Fig. 2.18. Eq. 2.46 of Wu et al.'s paper provides a formula for the factor, ΔP (in units of dB), by which the measured noise power is reduced by mode cooling:

$$\Delta P' = 10\log_{10}\frac{G_{\mathrm{LNA}}[(T_{\mathrm{min}}+T_{\mathrm{mode}})(1-|\Gamma_c|^2)+4T_0\frac{R_{\mathrm{n}}}{Z_0}\frac{|\Gamma_c-\Gamma_{\mathrm{opt}}|^2}{|1+\Gamma_{\mathrm{opt}}|^2}+T_{\mathrm{image}}]+T_{\mathrm{REC}}}{G_{\mathrm{LNA}}[(T_{\mathrm{min}}+T^0_{\mathrm{mode}})(1-|\Gamma^0_c|^2)+4T_0\frac{R_{\mathrm{n}}}{Z_0}\frac{|\Gamma^0_c-\Gamma_{\mathrm{opt}}|^2}{|1+\Gamma_{\mathrm{opt}}|^2}+T_{\mathrm{image}}]+T_{\mathrm{REC}}}, \tag{2.52}$$

However, this formula needs to be modified to suit my experimental set-up, and for the following reasons: (i) My current receiver is a homodyne, not a single-conversion superhet subject to additional image noise; one can thus set $T_{\mathrm{image}} = 0$. (ii) Even when monitoring (with the cooling LNA disconnected), the cavity mode is continuously cooled (albeit only slightly) by the receiver's front-end LNA, connected to the cavity's monitoring port via a lossy stub tuner and cable (substantially reducing the size of the the LNA's cooling effect). The ambient/reference mode temperature in the above formula, namely T^0_{mode}, should thus be set equal to $T^{\mathrm{ambient}}_{\mathrm{mode}} \approx 257.6$ K, somewhat less than 290 K. Finally, (iii) the ambient (reference) and

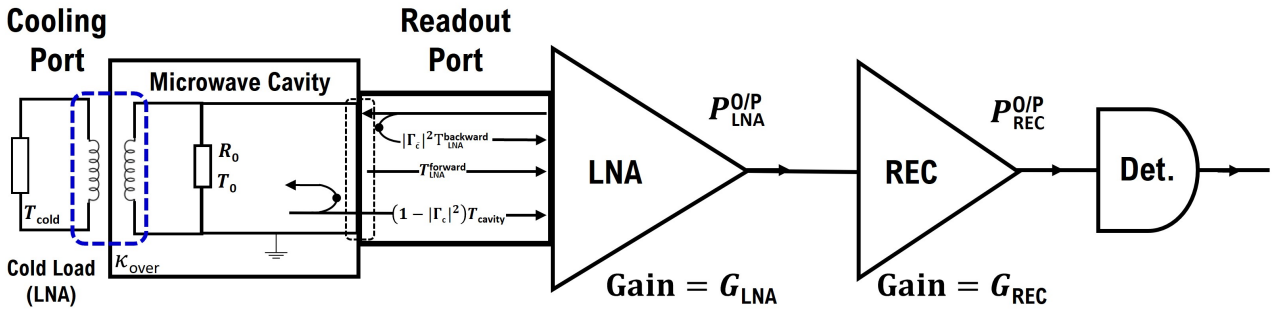

Figure 2.18: Anatomy of the signal path at the front end of the homodyne receiver, displaying the forward and backward noise powers between the LNA and microwave cavity.

post-cooled measurements are performed with the cavity under the same coupling conditions, namely with a single, critically-coupled monitoring port; the reflection amplitude off this port is always zero (during measurement of the noise power); thus, one can set $\Gamma_c = \Gamma_c^0 = 0$. These largely simplifying modifications lead to:

$$\Delta P = 10 \log_{10} \frac{G_{\mathrm{LNA}}[(T_{\mathrm{min}} + T_{\mathrm{mode}}) + 4T_0 \frac{R_{\mathrm{n}}}{Z_0} \frac{|\Gamma_{\mathrm{opt}}|^2}{|1+\Gamma_{\mathrm{opt}}|^2}] + T_{\mathrm{REC}}}{G_{\mathrm{LNA}}[(T_{\mathrm{min}} + T_{\mathrm{mode}}^{\mathrm{ambient}}) + 4T_0 \frac{R_{\mathrm{n}}}{Z_0} \frac{|\Gamma_{\mathrm{opt}}|^2}{|1+\Gamma_{\mathrm{opt}}|^2}] + T_{\mathrm{REC}}}, \tag{2.53}$$

where T_{mode} is the pre-cooled mode temperature; T_{min}, R_{n}, Γ_{opt} are the four noise parameters (being a complex number, Γ_{opt} counts double) of the monitoring LNA, namely a Qorvo QPL9547EVB-01; the reference impedance $Z_0 = 50\ \Omega$ throughout. The values assigned to these parameters, as shown in Table 2.1, have been interpolated to 1.45 GHz from measurements at straddling spot frequencies found in the manufacturer's data sheet [100]. The noise temperature of the rest of the receiver, treated as a cascade of amplifiers, was calculated using the Friis formula and the amplifiers' specified noise temperatures of equivalent figures [101]; see Table 2.1. The monitoring LNA's gain, G_{LNA}, was measured using a VNA and found to be consistent with the QPL9547's datasheet. The amplitude of the applied interrogating microwave tone was chosen to be sufficiently low that stimulated emission/absorption is very slow compared to the intrinsic spin dynamics of pentacene's optically excited triplet state.

2.3 Theory III. Pulse EPR Methods and Their Applications

2.3.1 Using Pulse EPR Measurement to Study Quantum Coherence in Electron Spin Systems

As described in Chapter 2.1, building upon the foundation established by CW EPR spectroscopy, pulsed EPR techniques offer advanced methods for probing quantum coherence and relaxation mechanisms in electron spin systems. By employing precisely timed microwave and radiofrequency pulses, pulsed EPR allows for the independent manipulation of electron and nuclear spins. This temporal control enhances the resolution and accuracy of spin dynamics studies, providing deeper insights into spin coherence, dephasing, and relaxation processes.

The principles of pulsed EPR are conceptually related to those of pulsed NMR spectroscopy, though tailored to address the unique dynamics of electron spins[88]. Pulsed EPR methodologies are broadly categorized into two complementary approaches. The first involves electron-nuclear double resonance (ENDOR) techniques[102], where signals arise from the excitation of nuclear spin transitions through combined MW and RF irradiation. ENDOR is particularly effective for systems with weak anisotropic hyperfine couplings. The second approach relies on ESEEM effects[12], measuring nuclear transition frequencies by applying MW pulses and detecting electron or nuclear coherences. ESEEM is well-suited for systems exhibiting strong anisotropic interactions. In this thesis, I will focus on ESEEM.

To explore quantum coherence in electron spin systems, various pulse sequences are employed to elucidate spin relaxation and coherence phenomena. The following subsections detail key pulsed EPR techniques used in this Thesis.

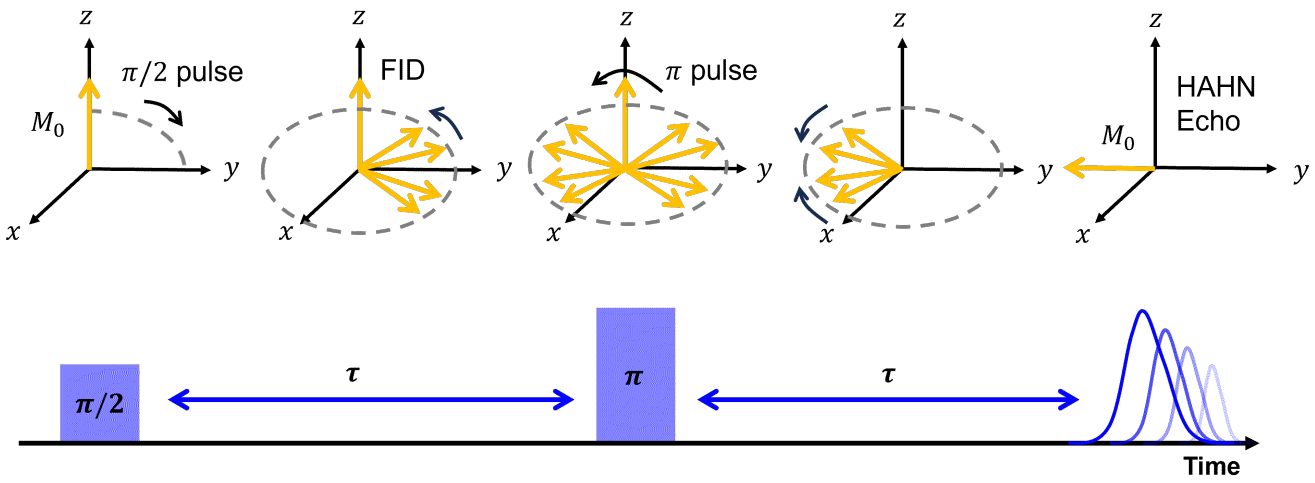

Figure 2.19: Hahn echo sequence illustrating the spin echo relaxation mechanism. The process begins with a $\pi/2$ pulse that rotates the initial magnetization vector M_0 from the z-axis to the transverse plane (xy-plane), initiating FID. Over the interval τ, dephasing due to inhomogeneities in the magnetic field causes the spins to diverge. A subsequent π pulse inverts the spin vectors, effectively reversing their positions. This inversion enables the spins to rephase, culminating in the formation of a coherent spin echo at time 2τ. The amplitude of the echo, shown as progressively decaying echoes, reflects the T_{m} (phase memory time) relaxation and provides insights into spin coherence and dephasing effects[12, 13].

Electron Spin-Echo Relaxation

The spin echo technique is fundamental for measuring phase coherence and dephasing effects in spin systems. The Hahn echo sequence, depicted in Figure 2.19, serves as a primary example. The sequence commences with a $\pi/2$ pulse that rotates the net magnetization vector M_0 from its equilibrium position along the z-axis into the transverse plane (xy-plane), creating a coherent superposition of spin states and initiating free induction decay (FID)[12].

During the subsequent interval τ, individual spins experience dephasing due to magnetic field inhomogeneities, causing them to precess at slightly different frequencies. A π pulse is then applied, inverting the spin vectors in the transverse plane and effectively reversing their positions relative to their original alignment. This inversion enables the spins to rephase, and at time 2τ, they converge to form a coherent spin echo. The echo amplitude decreases with each repetition due to spin-spin interactions and other dephasing mechanisms, characterized by the phase memory time T_{m}. Analyzing the decay of the echo amplitude over time yields valuable information about spin coherence and relaxation processes.

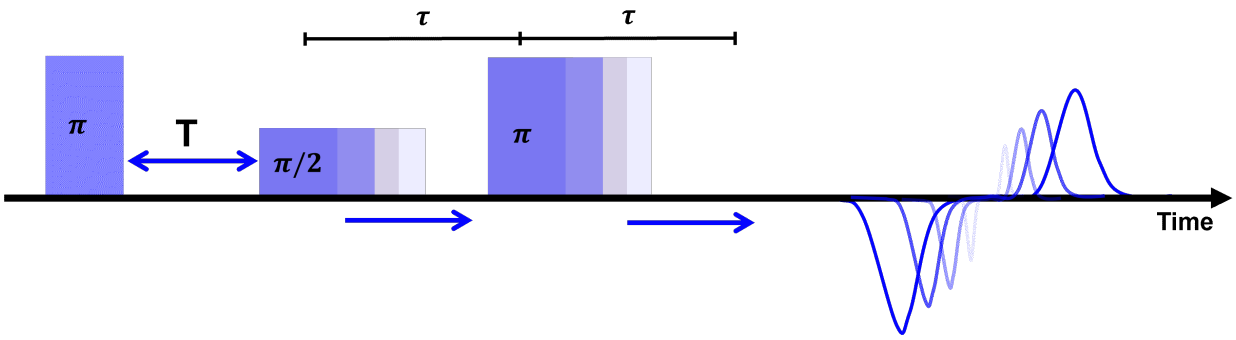

Figure 2.20: Pulse sequence diagram illustrating the inversion recovery method for measuring spin-lattice relaxation time (T_1). The sequence begins with an initial π pulse that inverts the magnetization along the z-axis, followed by a variable delay time T during which longitudinal relaxation occurs. A subsequent $\pi/2$ pulse rotates the partially recovered magnetization into the transverse plane, initiating FID. The signal intensity as a function of the recovery time T allows for the determination of T_1 by fitting the resulting curve to an exponential recovery model[14, 13].

Inversion Recovery

The spin-lattice relaxation time T_1 describes how quickly a spin system returns to thermal equilibrium along the z-axis after perturbation. The inversion recovery method, illustrated in Figure 2.20, employs a three-pulse sequence to measure T_1. It begins with a π pulse that inverts the population of spin states, effectively flipping the magnetization along the z-axis. A variable delay time T follows, during which the spins undergo longitudinal relaxation, gradually returning toward equilibrium[14].

After the delay, a $\pi/2$ pulse rotates the partially recovered magnetization into the transverse plane, initiating FID. By varying the recovery time T and recording the corresponding signal intensities, a recovery curve reflecting the exponential return of magnetization to equilibrium is constructed. Fitting this curve to an exponential model allows for the determination of T_1, providing insights into the energy exchange processes between the spins and their surrounding lattice.

Carr-Purcell-Meiboom-Gill Pulse Sequence

The Carr-Purcell-Meiboom-Gill (CPMG) sequence enhances the measurement of the spin-spin relaxation time T_m by mitigating effects of inhomogeneous broadening and extending signal

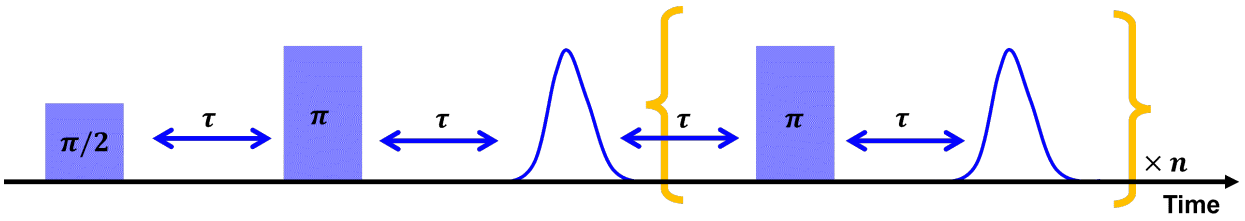

Figure 2.21: Pulse sequence diagram of the CPMG experiment, used for measuring the spin-spin relaxation time (T_m). The sequence begins with an initial $\pi/2$ pulse that rotates the magnetization into the transverse plane, followed by a time interval τ. A train of π pulses is applied at intervals of 2τ to refocus the dephasing spins and produce successive echo signals. This process is repeated n times to create a series of echoes, each separated by 2τ. The decay of the echo amplitudes provides valuable information for determining T_m, revealing spin dephasing and coherence properties[15, 13].

detection. As shown in Figure 2.21, the sequence starts with a $\pi/2$ pulse that rotates the magnetization into the transverse plane. After a time interval τ, a series of π pulses is applied at regular intervals of 2τ[15].

Each π pulse inverts the dephasing spins, causing them to rephase and produce successive echo signals. Repeating this process multiple times generates a series of echoes, each separated by 2τ. The decay of the echo amplitudes over time reflects the loss of coherence due to spin-spin interactions and other dephasing mechanisms. By analyzing this decay, T_m can be determined with greater precision. The CPMG sequence is particularly useful when rapid dephasing or experimental limitations make single-echo measurements challenging.

Rabi Oscillation

Rabi oscillations occur when a two-level quantum system is driven by a resonant oscillating field, leading to coherent oscillations of the spin populations between the two states. The Rabi oscillation experiment, depicted in Figure 2.22, measures these oscillations to gain insights into the coherence and interaction strength of the spins with the driving field[16].

The sequence begins with a preparation pulse of variable duration t_p, setting the initial state of the spin system by creating a superposition of spin states. After a variable waiting period T, a $\pi/2$ pulse rotates the magnetization into the transverse plane, initiating FID. Following a delay τ, a π pulse is applied to refocus the spins, generating an echo signal after another interval τ.

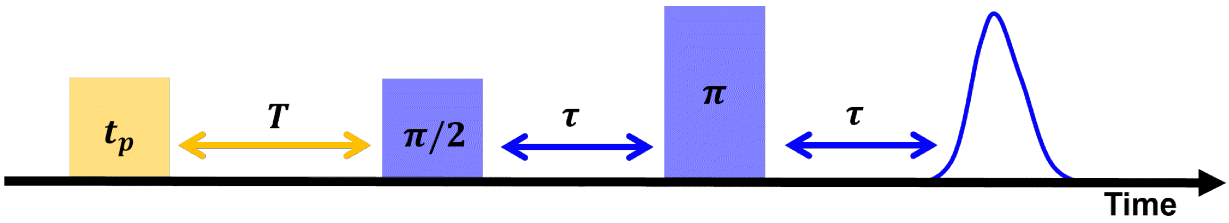

Figure 2.22: Pulse sequence diagram illustrating the Rabi oscillation experiment, which measures the coherent oscillations of spin populations under a resonant driving field. The sequence begins with a preparation pulse of duration t_p to set the initial state, followed by a variable waiting period T. A $\pi/2$ pulse rotates the magnetization into the transverse plane, initiating FID. After a time interval τ, a π pulse is applied to refocus the spins and generate an echo signal at the end of another τ interval. The observed echo amplitude as a function of t_p reveals the Rabi oscillations, providing insights into the coherence and interaction strength of the spins[16, 13].

By varying the preparation pulse duration t_p and recording the corresponding echo amplitudes, oscillations in the signal intensity corresponding to coherent transitions between spin states are observed. The frequency and damping of these Rabi oscillations provide quantitative information about the coupling between the spins and the MW field, as well as decoherence effects due to environmental interactions.

By employing these pulse sequences, pulsed EPR spectroscopy enables detailed studies of spin relaxation times, coherence properties, and interactions within electron spin systems. This information is crucial for advancing the understanding of quantum coherence and for developing applications in quantum information processing and spin-based technologies.

2.4 Theory IV. Quality Factor Definitions in Microwave Systems

2.4.1 How to Measure Q-factor?

The design of a cavity resonator plays a pivotal role in quantum sensing and metrology applications, such as EPR spectroscopy (as discussed in Chapter 2.1). A key parameter in evaluating resonator performance is the Q-factor, or Q-factor, which quantifies the efficiency of energy storage within the resonator relative to energy loss per oscillation cycle. The Q-factor is mathematically defined as[103]:

$$Q = 2\pi \frac{\text{Maximum energy stored in a cycle}}{\text{Average energy dissipated per cycle}} = 2\pi f_{\text{mode}} \frac{\text{Energy stored}}{\text{Average power dissipated}} \tag{2.54}$$

where f_{mode} is the resonant frequency of the mode being excited. A higher Q-factor indicates that the resonator is more efficient at storing energy, with minimal losses due to dissipation in the cavity walls or circuit resistance.

In practical measurements, the Q-factor obtained is often the **loaded Q-factor** (Q_L), which accounts for the resonator's coupling to external systems like transmission lines. This is the value typically measured using instruments such as a vector network analyzer (VNA). Conversely, the **unloaded Q-factor** (Q_u) represents the intrinsic Q-factor of the resonator when it is isolated from any external coupling. For a resonator that is critically coupled and without a sample, the relationship between the unloaded and loaded Q-factors is given by $Q_u = 2Q_L$.

To thoroughly assess the performance of a microwave cavity, three fundamental parameters must be determined: (1) the resonant frequency (f_{mode}), (2) the coupling factor, and (3) the unloaded Q-factor (Q_u). These parameters are essential for characterizing the resonator's behavior and are typically measured using a VNA. Various methods exist for determining these parameters, including the three-point measurement method, lumped-circuit transmission-line analysis, and one-port wave-approach analysis. These methodologies will be explored in the

following sections.

Smith Chart and S_{11} Reflection-Type Measurement

In this analysis, I use a VNA to measure the scattering parameters of the microwave cavity to evaluate its performance. The scattering matrix characterizes a high-frequency network by relating the incident, reflected, and transmitted waves at its ports. As illustrated in Fig. 2.23, the S_{11} measurement provides a direct description of the network as seen from the VNA's port by correlating the voltage wave incident on the port with the wave reflected from it. The scattering parameter S_{11} measured by the VNA is defined as:

$$S_{11} = \frac{V_1^-}{V_1^+} \tag{2.55}$$

For this one-port measurement, the resonator requires only a single port to analyze the forward reflection S_{11}. Additionally, I use a Smith chart to represent the concept of a *Q-circle*, as shown in Fig. 2.24, which helps us determine the resonant frequency and coupling factor.

According to Kajfez's work [17], the Q-circle represents the measured input reflection coefficient S_{11}, a complex quantity, as plotted on the Smith chart. There may be a rotation by an angle ϕ of the Q-circle relative to the Smith chart; however, this rotation does not affect the determination of the Q-factor Q and the coupling factor κ. To estimate the Q-factor using the Q-circle, we

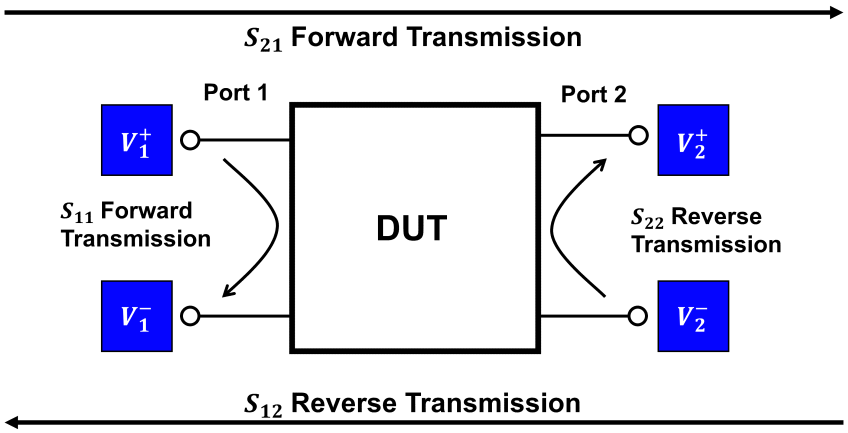

Figure 2.23: An illustration of the device-under-test (DUT) showing the incident, reflected, and transmitted waves.

can apply the three-point method to solve Eq. (2.56), where the point closest to the center is at frequency f_0, and the two points inclined by $\phi = 45°$ on each side of the centerline are at frequencies f_1 and f_2, respectively [104]. Additionally, the loaded quality factor can be estimated using the "3 dB" method, where $\Delta f_{-3\text{dB}}$ represents the bandwidth between the two frequencies of the resonator's resonance peak at -3 dB amplitude levels[105].

$$Q_L = \frac{f_0}{f_2 - f_1} = \frac{f_0}{\Delta f_{-3\text{dB}}} \tag{2.56}$$

Coupling Effect on Loaded Quality Factor

Q_L can also be determined by the coupling factor between the port and the resonator. The loaded quality factor Q_L of a resonator is influenced not only by its intrinsic properties but also by its coupling to external circuitry. The sensitivity to EPR) signals is maximized near critical coupling, where the impedance is matched to the resonator's port. The coupling strength is quantified by the coupling coefficient κ. For a critically coupled port, $\kappa = 1$; for an undercoupled port, $0 < \kappa < 1$; and for an overcoupled port, $\kappa > 1$.

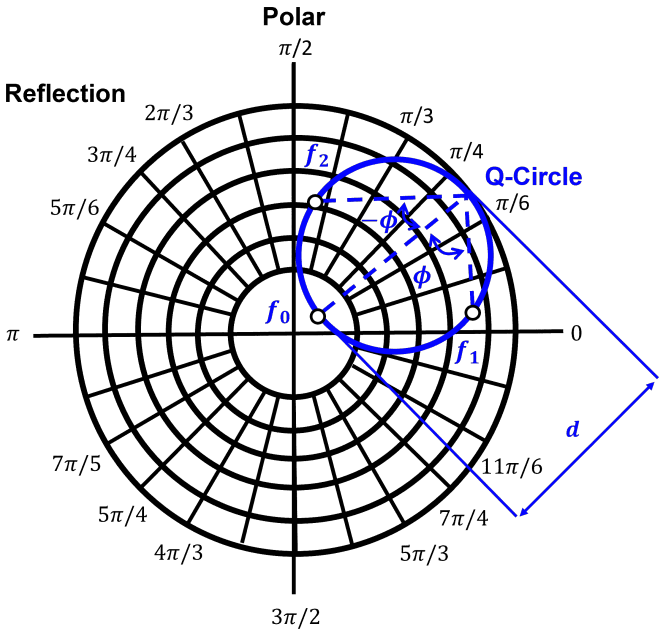

Figure 2.24: The Q-circle in polar coordinates used for transmission-line analysis.

The measurement of Q_L through transmission (using two ports) or reflection (using one port) depends on the coupling coefficients of the ports [105]:

$$Q_{L,\text{trans}} = \frac{Q_u}{1 + \kappa_1 + \kappa_2} \tag{2.57}$$

$$Q_{L,\text{ref}} = \frac{Q_u}{1 + \kappa_1} \tag{2.58}$$

Here, κ_1 and κ_2 are the coupling coefficients for port 1 and port 2, respectively. The unloaded quality factor Q_u, being intrinsic to the resonator, remains constant across different measurement methods. Although Q_L can be measured via reflection, transmission measurements are often more convenient, as they allow Q_L to be directly obtained from the resonance peak. To determine Q_L when only one port is critically coupled, one can critically couple port 1 while severely undercoupling port 2. As κ_2 approaches zero, Equation (2.57) approximates Equation (2.58).

While calculating the exact coupling coefficients requires an in-depth understanding of the Smith chart, an approximate estimation can be easily made using the Q-circle method. The relationship between the coupling coefficient κ and the diameter d of the Q-circle is given by:

$$\kappa = \frac{1}{\frac{2}{d} - 1} \tag{2.59}$$

According to Eq. 2.59, a diameter of $d = 1$ indicates critical coupling, $d > 1$ signifies overcoupling, and $d < 1$ represents undercoupling.

Model Fitting by the Wave-Approach Method for Coupling Factor and Q-Factor

To obtain more precise parameters, we can use the Levenberg–Marquardt algorithm [106] to fit the measured data to the wave-approach model, which is determined by the reflection coefficient

Γ, as shown in Eq. (2.60). For the cavity resonator connected to a VNA to determine S_{11}, the input reflection coefficient Γ can be described as [104]:

$$\Gamma = \Gamma_d + \frac{de^{j\gamma}}{1 + jQ_L\, 2\dfrac{\omega - \omega_L}{\omega_0}} \tag{2.60}$$

where ω_0 and ω_L are the unloaded and loaded resonant frequencies, respectively. d is the diameter of the Q-circle, Q_L is the loaded Q-factor, and $\dfrac{\omega - \omega_L}{\omega_0}$ is the frequency detuning. Γ_d is the detuned input reflection coefficient, which is further defined as:

$$\Gamma_d = \rho e^{j\phi} \tag{2.61}$$

When the cavity resonator is measured using a one-port VNA, the magnitude of S_{11}, denoted P_{S11}, can be described as:

$$P_{S11} = 10\log_{10}\left(|\Gamma|^2\right) \tag{2.62}$$

We can then combine Eq. (2.60) and Eq. (2.62) to derive the model for P_{S11}. The squared magnitude of the reflection coefficient $|\Gamma|^2$ can be expressed as:

$$|\Gamma|^2 = -a_1 t^2 |\Gamma|^2 + a_2 t^2 + a_3 + a_4 t \tag{2.63}$$

where the coefficients are determined as follows:

$$
\begin{aligned}
a_1 &= Q_L^2, \\
a_2 &= Q_L^2 \rho^2, \\
a_3 &= \rho^2 + 2\rho d \cos\theta + d^2, \\
a_4 &= -2\rho d Q_L \sin\theta, \\
t &= 2\frac{\omega - \omega_L}{\omega_L}.
\end{aligned}
\tag{2.64}
$$

Finally, we can define the model for the P_{S11} measurement of the cavity resonator using the power function:

$$
P_{S11} = 10\log_{10}\left(\frac{a_2\left(2\dfrac{f-f_L}{f_L}\right)^2 + a_3 + a_4\left(\dfrac{f-f_L}{f_L}\right)}{1 + a_1\left(2\dfrac{f-f_L}{f_L}\right)^2}\right) \tag{2.65}
$$

Transmission-Line Characterization of the Microwave Cavity Using Kajfez's One-Port Model

In the previous part, I determined the performance parameters of the microwave cavity, including (1) the resonant frequency, (2) the coupling factor, and (3) the unloaded Q-factor, using the wave-approach method. To complement this analysis, I employ an alternative technique for characterizing the microwave cavity's performance: transmission-line analysis using the lumped-circuit method.

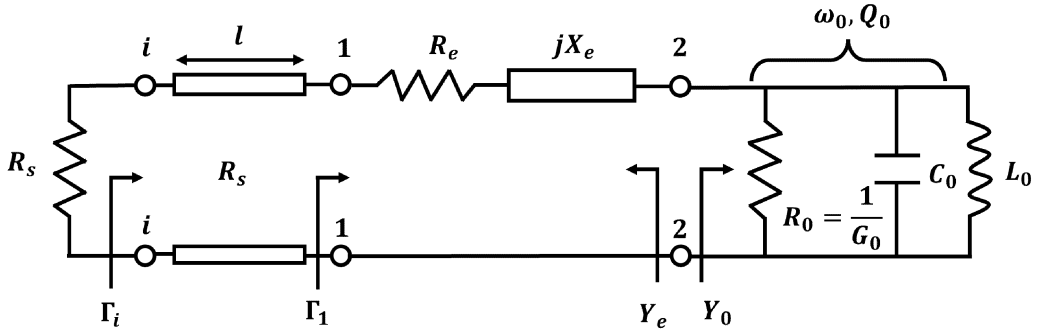

Figure 2.25: Kajfez's equivalent circuit model for transmission-line analysis [17].

Table 2.2: Symbols in Kajfez's Equivalent Circuit for the Microwave Cavity

Symbol	**Component**
R_s	Equivalent resistance of the external load (typically 50 Ω for a VNA)
R_e	Equivalent resistance of the coupler
X_e	Equivalent reactance of the coupler
R_0	Equivalent resistance of the microwave cavity
C_0	Equivalent capacitance of the microwave cavity
L_0	Equivalent inductance of the microwave cavity

Fig. 2.25 illustrates the equivalent circuit model used to characterize the microwave cavity. In this model, the unloaded resonator is represented by a parallel circuit consisting of a resistor (R_0), a capacitor (C_0), and an inductor (L_0). The resistance R_0 accounts for power dissipation within the resonator, and the unloaded Q-factor is denoted as Q_0 (previously referred to as Q_u in earlier chapters) [17].

On the left side of Fig. 2.25, the resistance R_s represents the external resistance of the VNA, typically 50 Ω. This external resistor is connected to the resonator, a transmission line, and a coupling port. The coupling mechanism is characterized by the impedance (Z_e):

$$Z_e = R_e + jX_e \tag{2.66}$$

The coupling mechanism accounts for losses through the resistance R_e and additional energy storage via the reactance X_e. The reactance X_e can be either inductive or capacitive depending on the coupling mechanism employed. For a small coupling loop, the reactance is inductive, thus $X_e = \omega L_e$. Conversely, for a probe coupling loop, the reactance is capacitive, given by $X_e = -1/(\omega C_e)$. In my design, a small coupling loop with inductive reactance is utilized.

In this section, I follow the transmission-line analysis approach developed by Chua et al. [18]. The first step involves extracting the circuit elements by determining the group delay introduced by the connecting transmission line. The model is then solved by measuring the input reflection coefficients $\Gamma_{in,a}$ and $\Gamma_{in,b}$ of transmission lines with lengths l_a and l_b, respectively, according to Kajfez's model [17]:

$$\begin{aligned} \Gamma_{in,a} &= e^{-2\gamma l_a}\Gamma_t, \\ \Gamma_{in,b} &= e^{-2\gamma l_b}\Gamma_t, \end{aligned} \tag{2.67}$$

where γ is the propagation constant of the transmission line. For low-loss lines, $\gamma = \alpha + j\beta \approx j\beta$, and the phase constant β is defined by:

$$\beta = \frac{-0.5}{l_b - l_a} \cdot \text{phase}\left(\frac{\Gamma_{in,b}}{\Gamma_{in,a}}\right) = \frac{-0.5}{\Delta l} \cdot \text{phase}\left(\frac{\Gamma_{in,b}}{\Gamma_{in,a}}\right), \tag{2.68}$$

where $\Delta l = l_b - l_a$.

In the equivalent circuit model shown in Fig. 2.25, the small loss is represented by the lumped resistor R_e, which accounts for losses within the coupling mechanism. The effect of delay introduced by the coaxial cable is de-embedded from the measured input reflection coefficient (Γ_i) to obtain the reflection coefficient at port 1 (Γ_1) using the following equation [18]:

$$\Gamma_1 = e^{2j\beta l}\Gamma_i, \tag{2.69}$$

where l is the length of the transmission line.

At port 1, the input impedance $Z_1(\omega)$ is defined as:

$$Z_1(\omega) = R_e + jX_e + Z_0 = R_e + jX_e + \frac{R_0}{1 + jQ_0\left(\frac{\omega}{\omega_0} - \frac{\omega_0}{\omega}\right)}, \tag{2.70}$$

where the relevant parameters of the microwave cavity are expressed as:

$$\begin{aligned} \omega_0 &= \frac{1}{\sqrt{L_0 C_0}}, \\ Q_0 &= \frac{\omega_0 C_0}{G_0} = \frac{R_0}{\omega_0 L_0} = R_0\sqrt{\frac{C_0}{L_0}}, \end{aligned} \tag{2.71}$$

and

$$\begin{aligned} X_e &= \omega L_e \quad \text{(inductive coupling)}, \\ X_e &= \frac{-1}{\omega C_e} \quad \text{(capacitive coupling)}. \end{aligned} \tag{2.72}$$

Additionally, the frequency-tuning parameter and the deviation factor of linearity are defined as:

$$\begin{aligned} \delta_m &= \frac{\omega_m - \omega_0}{\omega_0}, \\ D_m &= \frac{1 + \frac{\delta_m}{2}}{1 + \delta_m}, \\ \frac{\omega_m}{\omega_0} - \frac{\omega_0}{\omega_m} &= 2\delta_m D_m \approx 2\delta_m \quad \text{for} \quad \delta_m \ll 1. \end{aligned} \tag{2.73}$$

Using the three-point method illustrated in Fig. 2.26, the unloaded Q-factor Q_0 can be defined as [18]:

$$Q_0 = \frac{\omega_0}{|\omega_1 - \omega_2|}|x| \approx \frac{\omega_0}{\omega_1 - \omega_2} \quad \text{for} \quad |x| \approx 1, \tag{2.74}$$

where

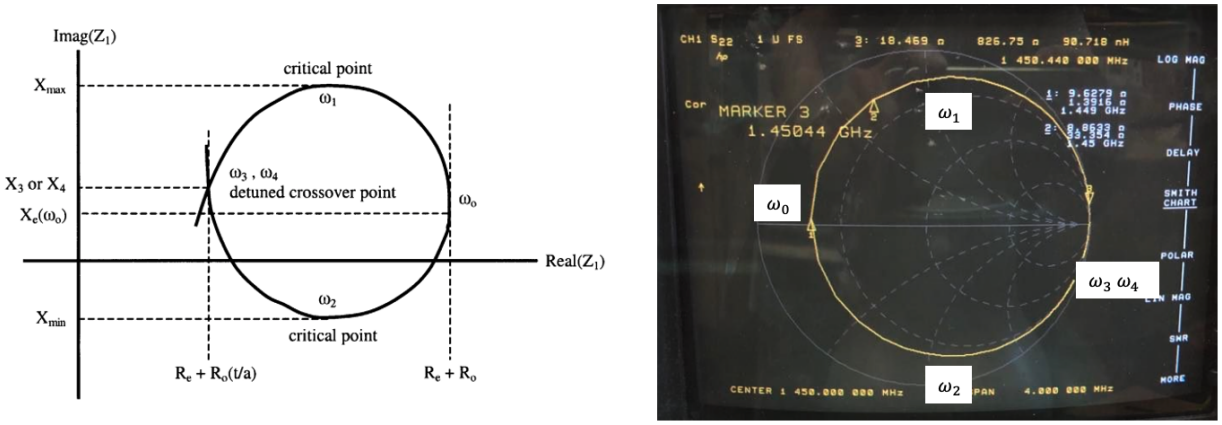

Figure 2.26: Left: Five-point measurement method on the Smith chart [18]. Right: Measured data of the designed cavity resonator.

$$\begin{aligned}
\omega_0 &= \frac{\omega_1 + \omega_2}{2}, \\
a &= 2\left(\frac{1}{D_3} + \frac{1}{D_4}\right)^{-1}, \\
b &= \frac{\delta_4 D_4 - \delta_3 D_3}{\delta_2 - \delta_1}, \\
x &= \sqrt{\frac{1}{2}\left(\frac{b-2a-1}{a+b}\right) + \sqrt{\frac{1}{4}\left(\frac{b-2a-1}{a+b}\right)^2 - \frac{a-1}{a+b}}}.
\end{aligned} \tag{2.75}$$

At the resonant frequency ω_0, the impedance is defined as:

$$Z_1(\omega_0) = (R_e + R_0) + jX_e(\omega_0), \tag{2.76}$$

and the impedance at the detuned crossover points ω_3 and ω_4 is given by:

$$Z_1(\omega_3) = Z_1(\omega_4) = \left[R_e + R_0\left(\frac{t}{a}\right)\right] + jX_3, \tag{2.77}$$

where

$$\begin{aligned}
t &= \frac{a}{1+bx^2}, \\
X_3 = X_4 &= \omega_0 L_e\left[1 + \frac{1}{2}(\delta_3 + \delta_4)\right] \quad \text{(inductive coupling)}, \\
X_3 = X_4 &= -\frac{1 + \frac{1}{2}(\delta_3 + \delta_4)}{\omega_0 C_e(1+\delta_3)(1+\delta_4)} \quad \text{(capacitive coupling)}.
\end{aligned} \tag{2.78}$$

To solve for the five characteristics of the equivalent circuit (R_0, R_e, L_0, L_e, and C_0), I require five equations corresponding to five different frequencies: ω_0, ω_1, ω_2, ω_3, and ω_4, as depicted in Fig. 2.26.

Thus, from Equations (2.76) through (2.78), each parameter is determined as follows [18]:

$$
\begin{aligned}
R_0 &= \frac{\mathrm{Re}\left[Z_1(\omega_0) - 0.5\left(Z_1(\omega_3) + Z_1(\omega_4)\right)\right]}{1 - \frac{t}{a}}, \\
L_0 &= \frac{R_0}{\omega_0 Q_0}, \\
C_0 &= \frac{Q_0^2}{R_0^2} L_0, \\
R_e &= \frac{\mathrm{Re}\left[0.5\left(Z_1(\omega_3) + Z_1(\omega_4)\right) - \frac{t}{a} Z_1(\omega_0)\right]}{1 - \frac{t}{a}}, \\
L_e &= \frac{X_3 + X_4}{\omega_0\left[2 + \delta_3 + \delta_4\right]}.
\end{aligned}
\tag{2.79}
$$

Chapter 3

Overcoming the Thermal-Noise Limit of Microwave Measurements by Pre-cooling with an Active Cold Load

I introduce a method, which I here name "active pre-cooling" (APC), for removing, just prior to performing a measurement, a large fraction of the deleterious thermal photons that would otherwise occupy the electromagnetic modes of a microwave cavity or some alternative form of radio-frequency resonator. The removal is achieved by temporarily over-coupling the cavity's modes to an active cold load (ACL). I report a room-temperature bench-top demonstration of the method, where this load takes the form of the input of a commercial low-noise amplifier (LNA). No isolator is inserted between the LNA's input and the cavity's coupling port.

Specifically, I established a time-resolved EPR experiment to demonstrate the application of active pre-cooling as a proof-of-concept (Fig. 3.7). Notably, the synchronization of the OPO laser and the selection of the microwave switch were among the most challenging aspects of this setup (Fig. 3.2), because the cavity must be cooled within a limited timescale. Consequently, it is crucial to maintain proper synchronization and to mitigate any adverse effects from the microwave switch, such as insertion loss, long switching times, or noise introduced by switching on and off. I designed an optimized synchronization scheme and selected a suitable microwave

switch to ensure robust operation. In addition, I developed a theoretical model and performed data analysis on the experimental results. The frequency-domain analysis was conducted using MATLAB (Fig. 3.10(b)), while the time-domain analysis was carried out using Python (Fig. 3.12).

The noise temperature of a monitored microwave mode drops to ∼75 K. Upon incorporating my pre-coolable cavity into a time-resolved (tr-) EPR spectrometer, a commensurate improvement in the signal-to-noise ratio is observed, corresponding to a factor-of-5 speed up over a conventional tr-EPR measurement at room temperature for the same precision and/or sensitivity. Modeling indicates the feasibility, for realistic mode quality factors and couplings, of cooling the room-temperature cavity's modes down to a few tens of K, and for this coldness to last several tens of μs, whilst the cavity and its contents are optimally interrogated by a microwave tone or pulse sequence. The method thus provides a simple and generally applicable approach to improving the sensitivity and/or read-out speed in pulsed and time-resolved EPR spectroscopy, quantum detection and other radiometric measurements. It provides a first-stage cold reservoir (of microwave photons) for other, deeper cooling methods to work from and, through the use of cryogenic ACLs (realized, in the first instance, as the inputs of existing cryogenic low-noise amplifiers), the method could itself be directly extended to lower temperature regimes.

3.1 Introduction of APC with Active Cold Loads

In the face of thermal noise, quantum measurements very often require cryogenic environments to achieve sufficient sensitivity and/or fidelity. In the microwave regime of frequencies, this involves cooling the hardware's cavities and connecting waveguides down to a temperature of a few tens of millikelvin (mK) so as to reliably eliminate the incoherent thermal photons that would otherwise reside within them and cause havoc. Obeying Bose-Einstein statistics, the expected number of such photons occupying any one of the cavity's electromagnetic (EM) modes is given by $\bar{n} = [e^{(hf_{\mathrm{mode}}/k_{\mathrm{B}}T)} - 1]^{-1}$, where f_{mode} is the mode's frequency. This level of cooling can be achieved, albeit onerously, by installing the hardware within a deeply cryogenic

refrigerator, most often a dilution or adiabatic-demagnetization fridge.

Though currently still a few factors of ten greater in temperature/photon number than what can be achieved through standard mK refrigeration (as involves the removal of thermal phonons from the materials that surround or fill an electromagnetic cavity), recent studies[44, 107, 108, 109, 110] have demonstrated the direct removal of thermal photons from particular microwave modes inside bench-top cavities at room temperature through the stimulated absorption of these photons by an optically spin-polarised medium placed inside the cavity. While obviating the need for physical refrigeration, this hybrid (optical-microwave) approach still requires a sufficiently powerful optical pump source for spin-polarizing the absorbing medium. This results in still quite a bulky and power-hungry system, even when a miniaturized microwave cavity of high magnetic Purcell factor[111, 112] is used to reduce the optical pump power/energy needed.

Within microwave instrumentation, electrically powered LNAs are ubiquitously used to increase the amplitude (and thus power) of weak signals. Guided quantitatively by Friis' formula[113], the deployment of the quietest LNA available at the front end of an instrument's amplification chain will minimize the amount of deleterious noise added to the measured signal, thereby maximize the overall signal-to-noise ratio (SNR) and measurement sensitivity[114]. Compared to their manifest utility in radio-astronomy[115] and deep-space communication[116], the gains in sensitivity from installing a lower-noise (cryogenic) preamplifier into an electron paramagnetic resonance (EPR) or nuclear magnetic resonance (NMR) spectrometer are found, empirically, to be both (i) modest[117, 118, 119], especially when the spectrometer's microwave or radio-frequency (RF) cavity is not itself refrigerated, and (ii) dependent on the degree of cavity-amplifier coupling[120].

Various schemes such as Townes' "Q-multiplier"[121], involving the incorporation of a maser gain medium inside the cavity itself, have been proposed over the years towards improving measurement sensitivity. It was Mollier *et al.*[10] who cut through the confusion to affirm that, no matter how low-noise the receiving LNA gain medium, the sensitivity of an EPR (or NMR) spectrometer is ultimately limited by thermal noise (*i.e.* incoherent microwave photons) generated from within the EPR cavity itself. An ultra-low-noise receiving amplifier attached

directly to the cavity's coupling port, or even an ultra-low-noise gain medium resident inside the cavity, will amplify both the signal and this noise equally; thus, the SNR won't improve. As addressed quantitatively by Poole[75] and others[122, 123] since, the only ways to improve sensitivity (for a given sample, completely filling the cavity, at a given temperature) are to either increase the cavity's quality factor Q (albeit at the expense of measurement bandwidth), so increasing the photon cavity lifetime, or to increase the EPR transition frequency (by applying a strong d.c. magnetic field to the sample), so reducing the number of thermal photons in the cavity's operational mode. Or else (back to where this argument began:) to physically cool the cavity or otherwise "state-prepare" its operational microwave mode(s).

At least for frequencies in the low-GHz region, today's solid-state LNAs, in the form of monolithic microwave integrated circuits (MMICs) or else as hybrids composed of interconnected discrete components, containing either InP- or GaAs-based high-electron-mobility transistors (HEMTs) or else SiGe-based heterojunction bipolar transistors (HBTs), offer impressively low noise temperatures (referred to input) of 50 K or less –even when operating at room temperature. As mature commercial-off-the-shelf (COTS) components, they are readily purchasable. If suitably designed/chosen, the noise temperature of such an LNA will decrease by a further order of magnitude or so upon cooling to liquid-helium temperature[124, 125]. With such low amplifier noise temperatures available, the sensitivity with which the field-amplitude/energy (= number of photons) inside a room-temperature microwave cavity can be measured is determined almost entirely by the cavity's own thermal noise (as is associated with the rate at which electromagnetic energy is dissipated inside the cavity) –not the small amount of extra noise imparted by the receiving amplifier chain used to monitor the cavity's field amplitude through a port attached to the cavity.

As already mentioned above, Wu *et al.*[44] demonstrated the cooling of an electromagnetic (EM) mode by coupling it to a "spin-cold" reservoir in the form of an optically excited crystal of pentacene-doped *para*-terphenyl (Pc:PTP). Ng *et al.*[107], Blank *et al.*[126], and Day *et al.*[110], have since demonstrated quasi-continuous mode cooling using photoexcited negatively charged nitrogen vacancies (NV^-) in diamond as a spin-polarised absorber. In a similar vein, Englund, Trusheim and co-workers[108, 109] have exploited mode cooling with NV^- diamond to enhance

the sensitivity of a magnetometer. All of these works use a cm-sized "3-D" dielectrically-loaded cavity to support a $TE_{01\delta}$ mode affording a high magnetic Purcell factor[111]. The frequency f_0 of this mode is adjusted, or a d.c. magnetic field is applied, to align it with the absorptive paramagnetic transition being targeted. Since the linewidth of this transition is narrow (a few MHz for pentacene, a few hundreds of kHz for NV^- diamond), these approaches to mode cooling are intrinsically narrow-band.

3.2 Experimental Setup of a Active-Pre-Cooled tr-EPR Spectrometer

The anatomy of the microwave cavity used in my zero-field time-resolved (tr-) electron paramagnetic resonance (EPR) spectrometer for cavity pre-cooling demonstrations is shown in Fig. 3.1. This cavity supports a $TE_{01\delta}$ mode at 1.4495 GHz, exhibiting a loaded quality factor of $Q_{\text{loaded}} = 82,000$ when critically coupled, corresponding to an unloaded quality factor of $Q_0 = 164,000$. The cavity consists of five main components: (i) a cylindrical brass enclosure, whose internal walls are plated with silver, (ii) a monocrystalline sapphire ring (supplied by J-Crystal Photoelectric Technology, China) exhibiting low dielectric loss, (iii) an EPR sample, namely a 0.1% pentacene-doped para-terphenyl (PC: PTP) crystal, located in the ring's bore, (iv) an over-coupling loop (coupling factor = 6.1) connected through a single-pole-double-throw (SPDT) RF switch [*viz.* a Qorvo RFSW1012PCK-411 mounted on an evaluation (eval.) printed circuit board] to a low-noise amplifier (LNA) [*viz.* a Qorvo QPL9547EVB-01 on an eval. board], functioning as an ACL, and (v) a critical-coupling loop connected, via a stub tuner, to a second identical LNA (another QPL9547EVB-01), functioning as the front-end pre-amplifier of a tuned homodyne receiver. The sample receives a Q-switched optical pulse at 532 nm, approximately 5.5 ns in duration and 2 mJ in energy, at a 10 Hz repetition rate, from an integrated Nd:YAG-pumped type-II-phased-matched β-barium-borate (BBO) Optical Parametric Oscillator (OPO)

(*viz.* a Litron Aurora II Integra). The cavity's internal cylindrical sapphire ring measured 40 mm in height with outer and inner diameters of 68 mm and 10 mm, respectively. The optical "c"-axis of the sapphire (a monocrystal) was aligned with the cylindrical axis. By rotating a screw, the cavity's axial length (*i.e.* the internal height of the cavity's ceiling above its "floor") could be varied from 150 mm down to 95 mm, allowing wide adjustment in the frequency of the cavity's $TE_{01\delta}$ mode. The sapphire ring's hollow supporting pillar was made of cross-linked polystyrene, a solid material offering both low dielectric loss and (unlike polytetrafluoroethylene or polyethylene) precision-machineability. This pillar was securely seated into a central hole in the cavity's floor, holding the sapphire ring 16 mm above the floor. The pillar's bore allowed for the transfer of pump light, up the cavity's axis, to the EPR sample. The cavity's silvered internal surfaces were finely buffed with an abrasive pad, removing patina, then solvent-wiped clean, to leave a gleaming finish.

By constructing a suitable model in COMSOL Multiphysics (a finite-element-based PDE solver) [127], the magnetic mode volume V_{mode} of the microwave cavity's $T_{01\delta}$ mode was calculated to be 29 cm^3. Experimentally, using a vector network analyser (= VNA, *viz.* an HP-8753C), the

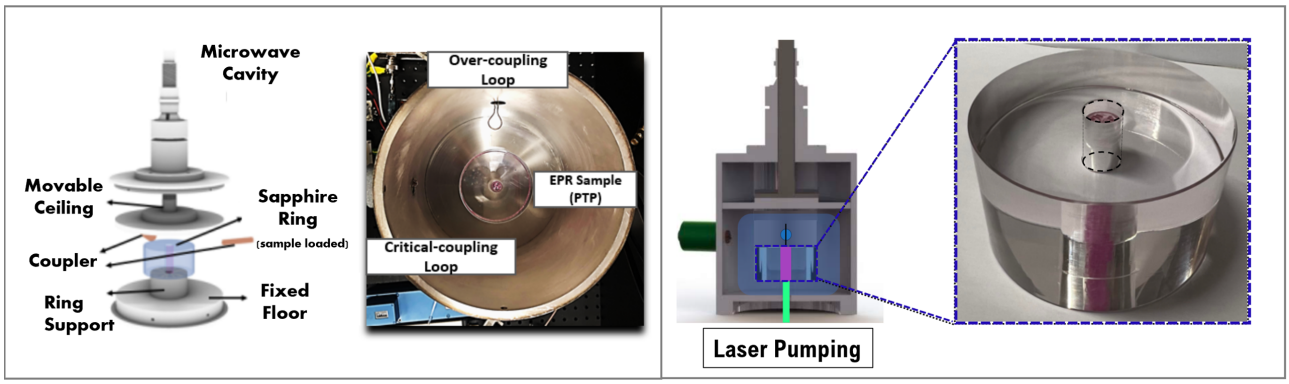

Figure 3.1: The left image presents the 3D CAD assembly of the microwave cavity (without microwave walls), featuring a movable "ceiling" (= plunger), raised and lowered by a rotating a helical screw (to which the ceiling is mechanically attached) seated in a matching helical thread tapped into the cavity's "roof" along the cavity's cylindrical axis. The photo to the right of the drawing shows the cavity's innards with the ceiling and roof removed. The cavity includes two ports: an over-coupling loop (at 12 o'clock in the photo) and a smaller critical-coupling loop (at 9 o'clock) just poking out of the cavity's internally-silver-plated wall. The right figure displays the microwave cavity in 2D cross-section. Here, the high-Q sapphire ring is located concentrically on top of a cross-linked polystyrene stand (not shown); its on-axis bore hole, 10 mm in diameter, is filled with the EPR sample (a 0.1% PC:PTP crystal).

cavity's loaded quality factor ($Q_{\text{loaded}} = 82,000$) and the coupling factors of each of its two ports ($\kappa_{\text{over}} = 6.1$ and $\kappa_{\text{crit.}} = 1$) were inferred by the method(s) of Kajfez and Hwan [40]. The PC:PTP crystal, used as my tr-EPR test sample, was grown by the vertical Bridgman method; it fitted into the 10-mm bore of the sapphire ring. The pulsed optical beam from a Q-switched OPO was directed into the microwave cavity via a multimode optical fiber, entering through an 8-mm coaxial hole in the centre of the cavity's floor.

The homodyne receiver for my tr-EPR measurements used a setup akin to Wu et al.'s previous work [20], albeit with the microwave cavity (resonator) now connected to an additional port (for cooling) and with additional routing switches and associated synchronization circuitry - see Fig. 3.6(c) and Fig. 3.2 below. A sync. pulse from the OPO's Q-switch driver is used to trigger two pulse generators [both Thandar TG105, one triggered by (= "slaved to") the other] providing appropriate TTL voltage transitions ("edges") to connect/disconnect the precooler and switch on/off the EPR spectrometer's interrogating microwave tone. The most critical switch, needed to perform a clean, abrupt disconnect of the precooling LNA, was a Qorvo RFSW101 SPDT switch, chosen for its low insertion loss, high isolation and sufficient speed; this routes the cooling port's over-coupling loop first to the ACL (embodied as the input of a Qorvo QPL9547 LNA) for cooling and, subsequently, to an "open" load (reflecting power back into the cavity, effectively neutralizing the port) for the tr-EPR measurement, when the interrogating microwave tone is applied through the cavity's critically-coupled monitoring

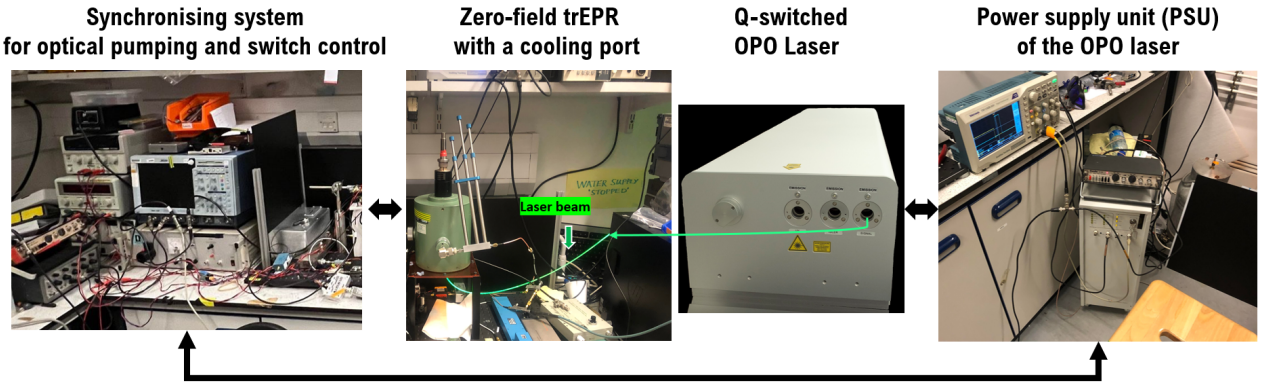

Figure 3.2: The experimental rig (here emphasizing its electrical synchronization and light path) encompassing, from right to left: the OPO's power supply unit (PSU), the OPO laser head itself, the resonator and it surrounding microwave "plumbing", and the tr-EPR spectrometer's support electronics.

port. To achieve sufficient measurement sensitivity, the homodyne receiver employs a cascade of legacy r.f. amplifiers (total gain ≈ 70 dB). Upon mixing (= homodyning) down to baseband, the transient tr-EPR signal is channeled (via a DC block) into a fast DC amplifier (*viz.* a Comlinear E103-I-BNC). All components operate under ambient lab conditions.

3.3 A Low-Noise Amplifier as an Active Cold Load

In microwave radiometry, cooled coaxial or waveguide terminations, also known as "cold loads", are used both as sources of noise and as absorbers[128] of unwanted signals. Such a cryogenic load is a passive component requiring no source of power. To be useful as an accurately quantified noise source or "reference", it must be anchored thermally to a heat bath (such as a "cold plate" within a cryostat) whose temperature is accurately known. A cryogenic load can be connected to one of the ports of a (cryogenic) circulator to form an isolator. At least within the circulator's operational bandwidth, this isolator can be used to protect a sensitive quantum circuit from backwardly propagating thermal noise and/or coherent signals unintentionally generated by reflections further up/along the signal path. In this context, I point out that the pre-cooling method introduced here draws parallels with the radiative cooling of a spin ensemble or resonator, held physically at liquid-helium temperature, by coupling it electromagnetically to an absorber (in the form of either a passive load or active device) held at mK temperature[129, 130].

A convenient alternative to a physically cryogenic termination is an *active* cryogenic load[131, 132], which, though a powered device, mimics the former's behavior. ACLs can be made from the inputs (gates/bases) of suitably biased low-noise transistors configured as single-port terminated amplifiers[133, 134, 135]. Though not always cold enough (nor broad-band or stable enough) to replace truly cryogenic terminations in all applications, they can be used advantageously in airborne and space applications to calibrate (or at least drift-correct) earth-monitoring radiometers[136, 135], dispensing with the encumbrance of mobile refrigeration and/or the operational need to "roll" the instrument's platform to point the radiometer at dark sky (*i.e.*, at 2.7 K cosmic background radiation –serving as an absolute temperature

reference).

Acknowledging that other approaches exist[137], I here apply the so-called "wave approach" to analyse the generation and flow of noise in realistic microwave circuits (see chapter 8 of Ref. [11], or Refs. [138, 99]). Through the construction of flow graphs combined with the application of Mason's "non-touching loop" rule[139, 140], this diagrammatic approach readily encompasses the frequently encountered complexity of what a laser physicist would describe as "etalon effects", where simultaneously forward- and back-propagating noise waves form (partial) standing waves along sections of transmission line between two or more impedance mismatches (the equivalent of partially reflecting mirrors functioning as beamsplitters/combiners). The *available* noise temperature from the input of an LNA (of sufficiently high gain) that is terminated by a matched and sufficiently cold load can thereby be quantified as[138, 141]:

$$T_{\mathrm{cold}} = -T_{\mathrm{min}} + 4T_0 \frac{R_{\mathrm{n}}}{Z_0} \frac{|1 - S_{11}\Gamma_{\mathrm{opt}}|^2}{(1 - |S_{11}|^2)|1 + \Gamma_{\mathrm{opt}}|^2}, \tag{3.1}$$

where S_{11} is the (in general complex) scattering parameter for reflection off the LNA's input and where T_{min} [K], R_{n} [Ω], and Γ_{opt} [dimensionless, complex] compose the LNA's set of industry-standard noise parameters[142, 143] (the associated unit of each is given in square brackets), and where T_0 and Z_0 are the reference temperature and line impedance associated with the definitions of same. For an LNA intended to operate at room temperature, that is constructed and noise-calibrated using the most common types of waveguide/cable and connector at low microwave frequencies, its is likely that $Z_0 = 50\ \Omega$, and $T_0 = 290$ K for the noise parameters provided (if one is lucky) by the LNA's manufacturer. At the cost of more complicated expressions (incorporating contributions from additional paths/loops according to Mason's rule, thereby involving more of the LNA's scattering parameters), the above formula can be extended to include the effects of a both warm and non-matched (thus partially reflecting) termination at the LNA's output[144, 145, 141].

Note that the minus sign in front of T_{min} in Eq. 3.1 can lead to (partial) cancellation between the two terms on the r.h.s. of the same, all depending on the exact magnitude of R_{n} and the locations of S_{11} and Γ_{opt} in the complex plane. For the particular LNA used in my

room-temperature experiments reported here, namely a Qorvo QPL9547, I calculate, from its specification sheet[100], that $T_{\text{cold}} = 29.1$ K at 1.45 GHz –around 10 times lower than the LNA's operating temperature.

Alas, complete sets of scattering and noise parameters are rarely published for cryogenic amplifiers, preventing immediate off-paper predictions of their performance when repurposed as cryo-ACLs. One informative exception is the noise calibration, exploiting a cryogenic impedance tuner, of the type of LNA used for the "ALPACA" phased-array radio telescope, as reported in ref. [146]. Though only the magnitude of S_{11} (not its angle) is provided, upon reading off from Figs. 12 and 13, *ibid.*, one can frame this LNA's available input noise temperature to within: 6.2 K $< T_{\text{rev}} <$ 7.3 K at 1.5 GHz, when operating at 20 K. Equivalent characterizations (including complex scattering parameters) of transistor-based, maser, and parametric amplifiers operating at even lower temperatures would enable the rational design of improved cryo-ACLs.

Finally, it is instructive to compare Eq. 3.1 against the standard expression for the effective noise temperature of an LNA[144, 142, 143] when used, as intended, as an amplifier:

$$T_{\text{eff.}} = T_{\text{min}} + 4T_0 \frac{R_{\text{n}}}{Z_0} \frac{(|\Gamma_{\text{s}} - |\Gamma_{\text{opt}}|^2)}{|1 + \Gamma_{\text{opt}}|^2 (1 - |\Gamma_{\text{s}}|^2)}, \tag{3.2}$$

where Γ_{s} is the coefficient of reflection off the source connected to the input of the LNA –in my case the port of a microwave cavity (see Fig. 3.3), possibly with a matching circuit/stub interposed. This expression will be needed later on for determining the temperature of a microwave mode. $T_{\text{eff.}}$ can be minimized by "noise matching", *i.e.* adjusting Γ_{s} to equal Γ_{opt} in

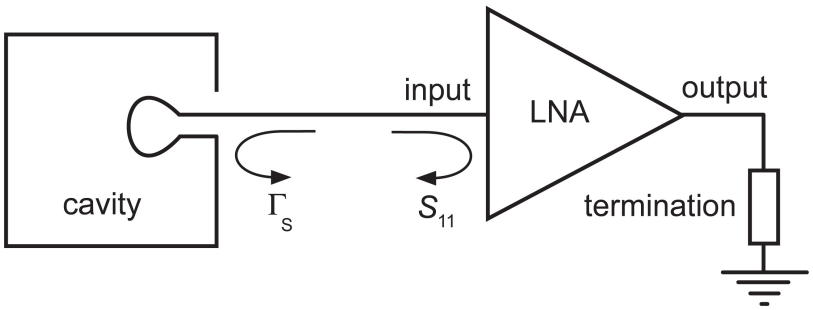

Figure 3.3: Paradigm of a cavity that is externally coupled to an ACL in the form of the input of an LNA whose output in terminated.

the complex plane (*viz.* on the Smith chart). Note that minimizing T_{cold} for an ACL constructed from an LNA is a different task (their respective formulae 3.1 and 3.2 above are different).

3.4 The Practical Active Pre-Cooling Protocol

The method's essential idea is to first (i) cool the electromagnetic modes of a microwave cavity containing a sample by over-coupling them to an external ACL and then (ii) swiftly reduce this coupling such that the sample can be interrogated in an electromagnetically cold (and thus quiet) environment before the modes warm back up to ambient temperature. Doing so may enable a more sensitive measurement than otherwise possible.

The first, cooling step is depicted in Figs. 3.3 and 3.4(a). In the bench-top experiments I report in this section, the physical walls and contents of the cavity, and the ACL attached to it, all lie at room temperature (nominally, 290 K). Note that the ACL is an electrically powered, single-port device. The *output* from the LNA that realizes the ACL does not (need to) go anywhere; it can be sunk into a matched passive load at ambient temperature or, if the attenuation backwards through the cooling LNA (essentially $|S12|$) is insufficient, into a second ACL –provided by the input of an additional LNA whose output is terminated by an ambient matched load. [I point out parenthetically that the idea of advantageously terminating the output of the "primary" cooling LNA with a "secondary" cooling LNA (and so on in cascade, as far as needs be) is not new[147].] In my experiments, the input of the cooling LNA is connected via a low-insertion-loss switch to a large loop of wire located inside the cavity, which serves as an over-coupled port.

For understanding and quantifying the effects of coupling an external ACL to a microwave cavity, I now appeal to what Siegman describes simply as a "useful noise theorem" in section 8.3 of his book[11]. Consider a cavity whose internal electromagnetic field is monitored by a small (weakly coupled) probe attached to an external port, so providing an output ("O/P"; see Fig. 3.5 –the equivalent of Fig. 8-10, *ibid.*). Here, one should regard the cavity's field as the common "bus" (or "loss-less network" –in Siegman's more circuit-oriented parlance)

through which all of it components, including external loads, interact. Applying the theorem: The available noise power per unit bandwidth B of an electromagnetic mode inside the cavity expressed in units of temperature, namely $T_{\text{mode}} = P_{\text{O/P}}/[k_{\text{B}}B(1 - |\Gamma_{\text{O/P}}|^2)]$, will equal the weighted sum of the temperatures T_i of the N bodies that dissipate the mode's energy, where the weighting p_i given to each body equals the fraction of the mode's energy that it dissipates, and where the sum of these fractions adds up to unity: $\sum_i^N p_i = 1$. Mathematically (*cf.* equation 8-3-3 in Ref. [11]): $T_{\text{mode}} = \sum_i^N p_i T_i$. I stress that T_{mode} quantifies the *available* noise power (per unit bandwidth), taking into account, through the above factor of $(1 - |\Gamma_{\text{O/P}}|^2)$, the rate

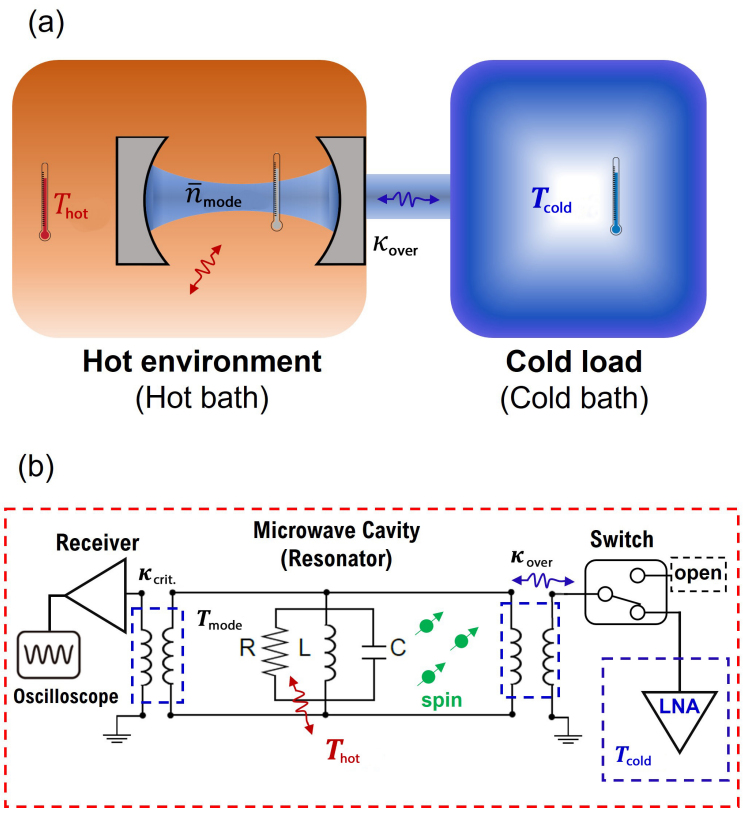

Figure 3.4: (a) Conceptual mechanism of active pre-cooling (APC): A microwave resonator is physically maintained at a temperature T_{hot} (in this article, T_{hot} equals room temperature, denoted as T_0) and supports an electromagnetic mode whose photon occupation number is $\bar{n}_{\text{mode}}$. This mode is coupled to a cold load maintained at a lower temperature T_{cold} with a coupling factor of κ_{over} between the load and the mode. (b) Simplified equivalent electrical circuit: The resonator, here drawn as an LCR tank circuit, is over-coupled (right) through a (SPDT) switch to either a cold load (in the form of the input of an LNA) or an open circuit –depending on the position of the switch. The mode's field amplitude (as generates a voltage across the tank circuit) can be measured by a second LNA through its own coupling port (left –this port's coupling is usually adjusted to be at critical coupling when the cooling LNA is switched out) whose output is recorded on a digital oscilloscope.

at which noise energy is extracted by the probe, where $\Gamma_{\mathrm{O/P}}$ is the reflection coefficient off the probe's port (again, see Fig. 3.5). For the sake of the argument here, I assume that the probe's coupling and thus the noise power the probe itself extracts, as will get sunk into a matched load (at the input of a monitoring instrument), is infinitessimally small, such that this load's dissipation does not contribute to the $\sum_i^N$ sum. One must regard the cavity's enclosing metal walls (of finite conductivity), any dielectric or magnetic material (of finite loss tangent) inside the cavity, plus any other components that contribute to the mode's intrinsic loss, as such dissipating bodies. External loads coupled to the cavity, such as an active cryogenic load, also count. The thermodynamic temperature that the electromagnetic mode itself adopts is a dissipation-weighted balance between them all.

Over-coupling to an external cold load (passive or active) guaranties that the temperature of a microwave mode is dominated by the load's available input noise temperature as opposed to the temperature(s) of the cavity's own intrinsic dissipators. Note that the method affords wide-band cooling: it will cool all of the modes lying within the cold load's bandwidth, provided they are sufficiently coupled to the load. Quantitatively, what depth of cooling can one expect? Referring back to Figs. 3.4(a) and 3.5: I suppose for simplicity that all dissipating components of the microwave cavity (grey) are kept at the same common physical temperature of $T_{\mathrm{hot}} = T_0$ (orangey brown). Consider a microwave mode within the cavity that is coupled, with a coupling factor of κ, to a cold load (blue), whose available temperature is T_{cold}. The dissipation generated in the external load will be κ times that of the mode's own intrinsic (*i.e.* internal)

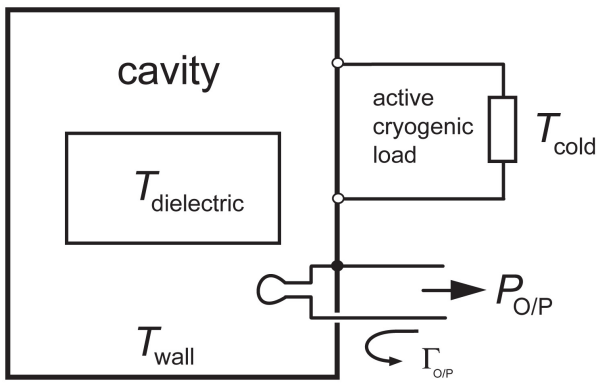

Figure 3.5: The cavity's dissipators, their temperatures, and the resultant noise power outputted.

dissipation. Applying my implementation of Siegman's useful noise theorem: on average, $\bar{n}_{\mathrm{mode}}$ thermal photons will occupy the mode, corresponding to a mode temperature of $T_{\mathrm{mode}} = hf_{\mathrm{mode}}/[k_{\mathrm{B}}\ln(1+1/\bar{n}_{\mathrm{mode}})]$, where

$$T_{\mathrm{mode}} = \frac{T_0 + \kappa T_{\mathrm{cold}}}{1+\kappa} \tag{3.3}$$

One immediately sees from this equation that, for a high coupling factor $\kappa = \kappa_{\mathrm{over}} \gg 1$, corresponding to a substantially over-coupled port, the microwave cavity's noise temperature will approach that of the cold load, T_{cold}. The dynamics of the cooling process is treated around Eqs. 2.39 and 2.40, whose steady-state solution (2.41) agrees with the thermodynamic treatment above. The time scale on which the mode is cooled is set by the mode's as-loaded photon lifetime, namely $Q_0/[2\pi f_{\mathrm{mode}}(1+\kappa_{\mathrm{over}})]$.

In the case of an ACL formed by the (gated) channel of the LNA's input HEMT, the height of this channel is just a few nm (defining a layer of two-dimensional electron gas: a "2-DEG") and its lateral dimensions (length and width) are sub-microns[148]. The cooling capacity of this atto-liter volume of semiconductor is limited. Operationally, one requires that the density, in frequency space, of the electromagnetic modes to be cooled is sufficiently low such that the noise power provided by the total number of modes within the input HEMT's operating bandwidth is insufficient to saturate/overload its channel. This means that the cavity enclosing and defining the modes must not be too large (to prevent the spectral density of modes becoming too high) nor too hot, and the coupling factors of its modes to the ACL must not be too high. As a last resort, saturation could be thwarted by inserting a low-loss band-pass filter between the cooling LNA and the cavity to act as a pre-selector, so coupling the ACL to fewer modes. A sense of scale is useful with regards to these concerns, however: The noise power impinging on the LNA's input, at a coupling factor of κ, from a cavity mode at absolute temperature T, equals $2\pi f_{\mathrm{mode}}\kappa k_{\mathrm{B}}T/Q_0$, where k_{B} is Boltzmann's constant. For the experimental parameters of the demonstrations reported in this article, this amounts to -121 dBm per mode. The combined power from the several dozen modes lying within my LNA's frequency range (for the dimensions and dielectric loading of the cavity that I used) is thus still around ten orders of

magnitude weaker than my LNA's specified saturation input power (at -1 dB compression). How the LNA's noise parameters themselves depend on the input (noise) power at elevated power levels is seldom reported, though this huge ratio suggests that the cooling capacity of an ACL constructed from a solid-state LNA enjoys substantial headroom.

Practicalities (that complicate matters somewhat):

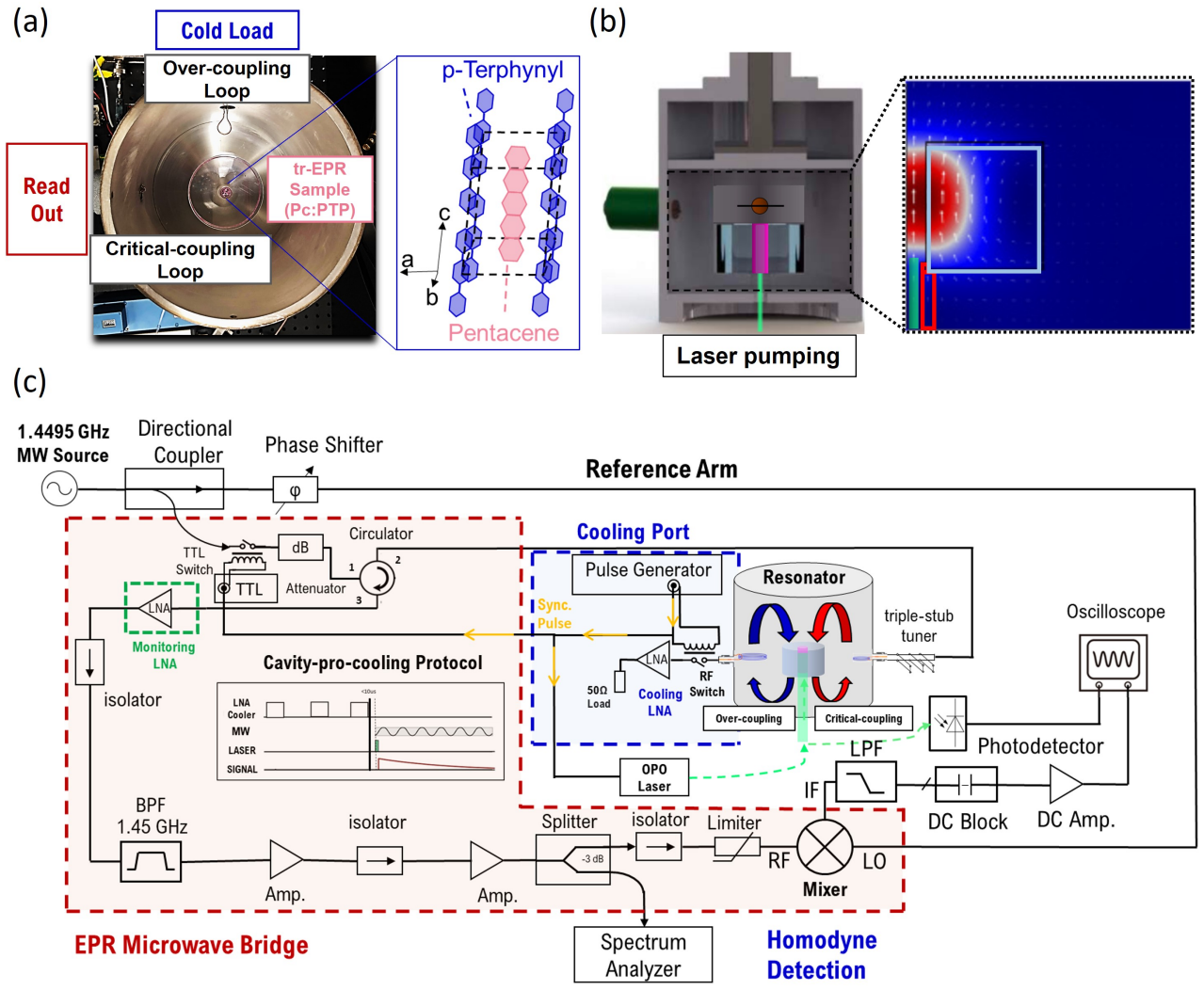

Figure 3.6: (a) Photograph of the experimental resonator's interior: a sapphire ring holding a 0.1% Pc:PTP crystal, surrounded by the silver-plated walls of a cylindrical brass enclosure. (b) CAD diagram of the same resonator with a two-dimensional axisymmetric simulation of the magnetic flux (white arrows) and magnetic energy density of the $TE_{01\delta}$ microwave mode[19] that this resonator supports. (c) Signal-path anatomy of the experimental time-resolved EPR spectrometer used to demonstrate active pre-cooling. This circuit incorporates homodyne detection of the transient EPR signal. The firing of the optical-parametric oscillator (OPO) laser system and the closing/opening of the two microwave switches are scheduled via transistor–transistor logic (TTL) control pulses (generated by two cascaded pulse generators –both a Thandar TG105) as explained in Fig. 3.7.

[1] The value of the external coupling, κ, associated with a port of the cavity is usually determined by interrogating the port with a vector network analyzer (VNA) whose connecting leads have a known line impedance –usually 50 Ω. The input of an ACL that subsequently gets attached to the port will never perfectly match this impedance and so the cavity's coupling to the ACL will be different. One can pragmatically take this into account by defining a modified coupling: $\kappa' = \frac{\mathrm{Re}[Z]}{Z_0}\kappa$, where $\mathrm{Re}[Z]$ is the real part of the ACL's input impedance Z. Or else one can add a low-loss matching network (equivalent to a series reactance equal to $-\mathrm{Im}[Z]$) to the ACL's input. The input impedance of the Qorvo QPL9547 LNA (mounted on an evaluation board) at 1.45 GHz that I here repurpose to function as an ACL is $Z = (36.5 - \mathrm{i}\ 18.3)\ \Omega$ (from its specification sheet). Its departure from $Z = 50\ \Omega$ will cause a 27% drop in the coupling without a compensating network. Also, the partial standing wave (VSWR = 1.35) along the connection between the ACL and the cavity's over coupled port will cause the coupling to vary with the connection's phase length. This can be straightforwardly modeled though, in my experiments, this length was kept as short as possible (much less than a wavelength at 1.45 GHz) to avoid the complexity.

[2] The noise temperature on the same port as seen/felt by the cavity will also be slightly higher than the cooling LNA's (available) input noise temperature due to insertion losses (I.L.) along this same connection. These losses comprise [see Fig. 3.6(c)] the I.L. of the single-pole double-throw (SPDT) switch itself plus those of the two short connecting coaxial cables on either side of it. The increased noise temperature generated by them equals λT_0, with $\lambda \equiv L_{\mathrm{dB}}/4.34$, L_{dB} being the overall I.L. in units of dB[11]; I measured this loss to be 0.19 dB.

[3] In the experiments reported here, the temperature of a particular ("target") mode at 1.45 GHz is monitored through an additional second port into the cavity, to which the input of a second LNA is critically coupled (when the cooling LNA on the overcoupled port has been disconnected) –see Step 3 of Fig. 3.7. The output of this monitoring LNA feeds a homodyne receiver tuned to the target mode's center frequency. When modeling the cavity's noise, one needs to include the (albeit relatively modest) cooling effect of this critically-coupled monitoring LNA (*viz.* a second, nominally identical, Qorvo QPL9547EVB-01) that is permanently coupled to the mode.

Including all of the above additional contributions (as per Eq. 2.49), the lowest obtainable mode

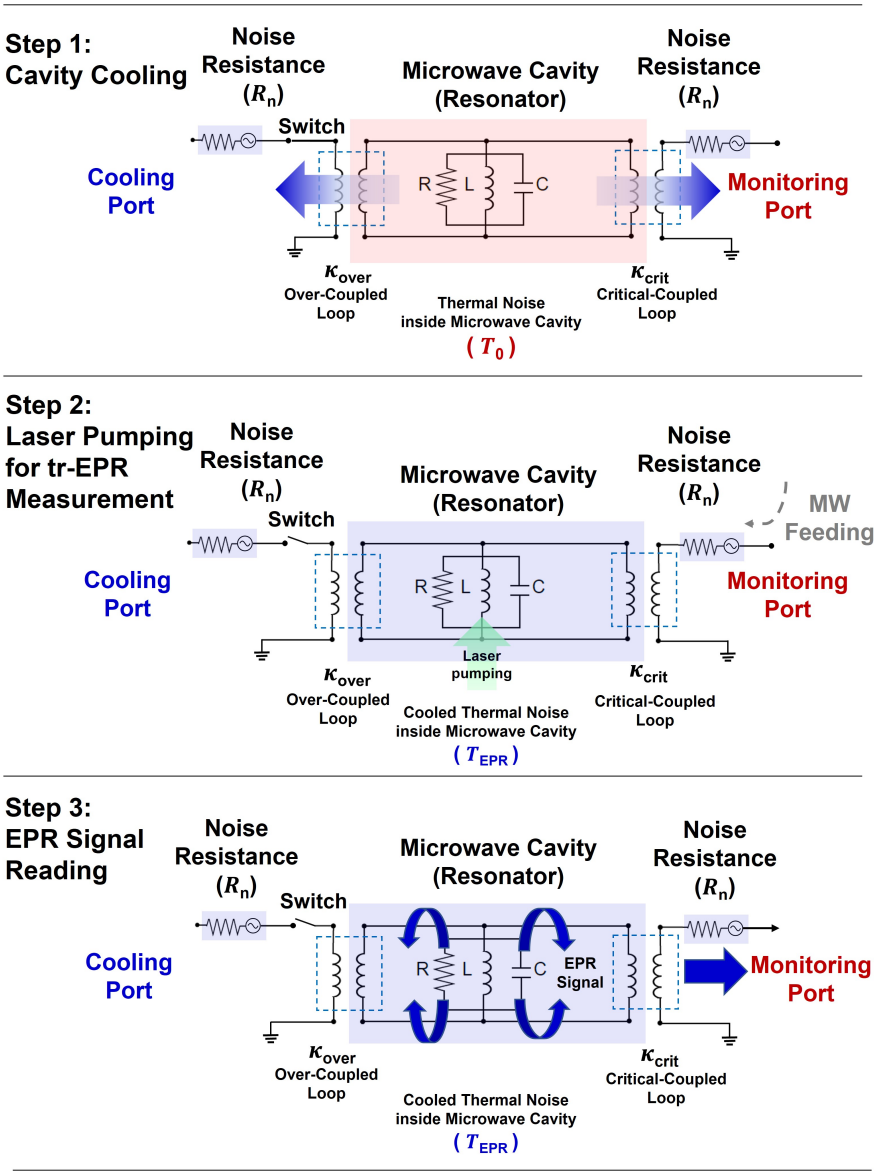

Figure 3.7: Active pre-cooling as applied to time-resolved (tr-) EPR: In Step 1, an LNA connected to an over-coupled cooling port extracts thermal noise (energy) from the microwave cavity (represented here as an LCR circuit); this also pulls the cavity mode's resonance frequency away from f_0 –slightly. Next (Step 2), a switch disconnects the cooling LNA, bringing the mode back on resonance (*i.e.*, its frequency coincident with the EPR transition's line center at 1.45 GHz). Instantaneously with this microwave switching, a q-switched optical pulse (around 7 nanoseconds in duration) of 532-nm pump light is shone on the EPR sample within the cavity. Step 3: a continuous-wave (CW) interrogating microwave tone is thereupon applied via a circulator to the cavity's monitoring port, as shown in Fig. 3.6 (c), which, upon re-emerging from the cavity through the circulator's third arm, provides a tr-EPR signal characterizing the EPR sample.

temperature, $T_{\text{mode}}^{\text{cooled}}$, is predicted to be

$$T_{\text{mode}}^{\text{cooled}} = \frac{(1+\kappa'_{\text{over}}\lambda)T_0 + \kappa'_{\text{over}}(1-\lambda)T_{\text{cold}} + T_{\text{mon.}}}{2+\kappa'_{\text{over}}}, \tag{3.4}$$

where $T_{\text{mon.}}$ is the effective cooling temperature of the monitoring LNA taking into account the unavoidable I.L. of the triple-stub tuner connecting it to the cavity's monitoring port; this was measured to be 0.9 dB and takes $T_{\text{mon.}}$ up to 78.0 K. The expected noise temperature inside the cavity after pre-cooling, as calculated from Eq. 3.4 above (see Eq. 3.5), is $T_{\text{mode}}^{\text{cooled}} = 85.0$ K.

3.5 Switchover followed by Interrogation

The second essential step in my pre-cooling method is to rapidly disconnect the over-coupled ACL from the cavity without excessively disturbing the pre-cooled mode(s). For the method to work and be useful: (i) the over-coupling factor, κ_{over} must be sufficiently large to provide a worthwhile depth of cooling, but also (ii) the switchover between the cavity's over- and critically-coupled configurations must be sufficiently adiabatic, whilst (iii) the time required to perform the switchover must be a sufficiently small fraction of the cavity's photon lifetime to leave enough time to exploit the pre-cooling before the cavity re-thermalizes. Obtaining a sufficiently high external coupling whilst maintaining the cavity's quality factor when this coupling is switched out, represents an engineering challenge –though a surmountable one. The optimal switching time is a happy balance between (i), (ii) and (iii).

The well-known Landau-Zener (L-Z) model[149, 150] provides quantitative insight into the location of this balance. Since, for the relatively high-Q (by room-temperature standards) sapphire-loaded dielectric resonator that I use in my demonstration, the distances in frequency between the operational microwave mode and its neighboring ones correspond to many thousands of cavity linewidths, a switching time that is a tenth or a hundredth of the cavity lifetime easily satisfies adiabaticity according to the L-Z formula (for the probability of a non-adiabatic transition). Note also that even if adiabaticity is compromised by using a very high over-coupling factor (so perturbing the frequencies and shapes of the cavity electromagnetic modes)

and/or a too-rapid switchover, the pre-cooling effect is still protected by the fact that those modes closest in frequency to the operational mode, and thus those that stand to get substantially mixed with it (at anti-crossings), will also lie within the bandwidth of the ACL, and thus stand to be cooled by it also (though admittedly their couplings to the ACL and thus their cooling depths will vary). The mixing in of these nearby modes with the operational mode should thus not substantially raise the temperature. In practice, there is a limit to the amount of switchable external coupling (usually in the form of metal stubs or loops) that can be added to a cavity without reducing the intrinsic quality factor (*i.e.* photon lifetime) of its modes when the external coupling is switched out (disconnected). The frequency shift Δf associated with the imperfect switching in and out of an overcoupled ACL, is shown in Fig. 3.8. If the cavity's mode structure gets excessively scrambled, more distant "hot" modes beyond the ACL's cooling bandwidth risk getting mixed into the operational mode at switchover so raising its temperature. I point out here parenthetically that the engineering challenge of achieving a large change in coupling while incurring only a small Δf (or at least the avoidance of anticrossings and mode scrambling) draws parallels to the realization of switchable attenuators exhibiting low dispersion, for which proven design strategies/solutions are known. Based on my crude L-Z analysis, there would appear to be at least two decades of headroom for raising κ_{over} to the point of

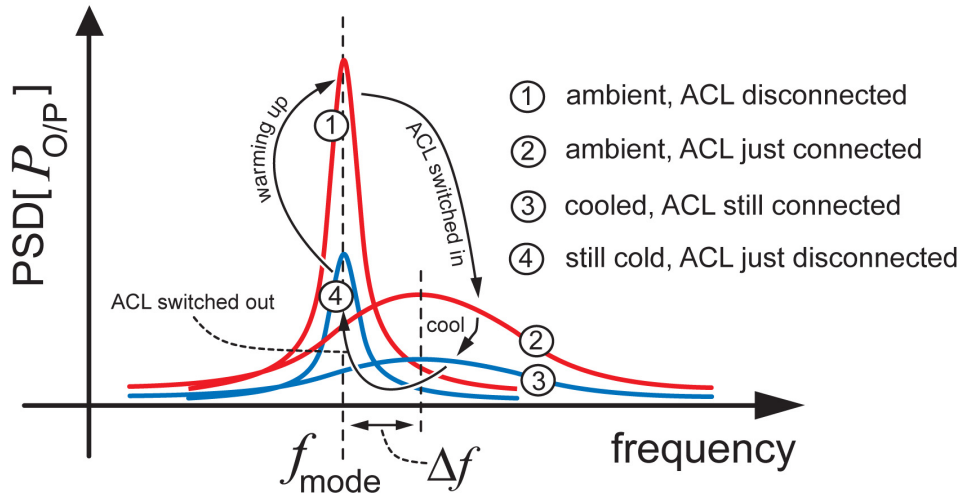

Figure 3.8: Active pre-cooling in the frequency domain. The vertical axis is the power spectral density (PSD) of the noise signal extracted by a (small) monitoring probe inserted into the cavity (like what is shown at the bottom right of Fig. 3.5). Here, the linewidth of the thermal noise associated with a mode is inversely proportional to the mode's loaded Q. The area under the curve for curves of the same color is the same.

"diminishing returns", where it is no longer the external coupling but the noise temperature of the room-temperature ACL itself that limits the cooling depth. Upon hitting this floor, the only route to lowering the mode temperature still further would be the design and realization of improved low-noise transistor gates/channels, or whatever other active device structure or state of matter (beyond 2-DEGs) that can be co-opted to serve as an improved ACL, whose noise parameters can more severely reduce T_{cold} as per Eq. 3.1.

Further experimental details: My implemented experimental set-up is shown in Fig. 3.6. However, when solely demonstrating mode cooling, (i) the cavity need not be loaded with an EPR sample, and (ii), the EPR bridge's circulator can be removed with the monitoring LNA (inside the dashed green box in Fig. 3.6) connected directly to the critically-coupled port's stub tuner. My resonator is a cylindrical brass cavity, internally plated with silver, whose internal volume is partially filled by a concentrically located ring of monocrystalline sapphire (supplied by J-Crystal Photoelectric Technology, China) whose c-axis lies parallel to the cavity's axis of rotational symmetry[19]. This ring supports a $\text{TE}_{01\delta}$ mode at 1.45 GHz, whose intrinsic quality factor $Q_{\text{cav.}} = 164{,}000$, providing a loaded quality factor at critical coupling ($\kappa_{\text{crit.}} = 1$) of $Q_{\text{crit.}} = Q_{\text{cav.}}/2 = 82{,}000$. The frequency f_0 and field profile of this mode were accurately modeled using COMSOL Multiphysics[127]. Unlike the superheterodyne receiver (incorporating a narrowly filtered 70-MHz IF strip) used in the previous cavity-cooling works by Wu and Ng *et al.*[44, 107], I here use a simpler high-gain homodyne receiver to monitor the amplitude/excitation of the $\text{TE}_{01\delta}$, recording the receiver's output into a Tektronix TBS 1102B-EDU oscilloscope.

It is worth pointing out that both the cooling and the monitoring of the $\text{TE}_{01\delta}$ mode *could* alternatively be implemented using just a single port attached to a single LNA, *if* this port's coupling to the mode *were* made dynamically adjustable. The LNA would be alternatively connected ("toggled"), at sufficient speed and glitch-free, between (say) a larger and a smaller coupling loop. However, given that my cavity already had two separate coaxial ports (feedthroughs), it was simpler, with the components immediately available to us, to use both of these ports set to different fixed couplings κ, namely: (i) an over-coupled "cooling" port ($\kappa = \kappa_{\text{over}} = 6.1$), connected through a low-insertion-loss single-pole double-throw (SPDT) switch (*viz.* a Qorvo

RFSW1012 mounted on an evaluation board) to either the ACL (*viz.* the input of a Qorvo QPL9547 LNA mounted on an eval. board) or to an "open" termination –the choice being determined by the control voltage applied to the RFSW1012 switch; and (ii) a "monitoring/interrogation" port, critically coupled ($\kappa = \kappa_{\text{crit.}} = 1$) to the $\text{TE}_{01\delta}$ mode through a Maury Microwave 1819A triple-stub tuner, and used to monitor the mode's field amplitude (and thus noise temperature). These two different ports are depicted, conceptually, in Fig. 3.4(b); their experimental embodiments are displayed in Figs. 3.6(a) and 3.6(c). The coupling factors of both ports (cooling and monitoring), as well as the quality factor of the sapphire resonator's $\text{TE}_{01\delta}$ mode, were accurately determined using an HP8753C vector network analyzer (VNA)[40, 18].

It is worth pointing out how the monitoring LNA itself helps to cool the mode that it monitors. This would not happen if, as is often done, a microwave isolator were inserted between the monitoring LNA and the cavity –so as to "protect" the cavity from external noise. Noise (and thus sensitivity) wise, it is always advantageous to connect the monitoring LNA directly to the cavity, so long as its input noise temperature is lower that the physical temperature of the isolator's internal termination.

The reduction in thermal noise will persist so long as the cooling LNA is connected. Upon disconnecting it and connecting the over-coupling loop (port) instead to a reflective "open", the mode regains its higher quality factor, namely $Q_{\text{crit.}}$, and warms up on a timescale set by the mode's photon lifetime[151], namely $\tau_{\text{warm up}} = \frac{Q_{\text{crit.}}}{2\pi f_0}$. Note that this is substantially longer than the time required for cool down. [Parenthetically: any perfectly reflecting impedance, like a "short", could serve just at well as the open that I employ here.] Since the monitoring port is critically coupled to the $\text{TE}_{01\delta}$ mode, this mode's temperature will settle at the (equally weighted) average of $T_{\text{hot}} = 290$ K and $T_{\text{mon.}}$, namely $T_{\text{mode}}^{\text{ambient}} = 184.0$ K for my particular experiment.

3.6 Results and Analysis

I verified the noise characteristics of my cooling LNA (*viz.* a Qorvo QPL9547EVB-01 operating at room temperature) using the industry-standard Y-factor method[152]. This included connecting the LNA's input to a passive load, well matched to 50 Ω, both at room temperature and when immersed in a small dewar filled with liquid nitrogen. Within experimental error (taking noise generated by losses along lengths of line into account), my own measurements were wholly consistent with the manufacturer's specification sheet. When used as an amplifier, this LNA exhibits, at 1.45 GHz, an impressive noise figure of just 0.182 dB (for $\Gamma_s = 0$; referenced on the device's leads), equivalent to an effective noise temperature (referred to input) of just $T_{\text{eff.}} = 12.4$ K; see Table 2.1 for this LNA's full noise parameters interpolated to 1.45 GHz, and Refs. [142, 143] for associated definitions. Note that $T_{\text{eff.}}$, calculated using Eq. 3.2, is substantially smaller that the temperature of the same device when configured as a cold load, namely $T_{\text{cold}} = 29.1$ K, calculated using Eq. 3.1. Since the QPL9547 MMIC was designed/optimized by its manufacturer for use as a LNA, this should not be hugely surprising.

Experimentally, I observed a reproducible transient on the EPR (homodyne) signal as the SPDT switch (*viz.* a Qorvo RFSW1012EVB-01) opened and disconnected the pre-cooling LNA from the microwave cavity. This artefact, lasting less than 3 μs in my experiment, could be substantially removed by measuring it for multiple switch openings then subtracting the average from my measured traces.

Mode Cooling: The effect of connecting and then disconnecting the over-coupled cooling LNA to my cavity's $\text{TE}_{01\delta}$ mode at $f_0 = 1.45$ GHz is shown in Fig. 3.9. From the difference in the time average of the measured noise voltage squared for the mode under cooled and ambient conditions, the depth of cooling is estimated to be $\Delta P_{\text{exp-Cool}} = -3.5 \pm 0.4$ dB. This agrees reasonably well with both my theoretical estimate ΔP_{model} and my analysis using the noise spectrum from experimental time-resolved-EPR data, namely $\Delta P_{\text{exp-EPR}}$, as shown in Fig. 3.10(b). All my estimates are summarized in Table 3.1. Upon curve-fitting to the rise in the measured noise voltage squared as a function of time, the characteristic time quantifying the persistence of the mode's coldness after disconnection from the cooling LNA is estimated

to be $\tau^{\text{exp.}}_{\text{warm up}} = 9 \pm 1\ \mu$s; see Fig. 3.12.

Applicaton to EPR: The protocol used to implement active pre-cooling (APC) is depicted in Fig. 3.7 and consists of three stages: initial noise reduction (mode cooling) with the over-coupled port connected to an ACL. T; tis is followed by disconnection of the ACL, re-tuning the operational mode of the cavity back onto the line center of the target EPR transition. A nano-second optical pump pulse [provided by an optical parametric oscillator (OPO) pumped by a q-switched laser] is then immediately applied, followed by a continuous-wave (CW) microwave tone, whose reflection off the now critically-coupled cavity provides, upon homodyne detection (with filtering and amplification both before and after downshifting), a time-resolved EPR signal.

To demonstrate the utility of active pre-cooling, I studied the signal-to-noise ratio (SNR) and noise spectrum of traces obtained from performing tr-EPR on a photo-excited sample of pentacene-doped *para*-terphenyl (Pc:PTP) at room temperature in zero applied magnetic

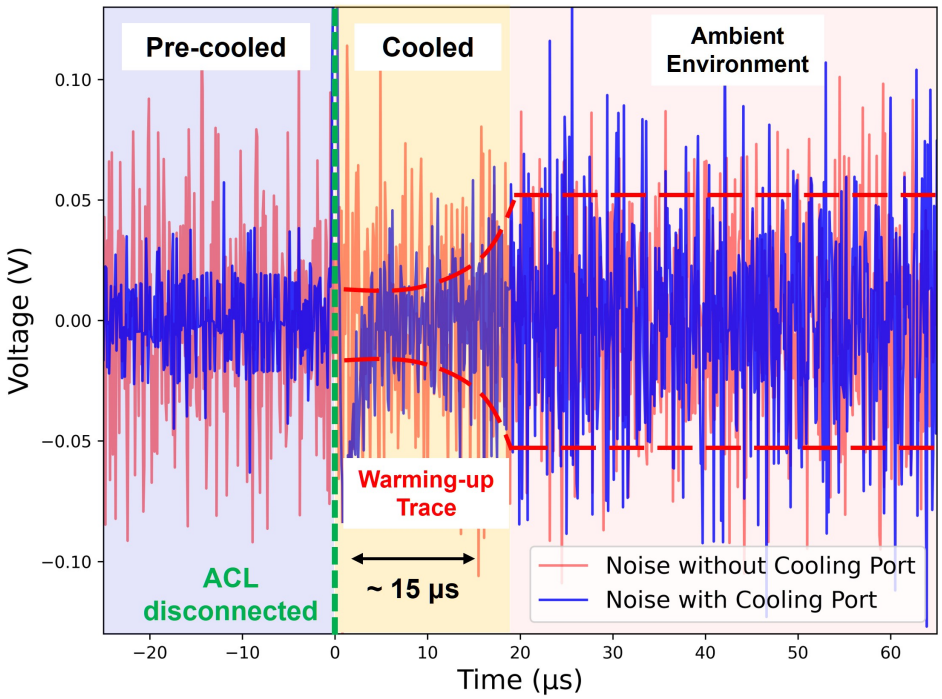

Figure 3.9: Increase in measured noise over time as the experimental cavity's monitored microwave mode warms up from "pre-cooled" to ambient conditions. The two red dashed lines track the envelope of the voltage noise. Upon curve-fitting to this envelope (see Fig. 3.12), the characteristic time of the warming up is determined to be $\tau^{\text{exp.}}_{\text{warm up}} \approx 9 \pm 1\mu$s.

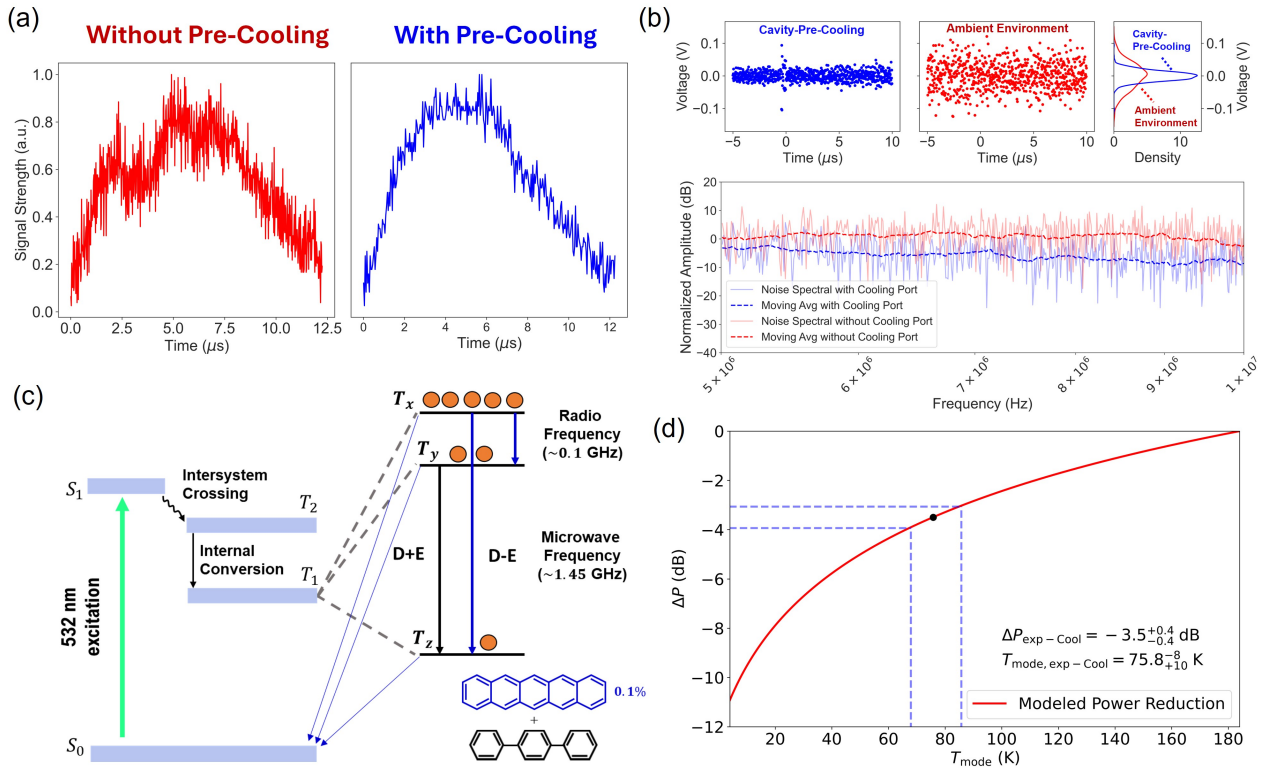

Figure 3.10: (a) Zero-field (ZF) tr-EPR signal of Pc:PTP's $T_x - T_z$ transition[20] without (red) and with (blue) pre-cooling. (b) Thermal noise (in the time domain) extracted from each of these ZF tr-EPR signals and, below, their corresponding spectral densities; as before, blue and red correspond to the pre-cooled (with) and ambient (without) conditions, respectively. (c) Simplified Jablonski (= energy-level) diagram of the ZF sublevels (T_x, T_y, T_z) of pentacene's triplet ground state, where D and E denote the ZF splitting (ZFS) parameters. (d) Modeled noise power reduction (ΔP) at the homodyne receiver's input as a function of the noise temperature of the EPR cavity's operational mode, T_{mode}. Since its uncertainty is lower, the estimated depth of cooling presented here ($\Delta P_{exp\text{-}Cool}$) corresponds to that achieved by active pre-cooling alone (see Table 3.1). The depth's standard error is indicated by dashed cornflower-blue lines.

field. This sample and the complete spectrometer around it are shown in Fig. 3.6. Fig. 3.10(a) displays tr-EPR signals for the Pc:PTP triplet's Tx-Tz transition at 1.4495 GHz [as shown in Fig. 3.10(c)] both without (red) and with (blue) pre-cooling. The noise on each of the measured tr-EPR signals shown in Fig. 3.10(a) was extracted from the causal EPR response by first (i) generating a smoothed-out version of the measured data by boxcar averaging, the width of each averaging box being set at 100 ns, then (ii) subtracting this version from the directly measured data to provide the traces shown at the top of Fig. 3.10(b). Their respective spectral densities (modulus squared of Fourier transform) are displayed underneath. Here, only the section dominated by white noise, above the corner frequency of the observed $1/f$ noise (at around 1 MHz) generated by the receiver's LNAs, is shown. These plots attest to the significant reduction in white (thermal) noise that pre-cooling can provide, the SNR (immediately after pre-cooling) being enhanced by $3.5^{+0.4}_{-0.4}$ dB. The relationship between the reduction in the noise power and the achieved noise temperature of the $\mathrm{TE}_{01\delta}$ mode at 1.45 GHz is shown in Fig. 3.10(d). In my demonstration, the mode temperature drops from an initial $T_{\mathrm{mode}}^{\mathrm{ambient}} = 184.0$ K to a pre-cooled $T_{\mathrm{mode}}^{\mathrm{cooled}} = 75.8$ K (measured).

The plot shown in Fig. 3.11 indicates that, at room temperature, the number of thermal photons in a mode at 1.45 GHz can be reduced to just a few hundred (*cf.* ref. [[153]]) given a sufficiently over-coupled port ($\kappa_{\mathrm{over}} > 10$) and quiet LNA ($T_{\mathrm{cold}} < 20\,\mathrm{K}$).

Given the parameters appearing in Table 2.1, whose values compose the noise calibration of my tr-EPR spectrometer, the observed reduction in noise power provided by precooling the cavity, as predicted by Eq. 2.53, depends on the value T_{mode} in the numerator versus that of $T_{\mathrm{mode}}^{\mathrm{ambient}}$ in the denominator. The latter, corresponding to when the cavity's $\mathrm{TE}_{01\delta}$ mode is critically coupled to its monitoring LNA via a lossy stub tuner, should equal $(T_0 + T_{\mathrm{mon.}})/2 = 184.0$ K, where $T_{\mathrm{mon.}} = 10^{-\frac{L_{\mathrm{dB},2}}{10}} T_{\mathrm{cold}} + (1 - 10^{-\frac{L_{\mathrm{dB},2}}{10}}) T_0 \approx 78.0$ K according to Eq. 2.50. Upon fixing the value of $T_{\mathrm{mode}}^{\mathrm{ambient}}$, Eq. 2.53 can be used to infer T_{mode} from the experimentally observed reduction in noise power ΔP. Using the data shown in Fig. 3.10(b), a rough estimate of ΔP can be arrived at from the difference in the spectral noise power, averaged from 5 to 10 MHz (so avoiding the 1/f noise prevalent below 1 MHz), between "pre-cooled" and "ambient" conditions; one obtains: $\Delta P_{\text{exp-EPR}} = -3.7 \pm 1$ dB. Since this estimate of ΔP has greater uncertainty than

that derived directly from monitoring the pre-cooling in the time domain, namely $\Delta P_{\text{exp-Cool}}$, it is not further used.

The mode temperature T_{mode} can be separately predicted using my model, namely Eq. 2.51 above; it depends on the (presumed identical) noise temperature of the two LNAs, T_{cold}, the coupling factor of the over-coupling loop κ_{over}, and the insertion losses of the RF switch $L_{\text{dB, 1}}$ and the monitoring LNA's connection to the cavity line $L_{\text{dB,2}}$. One arrives at

$$T_{\text{mode}} = \frac{T_0 + \kappa'_{\text{over}}[(1 - \frac{L_{\text{dB,1}}}{4.34})T_{\text{cold}} + \frac{L_{\text{dB,1}}}{4.34}T_0] + [10^{-\frac{L_{\text{dB,2}}}{10}}T_{\text{cold}} + (1 - 10^{-\frac{L_{\text{dB,2}}}{10}})T_0]}{2 + \kappa'_{\text{over}}} \approx 85.0 \pm 5 \text{ K}. \tag{3.5}$$

The values of $L_{\text{dB,1}}$ and $L_{\text{dB,2}}$ at 1.4495 GHz were measured using my VNA (HP-8753C) to be 0.19 ± 0.01 dB and 0.9 ± 0.01 dB, respectively. The coupling factor between the cavity and the cold load was characterized by the method(s) of Kajfez and Hwan [40] using the same VNA; I obtained $\kappa_{\text{over}} = 6.1 \pm 0.3$. The value of T_{cold} is calculated to be 29.1 ± 0.5 K based on the definition of noise parameters [154, 141] utilizing the parameters listed in Table 2.1. T_0 represents room temperature, set at 290 K. The uncertainty of T_{mode} shown in Eq. 3.5 is

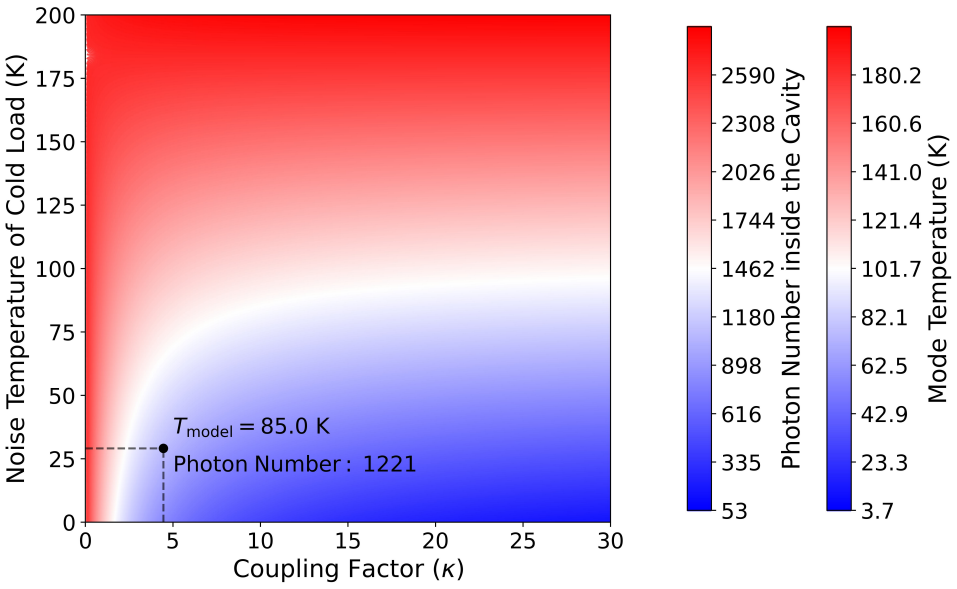

Figure 3.11: Modeled average number of thermal photons occupying the cavity's $\text{TE}_{01\delta}$ mode and the mode's corresponding temperature (T_{mode}) as a function of the cold load's own noise temperature (T_{cold}) and its coupling factor (κ) to the mode. In my experimental demonstration, this mode's temperature is reduced from 184.0 K to 85.0 K (modeled), the latter temperature corresponding to an average occupancy of 1221 photons.

calculated by applying Pythagoras' theorem to error propagation. Based on this result, I can use Eq. 2.53 to obtain $\Delta P_{\text{model}} = -3.1 \pm 0.2$ dB.

The depth of mode cooling was also estimated by fitting a bi-exponential function to the increase in measured noise power upon switching out the cooling LNA, as shown in Figs. 3.6(c) and 3.7. The best-fit curve, with its associated standard error band, is depicted in Fig. 3.12; this determines $\Delta P_{\text{exp-Cool}} = -3.5 \pm 0.4$ dB, agreeing (within error bars) of both my model's prediction ΔP_{model} and my analysis using the noise spectrum from tr-EPR data, namely $\Delta P_{\text{exp-EPR}}$ as shown in Fig. 3.10(b). My estimates are summarized in Table 3.1.

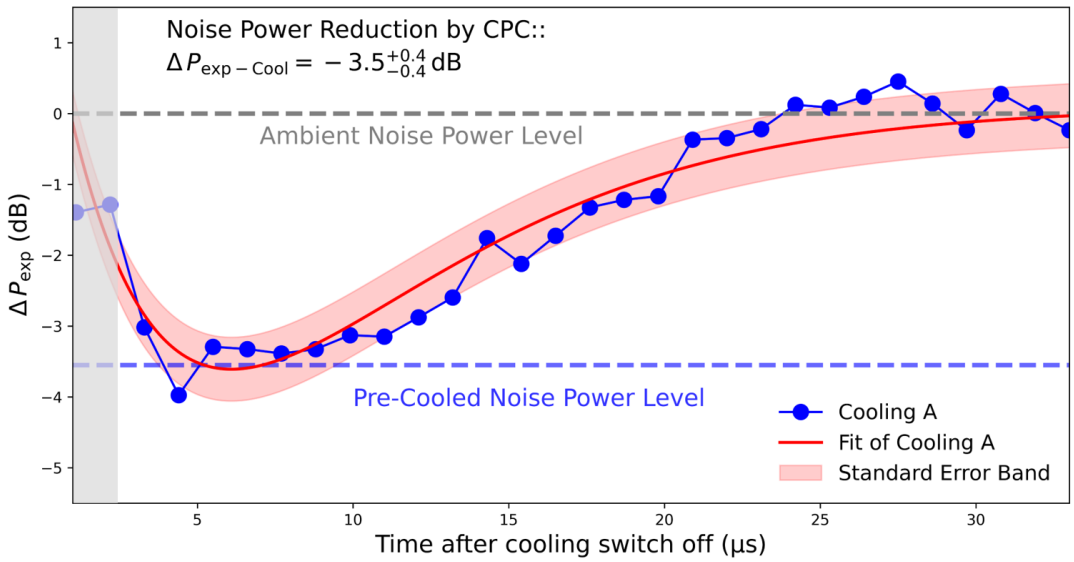

Figure 3.12: Error analysis and fitting of the experimental warming-up signal as presented in Fig. 3.9. The grey area at shorts times (after switching off the cooling LNA) on the far left represents the period when the double-throw switch is still transitioning to connect the over-coupled port to an "open" load, disconnecting the ACL from the resonator; this takes around $t_{\text{switch}} = 2\ \mu$s. Each blue dot plots $\Delta P_{\text{exp}} = 10 \log_{10}(< V^2_{\text{cold}} > / < V^2_{\text{ambient}} >)$ in units of dB[21], where $< V^2_{\text{cold}} >$ is the mean-squared received noise voltage averaged over ten consecutive data points, spaced 100 ns apart, spanning one microsecond; $< V^2_{\text{ambient}} >$ is the equivalent mean-squared noise voltage under ambient conditions (based on an adjoining sample spanning several hundred microseconds). The solid red line, along with its surrounding salmon pink standard error band, was obtained by least-squares fitting a bi-exponential to the evolution of ΔP_{exp} excluding the initial switching period. The longer of the two decay constants was determined to be $\tau^{\text{exp.}}_{\text{warm up}} \approx 9 \pm 1 \mu$s.

Table 3.1: Modeled and experimentally-inferred depth of cooling

method:	Model	Direct monitoring (time-domain)	EPR data analysis (frequency-domain)
label:	model	exp-Cool	exp-EPR
Noise-power reduction (ΔP) in dB:	3.1	3.5	3.7
Standard deviation of ΔP in dB:	± 0.2	± 0.4	± 1.0
Inferred mode temperature (T_{mode}) in K	85.0	75.8	-
Error in T_{mode} in K	{+5,-4}	{+10, -8}	-

3.7 Conclusion

Restricting myself to work done on bench-tops at room temperature, I here briefly compare the performance achieved by my demonstration of active pre-cooling (APC) to that achieved by removing thermal photons via stimulated absorption in an absorptively spin-polarised medium resident inside the cavity. In the literature, this latter approach has been dubbed "masar"[44] or "anti-maser"[126]. Using photo-excited Pc:PTP as the absorber, Wu *et al.*[44] cooled a $\mathrm{TE}_{01\delta}$ mode at 1.45 GHz down to around 50 K –though only in bursts. Using NV^- diamond, Ng *et al.*[107] and Day *et al.*[110] cooled the same type of mode continuously to 188 K at 2.9 GHz and to 70 K at 9.8 GHz, respectively. Given that these temperatures straddle what I here achieve using APC, one may conclude that, currently, there is no clear winner. Both approaches can assuredly be improved upon through focused material science and device engineering. Beyond cost and convenience, a salient advantage of APC is that the disturbance on the microwave cavity imposed by the cooling mechanism can be removed at the flick of a (microwave) switch. Methods based on internal stimulated absorption are, in contrast, beholden to the particular spin dynamics of the cooling medium. One could however use an *external* masar/anti-maser (operated either in CW mode or quasi-continuously[155]) as the ACL to implement pre-cooling instead of a HEMT-based LNA, with the connection between the resonator and the anti-maser's coupling port gated by a microwave switch. As with other pulse-based techniques at microwave frequencies, a successful implementation of APC relies heavily on the availability of a sufficiently fast, low-loss and glitch-free switch.

To conclude, I have demonstrated a method for actively pre-cooling the modes of a microwave

cavity by temporarily over-coupling them to the input of an LNA serving as an ACL. Beyond tr-EPR, other pulsed-EPR techniques such as electron spin-echo envelope modulation (ESEEM), hyperfine sublevel correlation spectroscopy (HYSCORE), and pulsed electron-electron double resonance (PELDOR) could be accelerated by APC, reducing measurement times[75]. Furthermore, my analysis identifies how an LNA that is *directly* coupled to a cavity (*i.e.*, when no "protective" isolator/circulator is inserted in between), can play an active and beneficial role in reducing the number of thermal photons occupying the cavity's modes (within the LNA's bandwidth), so reducing measurement noise.

The use of *cryogenic* ACLs, operating at (say) liquid-helium temperature yet providing input noise temperatures and thus mode cooling down into the mK regime, is perfectly conceivable. Unfortunately, due to self-heating within the device's active channel/layer, the noise temperatures of what are currently the quietest semiconductor-based LNAs hit, upon physical cooling, plateaux of a few K[156, 157, 158]. The construction of effective cryo-ACLs to achieve mK-level mode cooling may well require new materials and/or architectures (and the equipment to fabricate such), optimized expressly for mode-cooling –as opposed to the repurposing of existing devices (designed with other applications mind) like what my current exploration has been based upon. At a more general, sociologically level, acknowledging that the levels of cooling I have here achieved using APC are still far away from the single-photon regime, it is hoped that this paper induces greater cross-fertilization between wisdom embedded within the discipline of microwave radiometry[159, 135], activities across the EPR/NMR communities[160, 161], and hardware innovations in quantum computing/detection, particularly those targeting room-temperature operation[162, 163].

Future work will focus on the engineering of cavity designs that allow for higher over-coupling factors, whilst providing sufficient adiabaticity and switch-over speed, such that the cooling depth is limited more by the noise temperatures of available ACLs. Integrating these advancements with existing microwave-based quantum sensing instruments beyond time-resolved EPR would demonstrate the broader utility of my approach.

Chapter 4

Stable and Processable Photoexcited Molecular Electron Spins

Future information processing technologies like quantum memory devices have the potential to store and transfer quantum states to enable quantum sensing and networking. A central consideration in practical applications for such devices is the nature of the light-matter interface which determines the storage state density and efficiency. Here, I employ an organic radical, α,γ-bisdiphenylene-β-phenylallyl (BDPA) doped into an o-terphenyl (OTP) host to explore the potential for using tuneable and high-performance molecular media in microwave-based quantum applications. I demonstrate that this radical system exhibits millisecond-long spin-lattice relaxation and microsecond-long phase memory times at room temperature, while also having the capability to generate an oscillating spin-polarized state using a co-dissolved photo-activated tetraphenylporphyrin moiety, all enabled by using a viscous liquid host.

The sample (BDPA) was selected and synthesized with assistance from Dr. Max Attwood. Owing to its ease of processing, controlling only the BDPA concentration and melting point (see Section 4.2 for the experimental setup) is sufficient to produce the required material. A notable characteristic of BDPA is that at room temperature, it can exist in a stable liquid state or remain a stable solid. If it starts in a solid state and is heated, it transitions to and remains in a stable liquid state.

To characterize the quantum properties of the material at various concentrations and temperatures, I employed pulsed EPR. Under the supervision of Dr. Alberto Collauto (the pulsed EPR lab manager), I set up and operated the measurement protocols. After completing the experiments, I used MATLAB to perform parameter fitting (see Section 4.3).

This latest system builds upon collective wisdom from previous molecules-for-quantum literature by combining careful host matrix selection, with dynamical decoupling, and photoexcited triplet-radical spin polarisation to realise a versatile and robust quantum spin medium.

4.1 Introduction of Photoexcited Molecular Electron Spins

The essence of quantum technology lies in the ability to exert coherent control over two or more energy levels, corresponding to qubits[164] and qudits[165], respectively. Across coherent quantum computing platforms, such as superconducting circuits[164] and silicon spin qubits[166], cryogenic conditions are required to mitigate the effects of environmental thermal noise (associated with qubit fidelity[167]) and to enhance the efficacy of quantum operations. There are two approaches to improve the efficacy of quantum operations: one involves reducing the quantum gate error rate through the pulsed protocol of quantum gates[168], and the other involves enhancing the material's inherent coherence and decoherence times through material design[23, 169, 170, 171].

From the perspective of material design[172], particularly for materials relying on electronic spins, the primary objective is to obtain long spin-lattice relaxation time (T_1) and long phase memory times (T_m) such that spins can be manipulated and measured without undesirable spin decay associated with processing errors and loss of sensitivity[173]. Further practical caveats become important for particular applications. For example, in quantum sensing and information processing it is necessary to initiate a spin-polarised quantum state usually via optical excitation before spin manipulation and readout[174, 50]. While spin manipulation is most commonly performed using microwave pulses, the readout mechanism can be based on microwave or optical regimes with the latter being generally desirable because it is instantaneous. For quantum

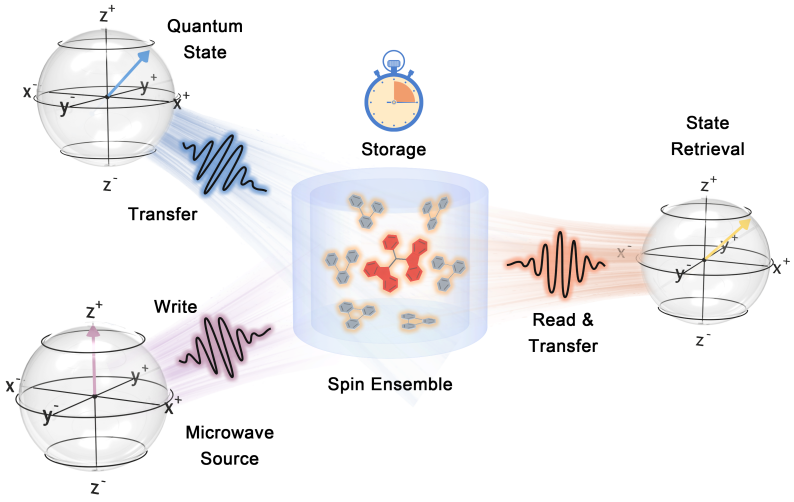

Figure 4.1: Conceptual diagram of molecular spin ensembles for microwave storage and quantum memory.

memory (Fig. 4.1), the storage efficiency of a quantum state or microwave pulse is determined by the coupling strength between a superconducting circuit or microwave resonator and a spin ensemble, which scales by $\sqrt{N}$, where N is the number of spins[175]. However, the storage time is determined by the spin dephasing time (T_2^*) and in randomly doped solid-state materials T_2^* is proportional to $1/N$. These contrasting performance relationships make it particularly challenging to engineer a family of quantum materials for diverse applications, especially since T_2^* is challenging to measure precisely without an optical readout [176].

In this chapter, I reveal my initial explorations using stable organic radicals to generate robust RT quantum technologies, and in particular focus here on their potential application in memory. By utilizing the well-known organic radical, BDPA doped into an organic host, OTP, I demonstrate a long and temperature-insensitive T_m reaching 2.33 μs at room temperature (RT) with a relatively high molar concentration of 0.1%. The effective coherence time was significantly lengthened using a dynamical decoupling approach to 11.5 μs. It is shown that the temperature insensitivity is due to dilution in the OTP host, which becomes a metastable and optically transparent viscous liquid after melting and cooling to RT. I finally demonstrate that the long T_1 associated with BDPA can be used in conjunction with photo-activated triplets to realize record long-lived and even aberrant modes of spin polarisation.

4.2 Experimental Setup

BDPA (Sigma-Aldrich) and ortho-terphenyl (OTP, 99%, Sigma-Aldrich) were used without further purification. H_2TPP was synthesized according to the literature [177] and recrystallized from $CHCl_3$. UV-Vis spectroscopy was performed using rectangular 60 mm × 4 mm × 0.2 mm glass tubes (VitroTubes^{TM}, CMScientific). To load the samples, powders of BDPA and, separately, H_2TPP in OTP (0.1% mol/mol) were decanted into glass vials made by sealing the end of a glass Pasteur pipette. The capillary tube was inserted into the powder, and the vial was placed under an argon atmosphere inside a larger glass tube. The powder was then carefully melted at 60°C, causing the materials to enter the tube by capillary action. The tube was allowed to cool and was used directly to measure transmission spectra after cleaning the outside with acetone. Loss of transparency could be restored by gently reheating the tube. Data were captured using an Agilent Cary 5000 UV/Vis/NIR spectrophotometer.

Steady-state and time-resolved (tr) X-band EPR spectroscopy were performed under ambient conditions using a Bruker ELEXSYS-II E500 spectrometer equipped with a Bruker ER4118-X MD5 resonator. The loaded Q-factor was estimated at approximately 7300 by setting the attenuation to 33 dB. Least squares fitting of X-band triplet signals was performed using the `esfit` function within the EasySpin package (v6.0.0 dev.51) for MATLAB 2023a [178]. The data were fitted "as is," with the baseline set to "none," using the Nelder–Mead simplex algorithm. The typical script used to load and fit the data is provided below for compatibility with EasySpin v6.0.0 dev.51.

Pulse EPR experiments were performed on a Bruker Elexsys E580 spectrometer equipped with an ER4118X-MD5 dielectric ring resonator (Bruker) and a 1 kW traveling-wave tube amplifier (Applied Systems Engineering Inc., Model 117X). A closed-circuit helium cryostat with front optical access (Cryogenic Ltd.) was used to control the temperature of the resonator and the sample. To enhance sensitivity, the microwave resonator was installed on a cryogenic HEMT probehead (Amplify My Probe Ltd.) containing a 36 dB low-noise preamplifier (Low Noise Factory AB, model LNF-LNC4_16C) and a 6 dB directional coupler (Pasternack Enterprises, Inc.) [179].

Inversion recovery and Hahn echo measurements were performed with an attenuation of 7 dB. An echo-detected field sweep (EDFS) was conducted for each sample at every temperature to locate the radical resonance (see Figure S2). The inversion recovery technique employed the following pulse sequence: $\pi - T - \pi/2 - \tau - \pi - \tau -$ echo, and was used to measure T_1, where $T = 1000$ ns. The π pulse lengths were set to 32 ns, and the $\pi/2$ pulses were set to 16 ns. The Hahn echo decay technique employed the pulse sequence: $\pi/2 - \tau - \pi - \tau -$ echo. Pulse lengths were as above.

Table 4.1: EasySpin fitting parameters for BDPA in OTP, modeled as an $S = \frac{1}{2}$ spin system.

Parameter	Value
g_x	1.9997
g_y	1.9997
g_z	2.0022
lw_1 (mT)	0.106
lw_2 (mT)	0.171
A_α (MHz)	4.2027
A_β (MHz)	5.466
A_γ (MHz)	9.982
A_δ (MHz)	7.296

4.3 Experimental Results

4.3.1 Investigation of spin coherence by pulsed EPR spectroscopy

The host OTP was chosen due to its structural similarity to p-terphenyl which acts as a light-stable inert host for aromatic hydrocarbons such as tetracene and pentacene and facilitates robust photoinduced quantum behaviours[180, 181]. However, unlike p-terphenyl, its RT quasi-glass phase can be used as a universal host to accommodate a range of structurally dissimilar and even paramagnetic molecules[182, 183]. Dissolution in OTP has previously been used to reduce dipole coupling and successfully increase T_m in radical graphenoids[35]. Experimentally, I estimate that close to 1% BDPA is the saturation concentration in OTP, however, to avoid uncertainty in my spin measurements, I restricted the highest concentration to 0.1%. The CW-EPR spectra of the glass phase 0.1%BDPA in OTP can be seen in Fig. 4.2(a). The centre field

signal exhibits a small degree of g-value anisotropy and proton hyperfine coupling that can be approximately fitted assuming four in-equivalent protons, typical for BDPA (see ESI)[184].

Using pulsed X-band EPR spectroscopy, I performed inversion recovery (π–T–$\pi/2$–τ–π–τ–echo) and Hahn-Echo ($\pi/2$–τ–π–τ–echo) experiments to assess the impact of temperature and dopant concentration on T_1 and T_m, respectively. The biexponential nature of the IR signal was fitted by $f(t) = A_0 + (1 - A_1e^{-t/T_r} - A_2e^{-t/T_s})$, and indicates distinct rapid and slow relaxation pathways[185]. In a representative case of a sample doped with 0.1% BDPA, the weight-averaged T_1 increases from 1.2 ms at 300 K to 120 ms at 5 K (Fig. 4.2(c)). In contrast, T_m exhibited a monoexponential decay pattern, indicative of a single dominant decoherence mechanism and demonstrates striking temperature independence (Fig. 4.2(b) and (c)). Specifically, T_m is measured at 2.57 μs at 5 K and 2.33 μs at 300 K for a 0.1% BDPA concentration. These spin coherence times are remarkably long for an organic radical, and to my knowledge, only previously achieved for BDPA in any medium at 4 K[186], potentially suggesting a protective function of the OTP glass phase which was found to vitrify below 15^oC. Interestingly, while T_1 increases with a reduction in temperature, it exhibits no clear correlation with the concentration of BDPA (see also ESI) suggesting that even at 0.1% the dipole interactions are minimised. The temperature dependence of T_1 aligns with the Raman spin relaxation process, as described by $\frac{1}{T_1} = aT^n$ [187, 188, 189, 39], where a is a pre-factor, T represents the temperature under measurement conditions, and n, with a range of 1.5-3, is the exponent characterizing the relationship. This range for n is notably lower than the commonly observed value of 9, suggesting these measurements are taken above the Debye relaxation temperature. A similar phenomenon has been observed in systems such as 1,3,6,8-tetrakis(4-aminophenyl) pyrene and 3,7-di(4-formylphenyl)-functionalized naphthalene diimide (TAPPy-ND)[188], as well as in vanadyl porphyrin[190] and vanadyl phthalocyanine (VOPc)[191], where n is approximately 3. Additionally, at higher temperatures, cross-relaxation likely contributes to spin relaxation, as evidenced by shorter T_1 values in samples with high spin concentration, whereas the opposite trend is observed at low temperatures. Furthermore, these results demonstrate the ability to tune the T_1/T_m ratio from a few hundred to a few hundred thousand (see ESI). This is particularly important in quantum memory applications, where microwave pulses and quantum

states are stored as partially excited spin states which thermalise on a T_1 timescale. The high T_1/T_m ratio indicates that a high number of states can be stored for long periods without loss or processing errors induced by thermalisation.

To explore the potential limits of my system for storing quantum coherent states, I employed a dynamical decoupling protocol at RT and on a sample of 0.1% BDPA in OTP according to the CPMG sequence (Fig. 4.2(d)). These sequences are capable of extending the effective T_m by partially decoupling electron spins from the surrounding nuclear spin bath. Bonizzoni *et al.*, recently demonstrated the impact of CPMG on BDPA at low temperatures to prolong T_m and improve the sensitivity of BDPA as a magnetic field sensor[192]. Here, the sequence was optimised by varying the length of the interpulse delay, τ, enabling the application of up to 70

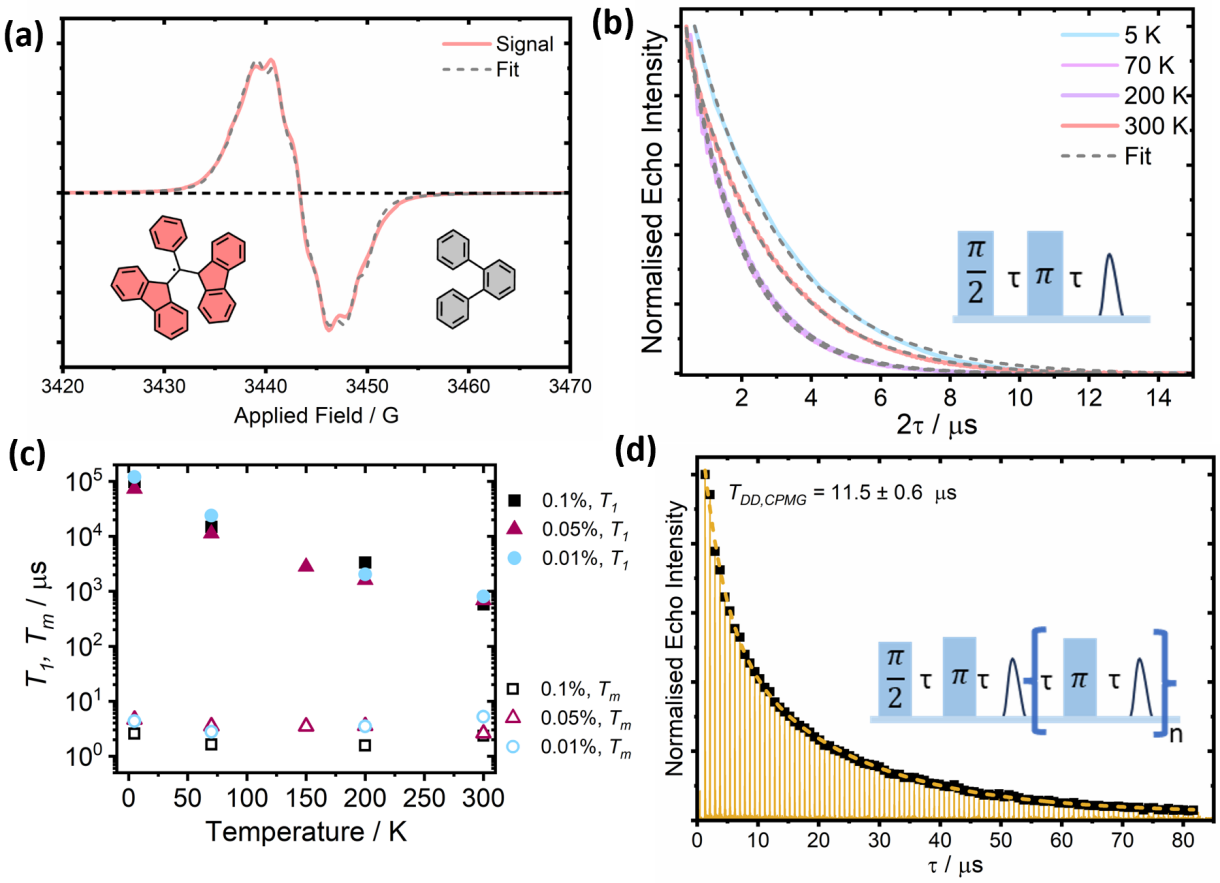

Figure 4.2: (a) Steady-state EPR signal at RT for BDPA in OTP, with S=1/2 fit shown by the grey dashed line; (b) Pulsed EPR measurements of the Hahn echo decay for 0.1%BDPA in OTP; (c) Summary plot showing the variation of T_1 and T_m over different temperatures and spin concentrations; (d) Carr-Purcell-Meiboom-Gill (CPMG) pulsed sequence with an interpulse delay of 410 ns, overlaid a monoexponential fit.

pulses to extend T_m (termed T_{DD}). T_{DD} was determined by fitting the extended decay trace to a monoexponential function, revealing an extended effective coherence up to 11.5 μs, similar to the values achieved by Bonizzoni *et al.,* at 3 K using a coplanar waveguide and 20 refocusing π pulses[192].

4.3.2 Probing two-level quantum dynamics at room temperature

Next, to determine whether this spin system would be suitable as a two-level quantum system, I conducted Rabi oscillation experiments under different temperatures, phases, and microwave powers, as shown in Fig 4.3(a). Ideally, for quantum memory based on a cavity quantum electrodynamics (cQED) approach, a spin ensemble should exhibit strong spin-photon coupling to store quantum states for prolonged periods efficiently. The threshold for strong spin-photon coupling can be effectively described by a system's "cooperativity", $C = 4g_e^2/(\kappa_c\kappa_s)$, where g_e is the spin-photon coupling strength, κ_c is the cavity-photon decay rate, and $\kappa_s = 2/T_2^*$[181]. Here, $\kappa_c = 2\pi f_{mode}/Q_L$, where Q_L is the loaded quality factor of the resonator ($\approx$ 200), and f_{mode} is the microwave frequency ($\approx$ 9.65 GHz), giving a κ_c-value $\approx$ 300 MHz. In strong spin-photon coupling systems where C¿1, g_e is often taken as $\Omega/2$, where Ω is the Rabi oscillation frequency.

According to my measurements using a sample at 0.1% BDPA concentration at RT, the Rabi frequency ranges between 4.1 and 16.5 MHz depending on the applied microwave power (Fig. 4.3(a) and (b)). While this demonstrates the ability to coherently drive BDPA as a two-level quantum system, the Rabi frequency is below the strong coupling threshold, which is confirmed by the proportional dependence of the Rabi oscillation frequency on the microwave power (Fig. 4.3(b)). While I were unable to directly measure T_2^* in my experiments, an estimate can be made from the full-width half maximum (FWHM) of the inhomogeneous linewidth ($=1/\pi T_2^*$) measured from the steady-state radical resonance (FWHM $\approx$ 22 MHz $\approx$ 14 ns, Fig. 4.2(a)). From this, and using $g_e = 8$ MHz, then C $\approx$ 0.01. Improving to $C > 1$ would thus require improvements in Q_L, reduction in f_{mode}, or, most significantly due to the g_e^2 term, an improvement in the spin-photon coupling strength. For example, critically coupled sapphire resonators with $Q_L > 10,000$ are

common in X-band EPR spectroscopy and could offer a potential factor of 50 improvement in κ_c. Furthermore, assuming that all spins exhibit an equal individual coupling strength, then $g_e \approx g_s\sqrt{N}$, where $g_s = \gamma\sqrt{\mu_0\hbar f_{mode}\pi/V_m}$. Here, γ is the electron gyromagnetic ratio ($\approx$ 28.024 GHz/T for an organic radical), μ_0 is the permeability of free space, $\hbar$ is the reduced Planck constant, and V_m is the resonator's magnetic mode volume. From this relationship, it becomes apparent that the principal routes to improving g_e are increasing $\sqrt{N}$, reducing f_{mode} or V_m. To reduce V_m, it would be necessary to design a new microwave resonator using materials with a significantly higher dielectric permittivity (ϵ_r), since V_m scales by $\epsilon_r^{-3/2}$. This approach has been successful in the field of maser research, where switching from a sapphire ($\epsilon_r = 9$) to strontium titanate (STO, $\epsilon_r = 318$) resonator was used to generate Dicke states at RT using photoexcited pentacene or 6,13-diazapentacene-doped p-terphenyl[181, 193]. Furthermore, Lenz *et al.,* have measured a state of strong coupling for neat samples of 2,2-diphenyl-1-picrylhydrazyl (DPPH) and BDPA at RT using Fabry-Perot resonators at Q-band, despite each radical exhibiting significantly lower T_m values compared to my system[194, 195, 196]. I note that the high ϵ_r approach would also enable six-fold or more miniaturization in the resonator's size due to near-total confinement of the electric and magnetic fields of the $TE_{01\delta}$ mode compared to a sapphire resonator.

My Rabi oscillation experiments were conducted at various microwave attenuations (Fig. 4.3(a) and (b)) and temperatures (see ESI). To fit the Rabi oscillations, I employed a damped sinusoidal function defined by:

$$I(t) = Ae^{-\lambda t}\sin(2\pi\Omega_R t + \phi) + s \tag{4.1}$$

where $I(t)$ is the measured intensity as a function of time t, A is the amplitude of the oscillation, λ is the damping rate, Ω_R is the Rabi frequency, ϕ is the phase of the oscillation, and s is the offset. For microwave attenuations of 0 dB (baseline), 1.4 dB, 3.1 dB, 8 dB, and 12 dB, I obtained Rabi frequencies Ω_R of 16.5, 14.2, 10.3, 6.1, and 4.1 MHz at room temperature (RT), respectively. The linear relationships shown in Fig. 4.3(c) and (d) confirm that the oscillations are of pure Rabi type [197] and demonstrate the potential to drive BDPA as a quantum spin system. According to Mayländer *et al.* [37], the number of single-qubit logic operations

Ω_M can be calculated using $\Omega_M = 2T_m\Omega_R$. In my experiments, 0.1% BDPA in OTP at RT achieves a value exceeding 400, which is 20 times higher than previous molecular-spin-qubit research. Furthermore, these experiments highlight the remarkable thermal stability of solid-state

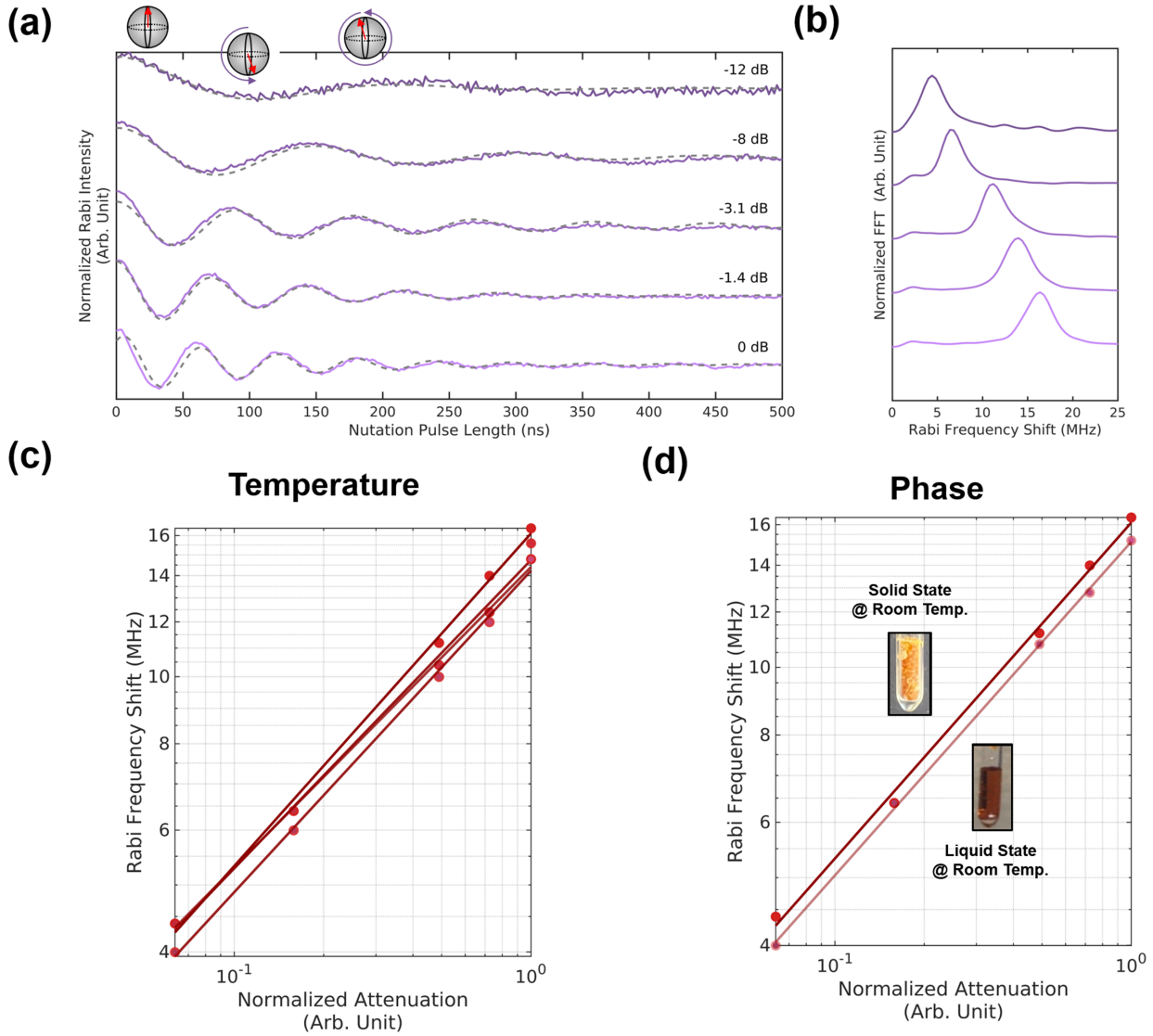

Figure 4.3: Rabi Oscillation Experiment for 0.1% BDPA over variable temperatures. (a) Nutation curves with normalized Rabi intensities as a function of nutation pulse length at various microwave attenuation levels measured at RT. The data points represent experimental measurements, while the grey dashed lines indicate the fits to a damped sinusoidal function, providing a precise determination of the Rabi frequencies. Insets illustrate the corresponding spin rotations on the Bloch sphere. (b) Shows the Rabi frequency shifts across a spectrum of microwave powers, reflecting the system's resonance characteristics. (c) and (d) plot the Rabi frequency shift against normalized microwave attenuation (arbitrary units), categorized by temperature (5K, 70K, 150K, 200K, and 300K from light to dark) and phase (liquid and solid state), respectively. The fitting curves illustrate the model's alignment with the experimental data, accentuating the temperature's role in modulating electron spin coherence. All fitting results are shown in the Appendix C.

BDPA-doped OTP, demonstrating consistent performance across a temperature range of 5 K to 300 K. This stability is evidenced by the Rabi oscillation frequencies and nutation curves, which remain largely invariant throughout this extensive temperature spectrum. Additionally, Fig. 4.3(d) highlights the significant phase stability of BDPA-doped OTP at RT, as consistent Rabi oscillation frequencies are observed in both solid and liquid phases. This uniform behavior across different phases underscores the material's robust coherence properties, which are crucial for developing reliable quantum memory systems. Notably, the transition between solid and liquid states does not result in appreciable dephasing, thereby preserving the integrity of qubit systems.

4.3.3 Generation of radical spin polarisation using photoexcited triplets

To further explore the versatility of BDPA as a platform for quantum applications, I sought to introduce mechanism to introduce a photoexcited spin polarisation state using the electron spin polarisation transfer mechanism (ESPT) and radical-triplet pair mechanism (RTPM) which was previously explored by Blank and Levanon for the BDPA radical[198, 199]. These reports established H_2TPP and BDPA as a promising system for quantum amplifiers due to the system's remarkable ability to induce a spin-polarised state lasting ¿100 μs in vicious solutions of 1-chloronaphthalene and paraffin. However, I noted that the T_1 ($\approx$ 1.2 ms measured for BDPA in OTP was significantly longer than the T_1 = 6.9 μs measured in their work, and thus postulated that this would result in a significantly longer spin polarisation. I prepared samples by dissolving powders of H_2TPP and BDPA in OTP at 0.1% total spin concentration by melting the mixture at 60°C and allowing it to cool. Samples were then measured by time-resolved (tr)EPR spectroscopy using pulsed photoexcitation at 650 nm to generate H_2TPP triplet states.

Remarkably, these measurements revealed a pronounced oscillating spin polarisation with an overall net emissive gain (Fig. 4.4(a) and (b)). The sequential emissive and absorptive phases peak at 0.15, 0.5, 1.25, 2.5 and 4.5 ms, lasting 0.25, 0.6, 1.1, 1.6 and 3.3 ms, respectively. The absolute polarisation reduces monoexponentially with a decay lifetime (t_{decay}) of 1.7 ms (Fig. 4.4(c)), which is slightly longer than the T_1 measured for BDPA. Notably, these oscillations

were not present in the solid state following vitrification of the OTP and are also dependent on the sample's composition (see ESI). These findings are consistent with both ESPT and RTPM which each require solution phase physical interactions between the radical and triplet moieties to induce spin polarisation. Interestingly, I further find that in the solid state, the sign of the radical polarisation is absorptive rather than emissive. Since the sign of the polarisation of determined by the multiplicity and exchange coupling of the interacting species, this could suggest a different polarisation mechanism. The triplet signal measured in the solid state could

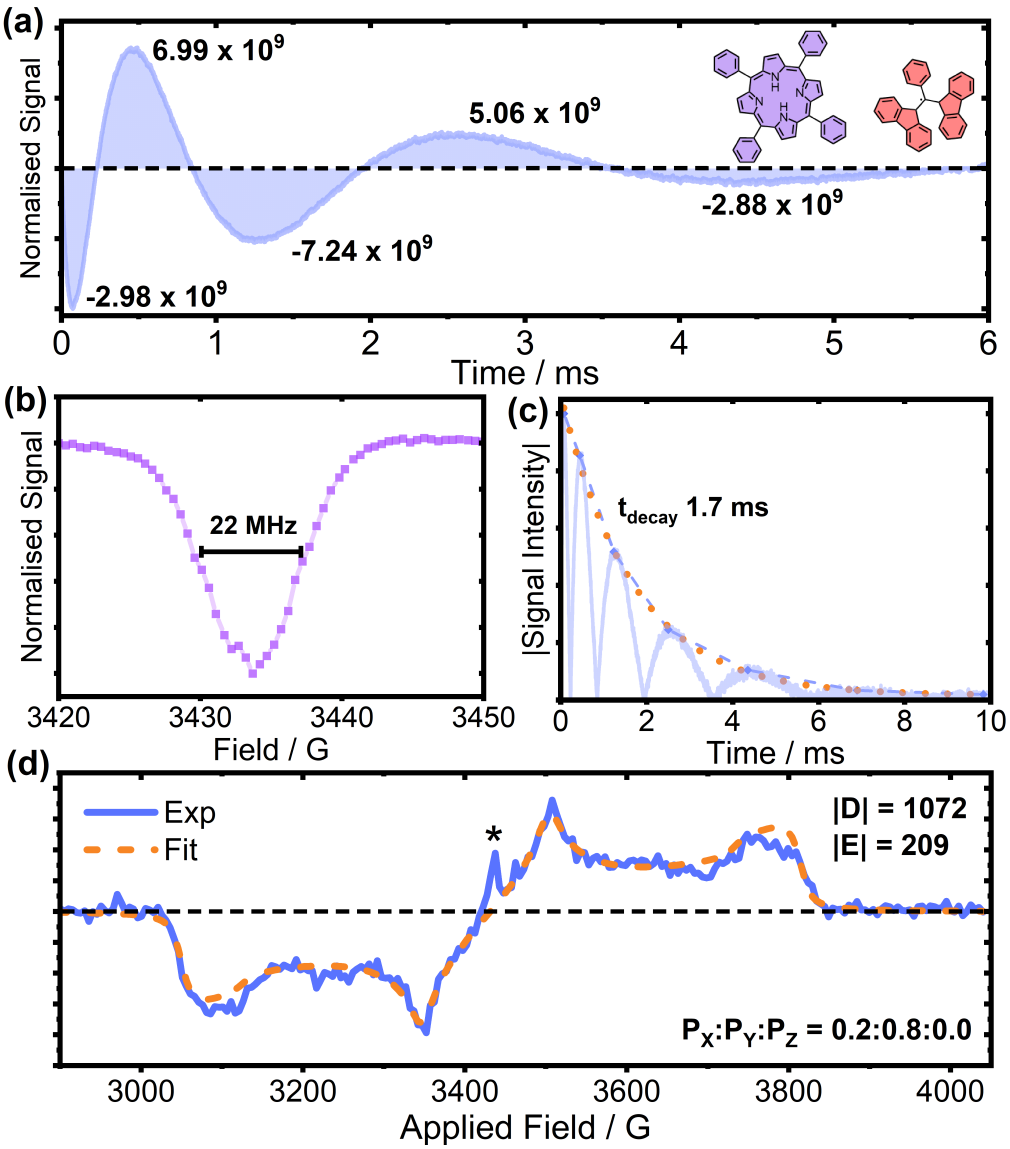

Figure 4.4: Photoexcited time-resolved EPR spectra for a mixture of 0.1% H_2TPP and BDPA in OTP, showing (a) triplet-radical pair spin polarisation oscillations over 6 ms; (b) field swept transient of the centrefield radical 160 μs after the laser flash; (c) spin polarisation decay of the absolute signal intensity and; (d) powder phase photoexcited EPR spectrum of H_2TPP 440 ns after laser flash.

be fitted to S = 1 Hamiltonian and found to agree with zero-field splitting values and triplet sublevel populations typically observed for free-base porphyrin[200, 201] (Fig. 4.4(d)). Attempts to measure the intermediate quartet state which considered to be responsible for generating an emissive radical in ESPT and RTPM failed. A much more comprehensive analysis of this new phenomenon will form the basis of future work.

4.4 Discussion

My results demonstrate that organic radicals in a suitable host matrix, in this case, BDPA in OTP, can harbour robust spin properties applicable to a range of quantum technologies including quantum memory, and potentially even quantum amplifiers and spin refrigerators. By employing OTP as a viscous liquid host, I show it is possible to exhibit remarkably long T_1 while also protecting electron spins from dipole coupling and thermally induced decoherence effects, both of which can be improved by employing more dilute spin mixtures or using dynamical decoupling protocols. I further demonstrate the capacity of BDPA act as a coherently manipulable system at RT close to the strong coupling limit, as well as its compatibility with spin polarisation methods by the inclusion of a photo-excitable triplet moiety to realise a rich variety of unique quantum behaviours.

Molecular electron spins are subject to various burdensome decoherence sources, including nuclear spins, phonons, and intermolecular electron dipole interactions, which have effectively been probed during this investigation. The BDPA radical is stabilised by delocalisation of spin density over the fluorene groups, which also effectively acts to partially homogenise the local spin bath.[202, 203] In the dilute and fast-motion regime, BDPA measured in h^8-toluene at room temperature is known to exhibit an impressive T_m of 9.8 μs, limited by local mode relaxation.[38] However, in the solid-state or slow-motion regimes (as is the case here), one observes a resolved EPR resonance structure resulting from hyperfine coupling to four inequivalent protons that comprise the dominant source of electron spin decoherence. It is also notable that my spin systems appear to be close to (for 0.1%), or below (for 0.05 and 0.01%), the con-

centration limit for significant intermolecular dipole or exchange interactions. This is initially indicated by the similarity of T_1 measured for each spin concentration and also supported by comparison with data reported by Li *et al.,* wherein BDPA was measured in partially deuterated OTP at X- and Q-band frequencies.[204] In their study, and at concentrations two to eight times higher than my samples, the lineshape of BDPA exhibits broadened field-swept echos attributed to electron-electron interactions that become absent at low concentrations,

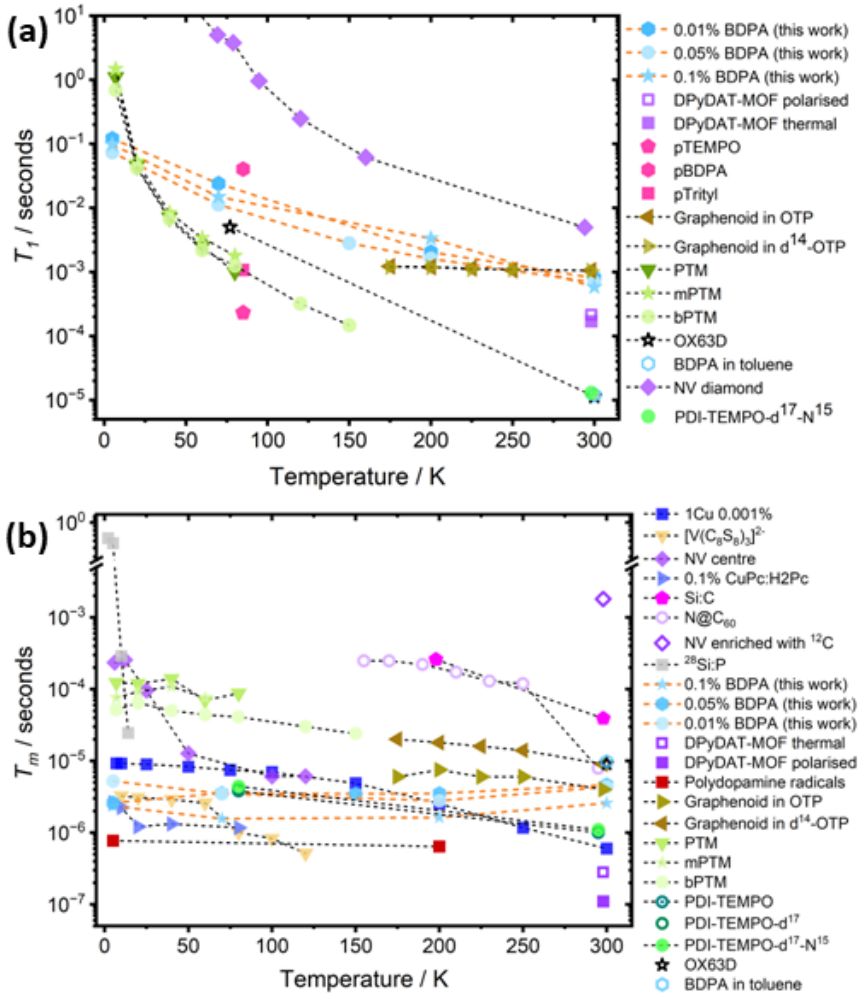

Figure 4.5: Comparison of (a) T_1 and (b) T_m for cutting-edge spin-qubit systems for QIP. The data for each spin system are sourced from 1Cu 0.001%[22], $[V(C_8S_8)_3]^{2-}$[23], NV center[24], 0.1% CuPc:H_2Pc, SiC[25], N@C_{60}[26], Fe_8[27], NV center in ^{12}C-enriched diamond[28], Pn-MOF[29], ^{28}Si:P[30], mPTM radical[31], DPyDAT-MOF [32], polydopamine radicals [33], pTEMPO, pBDPA, pTrityl [34], graphenoid in OTP [35], PTM, mPTM, bPTM [36], PDI-TEMPO [37], BDPA in toluene [38], OX63D [39]. It is important to note that the data included in this comparison were not all collected under identical magnetic field conditions, and for instances where a bi-exponential decay was reported, the slow decay constant has been used when available.

and yield lineshapes similar to my measurements. Notably, both the dilution of BDPA from 0.1% to 0.05%, and the employment of dynamical decoupling pulses significantly extended T_m, while the impact of the former on T_1 was less significant. Furthermore, the clear dependence of T_1 on temperature is consistent with the presence of phonon-mediated relaxation below RT, however, due to the length of T_1 compared to T_m, these effects did not appear to significantly impact T_m. Altogether, these findings are consistent with the main contributors to decoherence in BDPA being derived from electron spin dipole interactions and the nuclear spin bath. Indeed, relatively recent findings regarding organic radicals have predicted that proton spins up to 12 angstroms from the electron spin centre can contribute to decoherence[205]. As a result, extending T_m has often required impractical but nuclear spin-free solvents, like CS_2, or synthesis of novel molecules with reduced nuclear spin noise[206, 207]. Here, OTP is demonstrated to be a versatile and convenient alternative by enabling remarkable spin relaxation and decoherence parameters for BDPA (Fig. 4.5(a) and (b)), while also enabling other useful functionalities, such as adjustable composition and the ability to easily include photoactivated auxiliary molecules. These insights also underscore that, unlike with other solid-state inorganic spin defect systems based in diamond,[208, 209] silicon carbide,[210] or most recently, hexagonal boronitride,[211, 212, 213] molecular spin systems offer on-demand control over both temperature and dopant concentration can optimize T_1 and T_m, offering pivotal guidelines for designing materials with tailored coherence times suited for quantum memory applications.

The ability of BDPA-doped OTP to preserve quantum coherence from cryogenic to ambient conditions positions it as an adaptable material for QIP technologies. My Rabi oscillation experiments revealed the remarkable thermal and phase stability of BDPA-doped OTP and strongly suggest the ability to conduct over 400 coherent manipulations even at RT, significantly surpassing previous molecular benchmarks[37] To realise strong spin-photon coupling for efficient quantum memory and sensing applications it would be necessary to increase the Q_f of the resonator, increase the resonant frequency, increase spin concentration, and/or improve T_2^*. Lenz *et al.,* successfully demonstrated strong spin-photon coupling at Q-band by employing a Fabry-Perot resonator and pellets of the BDPA-benzene complex, and separately, DPPH[194, 196]. Importantly, these systems exhibit significantly lower T_m, and by extension,

likely T_2^*, which presents an opportunity for spin systems with longer T_ms to demonstrate strong spin-photon coupling while maintaining relatively low Q_f or spin concentrations.

Applications of BDPA towards a range of quantum technologies often require an initialisation step. For example, for QIP it is necessary to obtain a "pure" quantum state with a known two-level spin population, and similarly for quantum amplifiers based on masers, an emissive spin polarisation is required. My demonstration of inducing spin polarisation using photoexcitation combined with triplet-radical interactions affirms the versatility of molecular media for quantum applications. Furthermore, I note the strong and long-lived oscillations in spin polarisation could be useful for the development of (liquid phase) ultra-low noise amplifiers,[214] but could also be an enabling technology for high-temperature quantum technologies by acting as a microwave mode cooler[215, 216, 217]. Previous work by Blank and Levanon demonstrated that high-viscosity solvents facilitated longer spin polarization lifetimes [198, 199]. Hence, for my investigations, the RT glass phase of OTP was ideal due to its relatively high viscosity ($\eta \approx 8$ mPa s at 300 K)[218] and optical clarity. Organic glass hosts without appreciable flow properties, such as 1,3,5-tri(1-naphthyl)benzene[219, 220] or β-estradiol [221, 222], were not suitable since they prohibit transient short-range interactions required for ESPT and RTPM. While the origin of the oscillations has yet to be completely understood by my group, it could reasonably stem from extended contributions from RTPM resulting in further polarisation exchanges between the H_2TPP and BDPA. These intermolecular interactions on a millisecond time scale would be enabled by the long (≈ 6 ms) triplet lifetime of H_2TPP [223], the long T_1 of BDPA, and the inefficiency of triplet quenching associated with RTPM[224]. A key objective moving forward is to explore this regime further to understand the mechanism, and hopefully tune the behaviour towards particular applications.

4.5 Conclusion

An important objective in the development of quantum technologies is to develop alternative tunable qubit media to enable robust quantum activity and manipulation over a range

of temperatures. Here, by employing known chemical strategies to facilitate robust quantum behaviours, I have demonstrated remarkably long T_1 and T_m times for the well-known BDPA organic radical system, which compares favourably against state-of-the-art molecular qubit media (Fig. 4.5(a) and (b)), and established behavioural regimes applicable to several emerging quantum technologies. Moreover, I anticipate that by capitalising on the structural versatility enabled by chemical synthesis these remarkable quantum functionalities can be significantly improved upon. There are now several radical-chromophore systems[225, 226, 227, 228], some with already long-lived T_1 and T_m that could be improved at high temperatures simply by employing the appropriate host matrix. More vigorous strategies could also include deuteration [184] to improve T_m and T_2^*, or the use of alternative radicals [36, 35, 229] and alternative pulsed protocols[192]. I note, however, that in addition to the realisation of strong spin-photon coupling, additional design criteria are required in the realistic scenario for quantum computation. Most notably, spin qubits must be deployed in a controllable host matrix that enables intermolecular entanglement through dipole coupling or exchange interactions, whilst being compatible with appropriate substrates.[230] This is perhaps the most significant obstacle facing QIP-relevant molecular qubit technology due to the challenging synthetic chemistry involved, the employment of an appropriate deposition approach, and compensating for the reduced coherence associated with coupled paramagnetic states. However, the incorporation of a robust entanglement faculty in spin-ensemble quantum memories can also enable their application in quantum network and communications technology.

Chapter 5

HODSAR: Heterogeneous Optically-Detected Spin-Acoustic Resonance

In this chapter, I report a novel application of spin-acoustic resonance in pentacene-deposited molecular thin films integrated onto a high-Q Surface Acoustic Wave (SAW) resonator on a lithium niobate substrate. By leveraging the spin-triplet state of photo-excited pentacene at room temperature, I demonstrate coherent spin manipulation via acoustic waves without the need for an applied magnetic field.

Specifically, this experiment comprises three main parts. First, the SAW device was fabricated (Fig. 5.2) and characterized at the Henry Royce Institute (White City), Department of Materials, Imperial College London, and at Shenzhen University, with the assistance of Dr. Sami Ramadan and Dr. Chen Fu. Second, the HODSAR spectroscopy setup (Fig. 5.3) was established in the Maser Lab, with assistance from Dr. Yongqiang Wen, primarily involving the conversion of the ODMR measurement system into a HODSAR system. Third, I designed, performed, and analyzed all measurement protocols and data.

The heterogeneously integrated device, referred to as HODSAR, utilizes spin-phonon coupling

to achieve zero-field-controlled electron spin resonance, opening new avenues for quantum sensing and quantum memory. My findings reveal that the high-Q multimode resonance of the SAW device facilitates efficient acoustic coupling to specific spin transitions, providing enhanced control over spin coherence and relaxation. This advancement underscores the potential of spin-acoustic resonance as a scalable platform for room-temperature quantum metrology in molecular systems, with promising implications for mechanically addressable quantum networks, quantum sensors and quantum memory devices.

5.1 Introduction of HODSAR

When employed as spin materials, organic materials exhibit considerable promise for use in quantum metrology applications[74, 231, 232, 233, 161]. Their inherent chemically adjustable properties afford a substantially higher degree of freedom than that associated with inorganic spin defects, including those prevalent in semiconductor defects[234]. Notably, their ability to be controlled in zero-magnetic fields and their functionality at room temperature are attributes that greatly expand their practical utility in critical areas such as quantum sensing and quantum networks[235, 60, 236].

At present, the primary method used to manipulate and analyze these organic spin materials involves the use of EPR to investigate their spin dynamics, a technique also known as ESR[20]. However, ESR's dependence on electromagnetic wave processing introduces several challenges, particularly in designing high-Q microwave cavities for efficient microwave processing and in achieving the miniaturization of these devices. For instance, when in a zero-field state, certain organic spin materials exhibit triplet sub-level splitting with resonance frequencies around 100 MHz at zero-magnetic field[235]. This necessitates the use of centimetre-scale components for 3D high-Q resonators in quantum metrology applications, which would pose significant integration challenges for future developments.

To address the miniaturization and integration challenges in quantum metrology, microelectromechanical systems (MEMS), and particularly SAW devices, employed as resonators in

quantum sensors offer a viable solution through the effective "quantum acoustic" manipulation of spins. Recently, SAW-based quantum acoustics have attracted significant attention due to their versatility in coupling with diverse quantum systems, including superconducting qubits[237], artificial atom[238], nitrogen-vacancy (NV) centres in diamond[239, 240, 241, 242], and semiconductor quantum dots[243]. This approach introduces a novel coupling system, namely spin-acoustic (phonon) coupling, which is pertinent to quantum memory [244, 245]. While metrology using inorganic-based sensors, such as NV-centered diamonds or SiC-based devices [246, 245, 247], is well-established, the exploration of metrology utilizing the spin dynamics of organic materials represents a significant advance in the field, offering new possibilities for quantum sensing and information processing [248]. This type of system takes advantage of heterogeneous integration to couple spins in organic materials with phonons generated by interdigital transducers (IDTs) on piezoelectric materials. This process effectively facilitates the coupling of the microwave source to SAW phonons and integrating phonon and photon-excited spin coupling, which is subsequently monitored using a single photon detector. This results in an efficient multi-system coupling platform for quantum metrology, a system I refer to as the heterogeneous optically-detected spin-acoustic resonance (HODSAR).

In this chapter, I report the utilization of single-crystal-phase Pc:PTP thin film deposited on a $LiNbO_3$-based high-Q Multi-Mode SAW Resonator (MMSAR) to demonstrate acoustically mediated spin control in Pc:PTP. Pentacene has recently emerged as a promising candidate for quantum memory and quantum metrology due to its zero-field splitting (ZFS), spin-triplet state and exceptional spin coherence properties at room temperature [249, 20, 19, 74, 250]. My approach effectively couples strain-induced phonons to spins in the molecular thin film without inducing magnetic fields that would affect their splitting levels.

The resonant frequencies of the $LiNbO_3$-based MMSAR, ranging from MHz to GHz, can be finely tuned by modifying the design of its interdigital transducers [251]. This microwave resonator achieves a quality factor approaching 10 000. By integrating organic thin films as spin materials with piezoelectric materials as phonon sources, I realize spin-phonon coupling for quantum memory. This heterogeneous integration offers an efficient platform in which the layout constraints typically associated with ESR measurements and coherent spin control are

mitigated. Furthermore, the groundwork is laid for the direct integration of spins into wafer-level material platforms used in quantum sensing and quantum networks.

5.2 Experimental Setup of the HODSAR Spectrometer

In my experimental studies with pentacene-deposited MMSAR devices (hereafter referred to as HODSAR devices), I observed that photo-excited pentacene molecular thin films generate spin-triplet states, analogous to the findings reported by Lubert-Perquel *et al.* [249] but within a different spin-coupling system. The spin-triplet mechanism illustrated in Fig. 5.1(a) exploits spin-selective intersystem crossing into the triplet ground state of the pentacene thin film. Upon photo-excitation with a 532 nm wavelength, pentacene is excited from its singlet ground state, S_0, to its first excited singlet state, S_1, followed by intersystem crossing to its triplet ground state, T_1, resulting in a strong inverted spin population between the T_x-T_y and T_x-T_z spin sub-levels of T_1. These spin-triplet states enabled us to characterize the coupling between the acoustic modes and the spin sublevels of the molecules. In order to demonstrate the spin-acoustic coupling within the HODSAR devices, I designed interdigital transducers on a lithium niobate ($LiNbO_3$) substrate that do not produce magnetic field interference. These IDTs generate a 105 MHz Rayleigh surface acoustic wave, which couples with the T_x-T_y transition of the pentacene thin film, also at 105 MHz. The simulation result for the magnetic field generated by the SAW device in my system shows a magnetic coupling efficiency of 5.06×10^{-12}, which is deemed to be negligible for my analysis (see Appendix E), thereby justifying the status of my system as zero-field applied [252]. Similar to the analysis of the planar spin defect system[253], the spin-triplet states in my system are governed by a spin-strain coupling Hamiltonian, represented by the following equation (see Appendix D):

$$\hat{H}_{\text{strain}} = \sum_{i,j} h_{ij}\, \varepsilon_{ij}\, \hat{S}_i \hat{S}_j, \tag{5.1}$$

where $\hat{S}_i$ and $\hat{S}_j$ are the spin-1 operators along the Cartesian axes ($i, j = x, y, z$), ε_{ij} represent

the components of the strain tensor, and h_{ij} are the spin-strain coupling constants specific to my material. Due to the D_{2h} symmetry of my system, certain components of h_{ij} are constrained, reflecting the symmetry-induced selection rules in the spin-strain interactions. [see Appendix].

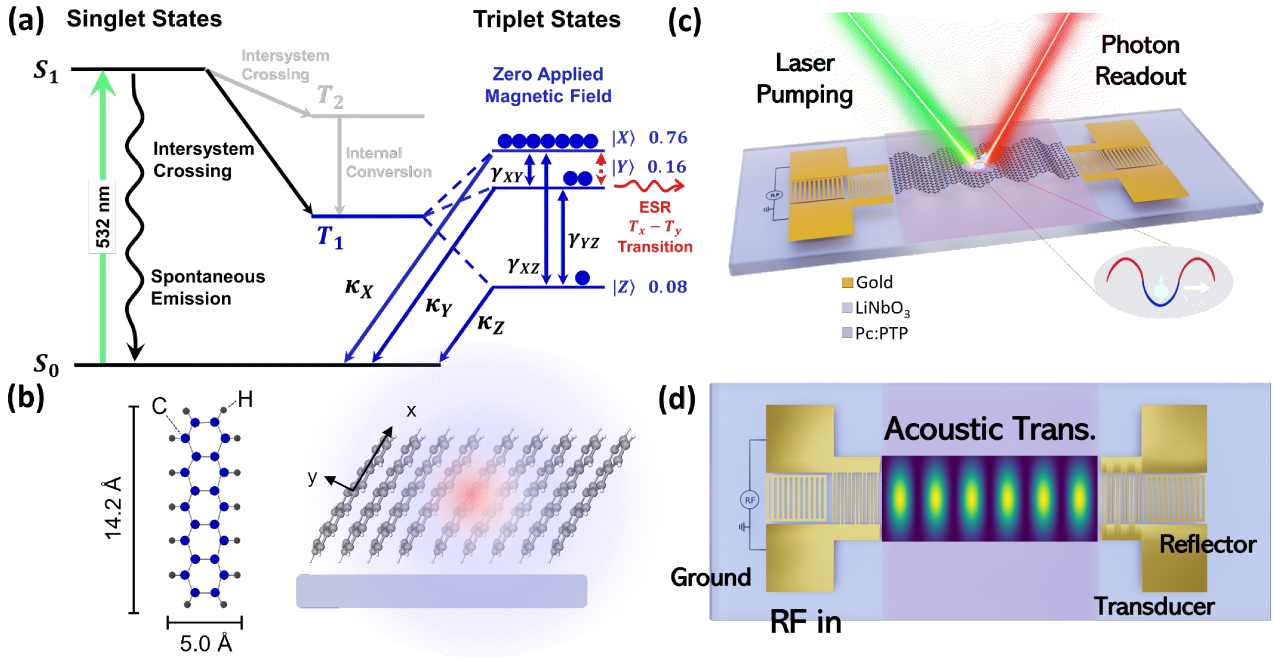

Figure 5.1: (a) Jablonski diagram illustrating the electronic state cycle in pentacene, responsible for spin-polarized triplet-state sublevels in pentacene:p-terphenyl. Optical excitation by a 532 nm laser promotes pentacene molecules from the ground state S_0 to the first singlet state S_1. Spin-orbit coupling mediates spin-selective intersystem crossing from the excited singlet state into the T_2 triplet manifold. The T_2 triplet states then decay non-radiatively to the T_1 triplet state, preserving the spin-polarized populations. Spin-lattice relaxation can occur between the triplet sublevels with rates γ_{XZ}, γ_{XY}, and γ_{YZ}, representing the $T_{X\to Z}$, $T_{X\to Y}$, and $T_{Y\to Z}$ transitions, respectively. The triplet sublevels ultimately decay back to the S_0 ground state with rates k_X, k_Y, k_Z, thus completing the cycle. My ESR readout targets the T_x-T_y transition near 105 MHz under zero applied magnetic field, leveraging the distinct resonance frequencies of the triplet sublevels for enhanced detection sensitivity. (b) Structural depiction of a pentacene thin film deposited on a $LiNbO_3$ substrate, indicating the molecular arrangement and orientation. (c) Schematic of the HODSAR device, featuring a high-Q multimode resonator that enables efficient laser pumping and photon readout for triplet state detection. (d) Alternative schematic of the device architecture, illustrating the integration of an acoustic transducer and RF input for resonance excitation.

5.2.1 HODSAR Device Fabrication

The IDTs of High-Q multi-mode SAW devices were fabricated on 128° YX-cut lithium niobate ($LiNbO_3$) wafers using a lift-off process. The wafers were sequentially cleaned with acetone,

methanol, and deionized (DI) water. A photoresist (AZ5214E, Clariant Co.) was uniformly spin-coated onto the wafers and subsequently exposed to ultraviolet (UV) light through a photomask. Following exposure, the wafers underwent a reversal bake, a flood exposure, and development, employing an image reversal process to achieve a negative-tone resist profile suitable for lift-off. A 150 nm thick gold (Au) film was deposited onto the patterned 128° YX $LiNbO_3$ wafers using a thermal evaporator. The wafers were then immersed in AZ 400T photoresist stripper to remove the unwanted metal, resulting in the desired Au IDT patterns on the $LiNbO_3$ substrates. After thorough rinsing with DI water, the wafers were diced into individual devices. For the deposition of organic molecular thin-film, pentacene (sourced from TCI UK Ltd. and purified by sublimation) and *p*-terphenyl (with over 99% purity from Alfa Aesar, further purified by zone refining) were deposited onto the SAW devices using organic molecular beam deposition (OMBD). The deposition process was carried out with a Kurt J. Lesker SPECTROS 100 system operating at a base pressure of 1×10^{-7} mbar. Quartz crystal microbalance sensors were utilized to precisely control the deposition rates, thereby determining

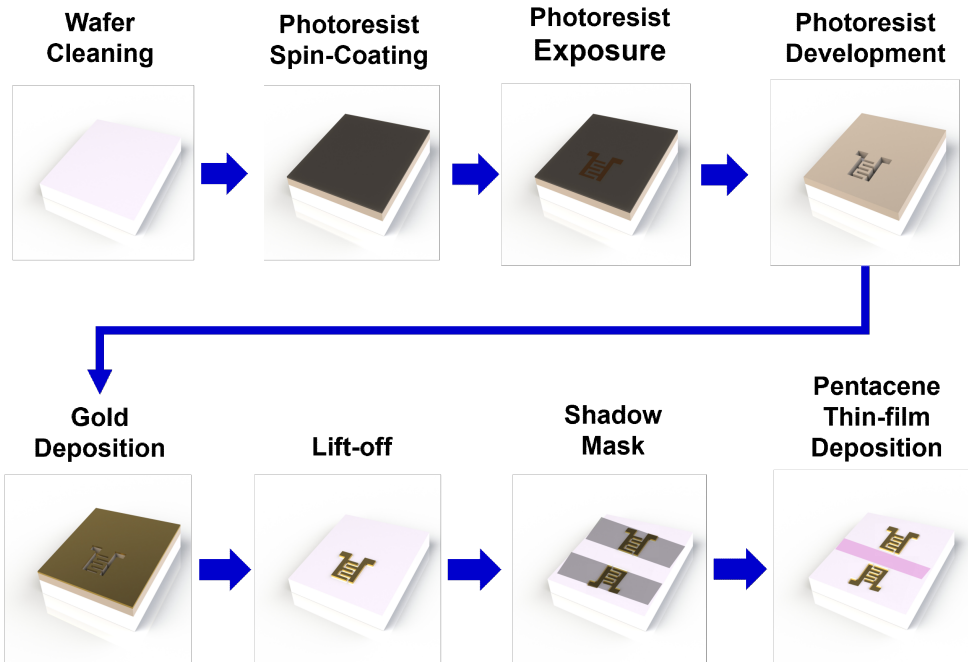

Figure 5.2: Fabrication process for a pentacene thin-film-based High-Q Organic Dielectric Surface Acoustic Resonator (HODSAR) device with gold electrodes. The procedure starts with wafer cleaning, followed by photoresist spin-coating. Photoresist exposure and development define the electrode pattern, followed by gold deposition and lift-off to establish the electrode structure. A shadow mask is then applied to enable selective deposition of the pentacene thin film on targeted areas.

the composition of the thin films. The concentrations were expressed as the volume ratio of pentacene to *p*-terphenyl, achieving a specific concentration of 1% pentacene in the thin film deposited on the SAW devices. FEM simulations are made using the COMSOL 5.6 Multiphysics package to simulate the electromagnetic Effect in the HODSAR system[252].

5.2.2 HODSAR System Setup

The HODSAR system setup is based on a confocal laser scanning microscope configured as follows. A 532 nm laser serves as the optical excitation source, modulated by a double-pass Isomet acousto-optic modulator (AOM). The microwave driving source is provided by a Tektronix TSG4106A RF signal generator and amplified by a Minicircuits ZHL-42W+ MW power amplifier, which delivers an output power of +35.29 dBm at 10 MHz. A Minicircuits ZFSWHA-1-20+ MW switch is used to modulate the MW signal. A wheel of dichroic filters reflects the green excitation light and transmits red fluorescence above 600 nm. An Olympus UPLXAPO 10× objective lens with a numerical aperture of 0.40 delivers the excitation to the SAW resonator and collects the fluorescence. Optical detection is performed using an Excelitas single-photon avalanche diode (SPAD). The output of the SPAD is fed into a Swabian Instruments Time Tagger Ultra, which records the arrival times of photons. A Swabian Instruments Pulse Streamer generates pulse sequences to modulate the AOM, the SPAD, and the MW switch. The experimental control system is based on the Qudi software suite. The pentacene-thin-film-deposited MMSAR device is connected to the RF signal generator and positioned under the objective for signal detection.

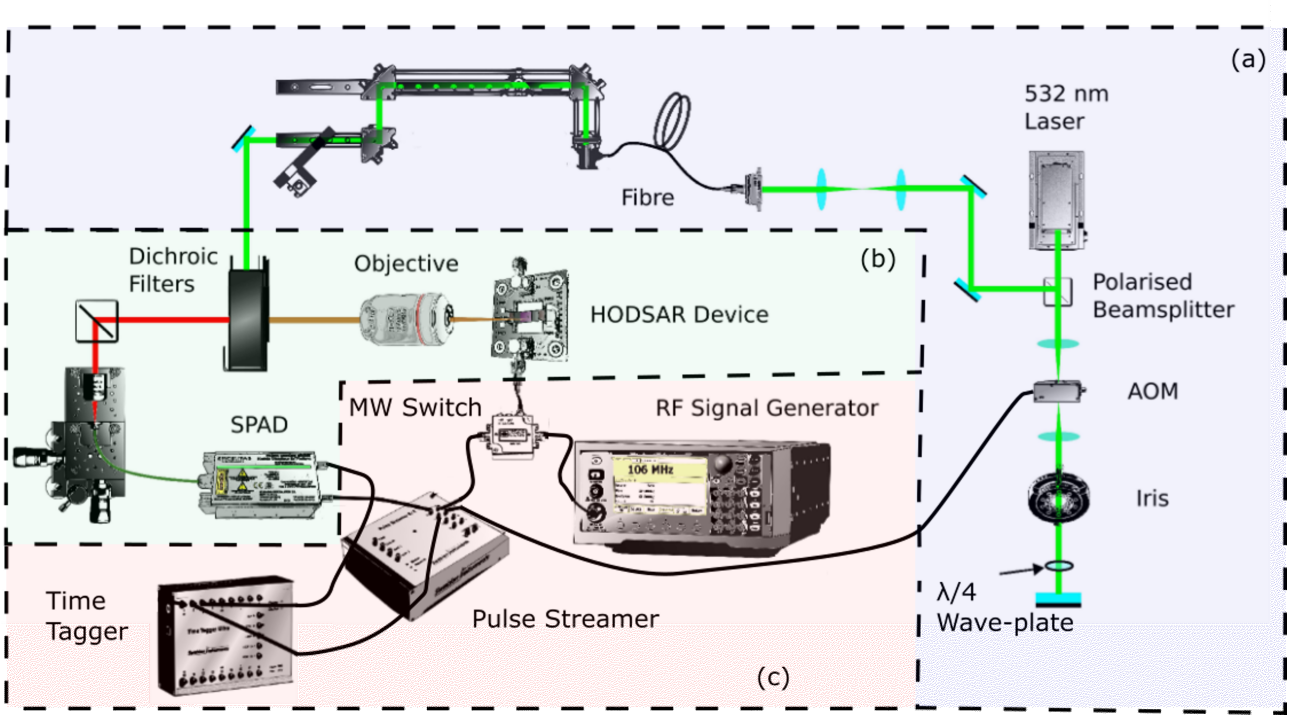

Figure 5.3: The schematic diagram of the CW and pulsed ODMR setup for the HODSAR device. (a) The HODSAR device is exited by a 532 nm laser that is modulated by a double-passed AOM. (b) The excitation laser is reflected towards the HODSAR device and the fluorescence is filted by a 600 nm long-pass dihroic mirror and transmitted to the SPAD. (c) The Pulse Streamer is used to generate the pulse sequences for the MW switch, the SPAD and the AOM, the Time Tagger counts the singals from the SPAD and the synchronisation signal from the Pulse Streamer. The RF signal generator generates a MW signal and it is modulated by the switched and delivered to the MMSAR device.

5.2.3 High-Q MMSAR Electro-Mechanical Characteristics

The electrical characterization of the HODSAR device was performed through two-port network measurements, shown in Fig. 5.4 and Fig. 5.5, capturing both the transmission (S_{21}) and reflection (S_{11}) responses across a broad frequency spectrum. This analysis aimed to identify and highlight the spectral region pertinent to the $T_x - T_y$ transition of photoexcited pentacene thin films, a critical feature for the device's sensing capability. The investigation focused on

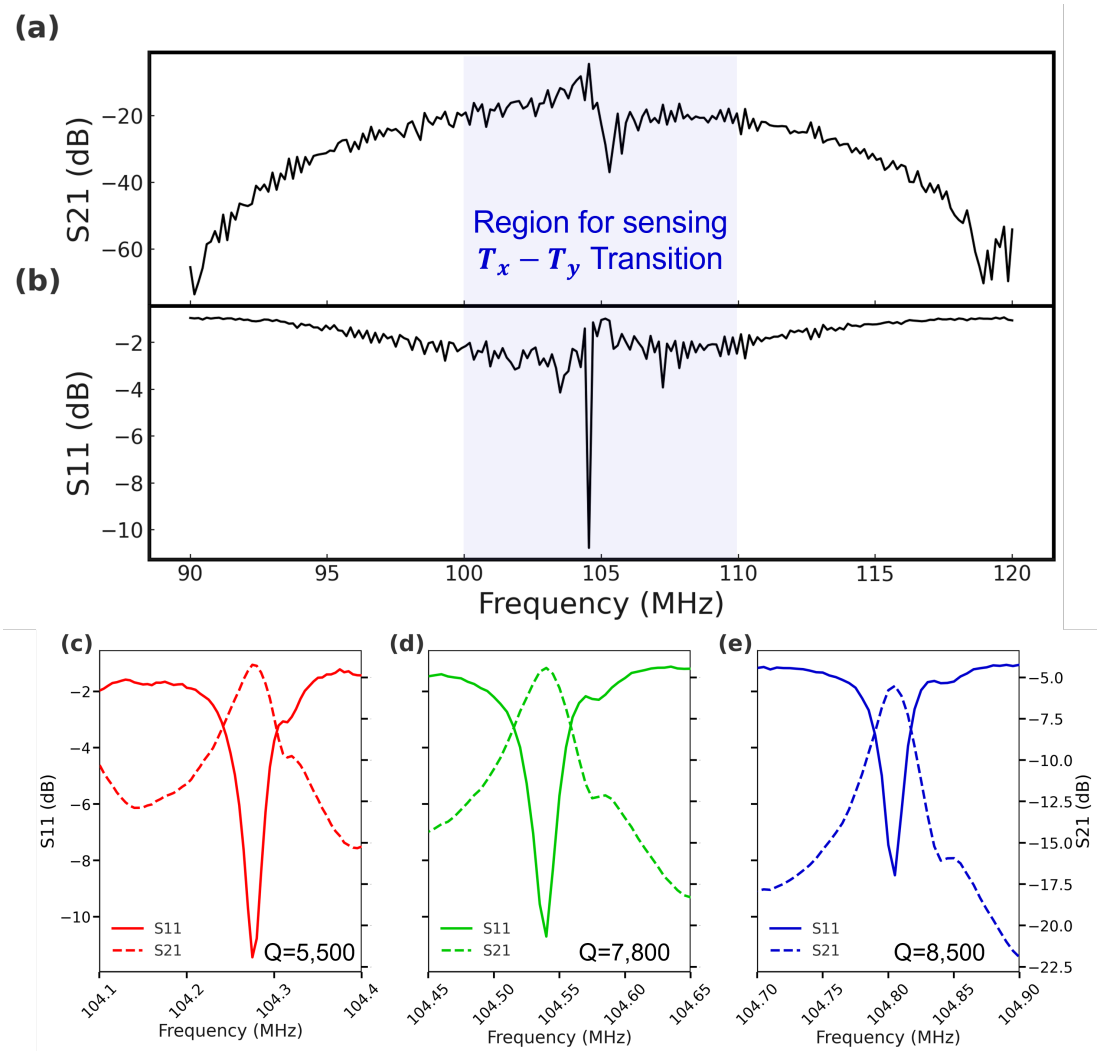

Figure 5.4: Two-port electrical measurements of the HODSAR device are presented. Panels (a) and (b) show the transmission (S_{21}) and reflection (S_{11}) spectra, respectively, over a wide frequency range, highlighting the region of interest for sensing the $T_x - T_y$ transition of photoexcited pentacene thin films. The blue-shaded region indicates the spectral range where these transitions occur. Panels (c), (d), and (e) display the highest Q-factor responses observed within the blue-shaded region, with corresponding Q-factors (calculated using the Q-circle method[40]) of 5,500, 7,800, and 8,500. These measurements demonstrate the exceptional performance of the HODSAR in the selected frequency range.

the resonant behavior within this designated range, revealing distinct Q-factors that signify the sharpness and efficiency of the resonances. The calculated Q-factors of 5,500, 7,800, and 8,500 underscore the high-quality factor performance of the device, indicative of its potential for precise and sensitive detection applications. This experimental approach validated the exceptional functionality of the HODSAR in the targeted frequency domain.

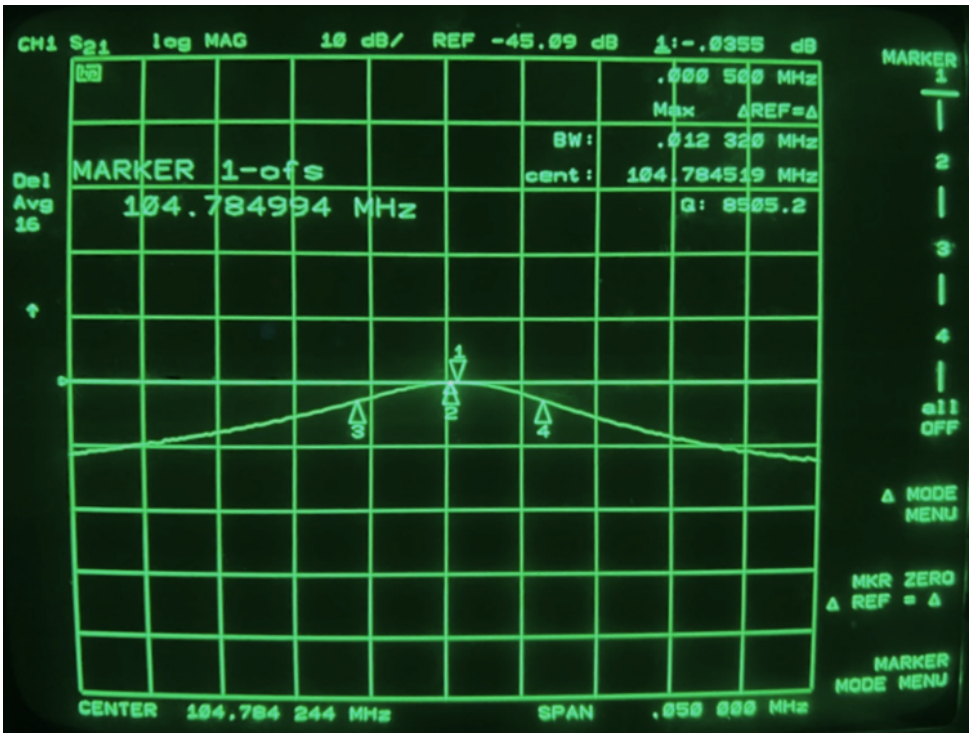

Figure 5.5: The HP8753C vector network analyzer (VNA) measurement illustrates the method used to determine the Q-factor values in Fig. 5.4, with a representative Q-factor of 8,505.2 at a frequency centered at 104.8MHz.

5.2.4 Pentacene Thin-Film Characterization

In this thesis, I benchmark the growth of pentacene thin films on a 128° Y-Cut $LiNbO_3$ substrate, comparing my results to those reported by Lubert et al[249] on SiO_2 substrates. The organic molecular beam deposition tool, deposition recipe, and conditions were maintained consistently across both substrate types. Characterization results shown in Fig. 5.6(a) indicate that the 1% Pc:PTP blend films exhibit a grain size of approximately 0.7 μm on $LiNbO_3$, which is smaller than the 1 μm grain size observed on SiO_2 substrates[249].

X-ray diffraction (XRD) analysis shown in Fig. 5.6(c) distinctly underscores the significant

influence of the piezoelectric $LiNbO_3$ substrate on the crystallinity and molecular orientation of the pentacene thin films, in contrast to films grown on non-piezoelectric glass substrates. Specifically, the emergence of a dominant peak around 30° 2θ on $LiNbO_3$, absent in the SiO_2 reference, suggests that the piezoelectric properties of $LiNbO_3$ induce unique strain environments or epitaxial relationships that enhance molecular ordering and potentially stabilize novel crystallographic phases of pentacene. Conversely, films grown on the glass substrate exhibit characteristic pentacene peaks at 6° and 18° 2θ, indicative of larger grain sizes and a more conventional phase distribution.

Furthermore, the pronounced peaks between 20° and 30° 2θ on $LiNbO_3$, along with an additional peak around 70° 2θ, imply enhanced crystalline alignment and possible secondary phase formation driven by substrate-induced anisotropic stress or electric field effects during deposition. Additionally, grain size and crystal quality analyses reveal that the $LiNbO_3$ substrate imposes distinct lattice-matching conditions, resulting in smaller but more oriented grains. This enhanced orientation could improve the electronic properties of the pentacene films.

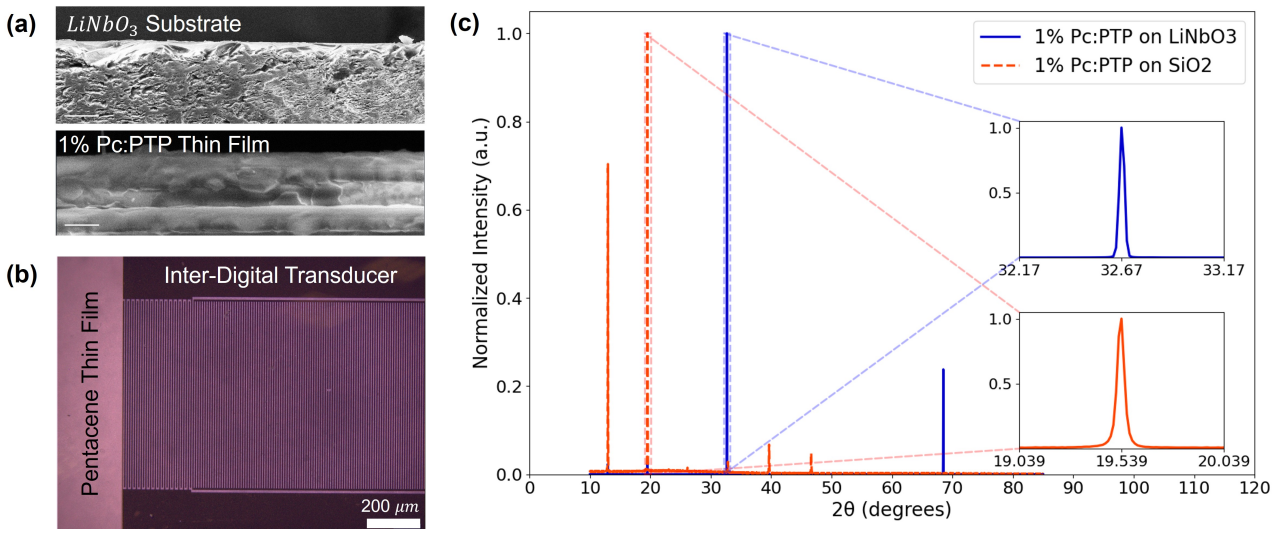

Figure 5.6: (a) SEM cross-sectional image of the MMSAR device, showing the 1% Pc:PTP thin film layer on a $LiNbO_3$ substrate with a 1 μm scale bar. (b) Optical microscope top view of the HODSAR device, highlighting the pentacene thin-film region and IDTs with a 200 μm scale bar. (c) XRD pattern comparison of the 1% Pc:PTP thin film on $LiNbO_3$ (solid blue line) and SiO_2 (dashed red line) substrates, demonstrating structural differences with expanded views of peak regions around 32.67° and 19.54°.

5.3 Coherent Acoustic Control of Molecular Thin Film

5.3.1 CW-HODSAR Measurement

To explore the room-temperature coherent acoustic control of molecular thin films for quantum metrology, I utilized continuous-wave HODSAR measurements on pentacene-deposited MMSAR devices. This technique enabled us to probe the spin-acoustic coupling by detecting resonant acoustic modes that interact with the triplet state transitions of pentacene molecules. The high-Q modes observed facilitate efficient coupling between the acoustic waves and the electronic spin states, allowing for coherent manipulation via acoustic excitation. By analyzing the fluorescence data across multiple measurements, as shown in Fig. 5.7 (a), I identified specific acoustic resonances that correspond to frequencies where the MMSAR device exhibits strong responses. In Fig. 5.7 (c), comparisons with CW-EPR spectroscopy showed that CW-HODSAR provides a similar bandwidth in detecting spin transitions, highlighting its effectiveness in probing spin dynamics within this system. The variations in line shapes between the two methods are attributed to the limited high-Q multimode response of the MMSAR device in the frequency range studied. These results underscore the potential of acoustic techniques for the control and understanding of spin states in molecular thin films, contributing valuable insights into spin-phonon interactions in solid-state systems.

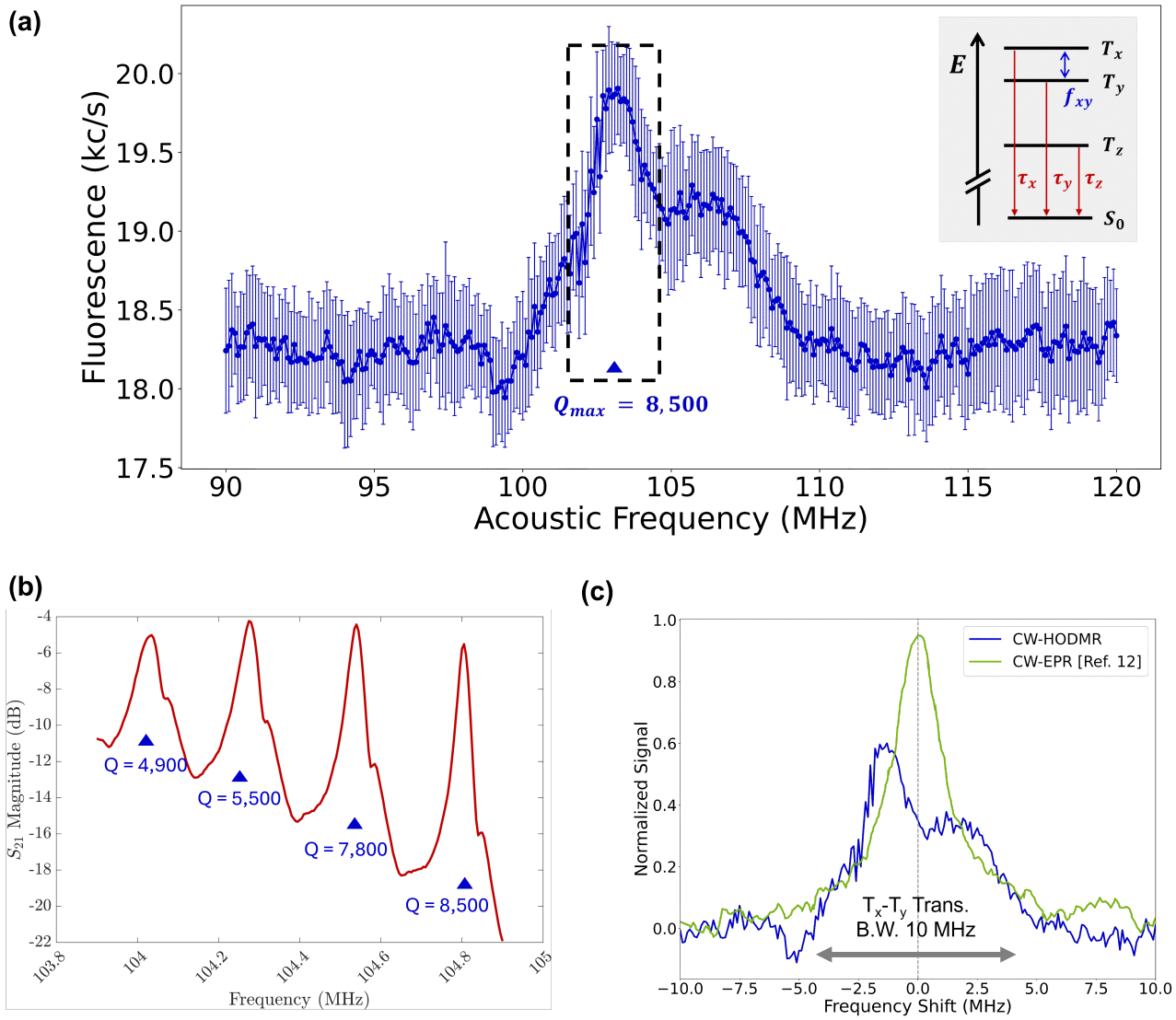

Figure 5.7: (a) Continuous-wave (CW) HODSAR measurements of the pentacene-deposited MMSAR device with 60 repetitions. The fluorescence data are presented with error bars indicating the standard deviation, with a resolution of 100 kHz. The dashed black box highlights a high-Q mode centered around 105 MHz. (b) S_{21} transmission measurements of the MMSAR device, focusing on the region within the black dashed box in (a). Four distinct high-Q resonant modes are observed, facilitating the coupling to the T_x-T_y transition of the pentacene triplet state. (c) HODSAR readout of the spin-acoustic coupling, shown in comparison with CW-EPR spectroscopy measurements of the hyperfine-coupled ESR. Notably, both readouts exhibit a similar bandwidth, although the line shape in (c) may be influenced by the limited high-Q multimode response of the MMSAR device across the 100-110 MHz range. The electro-mechanical properties of the MMSAR device are detailed in the Appendix.

5.3.2 Pulsed HODSAR Measurement (Rabi Oscillation)

Finally, in Fig. 5.8 I demonstrate the pulsed coherent control of HODSAR measurements in my pentacene thin-film-based device. Drawing inspiration from the work of Dietz et al.[254], the pulsed HODSAR technique enables state preparation and serves as a valuable resource for entanglement generation. Utilizing a driving radio frequency of 104.5MHz—which corresponds to the highest signal intensity observed in my previous measurements—I generate acoustic resonance through IDTs. By characterizing the Rabi oscillations under pulsed excitation, I confirm

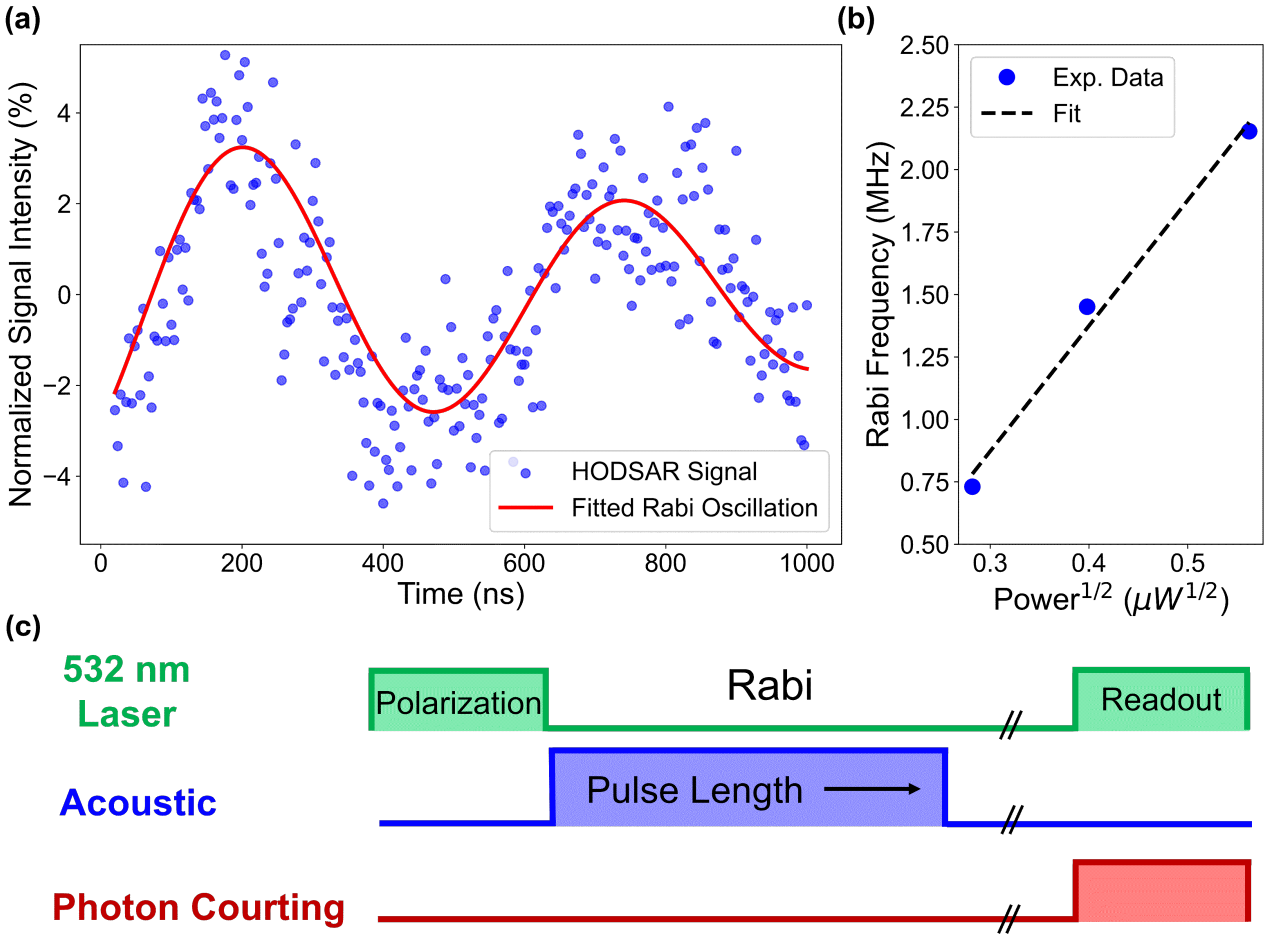

Figure 5.8: Characterization of Rabi oscillations in the pentacene thin-film-based HODSAR device. (a) Time-domain measurement of the HODSAR signal, showing normalized signal intensity as a function of time, with the fitted Rabi oscillation overlaid in red. (b) Rabi frequency plotted as a function of the square root of applied power, with experimental data points and a linear fit illustrating power dependence. (c) Schematic of the experimental setup for Rabi oscillation measurements, indicating the timing of laser polarization, acoustic pulse length, and photon counting readout. This characterization validates the coherence and control of Rabi oscillations in the device.

the coherence and controllability of quantum states within the system. The time-domain measurements exhibit clear oscillatory behavior, indicating effective coherent manipulation of spin states. Additionally, the linear dependence of the Rabi frequency on the square root of the applied power validates the efficiency of my control scheme. This advancement underscores the potential of my device for applications in quantum memory, where precise and rapid manipulation of quantum states is essential. The integration of molecular thin films with acoustic control not only offers a scalable platform but also opens avenues for exploring complex quantum phenomena in solid-state systems.

5.4 Conclusions

In this work, I have introduced a high-Q SAW device integrated with pentacene-deposited molecular thin films to realize HODSAR. Through spin-phonon coupling, my system achieves efficient zero-field spin control at room temperature, which I demonstrated using CW and pulsed HODSAR measurements. The results indicate that this device architecture can facilitate the precise and coherent manipulation of spin states via acoustic excitation, effectively bypassing the need for conventional magnetic resonance techniques. My findings validate the potential of organic molecular thin films as viable platforms for spin-based quantum memory, especially in contexts where magnetic field sensitivity is a limitation.

Moreover, the scalability and versatility of the SAW-based HODSAR system highlight its applicability in diverse quantum technologies, from quantum sensing to coherent spin manipulation. This study establishes a foundation for the further exploration of molecular spin-phonon interactions and their applications in high-sensitivity, room-temperature quantum devices. Future work will focus on enhancing the integration of organic spin systems with MEMS so as to expand the functionalities of and address scalability challenges in quantum memory.

Chapter 6

Conclusion

6.1 Summary

The advancements achieved in this thesis open several avenues for future research in room-temperature quantum technologies. Focusing on enhancing quantum measurement techniques, developing robust qubit media, and integrating novel spin control mechanisms can significantly propel the field forward

In the pursuit of efficient thermal management of microwave cavities, I have demonstrated a method for pre-cooling the modes of a microwave cavity by temporarily over-coupling them to the input of an LNA serving as an ACL. This APC technique effectively reduces the number of thermal photons occupying the cavity modes within the LNA's bandwidth, enhancing the sensitivity of quantum measurements without relying on cryogenic cooling. My comparative analysis with methods based on internal stimulated absorption, such as masers and anti-masers, indicates that while both approaches have their merits, APC offers the salient advantage of being readily switchable, allowing for minimal disturbance to the microwave cavity. This flexibility makes APC a promising candidate for accelerating various pulsed-EPR techniques, such as tr-EPR, ESEEM, HYSCORE, and PELDOR, thereby reducing measurement times and expanding the applicability of these methods in quantum technologies.

Building on the need for alternative tunable qubit media capable of robust quantum activity over a range of temperatures, I have employed known chemical strategies to facilitate long coherence times in organic radical systems. Specifically, I have demonstrated remarkably long spin-lattice (T_1) and spin coherence (T_m) relaxation times for the well-known BDPA organic radical system, comparing favorably against state-of-the-art molecular qubit media. By capitalizing on the structural versatility enabled by chemical synthesis, these quantum functionalities can be significantly enhanced, paving the way for the development of spin qubits suitable for quantum computation and quantum communication applications. While challenges remain in deploying spin qubits in controllable host matrices that enable intermolecular entanglement through dipole coupling or exchange interactions, my work establishes behavioral regimes applicable to several emerging quantum technologies and underscores the potential of organic radicals in advancing molecular qubit technology.

Furthermore, I have introduced a high-quality SAW device integrated with pentacene-deposited molecular thin films to realize HODSAR. Through spin-phonon coupling, this system achieves efficient zero-field spin control at room temperature, demonstrated using both continuous-wave and pulsed HODSAR measurements. This innovative device architecture facilitates precise and coherent manipulation of spin states via acoustic excitation, effectively bypassing the need for conventional magnetic resonance techniques and mitigating issues related to magnetic field sensitivity. The scalability and versatility of the SAW-based HODSAR system highlight its applicability in diverse quantum technologies, from quantum sensing to coherent spin manipulation, establishing a foundation for further exploration of molecular spin-phonon interactions and their applications in high-sensitivity, room-temperature quantum devices.

The techniques developed in this thesis, including cavity pre-cooling using an active cold load, the enhancement of coherence times in organic radical systems, and the integration of spin-phonon coupling via SAW devices, are general solutions that extend beyond the specific systems studied. For instance, the APC method can be employed in various pulsed-EPR techniques to reduce measurement times, and the strategies for improving Tand Ttimes in organic radicals can be applied to other molecular qubit systems. The SAW-based HODSAR platform offers a versatile approach for spin control that can be adapted to different materials and devices.

These advancements contribute to the broader field of quantum technology (especially quantum memory and quantum seeing) by providing practical approaches to manipulating spin systems at room temperature without reliance on cryogenics, vacuum chambers, or strong magnets. Future work will focus on enhancing these techniques through material science and device engineering, exploring new materials and architectures optimized for mode cooling, and improving the integration of organic spin systems with MEMS to address scalability challenges. Additionally, more vigorous strategies such as deuteration, the use of alternative radicals, and advanced pulsed protocols could further improve coherence times and quantum functionalities.

Collectively, this thesis fosters greater cross-fertilization between microwave radiometry, EPR, NMR communities, and hardware innovations in quantum computing & quantum networks, particularly those targeting room-temperature operation. By bridging these areas, I advance the development of robust, scalable, and practical quantum technologies, contributing to the realization of quantum networks, communications, and computation systems that operate efficiently under ambient conditions.

6.2 Future Work

Building upon the advancements presented in this thesis, several promising avenues for future research emerge, aiming to enhance room-temperature quantum technologies by improving measurement techniques, developing robust qubit media, and integrating novel spin control mechanisms into quantum devices.

Firstly, further development and optimization of APC methods are essential to enhance the sensitivity of quantum measurements without relying on cryogenic cooling. Investigating new materials and microwave cavity designs to maximize the efficiency of APC is a crucial step. This includes exploring alternative LNAs and ACLs to broaden the bandwidth and effectiveness of pre-cooling techniques. Optimizing cavity geometries and coupling mechanisms can reduce thermal photon occupancy, thereby enhancing measurement sensitivity. Applying APC methods to a wider range of pulsed EPR techniques will allow for systematic assessment of APC's

impact on measurement times and sensitivity. Collaborations with industry partners (such as Bruker or Ciqtek) to integrate APC into commercial quantum devices can facilitate the development of scalable systems compatible with existing quantum computing platforms, making room-temperature quantum technologies more accessible and cost-effective. Emphasis should be placed on designing APC setups that are modular and can be seamlessly incorporated into various quantum hardware architectures. Enhancing APC techniques will significantly contribute to the development of practical quantum devices that operate efficiently under ambient conditions, addressing key barriers to the widespread adoption of quantum technologies in real-world applications.

Secondly, improving spin coherence times in organic radical systems to create robust qubit media suitable for quantum computation and communication is another vital area of future research[255]. Employing advanced chemical strategies such as deuteration and the synthesis of alternative radical species can mitigate decoherence mechanisms. Designing organic molecules with tailored electronic and nuclear spin environments can enhance spin-lattice and spin coherence relaxation times. Investigations into the role of molecular symmetry, spin-orbit coupling, and hyperfine interactions will inform the synthesis of qubits with optimal coherence properties. Exploring controllable host matrices that facilitate intermolecular interactions through dipole-dipole coupling or exchange interactions is crucial. Solid-state environments, such as crystalline lattices or polymer matrices, can provide structural stability and enable coherent coupling between qubits. Studying the effects of matrix rigidity, dielectric properties, and phonon spectra will aid in identifying hosts that minimize decoherence. Developing sophisticated pulsed EPR techniques to manipulate spin states with greater precision, including the implementation of dynamic decoupling sequences like CPMG, can suppress decoherence due to environmental noise. Incorporating quantum-error-mitigation (QEM) protocols will further extend coherence times and improve qubit fidelity. Advancing organic spin qubits will pave the way for their integration into quantum networks and devices, leveraging the inherent structural versatility and scalability of organic materials.

Thirdly, enhancing the use of SAW devices for efficient spin control via spin-phonon coupling at room temperature presents a significant opportunity. Optimizing the design of SAW-based

HODSAR systems by experimenting with different molecular thin films and substrate materials can improve coupling efficiency and device performance. Engineering the piezoelectric properties of substrates and tuning the acoustic wavelength can enhance spin-phonon interactions. Incorporating MEMS technology to achieve greater scalability and integration density is another important direction. Developing chip-scale devices that combine SAW components with spin systems will facilitate their incorporation into larger quantum architectures. MEMS integration can provide precise control over acoustic wave propagation and enable device miniaturization. Exploring spin-phonon coupling mechanisms for high-sensitivity quantum sensors and secure communication channels is also promising. Investigating zero-field spin control methods can reduce susceptibility to magnetic field fluctuations, improving device robustness in practical applications. Utilizing spin-phonon interactions may enable novel protocols for quantum information transfer and processing. This work will contribute to the development of versatile quantum devices that operate effectively at room temperature, expanding the applicability of quantum technologies in sensing, communication, and computation.

Focusing on these future directions will address critical challenges in quantum information science. By enhancing room-temperature quantum measurement techniques, developing long-lived organic spin qubits, and integrating novel coupling mechanisms, this research will advance the state of the art in quantum technologies. These efforts are expected to facilitate the realization of robust, scalable, and practical quantum devices capable of operating under ambient conditions, thereby accelerating the integration of quantum systems into real-world applications.

Appendix A

Derivation of the SNR in EPR Spectroscopy and the Minimum Detectable Number of Spins

A.1 Signal-to-Noise Ratio

In EPR spectroscopy, the sensitivity of the spectrometer is proportional to the SNR observed on an oscilloscope. Poole has defined the total noise figure of the system and the minimum detectable RF susceptibility for a reflection-type microwave cavity [95]. Based on these results, the change in the reflected voltage ΔE_r for a linear detector with a reflection-type microwave cavity can be evaluated as:

$$\Delta E_r = \frac{1}{2}\chi'' \eta Q_u E, \tag{A.1}$$

where χ'' is the imaginary component of the magnetic susceptibility, η is the cavity coupling efficiency, Q_u is the unloaded quality factor of the cavity, and E is the incident electric field amplitude.

The root mean square (rms) noise voltage at the detector output, due to thermal noise, is given by:

$$\Delta E_n = \sqrt{4R_0 k_B T_d \Delta f}, \tag{A.2}$$

where R_0 is the characteristic impedance of the transmission line, k_B is Boltzmann's constant, T_d is the detection and amplification temperature, and Δf is the bandwidth.

By setting the minimum detectable signal equal to the noise voltage, $\Delta E_r = \Delta E_n$, the limit of detectability for the imaginary susceptibility $\chi''_{\min}$ can be derived:

$$\chi''_{\min} = \left(\frac{2}{\eta Q_u}\right)\left(\frac{k_B T_d \Delta f}{P_w}\right)^{1/2}, \tag{A.3}$$

where the incident power P_w is related to the incident electric field by:

$$P_w = \frac{E^2}{4R_0}. \tag{A.4}$$

Equation (A.3) represents the theoretical minimum detectable susceptibility $\chi''_{\min(\mathrm{TH})}$ under ideal conditions.

Considering the system noise figure using Friis's formula, the minimum detectable susceptibility at the output of the preamplifier, $\chi''_{\min(\mathrm{OB})}$, becomes [95]:

$$\chi''_{\min(\mathrm{OB})} = \left(\frac{2}{\eta Q_u}\right)\left([F_s - 1 + (F_{\mathrm{amp}} - 1)L]\frac{k_B T_d \Delta f}{P_w}\right)^{1/2}, \tag{A.5}$$

where F_s and F_{amp} are the noise figures of the system input and the preamplifier, respectively, and L is the insertion loss.

The ratio of the practical minimum detectable susceptibility to the theoretical limit is then given by:

$$\frac{\chi''_{\mathrm{min(OB)}}}{\chi''_{\mathrm{min(TH)}}} = [F_s - 1 + (F_{\mathrm{amp}} - 1)L]^{1/2} \geq 1. \tag{A.6}$$

For ideal sensitivity, the following conditions must be satisfied:

$$L = F_s = F_{\mathrm{amp}} = 1, \quad \chi''_{\mathrm{min(OB)}} = \chi''_{\mathrm{min(TH)}}. \tag{A.7}$$

A.2 Sensitivity: Minimum Detectable Number of Spins

The minimum detectable imaginary susceptibility $\chi''_{\mathrm{min(OB)}}$, as defined in Eq. (A.5), can be related to the solution of the Bloch equations. The frequency-dependent imaginary susceptibility $\chi''(\omega)$ is related to the static susceptibility χ_0 by [95]:

$$\chi''(\omega) = \frac{\frac{1}{2}\chi_0\omega_0 T_2}{1 + (\omega - \omega_0)^2 T_2^2}, \tag{A.8}$$

where ω_0 is the resonance angular frequency and T_2 is the spin-spin relaxation time. This expression reaches its maximum at $\omega = \omega_0$:

$$\chi''(\omega_0) = \frac{\chi_0\omega_0 T_2}{2}. \tag{A.9}$$

Since the linewidth $\Delta\omega_{\mathrm{pp}}$ is inversely proportional to T_2, we have:

$$T_2 = \frac{2}{\Delta\omega_{\mathrm{pp}}}. \tag{A.10}$$

Substituting Eq. (A.10) into Eq. (A.9), I get:

$$\chi''(\omega_0) = \frac{\chi_0\omega_0}{\Delta\omega_{\mathrm{pp}}}. \tag{A.11}$$

The static susceptibility χ_0 can be expressed using the Curie law:

$$\chi_0 = \frac{Ng^2\beta^2 S(S+1)}{3V_s k_B T_s}, \tag{A.12}$$

where N is the number of spins, g is the Landé g-factor, β is the Bohr magneton, S is the electron spin quantum number, V_s is the sample volume, k_B is Boltzmann's constant, and T_s is the sample temperature.

Combining Eqs. (A.5), (A.11), and (A.12), I derive the minimum detectable number of spins $N_{\min}$ for a system obeying the Curie law and the Bloch equations [95]:

$$N_{\min} = \frac{6V_s k_B T_s}{Q_u \eta g^2 \beta^2 S(S+1)} \left(\frac{\Delta\omega_{\text{pp}}}{\omega_0}\right) \left([F_s - 1 + (F_{\text{amp}} - 1)L]\frac{k_B T_d \Delta f}{P_w}\right). \tag{A.13}$$

In Eq. (A.13), to maximize the sensitivity of the EPR spectrometer, I aim to minimize $N_{\min}$. The number of spins in a sample can be expressed as:

$$N_{\text{spin}} = y'_m N_{\min}, \tag{A.14}$$

where y'_m is the SNR.

In practice, the number of spins in an unknown sample is determined by comparing it to a standard sample. If the measurements are carried out under identical conditions (constant η and V_s, negligible change in quality factor Q_u, same power P_w, and modulation amplitude H_{mod}), the comparison can be described as [95]:

$$\frac{N_{\text{spin}}^{(A)}}{N_{\text{spin}}^{(B)}} = \left(\frac{D^{(A)}}{D^{(B)}}\right) \left(\frac{g^{(B)}}{g^{(A)}}\right)^2 \left(\frac{S^{(B)}\left(S^{(B)}+1\right)}{S^{(A)}\left(S^{(A)}+1\right)}\right) \left(\frac{\Delta H_{\text{pp}}^{(A)}}{\Delta H_{\text{pp}}^{(B)}}\right)^2 \left(\frac{\Lambda'^{(A)}}{\Lambda'^{(B)}}\right) \left(\frac{H_{\text{mod}}^{(B)}}{H_{\text{mod}}^{(A)}}\right) \left(\frac{y_m'^{(A)}}{y_m'^{(B)}}\right), \tag{A.15}$$

where superscripts A and B denote the unknown and standard samples, respectively; D is the

density of states; ΔH_{pp} is the peak-to-peak linewidth; Λ' is a factor accounting for line shape and instrument response; H_{mod} is the modulation amplitude; and y'_m is the SNR.

Appendix B

Noise Analysis and Noise-Figure Characterization of LNAs

B.1 Noise Temperature in Devices and Thermal Noise Analysis of Circuits: An Introduction

B.1.1 Noise Parameters of HEMT Ultra-Low-Noise Amplifiers: Why HEMTs Can Achieve Such Low Noise Temperatures

In 1979, the HEMT was introduced by Takashi Mimura. His research on GaAs metal-oxide-semiconductor field-effect transistors (MOSFETs) predicted that HEMTs would exhibit high-speed performance and could be applied to the amplification of weak signals [41]. Due to the vertical architecture of HEMTs, the device physically separates conduction electrons from their parent donors, thereby reducing ionized impurity scattering [256]. Additionally, in a two-dimensional electron gas (2DEG), as shown in Fig. B.1, an undoped narrow-bandgap intrinsic semiconductor layer confines the carrier flow, leading to lower noise and higher gain compared to conventional GaAs MOSFETs [257].

In the cross-section of an AlGaAs/GaAs HEMT depicted in Fig. B.1, the bottom terminals

of the drain and source are based on n-doped GaAs thin films, providing low-resistance ohmic contacts. A high-κ metal gate is placed in a recessed trench to reduce access resistance. By physically separating the donor atoms from the accumulation layer, the undoped AlGaAs/GaAs spacer improves carrier mobility. Moreover, the n-doped AlGaAs layer supplies electrons for the conduction channel. Due to AlGaAs's larger bandgap compared to GaAs, a high-mobility channel (2DEG) is formed at the top of the undoped GaAs buffer layer [258]. Thus, between the undoped AlGaAs spacer and the undoped GaAs buffer, the electric field is strong enough to confine electrons to a triangular quantum well (within 20 nm) [256]. With recent advancements, HEMTs based on InP substrates (namely pHEMTs) have been developed as high-performance LNAs because of their wide bandwidth and low noise temperature [259].

Small-Signal Equivalent Circuit for Noise Parameter Analysis

A small-signal equivalent circuit is a useful tool for analyzing a device's performance. This lumped circuit model helps researchers simulate the device's scattering parameters precisely. The small-signal equivalent circuit of the HEMT device, as established by Bok-Hyung Lee *et*

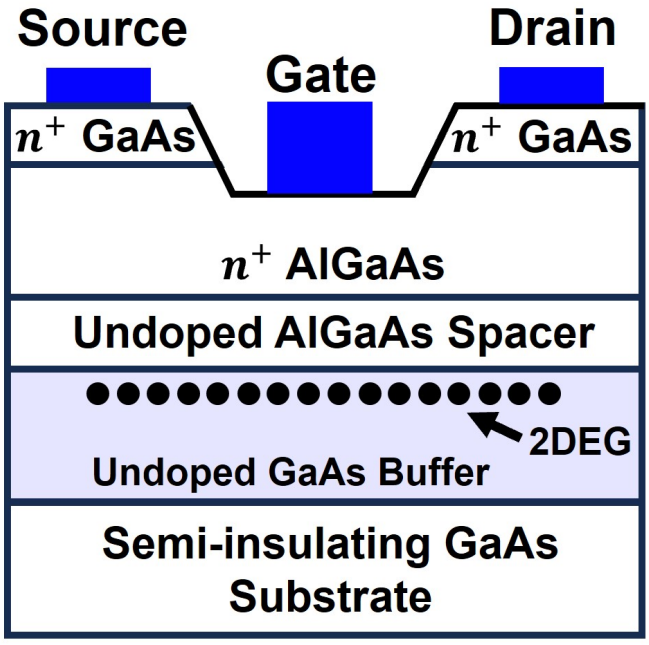

Figure B.1: Cross-section of a HEMT semiconductor device [41]. The 2DEG is formed in the undoped GaAs buffer layer near the interface with the undoped AlGaAs spacer. Carriers are supplied by the doped AlGaAs layer.

al., is provided in Fig. B.2 [42] and summarized in Table B.1.

Table B.1: Symbols in the Small-Signal Equivalent Circuit for HEMTs

Symbol	**Component**	**Intrinsic/Extrinsic**
g_0	Output conductance	Intrinsic
g_m	Intrinsic transconductance	Intrinsic
R_i	Intrinsic resistance	Intrinsic
R_s	Source resistance	Intrinsic
R_g	Gate resistance	Intrinsic
C_{gd}	Gate-to-drain capacitance	Intrinsic
C_{gs}	Gate-to-source capacitance	Intrinsic
L_g, L_s, L_d	Gate, source, and drain inductances, respectively	Extrinsic
R_g, R_s, R_d	Gate, source, and drain resistances, respectively	Extrinsic
C_g, C_s, C_d	Gate, source, and drain capacitances, respectively	Extrinsic

According to Fig. B.2, the two figures of merit, transition frequency f_T and maximum frequency of oscillation $f_{\max}$, can be simulated by this model [42]:

$$
\begin{aligned}
f_T &= \frac{g_m}{2\pi C_{gs}}, \\
f_{\max} &= \frac{f_T}{\sqrt{4\frac{g_0}{g_m}\left(g_m R_i + \frac{R_s + R_g}{1/g_m + R_s} + \frac{4}{5}\frac{C_{gd}}{C_{gs}}\left(1 + \frac{2.5C_{gd}}{C_{gs}}\right)(1 + g_m C_{gs})^2\right)}}.
\end{aligned}
\tag{B.1}
$$

In Chapter 1, according to the Johnson-Nyquist noise theory, the thermal noise inside the circuit is caused by the random motion of charge carriers due to thermal agitation and can be described as [260]:

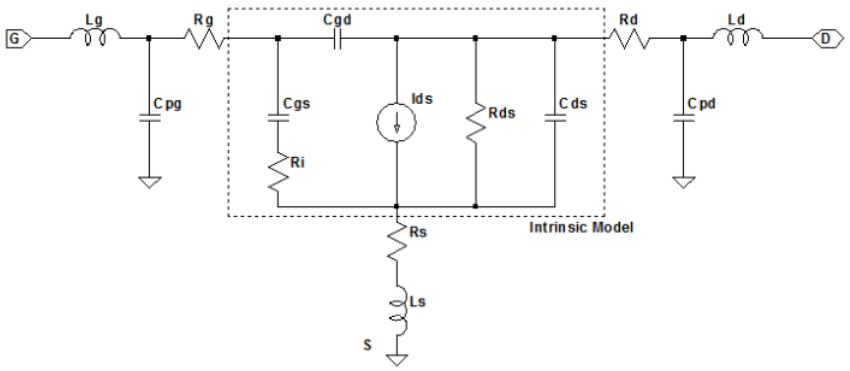

Figure B.2: Small-signal equivalent circuit for HEMTs [42]. Each component is summarized in Table B.1.

$$V = \sqrt{4kTR\Delta f}, \tag{B.2}$$

where V is the noise voltage, k is the Boltzmann constant, R is the resistance, T is the absolute temperature, and Δf is the bandwidth.

In FETs or HEMTs, charge carriers generate shot noise as they transmit through depletion regions. The noise current can be described by [261]:

$$i^2 = 2qI\Delta f, \tag{B.3}$$

where i is the noise current, q is the elementary charge, and I is the current.

Thermal noise of FETs/HEMTs was first modeled by van der Ziel using the concept of a current generator $\sqrt{i}$ (parallel to the output) to represent thermal noise [262]. Then, in 1989, Marian Pospieszalski proposed a model for noise parameter analysis, shown in Fig. B.3. In this model, two frequency-independent constants of an equivalent intrinsic transistor circuit predict the noise parameters [43].

By solving the thermal noise model of HEMTs, the four noise parameters can be calculated using the following equations:

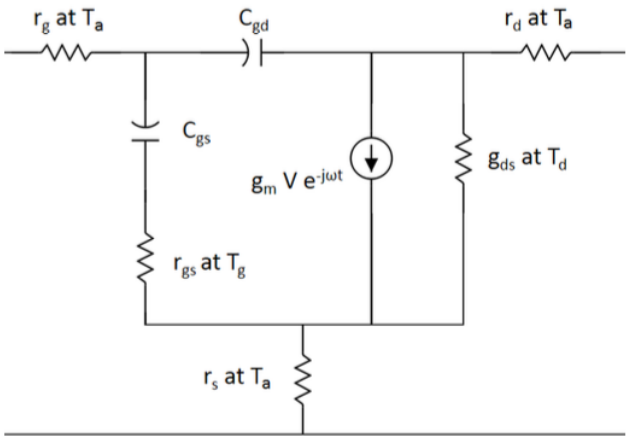

Figure B.3: Small-signal equivalent circuit for HEMT noise analysis [43].

$$
\begin{aligned}
X_{\text{opt}} &= \frac{1}{\omega C_{gs}}, \\
R_{\text{opt}} &= \sqrt{\left(\frac{f_T}{f}\right)^2 \frac{r_{gs}}{g_{ds}} \frac{T_g}{T_d} + r_{gs}^2}, \\
T_{\text{min}} &= 2\frac{f}{f_T}\sqrt{g_{ds} r_{gs} T_g T_d + \left(\frac{f}{f_T}\right)^2 r_{gs}^2 g_{ds}^2 T_d^2} + 2\left(\frac{f}{f_T}\right)^2 r_{gs} g_{ds} T_d, \\
R_n &= \frac{T_g}{T_0} r_{gs} + \frac{T_d}{T_0}\frac{g_{ds}}{g_m^2}\left(1 + \omega^2 C_{gs}^2 r_{gs}^2\right),
\end{aligned}
\tag{B.4}
$$

where R_{opt} and jX_{opt} are the real and imaginary parts of the optimal source impedance Z_{opt}, T_{min} is the minimum noise temperature, R_n is the noise resistance, g_{ds} is the output conductance, r_{gs} is the gate-source resistance, T_g and T_d are the temperatures of the gate and drain, respectively, and T_0 is the standard temperature.

Equation (2.4) provides guidance on how to minimize the noise temperature of HEMTs. By reducing g_{ds} and r_{gs}, a smaller noise temperature of HEMTs is obtained.

Industrial Standard Definition of Noise Parameters

Typical setups use $50\,\Omega$ interconnects (cables) between circuit elements. I can determine the device's noise parameters by measuring changes in the level of noise outputted from the device upon attaching different source impedances to its input. These parameters can be defined in various ways according to different conventions but are most commonly expressed as two scalars and one complex number: the noise figure (F_{min}, real), the noise resistance (R_n, real), and the optimum reflection coefficient (Γ_{opt}, a complex number defined by its magnitude and phase angle). The most common expression for the noise figure of a device is [263]:

$$
F = F_{\text{min}} + 4R_n \frac{|\Gamma_s - \Gamma_{\text{opt}}|^2}{|1 + \Gamma_{\text{opt}}|^2 (1 - |\Gamma_s|^2)}, \tag{B.5}
$$

where F is the linear noise figure, F_{min} is the minimum noise figure, Γ_{opt} is the optimum source reflection coefficient, R_n is the equivalent noise resistance, and Γ_s is the source reflection coefficient.

B.2 Wave-Approach Noise Analysis and Noise Parameter Measurement Using Heterodyne Detection

In this section, I calibrate and measure the noise parameters of an LNA (Qorvo QPL9547) using wave-approach analysis in a heterodyne detection system, as described by Wu *et al.* [44]. Fig. B.4 illustrates how noise propagates from the component connected to the LNA's output, which is then received and detected. The thermal noise at the LNA's input comprises the forward-propagating noise wave of the amplifier, denoted $+T_{\mathrm{LNA}}$, and a certain fraction (determined by the reflection coefficient Γ_c) of its backward-propagating noise wave, denoted $-\Gamma_c T_{\mathrm{LNA}}$. Additionally, the component's noise propagates to the amplifier, losing a fraction determined by $|\Gamma_c|^2$, leading to $(1-|\Gamma_c|^2)T_{\mathrm{mode}}$. Thus, the LNA's input noise temperature T_{ns} can be defined as [99, 44]:

$$T_{\mathrm{ns}} = (T_{\mathrm{mode}} + T_{\mathrm{LNA}})(1-|\Gamma_c|^2), \tag{B.6}$$

where T_{mode} is the source noise temperature of the component propagating through the LNA. The noise temperature of the LNA is defined by:

$$T_{\mathrm{LNA}} = T_{\mathrm{min}} + 4T_0 \frac{R_n}{Z_0} \frac{|\Gamma_c - \Gamma_{\mathrm{opt}}|^2}{|1+\Gamma_{\mathrm{opt}}|^2(1-|\Gamma_c|^2)}, \tag{B.7}$$

where T_{min} is the minimum noise temperature, T_0 is the standard temperature (usually 290 K), R_n is the noise resistance, Z_0 is the characteristic impedance (usually 50 Ω), and Γ_{opt} is the optimum source reflection coefficient.

In heterodyne detection, the image noise generated by a standard mixer's intermediate frequency (IF) port at 1.3095 GHz contributes to the noise power. To evaluate the image noise temperature T_i, the reflection coefficient Γ_c equals -1 because the first LNA can be considered as being connected to the cavity but off-resonance. Thus,

$$T_i = 4T_0 \frac{R_n}{Z_0} \frac{|-1-\Gamma_{\text{opt}}|^2}{|1+\Gamma_{\text{opt}}|^2}. \tag{B.8}$$

The total noise temperature at the output of the first LNA can then be expressed as:

$$T_{\text{front-end}} = (T_{\text{LNA}} + T_{\text{mode}})(1-|\Gamma_c|^2) + T_i. \tag{B.9}$$

According to the definition of noise power, the output noise power referenced to the first LNA is:

$$P_{\text{LNA}}^{\text{O/P}} = G_{\text{LNA}} k_B B_{\text{SAW}} T_{\text{front-end}}, \tag{B.10}$$

where G_{LNA} is the gain of the LNA, k_B is Boltzmann's constant, and B_{SAW} is the bandwidth of the heterodyne receiver.

Finally, according to Friis's formula, the heterodyne receiver's output power can be expressed as:

$$P_{\text{REC}}^{\text{O/P}} = G_{\text{REC}} k_B B_{\text{SAW}} \left(G_{\text{LNA}} \left[(T_{\text{min}} + T_{\text{mode}})(1-|\Gamma_c|^2) + 4T_0 \frac{R_n}{Z_0} \frac{|\Gamma_c - \Gamma_{\text{opt}}|^2}{|1+\Gamma_{\text{opt}}|^2} + T_i \right] + T_{\text{REC}} \right), \tag{B.11}$$

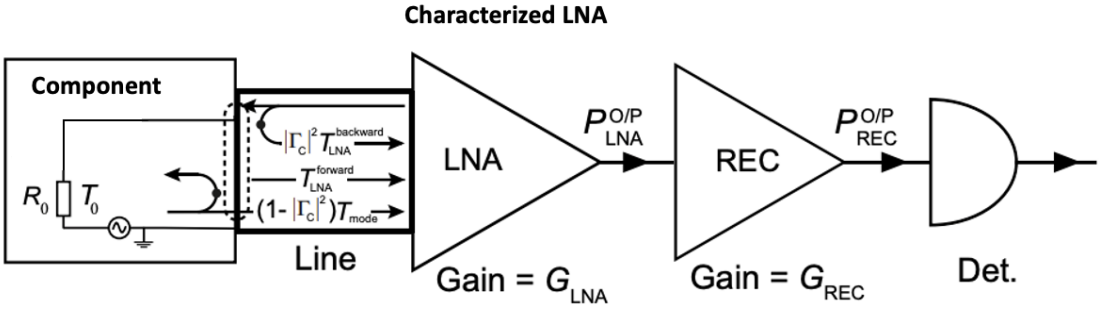

Figure B.4: Noise analysis using the wave-approach method to characterize the LNA's noise parameters with heterodyne detection [44].

where G_{REC} is the gain of the receiver and T_{REC} is the receiver's noise temperature.

Finally, according to the Friis formula, the heterodyne receiver's output power can be expressed as

$$P_{\mathrm{REC}}^{\mathrm{O/P}} = G_{\mathrm{REC}} k_B B_{\mathrm{SAW}} \left(G_{\mathrm{LNA}} \left[(T_{\mathrm{min}} + T_{\mathrm{mode}})(1 - |\Gamma_c|^2) + 4T_0 \frac{R_n}{Z_0} \frac{|\Gamma_c - \Gamma_{\mathrm{opt}}|^2}{|1 + \Gamma_{\mathrm{opt}}|^2} + T_i \right] + T_{\mathrm{REC}} \right) \tag{B.12}$$

B.2.1 OSL Y-Factor Method for Measuring Noise Parameters

The noise parameters, including the minimum noise figure F_{min}, noise resistance R_n, and optimum reflection coefficient Γ_{opt} (magnitude and phase), are crucial for analyzing the performance of low-noise amplifiers (LNAs). To determine these four noise parameters, I need to measure the device under four different conditions. The Open-Short-Load (OSL) measurement combined with the Y-factor method is an effective technique for measuring the noise parameters of an LNA by applying non-linear regression to the equations derived previously.

According to Eq. (B.12), if a short circuit is connected to the LNA input, the source reflection coefficient is $\Gamma_c = -1$. Therefore, the output power is defined as:

$$P_{\mathrm{Short}}^{\mathrm{O/P}} = G_{\mathrm{REC}} k_B B_{\mathrm{SAW}} \left(G_{\mathrm{LNA}} \left[4T_0 \frac{R_n}{Z_0} \frac{|-1 - \Gamma_{\mathrm{opt}}|^2}{|1 + \Gamma_{\mathrm{opt}}|^2} + T_i \right] + T_{\mathrm{REC}} \right) \tag{B.13}$$

Similarly, if an open circuit is connected to the LNA input, the source reflection coefficient is $\Gamma_c = 1$. Therefore, the output power is defined as:

$$P_{\mathrm{Open}}^{\mathrm{O/P}} = G_{\mathrm{REC}} k_B B_{\mathrm{SAW}} \left(G_{\mathrm{LNA}} \left[4T_0 \frac{R_n}{Z_0} \frac{|1 - \Gamma_{\mathrm{opt}}|^2}{|1 + \Gamma_{\mathrm{opt}}|^2} + T_i \right] + T_{\mathrm{REC}} \right) \tag{B.14}$$

If a hot $50\,\Omega$ load is connected to the LNA's input, then $\Gamma_c = 0$. Therefore, the output power is defined as:

$$P^{\mathrm{O/P}}_{\mathrm{Hot\,Load}} = G_{\mathrm{REC}} k_B B_{\mathrm{SAW}} \left(G_{\mathrm{LNA}} \left[T_{\mathrm{min}} + T_0 + 4T_0 \frac{R_n}{Z_0} \frac{|-\Gamma_{\mathrm{opt}}|^2}{|1+\Gamma_{\mathrm{opt}}|^2} + T_i \right] + T_{\mathrm{REC}} \right) \tag{B.15}$$

If a cold $50\,\Omega$ load is connected to the LNA's input, then $\Gamma_c = 0$. Therefore, the output power is defined as:

$$P^{\mathrm{O/P}}_{\mathrm{Cold\,Load}} = G_{\mathrm{REC}} k_B B_{\mathrm{SAW}} \left(G_{\mathrm{LNA}} \left[T_{\mathrm{min}} + T_{\mathrm{Cold}} + 4T_0 \frac{R_n}{Z_0} \frac{|-\Gamma_{\mathrm{opt}}|^2}{|1+\Gamma_{\mathrm{opt}}|^2} + T_i \right] + T_{\mathrm{REC}} \right) \tag{B.16}$$

From Eqs. (B.13)–(B.16), I can solve for the four noise parameters by considering the power differences between the different measurement conditions:

$$\Delta P^{\mathrm{O/P}}_{\mathrm{S/O}} = \frac{P^{\mathrm{O/P}}_{\mathrm{Short}}}{P^{\mathrm{O/P}}_{\mathrm{Open}}} = \frac{G_{\mathrm{LNA}} \left[4T_0 \frac{R_n}{Z_0} \frac{2|-1-\Gamma_{\mathrm{opt}}|^2}{|1+\Gamma_{\mathrm{opt}}|^2} \right] + T_{\mathrm{REC}}}{G_{\mathrm{LNA}} \left[4T_0 \frac{R_n}{Z_0} \frac{|1-\Gamma_{\mathrm{opt}}|^2 + |-1-\Gamma_{\mathrm{opt}}|^2}{|1+\Gamma_{\mathrm{opt}}|^2} \right] + T_{\mathrm{REC}}} \tag{B.17}$$

$$\Delta P^{\mathrm{O/P}}_{\mathrm{S/HL}} = \frac{P^{\mathrm{O/P}}_{\mathrm{Short}}}{P^{\mathrm{O/P}}_{\mathrm{Hot\,Load}}} = \frac{G_{\mathrm{LNA}} \left[4T_0 \frac{R_n}{Z_0} \frac{2|-1-\Gamma_{\mathrm{opt}}|^2}{|1+\Gamma_{\mathrm{opt}}|^2} \right] + T_{\mathrm{REC}}}{G_{\mathrm{LNA}} \left[T_{\mathrm{min}} + T_{\mathrm{Hot}} + 4T_0 \frac{R_n}{Z_0} \frac{|-\Gamma_{\mathrm{opt}}|^2 + |-1-\Gamma_{\mathrm{opt}}|^2}{|1+\Gamma_{\mathrm{opt}}|^2} \right] + T_{\mathrm{REC}}} \tag{B.18}$$

$$\Delta P^{\mathrm{O/P}}_{\mathrm{O/HL}} = \frac{P^{\mathrm{O/P}}_{\mathrm{Open}}}{P^{\mathrm{O/P}}_{\mathrm{Hot\,Load}}} = \frac{G_{\mathrm{LNA}} \left[4T_0 \frac{R_n}{Z_0} \frac{|1-\Gamma_{\mathrm{opt}}|^2 + |-1-\Gamma_{\mathrm{opt}}|^2}{|1+\Gamma_{\mathrm{opt}}|^2} \right] + T_{\mathrm{REC}}}{G_{\mathrm{LNA}} \left[T_{\mathrm{min}} + T_{\mathrm{Hot}} + 4T_0 \frac{R_n}{Z_0} \frac{|-\Gamma_{\mathrm{opt}}|^2 + |-1-\Gamma_{\mathrm{opt}}|^2}{|1+\Gamma_{\mathrm{opt}}|^2} \right] + T_{\mathrm{REC}}} \tag{B.19}$$

$$\Delta P_{\mathrm{HL/CL}}^{\mathrm{O/P}} = \frac{P_{\mathrm{Hot\,Load}}^{\mathrm{O/P}}}{P_{\mathrm{Cold\,Load}}^{\mathrm{O/P}}} = \frac{G_{\mathrm{LNA}}\left[T_{\mathrm{min}} + T_{\mathrm{Hot}} + 4T_0\frac{R_n}{Z_0}\frac{|-\Gamma_{\mathrm{opt}}|^2 + |-1-\Gamma_{\mathrm{opt}}|^2}{|1+\Gamma_{\mathrm{opt}}|^2}\right] + T_{\mathrm{REC}}}{G_{\mathrm{LNA}}\left[T_{\mathrm{min}} + T_{\mathrm{Cold}} + 4T_0\frac{R_n}{Z_0}\frac{|-\Gamma_{\mathrm{opt}}|^2 + |-1-\Gamma_{\mathrm{opt}}|^2}{|1+\Gamma_{\mathrm{opt}}|^2}\right] + T_{\mathrm{REC}}} \tag{B.20}$$

Here, $\Delta P_{\mathrm{S/O}}^{\mathrm{O/P}}$ is the power ratio between the short and open conditions, $\Delta P_{\mathrm{S/HL}}^{\mathrm{O/P}}$ is the power ratio between the short and hot load conditions, $\Delta P_{\mathrm{O/HL}}^{\mathrm{O/P}}$ is the power ratio between the open and hot load conditions, and $\Delta P_{\mathrm{HL/CL}}^{\mathrm{O/P}}$ is the power ratio between the hot load and cold load conditions.

By measuring these power ratios, I can solve the system of equations to determine the noise parameters T_{min}, R_n, and Γ_{opt}.

B.2.2 Setup of Heterodyne Detection for Noise Parameter Measurement and Calibration

To measure the output noise from the characterized LNA, I used a sensitive superheterodyne receiver, as shown in Fig. B.5 [264]. It uses a cascade of amplifiers (total gain around 100 dB) to achieve sufficient sensitivity. The output is fed into a logarithmic detector (Pascall, SDB-7040) through a narrow-bandpass SAW filter centered at 70 MHz, with a steep-skirted 1.25 MHz bandwidth. Furthermore, I characterized a Qorvo QPL9547 wideband HEMT LNA using the OSL Y-factor method. Following the OSL Y-factor method described in Section 2.1.3, I used calibration kits (open, short, and 50 Ω load) and a load soaked in liquid nitrogen, as shown in Fig. B.6. Additionally, to eliminate irrelevant noise from the signal path, various filters—high-pass filter (HPF), low-pass filter (LPF), and band-pass filter (BPF)—were inserted. Finally, the noise detected by the logarithmic detector was read by a precision voltmeter, as shown in Fig. B.6.

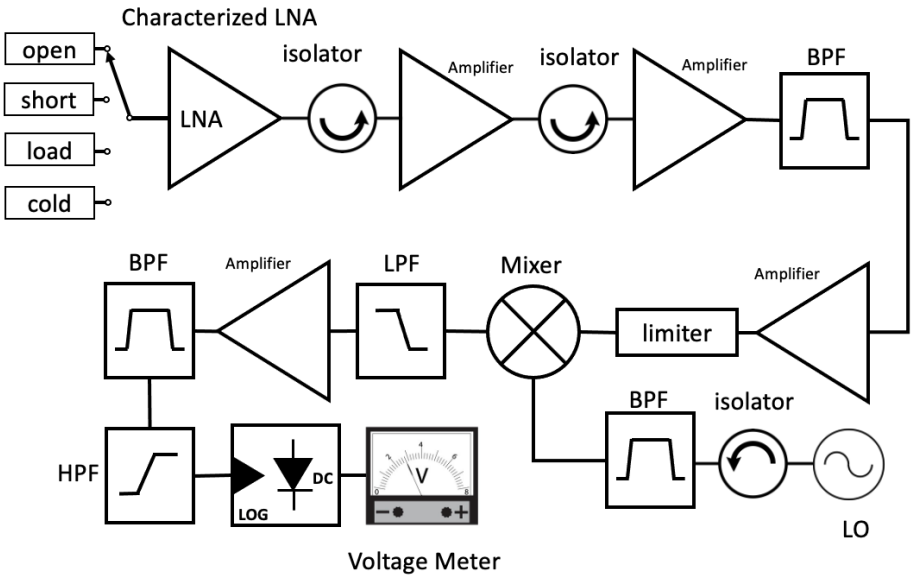

Figure B.5: Block diagram of the heterodyne detection setup for LNA characterization. The characterized LNA is connected to a heterodyne receiver and analyzed using a voltmeter with a logarithmic detector. Using the OSL Y-factor method, the LNA is connected among open, short, 50 Ω load, and cold 50 Ω load to collect data under four different conditions to solve the non-linear equations.

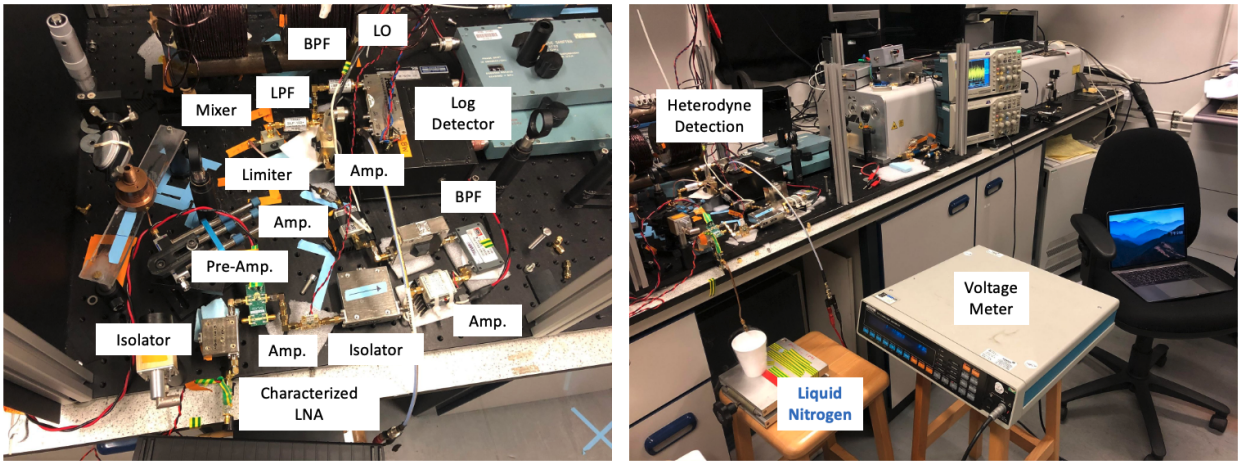

Figure B.6: Setup of the heterodyne detection for LNA characterization. Left: The heterodyne detection setup. Right: The cold 50 Ω load soaked in a cup of liquid nitrogen.

B.2.3 Markov Chain Monte Carlo for Noise Parameter Model Fitting

In the previous section, I set up a heterodyne detection system to measure the noise parameters of the LNA. However, there are two significant sources of measurement error: (1) measuring the noise temperature of the LNA at room temperature, and (2) using a conventional voltmeter for measurements. These errors make the model difficult to fit with high precision. Thus, I employed a noise-cancellation method called the Markov Chain Monte Carlo (MCMC) method to fit the model in the presence of these measurement errors.

First, I used the Levenberg–Marquardt method to solve the non-linear functions shown in Section 2.1.3, taking the result as an initial value for the next step, as illustrated in Fig. B.7. Next, I applied a phase shifter connected with calibration kits to collect more data points for model fitting. Then, I adopted the MCMC method, using random numbers to simulate measurement errors that encompass all measurement errors in my data, as shown in Fig. B.8. Using the data processed by the MCMC method, I generated a prior distribution of parameters using an appropriate function. Then, based on the proposed distribution, I calculated the probability of a proposed value from the random initial state, as shown in Fig. B.9. After calculating the proposed parameters based on previous values, I computed the likelihood of the proposed parameters from the measured data with the generated random values. Finally, if the result satisfies the convergence condition, I obtain the estimated parameters with standard deviation information. Otherwise, the loop continues to iterate until convergence is achieved [265].

After applying the MCMC method to calibrate the noise parameters of the LNA (QPL9547), I obtained the results shown in Fig. B.10. The noise parameters are almost the same as those in the specification sheet. Although the optimum reflection coefficient Γ_{opt} has slight differences due to the coplanar waveguide (CPW) package, the noise resistance and minimum noise temperature are shown in Table B.2.

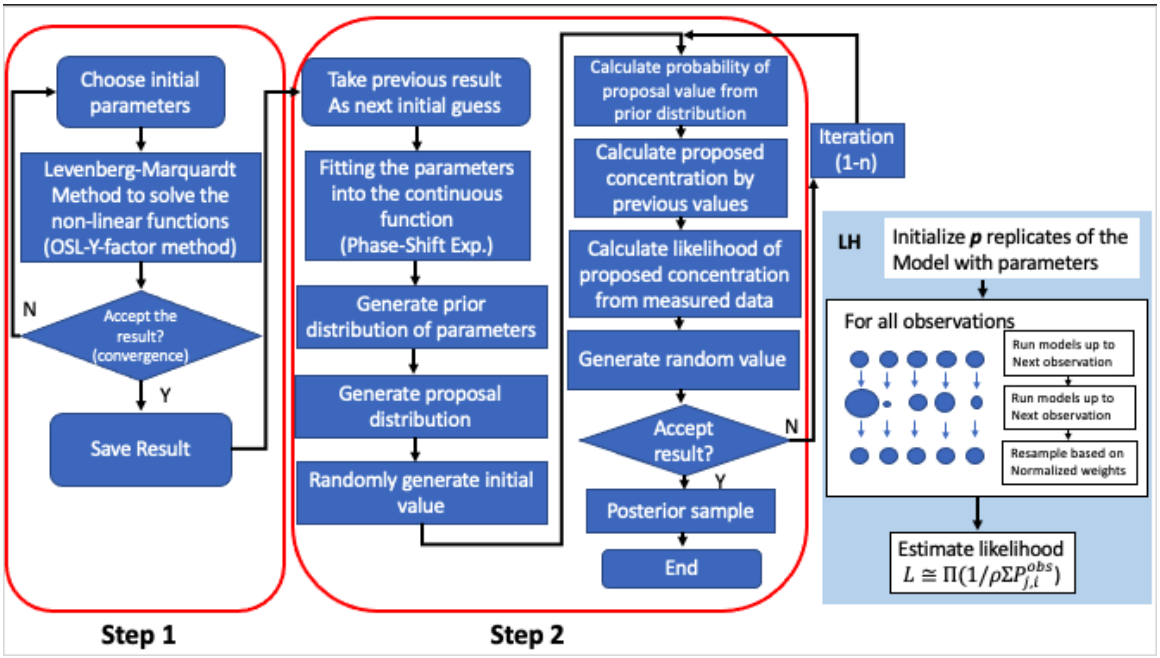

Figure B.7: Flow chart of the MCMC method for noise parameter model fitting.

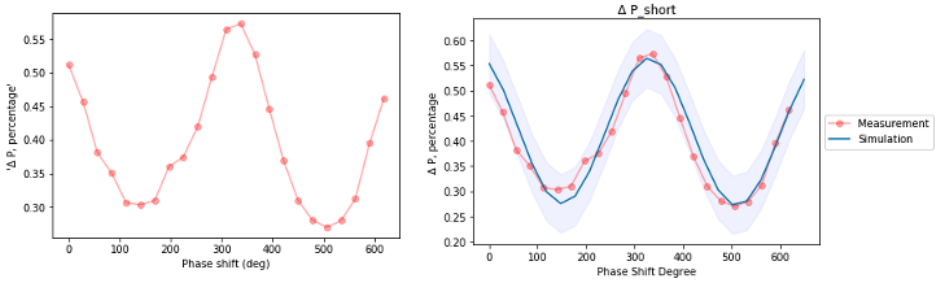

Figure B.8: Raw data measurement with phase shifter from 0 to 650° and initial curve fitting using the Levenberg–Marquardt method.

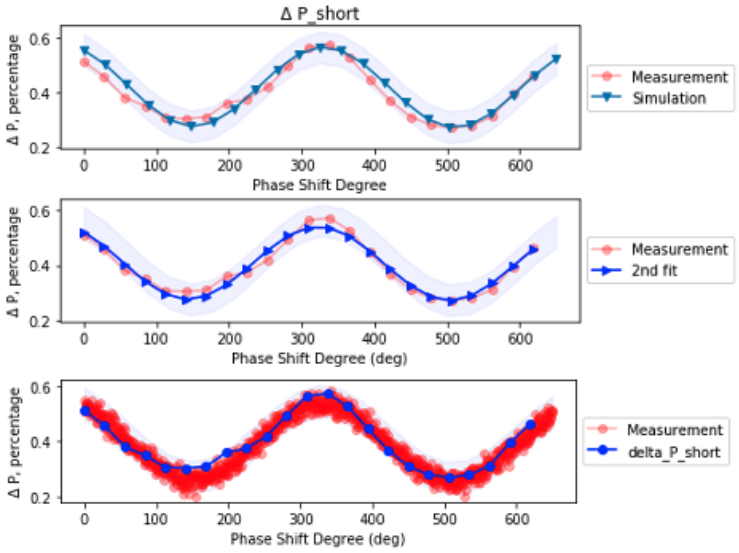

Figure B.9: The fitting process of the MCMC method.

Table B.2: Results of the Noise Parameter Characterization for QPL9547

Parameter	**Value**	**STD**	**Error (%)**	**Datasheet**
Γ_{opt} (mag)	0.303	±0.0016	0.54%	0.18
Γ_{opt} (deg)	233.6	±0.2624	0.11%	178
R_n	1.822	±0.2668	14.64%	1.5
T_{min}	18.97	±0.6955	3.67%	19.1

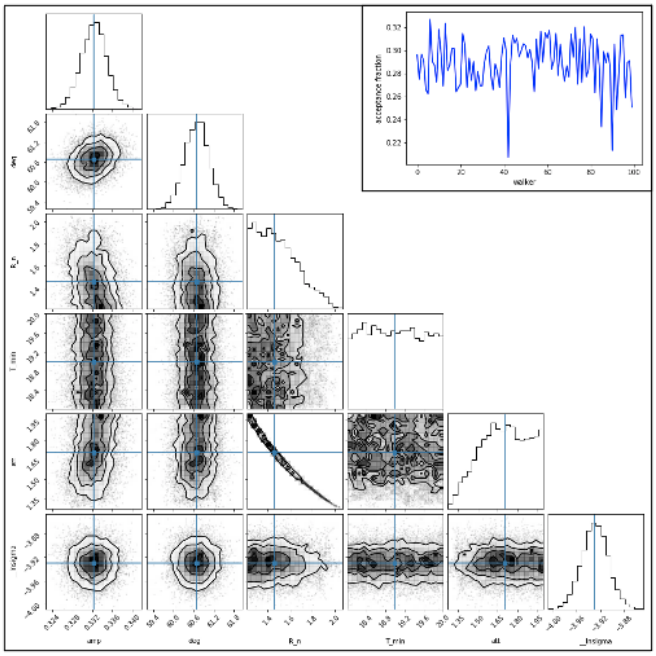

Figure B.10: Corner plot showing the relationships between noise parameters obtained using the MCMC method.

Appendix C

Pulse EPR Data Fitting for BDPA in OTP in Different Conditions

C.1 Fitting of Rabi Oscillation in Different Conditions

In this study, I analyzed Rabi oscillations at room temperature under various microwave attenuation levels (0 dB, -1.4 dB, -3.1 dB, -8 dB, and -12 dB) using pulsed EPR measurements. The data were processed by first loading the time-domain nutation data and then detrending the real part of the Rabi signals by subtracting their mean value. This detrending step was essential to remove any DC offset that could distort the fitting. Each signal was subsequently fitted to a damped sinusoidal function, defined as $y(t) = A\exp(-\lambda t)\sin(2\pi f t + \phi) + s$, where A is the amplitude, λ is the decay rate, f is the Rabi frequency, ϕ is the phase, and s is the offset. The initial guesses for the fitting parameters were based on the observed number of cycles and the maximum nutation pulse length for each dataset. The least-squares fitting procedure provided precise estimates of the Rabi frequencies, which were then normalized for comparison across different power levels.

To further analyze the frequency components of the Rabi oscillations, I performed a Fast Fourier Transform (FFT) on the detrended signals. The signals were zero-padded (with 1000 points) to increase frequency resolution, and the resulting FFT spectra were normalized. The

frequency domain axis was calculated using the time step from the time-domain data. The normalized FFT spectra, plotted against the Rabi frequency shifts in MHz, clearly showed the peak frequencies corresponding to the Rabi oscillations. Additionally, the relationship between the Rabi frequency and the normalized microwave power was examined using a log-log plot. The data points were fitted with a power-law dependence, indicating the expected scaling behavior.

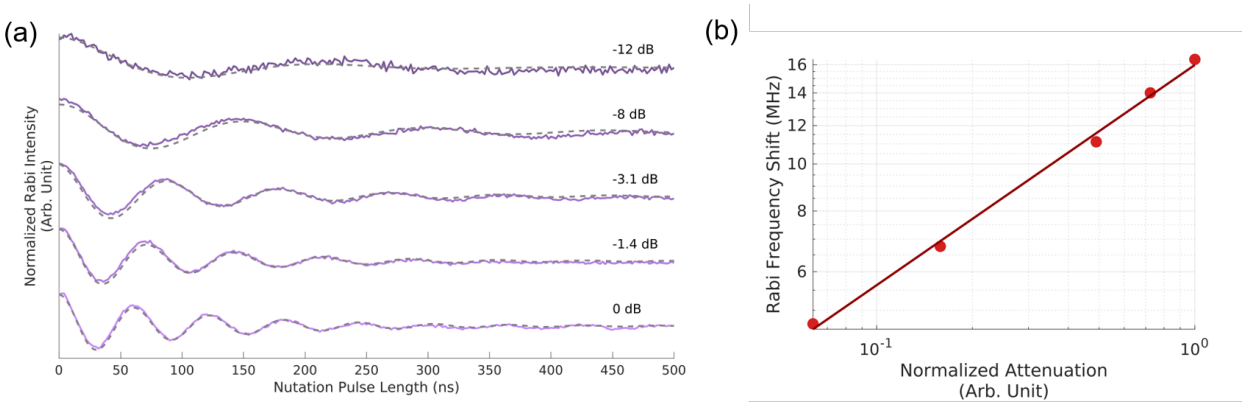

Figure C.1: Rabi oscillation experiments conducted at 300 K on 0.1% BDPA doped o-terphenyl in the solid phase. (a) Normalized Rabi intensity as a function of nutation pulse length for various attenuation levels (0 dB to -12 dB). The grey dashed lines represent the fitting curves. (b) Linear relationship between Rabi frequency shift and normalized attenuation, highlighting the proportional increase in Rabi frequency with decreasing attenuation.

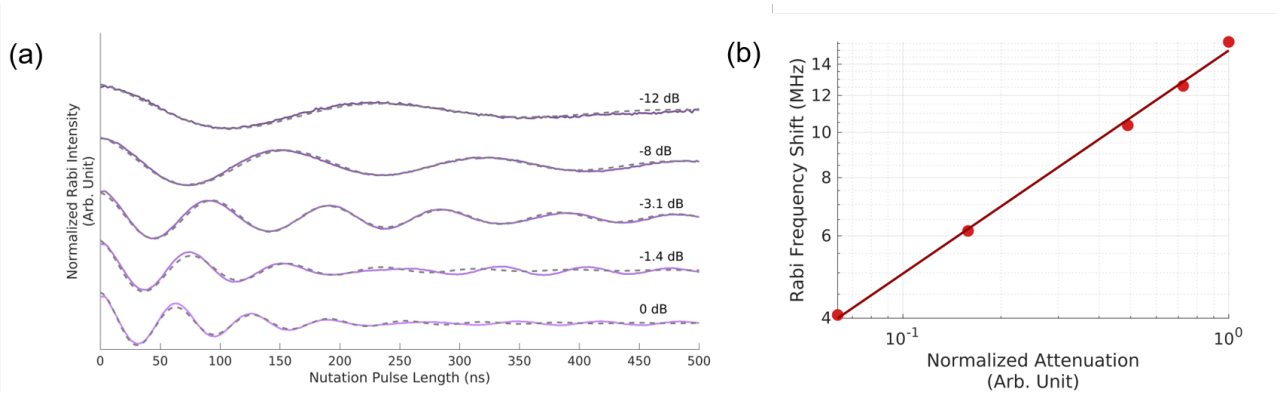

Figure C.2: Rabi oscillation experiments conducted at 200 K on 0.1% BDPA doped o-terphenyl in the solid phase. (a) Normalized Rabi intensity as a function of nutation pulse length for various attenuation levels (0 dB to -12 dB). The grey dashed lines represent the fitting curves. (b) Linear relationship between Rabi frequency shift and normalized attenuation, highlighting the proportional increase in Rabi frequency with decreasing attenuation.

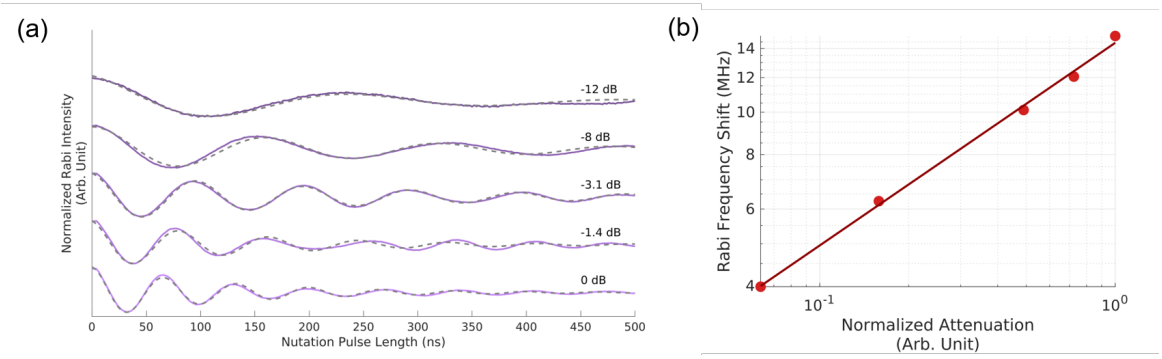

Figure C.3: Rabi oscillation experiments conducted at 150 K on 0.1% BDPA doped o-terphenyl in the solid phase. (a) Normalized Rabi intensity as a function of nutation pulse length for various attenuation levels (0 dB to -12 dB). The grey dashed lines represent the fitting curves. (b) Linear relationship between Rabi frequency shift and normalized attenuation, highlighting the proportional increase in Rabi frequency with decreasing attenuation.

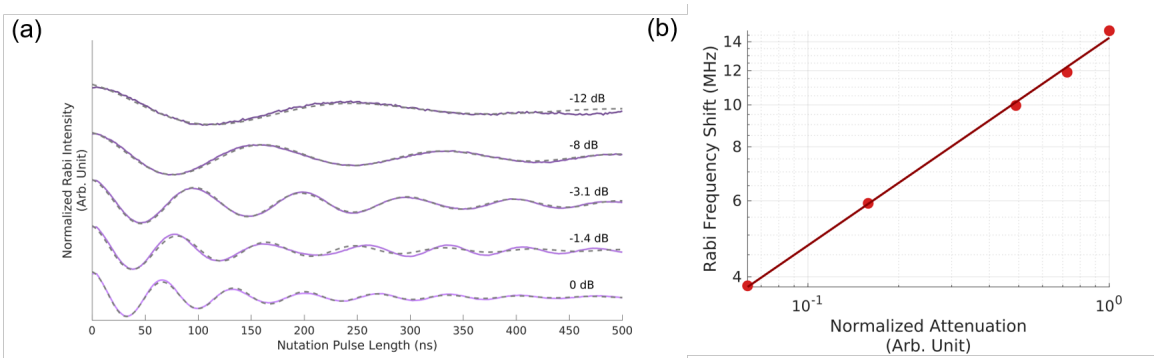

Figure C.4: Rabi oscillation experiments conducted at 70 K on 0.1% BDPA doped o-terphenyl in the solid phase. (a) Normalized Rabi intensity as a function of nutation pulse length for various attenuation levels (0 dB to -12 dB). The grey dashed lines represent the fitting curves. (b) Linear relationship between Rabi frequency shift and normalized attenuation, highlighting the proportional increase in Rabi frequency with decreasing attenuation.

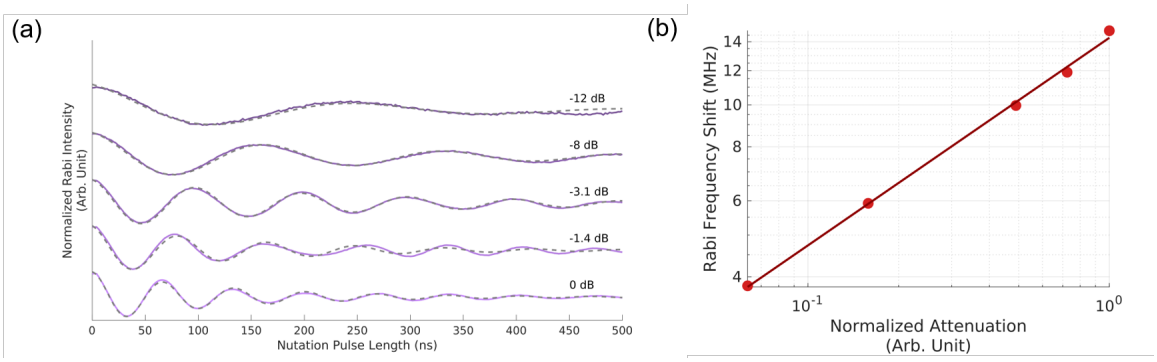

Figure C.5: Rabi oscillation experiments conducted at 5 K on 0.1% BDPA doped o-terphenyl in the solid phase. (a) Normalized Rabi intensity as a function of nutation pulse length for various attenuation levels (0 dB to -12 dB). The grey dashed lines represent the fitting curves. (b) Linear relationship between Rabi frequency shift and normalized attenuation, highlighting the proportional increase in Rabi frequency with decreasing attenuation.

Room Temperature (300K) - Solid Phase

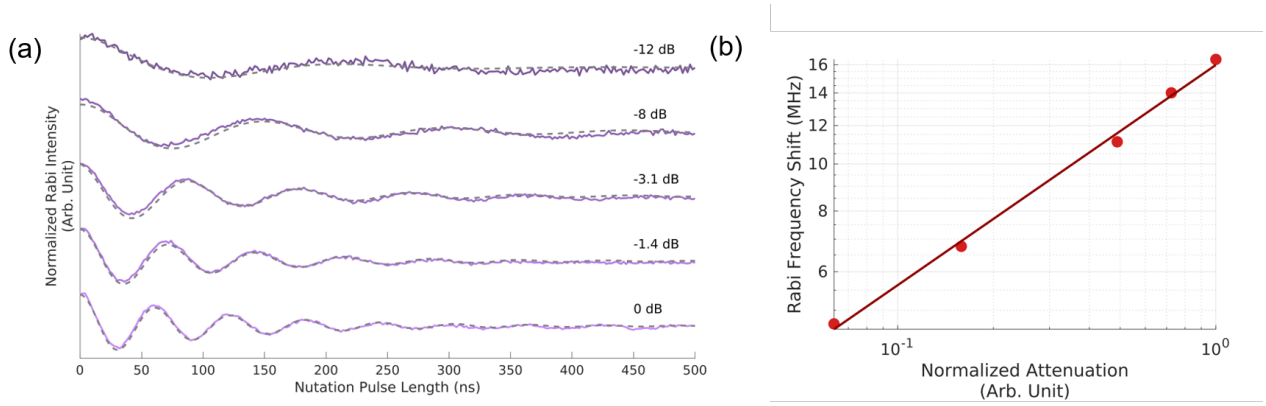

Figure C.6: Rabi oscillation experiments conducted at 300 K on 0.1% BDPA doped o-terphenyl in the solid phase. (a) Normalized Rabi intensity as a function of nutation pulse length for various attenuation levels (0 dB to -12 dB). The grey dashed lines represent the fitting curves. (b) Linear relationship between Rabi frequency shift and normalized attenuation, highlighting the proportional increase in Rabi frequency with decreasing attenuation.

Room Temperature (300K) - Liquid Phase

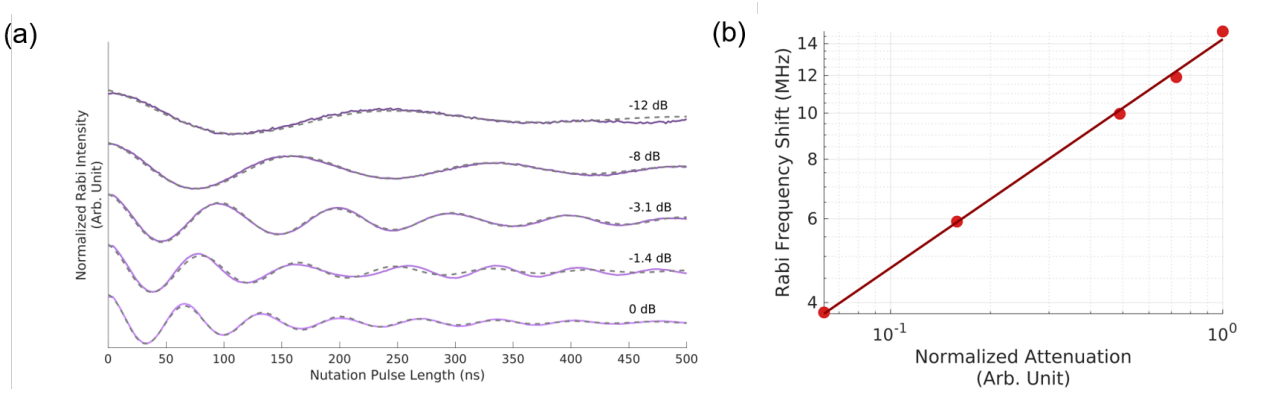

Figure C.7: Rabi oscillation experiments conducted at 300 K on 0.1% BDPA doped o-terphenyl in the liquid phase. (a) Normalized Rabi intensity as a function of nutation pulse length for various attenuation levels (0 dB to -12 dB). The grey dashed lines represent the fitting curves. (b) Linear relationship between Rabi frequency shift and normalized attenuation, highlighting the proportional increase in Rabi frequency with decreasing attenuation.

Appendix D

Quantum Metrology with Single-Strain Coupling in D_{2h} Group

D.1 Single-Strain Coupling in D2h Group

Pentacene molecules, when integrated as defects in thin films, exhibit remarkable spin dynamics suitable for high-precision sensing applications, particularly in zero-field environments where external magnetic fields are absent [249]. To harness these properties for spin-acoustic resonance experiments, a rigorous understanding of the ground-state spin Hamiltonian is essential. This requires a comprehensive, fully relativistic, multi-electron derivation that incorporates both spin-orbit (SO) and spin-spin (SS) interactions within the frameworks of quantum mechanics and group theory.

Pentacene belongs to the D_{2h} point group [266], characterized by high symmetry with multiple mirror planes, inversion centers, and two-fold rotational axes. This symmetry allows for the classification of molecular orbitals and spin states using group theoretical methods, significantly simplifying the derivation of the spin Hamiltonian by reducing the number of independent parameters and highlighting the allowed interactions[267].

The total spin Hamiltonian, incorporating SS and SO interactions as well as interactions with

external perturbations such as acoustic phonons, is expressed as:

$$\hat{H} = \hat{H}_{\text{ZFS}} + \hat{H}_{\text{SO}} + \hat{H}_{\text{strain}}, \tag{D.1}$$

where $\hat{H}_{\text{ZFS}}$ represents the zero-field splitting due to SS interactions, $\hat{H}_{\text{SO}}$ accounts for the SO coupling, and $\hat{H}_{\text{strain}}$ includes the spin-strain coupling due to external perturbations.

The ZFS arises from magnetic dipole-dipole interactions between unpaired electron spins and is given by:

$$\hat{H}_{\text{ZFS}} = D\left(\hat{S}_z^2 - \frac{1}{3}S(S+1)\right) + E\left(\hat{S}_x^2 - \hat{S}_y^2\right), \tag{D.2}$$

where D and E are the axial and rhombic ZFS parameters, respectively, and $\hat{\mathbf{S}} = (\hat{S}_x, \hat{S}_y, \hat{S}_z)$ is the spin operator for $S = 1$. For pentacene, experimental measurements yield $D = 1400\,\text{MHz}$ and $E = 50\,\text{MHz}$ [249], reflecting significant anisotropy in the electron spin interactions due to the molecular structure.

The spin-orbit interaction couples an electron's spin with its orbital angular momentum in the electric field of the nuclei. The SO Hamiltonian for a multi-electron system like pentacene can be expressed as:

$$\hat{H}_{\text{SO}} = \sum_i \xi_i \, \hat{\mathbf{L}}_i \cdot \hat{\mathbf{S}}_i, \tag{D.3}$$

where ξ_i is the SO coupling constant for the i-th electron, and $\hat{\mathbf{L}}_i$ and $\hat{\mathbf{S}}_i$ are the orbital and spin angular momentum operators of the i-th electron, respectively. In the context of pentacene, the SO coupling is relatively weak due to its light atomic constituents (carbon and hydrogen); however, it plays a crucial role in mixing spin states and enabling certain relaxation pathways.

The interaction with external perturbations, such as acoustic phonons, is captured by the spin-strain coupling Hamiltonian $\hat{H}_{\text{strain}}$. In a crystalline environment, strain modifies the electronic

energy levels and spin interactions. The spin-strain Hamiltonian is derived using symmetry-adapted forms based on the D_{2h} point group.

In D_{2h} symmetry, both the strain tensor components ε_{ij} and the spin operators $\hat{S}_i$ can be classified according to irreducible representations [268]. The strain components ε_{xx}, ε_{yy}, and ε_{zz} transform as A_g (the totally symmetric representation), while ε_{xy}, ε_{xz}, and ε_{yz} transform as B_{1g}, B_{2g}, and B_{3g}, respectively. Similarly, the bilinear spin operator products $\hat{S}_i\hat{S}_j$ transform according to these irreducible representations.

The spin-strain Hamiltonian must be invariant under all symmetry operations of the D_{2h} group. Therefore, only products of strain components and spin operators that result in the A_g representation are allowed[253]. The spin-strain Hamiltonian is then given by:

$$\begin{aligned}\hat{H}_{\text{strain}} = & g_1(\varepsilon_{xx}+\varepsilon_{yy}+\varepsilon_{zz})(\hat{S}_x^2+\hat{S}_y^2+\hat{S}_z^2-S(S+1)) \\ & + g_2(\varepsilon_{xx}-\varepsilon_{yy})(\hat{S}_x^2-\hat{S}_y^2)+g_3\varepsilon_{xy}(\hat{S}_x\hat{S}_y+\hat{S}_y\hat{S}_x) \\ & + g_4\varepsilon_{xz}(\hat{S}_x\hat{S}_z+\hat{S}_z\hat{S}_x)+g_5\varepsilon_{yz}(\hat{S}_y\hat{S}_z+\hat{S}_z\hat{S}_y),\end{aligned} \tag{D.4}$$

where g_i are the spin-strain coupling coefficients specific to pentacene.

For the $S=1$ system, the term $\hat{S}_x^2+\hat{S}_y^2+\hat{S}_z^2 = S(S+1) = 2$, making the first term involving g_1 vanish. Therefore, the spin-strain Hamiltonian simplifies to:

$$\begin{aligned}\hat{H}_{\text{strain}} = & g_2(\varepsilon_{xx}-\varepsilon_{yy})(\hat{S}_x^2-\hat{S}_y^2)+g_3\varepsilon_{xy}(\hat{S}_x\hat{S}_y+\hat{S}_y\hat{S}_x) \\ & + g_4\varepsilon_{xz}(\hat{S}_x\hat{S}_z+\hat{S}_z\hat{S}_x)+g_5\varepsilon_{yz}(\hat{S}_y\hat{S}_z+\hat{S}_z\hat{S}_y).\end{aligned} \tag{D.5}$$

Under zero-field conditions and considering only the dominant terms, the total spin Hamiltonian becomes:

$$\hat{H} = D\left(\hat{S}_z^2-\frac{1}{3}S(S+1)\right)+E\left(\hat{S}_x^2-\hat{S}_y^2\right)+\hat{H}_{\text{strain}}. \tag{D.6}$$

Acoustic phonons induce strain in the lattice, modulating the electronic environment and,

consequently, the spin interactions. The strain tensor components ε_{ij} associated with acoustic phonons can be expressed in terms of phonon creation and annihilation operators. The high symmetry of the D_{2h} point group imposes selection rules on the spin-phonon interactions. Only phonon modes transforming according to the same irreducible representations as the spin operator products in $\hat{H}_{\text{strain}}$ can couple to the spin states.

Phonons transforming as B_{1g} (shear strain in the xy-plane) couple to $(\hat{S}_x^2 - \hat{S}_y^2)$ and $(\hat{S}_x\hat{S}_y + \hat{S}_y\hat{S}_x)$. Phonons transforming as B_{2g} and B_{3g} couple to $(\hat{S}_x\hat{S}_z + \hat{S}_z\hat{S}_x)$ and $(\hat{S}_y\hat{S}_z + \hat{S}_z\hat{S}_y)$, respectively.

Spin-acoustic resonance occurs when the energy splitting between spin sublevels matches the energy of the acoustic phonons, allowing for coherent transitions driven by lattice vibrations without external magnetic fields. The resonance condition is given by:

$$\hbar\omega_{\text{phonon}} = E_{\text{spin}}, \tag{D.7}$$

where E_{spin} is the energy difference between spin states (e.g., between $m_S = 0$ and $m_S = \pm 1$).

The coupling coefficients g_i quantify the sensitivity of the spin system to strain and are given by:

$$g_i = \frac{\partial D_{\text{ZFS}}^{(i)}}{\partial \varepsilon_{ij}}, \tag{D.8}$$

where $D_{\text{ZFS}}^{(i)}$ represents the relevant component of the ZFS tensor affected by the strain ε_{ij}. These coefficients can be calculated using first-order perturbation theory and electronic structure methods, taking into account the change in electronic energies due to strain.

To calculate the coupling coefficients, I consider the perturbation of the ZFS parameters due to applied strain. The changes in the ZFS tensor components δD_{ij} are expressed as:

$$\delta D_{ij} = \sum_k \frac{\partial D_{ij}}{\partial \varepsilon_{kl}} \varepsilon_{kl}. \tag{D.9}$$

By applying a uniform strain corresponding to each non-equivalent strain tensor component and computing the resulting changes in the ZFS parameters, I can extract the values of the coupling coefficients g_i.

To incorporate the SO interaction into the ground-state wave function, I employ first-order perturbation theory:

$$\psi_{\mathrm{GS}} = \psi_0 + \sum_j \frac{\langle \psi_j | \hat{H}_{\mathrm{SO}} | \psi_0 \rangle}{E_0 - E_j} \psi_j, \tag{D.10}$$

where ψ_0 is the unperturbed ground-state wave function, ψ_j are excited-state wave functions, and E_0 and E_j are the energies of the ground and excited states, respectively. The SO interaction mixes the ground state with excited states of appropriate symmetry, modifying the spin properties and contributing to relaxation processes.

By understanding the spin-strain coupling mechanisms and quantifying the coupling coefficients, I can predict the conditions under which spin-acoustic resonance is most efficient. This knowledge enables the design of experiments to manipulate spin states using acoustic phonons and enhances the sensitivity of quantum sensors based on pentacene thin films.

The effective Hamiltonian governing the spin dynamics in the presence of acoustic phonons allows us to model spin transition rates and coherence properties. Spin transition rates are determined by the strength of the spin-phonon coupling and the phonon density of states, while coherence properties are influenced by spin relaxation and decoherence mechanisms, which are affected by lattice vibrations. This thesis focuses on the experimental aspects of spin-acoustic coupling. The simulation and theoretical exploration will be presented in the future.

Appendix E

Simulation for Electromagnetic Effect in the System

We employed COMSOL Multiphysics[127], a finite-element analysis software, to simulate the electromagnetic fields around the pentacene sample. My primary focus was on the magnetic field to rule out the possibility of spin-photon interactions mediated by the magnetic field. We adopted the method introduced by Xu *et al.*[252].

The simulation targeted the Rayleigh mode and concentrated on the area covered by the sample. As illustrated in Fig. E.1(a), the computational domain was divided into two regions by the surface of the lithium niobate substrate: an internal space representing the substrate and an external space representing the region above it. Two *Block*s (COMSOL terminology is italicized throughout), each with dimensions of 32 μm (width), 10 μm (depth), and 95 μm (height), were used to model these spaces. The substantial height was necessary to accommodate the transverse evanescent fields.

The external space was further partitioned to represent the pentacene sample and the surrounding air. Specifically, a *Block* with dimensions of 32 μm $\times$ 10 μm $\times$ 1 μm represented the pentacene sample. The mesh strategy is depicted in Fig. E.1(a). A *Free Quad* mesh was applied to the surfaces to ensure accurate field resolution.

The simulation results are presented in Fig. E.1, showing (b) the displacement field, (c) the electric field, and (d) the magnetic field around the pentacene sample. Deformation is added to the displacement field for visualization purposes.

To quantify the coupling coefficient η, I integrated the energy densities to calculate the total energy of each field component. The coupling coefficient is defined as

$$\eta = \frac{E_{\text{mag}}^{\text{ext}}}{E_{\text{ela}}^{\text{int}} + E_{\text{kin}}^{\text{int}} + E_{\text{ele}}^{\text{int}} + E_{\text{mag}}^{\text{int}} + E_{\text{ele}}^{\text{ext}} + E_{\text{mag}}^{\text{ext}}} = 5.07 \times 10^{-12}, \tag{E.1}$$

where $E_{\text{mag}}^{\text{ext}}$ is the magnetic energy in the external region, $E_{\text{ela}}^{\text{int}}$ is the elastic energy, $E_{\text{kin}}^{\text{int}}$ is the kinetic energy, $E_{\text{ele}}^{\text{int}}$ is the electric energy, and $E_{\text{mag}}^{\text{int}}$ is the magnetic energy in the internal region.

This negligible value of η indicates that the coupling between the pentacene sample and the magnetic field generated by the SAW device is insignificant, effectively ruling out the possibility of spin-photon interaction via the magnetic field.

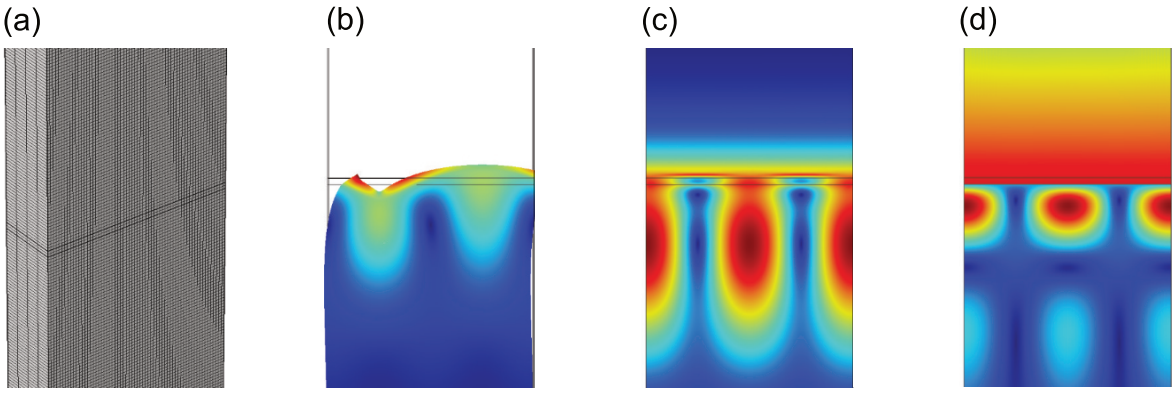

Figure E.1: (a) Schematic illustration of the simulation geometry with the used mesh showing the pentacene sample on the lithium niobate substrate. The corresponding simulation results are depicted in the subsequent three figures: (a) the displacement field, (b) the electric field, and (c) the magnetic field around the pentacene sample. Deformation is added to the displacement field for visualization purposes. [The simulation and calculation in the Appendix E are done by Xiaotian Xu.]

Bibliography

[1] Rüdiger-A Eichel and Arthur Schweiger. Electron-zeeman resolved electron paramagnetic resonance spectroscopy. *Journal of Magnetic Resonance*, 152(2):276–287, 2001.

[2] Tomoko Ohnishi. Iron–sulfur clusters/semiquinones in complex i. *Biochimica et Biophysica Acta (BBA)-Bioenergetics*, 1364(2):186–206, 1998.

[3] Erinn van Wynsberghe and Ayse Turak. Candidate materials as gain media in organic, triplet-based, room-temperature masers targeting the ism bands. *Optoelectronics: Advanced Device Structures*, page 211, 2017.

[4] Zurich Instruments. Principles of lock-in detection. `https://www.zhinst.com/europe/en/resources/principles-of-lock-in-detection#x1-10003r15`, 2022. Accessed on January 17, 2022.

[5] Christian Hintze, Ulrich E Steiner, and Malte Drescher. Photoexcited triplet state kinetics studied by electron paramagnetic resonance spectroscopy. *ChemPhysChem*, 18(1):6–16, 2017.

[6] Till Biskup. Structure–function relationship of organic semiconductors: Detailed insights from time-resolved epr spectroscopy. *Frontiers in chemistry*, 7:10, 2019.

[7] David Menard and Robert Barklie. Electron paramagnetic and ferromagnetic resonance. *Handbook of Magnetism and Magnetic Materials*, pages 1–35, 2020.

[8] Arthur Uhlir. Junction-diode amplifiers. *Scientific American*, 200(6):118–131, 1959.

[9] Melvin P Klein and George W Barton Jr. Enhancement of signal-to-noise ratio by continuous averaging: application to magnetic resonance. *Review of Scientific Instruments*, 34(7):754–759, 1963.

[10] JC Mollier, J Hardin, and J Uebersfeld. Theoretical and experimental sensitivities of esr spectrometers using maser techniques. *Review of Scientific Instruments*, 44(12):1763–1771, 1973.

[11] Anthony E. Siegman. *Microwave solid-state masers*. McGraw-Hill, 1964.

[12] Sergei A Dikanov and Yuri Tsvetkov. *Electron spin echo envelope modulation (ESEEM) spectroscopy*. CRC press, 2024.

[13] Arthur Schweiger and Gunnar Jeschke. *Principles of pulse electron paramagnetic resonance*. Oxford university press, 2001.

[14] E Hoffmann and A Schweiger. Inversion-recovery detected epr. *Applied Magnetic Resonance*, 9(1):1–22, 1995.

[15] Troy W Borneman, Martin D Hürlimann, and David G Cory. Application of optimal control to cpmg refocusing pulse design. *Journal of Magnetic Resonance*, 207(2):220–233, 2010.

[16] C Blake Wilson, Devin T Edwards, Jessica A Clayton, Songi Han, and Mark S Sherwin. Dressed rabi oscillation in a crystalline organic radical. *Physical review letters*, 124(4):047201, 2020.

[17] D Kajfez, S Chebolu, MR Abdul-Gaffoor, and AA Kishk. Uncertainty analysis of the transmission-type measurement of q-factor. *IEEE Transactions on Microwave Theory and Techniques*, 47(3):367–371, 1999.

[18] Lye Heng Chua and Dariush Mirshekar-Syahkal. Accurate and direct characterization of high-q microwave resonators using one-port measurement. *IEEE Trans. Microwave Theory and Tech.*, 51(3):978–985, 2003.

[19] Hao Wu, Shamil Mirkhanov, Wern Ng, Kuan-Cheng Chen, Yuling Xiong, and Mark Oxborrow. Invasive optical pumping for room-temperature masers, time-resolved epr, triplet-dnp, and quantum engines exploiting strong coupling. *Optics Express*, 28(20):29691–29702, 2020.

[20] Hao Wu, Wern Ng, Shamil Mirkhanov, Arman Amirzhan, Supamas Nitnara, and Mark Oxborrow. Unraveling the room-temperature spin dynamics of photoexcited pentacene in its lowest triplet state at zero field. *The Journal of Physical Chemistry C*, 123(39):24275–24279, 2019.

[21] Joon-Jea Sung, Guen-Soon Kang, and Suki Kim. A transient noise model for frequency-dependent noise sources. *IEEE Transactions on Computer-Aided Design of Integrated Circuits and Systems*, 22(8):1097–1104, 2003.

[22] Katharina Bader, Dominik Dengler, Samuel Lenz, Burkhard Endeward, Shang-Da Jiang, Petr Neugebauer, and Joris van Slageren. Room temperature quantum coherence in a potential molecular qubit. *Nature Communications*, 5(1):5304, oct 2014.

[23] Joseph M Zadrozny, Jens Niklas, Oleg G Poluektov, and Danna E Freedman. Millisecond coherence time in a tunable molecular electronic spin qubit. *ACS central science*, 1(9):488–492, 2015.

[24] Susumu Takahashi, Ronald Hanson, Johan Van Tol, Mark S Sherwin, and David D Awschalom. Quenching spin decoherence in diamond through spin bath polarization. *Physical review letters*, 101(4):047601, 2008.

[25] William F Koehl, Bob B Buckley, F Joseph Heremans, Greg Calusine, and David D Awschalom. Room temperature coherent control of defect spin qubits in silicon carbide. *Nature*, 479(7371):84–87, 2011.

[26] John JL Morton, Alexei M Tyryshkin, Arzhang Ardavan, Kyriakos Porfyrakis, SA Lyon, Andrew D Briggs, et al. Electron spin relaxation of n@ c60 in cs2. *The Journal of Chemical Physics*, 124(1), 2006.

[27] Susumu Takahashi, IS Tupitsyn, J Van Tol, CC Beedle, DN Hendrickson, and PCE Stamp. Decoherence in crystals of quantum molecular magnets. *Nature*, 476(7358):76–79, 2011.

[28] Gopalakrishnan Balasubramanian, Philipp Neumann, Daniel Twitchen, Matthew Markham, Roman Kolesov, Norikazu Mizuochi, Junichi Isoya, Jocelyn Achard, Johannes Beck, Julia Tissler, et al. Ultralong spin coherence time in isotopically engineered diamond. *Nature materials*, 8(5):383–387, 2009.

[29] Akio Yamauchi, Kentaro Tanaka, Masaaki Fuki, Saiya Fujiwara, Nobuo Kimizuka, Tomohiro Ryu, Masaki Saigo, Ken Onda, Ryota Kusumoto, Nami Ueno, et al. Room-temperature quantum coherence of entangled multiexcitons in a metal-organic framework. *Science Advances*, 10(1):eadi3147, 2024.

[30] Alexei M Tyryshkin, Shinichi Tojo, John JL Morton, Helge Riemann, Nikolai V Abrosimov, Peter Becker, Hans-Joachim Pohl, Thomas Schenkel, Michael LW Thewalt, Kohei M Itoh, et al. Electron spin coherence exceeding seconds in high-purity silicon. *Nature materials*, 11(2):143–147, 2012.

[31] Dennis Schäfter, Jonathan Wischnat, Lorenzo Tesi, J Alejandro De Sousa, Edmund Little, Jake McGuire, Marta Mas-Torrent, Concepció Rovira, Jaume Veciana, Floriana Tuna, et al. Molecular one-and two-qubit systems with very long coherence times. *Advanced Materials*, 35(38):2302114, 2023.

[32] Kana Orihashi, Akio Yamauchi, Saiya Fujiwara, Mizue Asada, Toshikazu Nakamura, Joseph Ka-Ho Hui, Nobuo Kimizuka, Kenichiro Tateishi, Tomohiro Uesaka, and Nobuhiro Yanai. Spin-Polarized Radicals with Extremely Long Spin–Lattice Relaxation Time at Room Temperature in a Metal–Organic Framework. *Journal of the American Chemical Society*, 145(50):27650–27656, dec 2023.

[33] Krzysztof Tadyszak, Radosław Mrówczyński, and Raanan Carmieli. Electron Spin Relaxation Studies of Polydopamine Radicals. *Journal of Physical Chemistry B*, 125(3):841–849, 2021.

[34] Claudia E. Avalos, Sabine Richert, Etienne Socie, Ganesan Karthikeyan, Gilles Casano, Gabriele Stevanato, Dominik J. Kubicki, Jacques E. Moser, Christiane R. Timmel, Moreno Lelli, Aaron J. Rossini, Olivier Ouari, and Lyndon Emsley. Enhanced Intersystem Crossing and Transient Electron Spin Polarization in a Photoexcited Pentacene-Trityl Radical. *Journal of Physical Chemistry A*, 124(29):6068–6075, 2020.

[35] Federico Lombardi, Ming-Yee Tsang, Michele Segantini, Ji Ma, William K. Myers, Xinliang Feng, Boris Naydenov, and Lapo Bogani. Room-temperature coherence boosting of molecular graphenoids by environmental spectral decomposition. *Physical Review B*, 105(9):094106, mar 2022.

[36] Dennis Schäfter, Jonathan Wischnat, Lorenzo Tesi, J. Alejandro De Sousa, Edmund Little, Jake McGuire, Marta Mas-Torrent, Concepció Rovira, Jaume Veciana, Floriana Tuna, Núria Crivillers, and Joris van Slageren. Molecular One- and Two-Qubit Systems with Very Long Coherence Times. *Advanced Materials*, 35(38):1–11, sep 2023.

[37] A. Mayländer and Others. Room temperature quantum spin systems. *Journal of Quantum Information*, 10:123–130, 2023.

[38] Virginia Meyer, Sandra S. Eaton, and Gareth R. Eaton. X-band Electron Spin Relaxation Times for Four Aromatic Radicals in Fluid Solution and Comparison with Other Organic Radicals. *Applied Magnetic Resonance*, 45(10):993–1007, oct 2014.

[39] Hanjiao Chen, Alexander G Maryasov, Olga Yu Rogozhnikova, Dmitry V Trukhin, Victor M Tormyshev, and Michael K Bowman. Electron spin dynamics and spin–lattice relaxation of trityl radicals in frozen solutions. *Physical Chemistry Chemical Physics*, 18(36):24954–24965, 2016.

[40] Darko Kajfez and Eugene J Hwan. Q-factor measurement with network analyzer. *IEEE Trans. Microwave Theory and Tech.*, 32(7):666–670, 1984.

[41] Takashi Mimura. The early history of the high electron mobility transistor (hemt). *IEEE Transactions on microwave theory and techniques*, 50(3):780–782, 2002.

[42] Bok-Hyung Lee, Sam-Dong Kim, and Jin-Koo Rhee. Small-signal analysis of high maximum frequency of oscillation 0.1-μm off-set gamma-shaped gate ingaas/inalas/gaas metamorphic high-electron-mobility transistors. *Japanese journal of applied physics*, 43(4S):1914, 2004.

[43] Marian W Pospieszalski. Extremely low-noise amplification with cryogenic fets and hfets: 1970-2004. *IEEE Microwave Magazine*, 6(3):62–75, 2005.

[44] Hao Wu, Shamil Mirkhanov, Wern Ng, and Mark Oxborrow. Bench-top cooling of a microwave mode using an optically pumped spin refrigerator. *Phys. Rev. Lett.*, 127(5):053604, 2021.

[45] Thaddeus D Ladd, Fedor Jelezko, Raymond Laflamme, Yasunobu Nakamura, Christopher Monroe, and Jeremy Lloyd O'Brien. Quantum computers. *nature*, 464(7285):45–53, 2010.

[46] Jeremy L O'brien. Optical quantum computing. *Science*, 318(5856):1567–1570, 2007.

[47] David P DiVincenzo. Quantum computation. *Science*, 270(5234):255–261, 1995.

[48] R Zhao, YO Dudin, SD Jenkins, CJ Campbell, DN Matsukevich, TAB Kennedy, and A Kuzmich. Long-lived quantum memory. *Nature Physics*, 5(2):100–104, 2009.

[49] Alexander I Lvovsky, Barry C Sanders, and Wolfgang Tittel. Optical quantum memory. *Nature photonics*, 3(12):706–714, 2009.

[50] Christian L Degen, Friedemann Reinhard, and Paola Cappellaro. Quantum sensing. *Reviews of modern physics*, 89(3):035002, 2017.

[51] Shi-Hai Wei, Bo Jing, Xue-Ying Zhang, Jin-Yu Liao, Chen-Zhi Yuan, Bo-Yu Fan, Chen Lyu, Dian-Li Zhou, You Wang, Guang-Wei Deng, et al. Towards real-world quantum networks: a review. *Laser & Photonics Reviews*, 16(3):2100219, 2022.

[52] Giulio Chiribella, Giacomo Mauro D'Ariano, and Paolo Perinotti. Theoretical framework for quantum networks. *Physical Review A—Atomic, Molecular, and Optical Physics*, 80(2):022339, 2009.

[53] Michael A Nielsen and Isaac L Chuang. *Quantum computation and quantum information*, volume 2. Cambridge university press Cambridge, 2001.

[54] Peter W Shor. Algorithms for quantum computation: discrete logarithms and factoring. In *Proceedings 35th annual symposium on foundations of computer science*, pages 124–134. Ieee, 1994.

[55] Edward Farhi, Jeffrey Goldstone, and Sam Gutmann. A quantum approximate optimization algorithm. *arXiv preprint arXiv:1411.4028*, 2014.

[56] Troels F Rønnow, Zhihui Wang, Joshua Job, Sergio Boixo, Sergei V Isakov, David Wecker, John M Martinis, Daniel A Lidar, and Matthias Troyer. Defining and detecting quantum speedup. *science*, 345(6195):420–424, 2014.

[57] Andrea Mari, Thomas R Bromley, Josh Izaac, Maria Schuld, and Nathan Killoran. Transfer learning in hybrid classical-quantum neural networks. *Quantum*, 4:340, 2020.

[58] Hsin-Yuan Huang, Michael Broughton, Masoud Mohseni, Ryan Babbush, Sergio Boixo, Hartmut Neven, and Jarrod R McClean. Power of data in quantum machine learning. *Nature communications*, 12(1):2631, 2021.

[59] Nabeel Aslam, Hengyun Zhou, Elana K Urbach, Matthew J Turner, Ronald L Walsworth, Mikhail D Lukin, and Hongkun Park. Quantum sensors for biomedical applications. *Nature Reviews Physics*, 5(3):157–169, 2023.

[60] Chung-Jui Yu, Stephen Von Kugelgen, Daniel W Laorenza, and Danna E Freedman. A molecular approach to quantum sensing. *ACS central science*, 7(5):712–723, 2021.

[61] Valerio Scarani, Helle Bechmann-Pasquinucci, Nicolas J Cerf, Miloslav Dušek, Norbert Lütkenhaus, and Momtchil Peev. The security of practical quantum key distribution. *Reviews of modern physics*, 81(3):1301–1350, 2009.

[62] Slawomir Simbierowicz, Massimo Borrelli, Volodymyr Monarkha, Ville Nuutinen, and Russell E Lake. Inherent thermal-noise problem in addressing qubits. *PRX Quantum*, 5(3):030302, 2024.

[63] John Preskill. Quantum computing in the nisq era and beyond. *Quantum*, 2:79, 2018.

[64] CJ Wellard and LCL Hollenberg. Thermal noise in a solid state quantum computer. *Journal of Physics D: Applied Physics*, 35(20):2499, 2002.

[65] H Zu, W Dai, and ATAM De Waele. Development of dilution refrigerators—a review. *Cryogenics*, 121:103390, 2022.

[66] Frank Schlawin, Dante M Kennes, and Michael A Sentef. Cavity quantum materials. *Applied Physics Reviews*, 9(1), 2022.

[67] B Keimer and JE Moore. The physics of quantum materials. *Nature Physics*, 13(11):1045–1055, 2017.

[68] KG Paulson and Subhashish Banerjee. Quantum speed limit time: role of coherence. *Journal of Physics A: Mathematical and Theoretical*, 55(50):505302, 2022.

[69] Miloš Rančić, Morgan P Hedges, Rose L Ahlefeldt, and Matthew J Sellars. Coherence time of over a second in a telecom-compatible quantum memory storage material. *Nature Physics*, 14(1):50–54, 2018.

[70] Peng Zhao, Yu Dian Lim, Hong Yu Li, Guidoni Luca, and Chuan Seng Tan. Advanced 3d integration technologies in various quantum computing devices. *IEEE Open Journal of Nanotechnology*, 2:101–110, 2021.

[71] Wern Ng, Yongqiang Wen, Max Attwood, Daniel C Jones, Mark Oxborrow, Neil McN Alford, and Daan M Arroo. "maser-in-a-shoebox": A portable plug-and-play maser device at room temperature and zero magnetic field. *Applied Physics Letters*, 124(4), 2024.

[72] Wern Ng, Yongqiang Wen, Neil Alford, and Daan M Arroo. Portable diamond maser with reduced magnetic field through orientation. *arXiv preprint arXiv:2404.05000*, 2024.

[73] Jonathan D Breeze, Enrico Salvadori, Juna Sathian, Neil McN Alford, and Christopher WM Kay. Continuous-wave room-temperature diamond maser. *Nature*, 555(7697):493–496, 2018.

[74] Mark Oxborrow, Jonathan D Breeze, and Neil M Alford. Room-temperature solid-state maser. *Nature*, 488(7411):353–356, 2012.

[75] Charles P Poole and Horacio A Farach. Electron spin resonance. In *Handbook of Spectroscopy*, pages 217–314. CRC Press, 2019.

[76] John A Weil and James R Bolton. *Electron paramagnetic resonance: elementary theory and practical applications*. John Wiley & Sons, 2007.

[77] Sabine Richert, Claudia E Tait, and Christiane R Timmel. Delocalisation of photoexcited triplet states probed by transient epr and hyperfine spectroscopy. *Journal of Magnetic Resonance*, 280:103–116, 2017.

[78] Mostafa A El-Sayed. Multiple resonance techniques in the study of the magnetic, radiative and non-radiative properties of the triplet state. *Pure and Applied Chemistry*, 24(3):475–494, 1970.

[79] Art van der Est, D Goldfarb, and S Stoll. *Continuous-wave EPR*. John Wiley & Sons Chichester, 2018.

[80] Noboru Hirota and Seigo Yamauchi. Short-lived excited triplet states studied by time-resolved epr spectroscopy. *Journal of Photochemistry and Photobiology C: Photochemistry Reviews*, 4(2):109–124, 2003.

[81] Martin Huisjen and James S Hyde. A pulsed epr spectrometer. *Review of Scientific Instruments*, 45(5):669–675, 1974.

[82] Joong-Ho Kwon, Hafiz Muhammad Shahbaz, and Jae-Jun Ahn. Advanced electron paramagnetic resonance spectroscopy for the identification of irradiated food. *American laboratory*, 46(1):26–+, 2014.

[83] Silvio Künstner, Anh Chu, Klaus-Peter Dinse, Alexander Schnegg, Joseph E McPeak, Boris Naydenov, Jens Anders, and Klaus Lips. Rapid-scan electron paramagnetic resonance using an epr-on-a-chip sensor. *Magnetic Resonance*, 2(2):673–687, 2021.

[84] AJ Hoff. Electron spin polarization of photosynthetic reactants. *Quarterly reviews of biophysics*, 17(2):153–282, 1984.

[85] P. A. De Jager and F. G. H. Van Wijk. Microsecond time resolution on a conventional epr spectrometer using 200 khz magnetic field modulation and phase-sensitive detection. *Review of Scientific Instruments*, 58(5):735–741, 1987.

[86] SI Weissman. Recent developments in electron paramagnetic resonance: Transient methods. *Annual Review of Physical Chemistry*, 33(1):301–318, 1982.

[87] Andreas Sperlich. *Electron paramagnetic resonance spectroscopy of conjugated polymers and fullerenes for organic photovoltaics*. PhD thesis, Universität Würzburg, 2013.

[88] Daniella Goldfarb and Stefan Stoll. *EPR spectroscopy: fundamentals and methods*. John Wiley & Sons, 2018.

[89] L_G Rowan, EL Hahn, and WB Mims. Electron-spin-echo envelope modulation. *Physical Review*, 137(1A):A61, 1965.

[90] James S Hyde, James CW Chien, and Jack H Freed. Electron–electron double resonance of free radicals in solution. *The Journal of Chemical Physics*, 48(9):4211–4226, 1968.

[91] Yuri D Tsvetkov, Michael K Bowman, and Yuri A Grishin. *Pulsed electron-electron double resonance*. Springer, 2019.

[92] Gunnar Jeschke. Characterization of protein conformational changes with sparse spin-label distance constraints. *Journal of chemical theory and computation*, 8(10):3854–3863, 2012.

[93] TF Prisner. Pulsed high-frequency/high-field epr. In *Advances in magnetic and optical resonance*, volume 20, pages 245–299. Elsevier, 1997.

[94] G Feher. Sensitivity considerations in microwave paramagnetic resonance absorption techniques. *Bell System Technical Journal*, 36(2):449–484, 1957.

[95] Charles P Poole. *Electron Spin Resonance: A Comprehensive Treatise on Experimental Techniques*. Courier Corporation, San Diego, CA, 2nd edition, 1996.

[96] John Bertrand Johnson. Thermal agitation of electricity in conductors. *Physical review*, 32(1):97, 1928.

[97] Albert W Hull and u NH Williams. Determination of elementary charge e from measurements of shot-effect. *Physical Review*, 25(2):147, 1925.

[98] Harald T Friis. Noise figures of radio receivers. *Proceedings of the IRE*, 32(7):419–422, 1944.

[99] V. Dordević, Z. Marinković, Giovanni Crupi, O. Pronić-Rančić, Vera Marković, and Alina Caddemi. Wave approach for noise modeling of gallium nitride high electron-mobility transistors. *International Journal of Numerical Modelling: Electronic Networks, Devices and Fields*, 30:e2138, 2015.

[100] Qorvo. *datasheet: QPL9547, 0.1 - 6 GHz Ultra Low-Noise LNA, Rev. D*, 2023.

[101] J Kraus. D.: Radio astronomy (cygnus-quasar books, powell, 1986.

[102] Claudius Gemperle and Arthur Schweiger. Pulsed electron-nuclear double resonance methodology. *Chemical reviews*, 91(7):1481–1505, 1991.

[103] Gareth R Eaton, Sandra S Eaton, David P Barr, and Ralph T Weber. *Quantitative Epr*. Springer Science & Business Media, 2010.

[104] Darko Kajfez. Q-factor. *Encyclopedia of RF and Microwave Engineering*, 2005.

[105] Darko Kajfez and Pierre Guillon. Dielectric resonators. *Norwood*, 1986.

[106] Jorge J Moré. The levenberg-marquardt algorithm: implementation and theory. In *Numerical analysis: proceedings of the biennial Conference held at Dundee, June 28–July 1, 1977*, pages 105–116. Springer, 2006.

[107] Wern Ng, Hao Wu, and Mark Oxborrow. Quasi-continuous cooling of a microwave mode on a benchtop using hyperpolarized nv- diamond. *Appl. Phys. Lett.*, 119(23):234001, 2021.

[108] D. P. Fahey, K. Jacobs, M. J. Turner, H. Choi, J. E. Hoffman, D. Englund, and M. E. Trusheim. Steady-state microwave mode cooling with a diamond n-v ensemble. *Phys. Rev. Appl. 20*, page 014033, 2023.

[109] H. Wang, K. L. Tiwari, K. Jacobs, M. Judy, X. Zhang, D. R. Englund, and M. E. Trusheim. A spin-refrigerated cavity quantum electrodynamic sensor. *arXiv quant-pph*, 16th April 2024.

[110] T. Day, M. Isarov, W. J. Pappas, B. C. Johnson, H. Abe, T. Ohshima, D. R. McCamey, A. Laucht, and J. J. Pla. A room-temperature solid-state maser amplifier. *arXiv:2405.07486v1 [quant-ph]*, 13 May 2024.

[111] J. Breeze, Ke-Jie Tan, B. Richards, J. Sathian, M. Oxborrow, and Neil NcN Alford. Enhanced magnetic purcell effect in room-temperature masers. *Nature Comm.*, 6:6215, 2015.

[112] R. Fleury, R. Xiang, P. Bugnon, and M. Khatibi. All-metallic magnetic purcell enhancement in a thermally stable room-temperature maser. *preprint: https://doi.org/10.21203/rs.3.rs-3536841/v1*, 2023.

[113] H. T. Friis. Noise figures of radio receivers. *Proc. IRE*, 32:419 – 422, July 1944.

[114] Mantas Šimėnas, James O'Sullivan, Christoph W Zollitsch, Oscar Kennedy, Maryam Seif-Eddine, Irina Ritsch, Miriam Hülsmann, Mian Qi, Adelheid Godt, Maxie M Roessler, et al. A sensitivity leap for x-band epr using a probehead with a cryogenic preamplifier. *J. Mag. Res.*, 322:106876, 2021.

[115] JA Giordmaine, LE Alsop, CH Mayer, and CH Townes. A maser amplifier for radio astronomy at x-band. *Proc. IRE*, 47(6):1062–1069, 1959.

[116] R. C. Clauss and J. S. Shell. Chapter 3: Ruby masers. In M. S. Reid, editor, *Low-Noise Systems in the Deep Space Network*, pages 95–158. JPL, NASA, 2008.

[117] R. J. Collier, M. A. Collins, and D. G. Moss. An x-band electron spin resonance spectrometer with a ruby maser preamplifier. *J. Phys. E: Sci. Instr.*, 1:607, 1968.

[118] R. Narkowicz, H. Ogata, E. Reijerse, and D. Suter. A cryogenic receiver for epr. *J. Mag. Res.*, 237:79–84, 2013.

[119] V. Kalendra, J. Turčak, J. Banys, J. J. L. Morton, and M. Šime. X- and q-band epr with cryogenic amplifiers independent of sample temperature. *J. Mag. Res.*, 343:107356, 2023.

[120] S. Pfenninger, W. Froncisz, and J. S. Hyde. Noise analysis of epr spectrometers with cryogenic microwave preamplifiers. *J. Mag. Res., Series A*, 113:32, 1995.

[121] CH Townes. Sensitivity of microwave spectrometers using maser techniques. *Phys. Rev. Lett.*, 5(9):428, 1960.

[122] HDW Hill and RE Richards. Limits of measurement in magnetic resonance. *J. Phys. E: Sci. Instr.*, 1(10):977, 1968.

[123] George A Rinard, Richard W Quine, James R Harbridge, Ruitian Song, Gareth R Eaton, and Sandra S Eaton. Frequency dependence of epr signal-to-noise. *J. Mag. Res.*, 140(1):218–227, 1999.

[124] Sander Weinreb, Dan L Fenstermacher, and Ronald W Harris. Ultra-low-noise 1.2-to 1.7-ghz cooled gaasfet amplifiers. *IEEE Trans. Microwave Theory and Tech.*, 30(6):849–853, 1982.

[125] M. Pospieszalski. Extremely low-noise amplification with cryogenic fets and hfets: 1970-2004. *IEEE Microwave Magazine*, 6:62–75, 2024.

[126] A. Blank, A. Sherman, B. Koren, and O. Zgadzai. An anti-maser for mode cooling of a microwave cavity. *J. Appl. Phys.*, 134:214401, 2023.

[127] Mark Oxborrow. Traceable 2-d finite-element simulation of the whispering-gallery modes of axisymmetric electromagnetic resonators. *IEEE Transactions on Microwave Theory and Techniques*, 55(6):1209–1218, 2007.

[128] M Gervasi, G Bonelli, G Sironi, F Cavaliere, A Passerini, and S Casani. An absolute cryogenic calibration source for a 2.5 ghz radiometer. *Rev. Sci. Instrum.*, 66(10):4798–4805, 1995.

[129] Bartolo Albanese, Sebastian Probst, Vishal Ranjan, Christoph W Zollitsch, Marek Pechal, Andreas Wallraff, John JL Morton, Denis Vion, Daniel Esteve, Emmanuel Flurin, et al. Radiative cooling of a spin ensemble. *Nature Physics*, 16(7):751–755, 2020.

[130] Z. Wang, M. Xu, X. Han, W. Fu, S. Puri, S. M. Girvin, H. X. Tang, S. Shankar, and M. H. Devoret. Quantum microwave radiometry with a superconducting qubit. *Phys. Rev. Lett.*, 26:180501, 2021.

[131] Robert H Frater and David R Williams. An active "cold" noise source. *IEEE Trans. Microwave Theory and Tech.*, 29(4):344–347, 1981.

[132] R.L. Forward and C. Terry. Electronically cold microwave artificial resistors. *IEEE Trans. Microwave Theory and Tech.*, 31:45–50, 2010.

[133] L. P. Dunleavy, M. C. Smith, S. M. Lardizabal, A. Fejzuli, and R. S. Roeder. Design and characterizaton of fet-based cold/hot noise sources. *IEEE Microwave Theory and Tech. Digest*, TH2B-6:1293, 1997.

[134] Emilia Leynia de la Jarrige, Laurent Escotte, Eric Gonneau, and Jean-Marc Goutele. Sige hbt-based active cold load for radiometer calibration. *IEEE Microwave and Wireless Components Letters*, 20(4):238–340, 2010.

[135] Ernst Weissbrodt. *Active Electronic Loads for Radiometric Calibration.* PhD thesis, Institute of Robust Power Semiconductor Systems, University of Stuttgart, 2017.

[136] N. Shou, S. S. Søbjærg, J. Balling, and S.S Kristensen. A second generation l-band digital

radiometer for sea salinity campaigns. *Proc. IEEE Geosc. Remote Sens. Symposium (IGARSS), Milan*, page 4742, 2015.

[137] Aashish A Clerk, Michel H Devoret, Steven M Girvin, Florian Marquardt, and Robert J Schoelkopf. Introduction to quantum noise, measurement, and amplification. *Reviews of Modern Physics*, 82(2):1155–1208, 2010.

[138] R. P. Meys. A wave approach to the noise properties of linear microwave devices. *IEEE Trans. Microwave. Theory and Tech.*, MTT-26:34, 1978.

[139] Hewlett Packard / Agilent. Application note 154: S-parameter design. Technical report, HP Memory Project, 1990.

[140] R. Hecken. Analysis of linear noisy two-ports using scattering waves. *IEEE Trans. Microwave. Theory and Tech.*, MTT-29:997, 1981.

[141] L. Escotte. Charge froides actives pour le calibrage des radiomètre micro-ondes ulitisés pour l'observation de la terre. *Synthèse: Revue des Sciences et de la Technologie [publ. Badji Mokhtar (Annaba) University, Algeria]*, 24:6–20, 2012; subsequently African Journals Online [AJOL] 2015.

[142] L. P. Dunleavy. Understanding noise parameter measurement. Technical Report Microwave Journal, Vol. 52, pp. 92, Horizon House Publications, 2009.

[143] Modelithics + Mini-Circuits. Application note an-60-040: Understanding noise parameter measurements. Technical report, Mini-Circuits, 2015.

[144] D. Wait and G. F. Engen. Application of radiometry to the accurate measurement of amplifier noise. *IEEE Trans. Instrumentation and Measurement*, 40:433, 1991.

[145] M. H. Weatherspoon and P. Dunleavy. Experimental validation of generalized equations of fet cold noise source design. *IEEE Trans. Microwave Theory and Tech.*, 54:608, 2006.

[146] A. Sheldon, L. Belostotski, H. Mani, C. E. Groppi, and K. F. Warnick. Cryogenic noise-parameter measurements. *IEEE Microwave Magazine*, August:52–64, 2021.

[147] S. M. Lardizabal. *Bias and temperature dependent noise modeling of microwave and millimeter-wave field effect transistors.* PhD thesis, Elect. Eng. Dept., Univ. South Florida, Tampa, FL, USA, 1997.

[148] J. J. Baustista. Chapter5: Low-noise amplifiers. In *Low-Noise Systems in the Deep Space Network, ed. M. S. Reid*, volume 10, page 195. Wiley, 2008.

[149] C. Zener. Non-adiabatic crossing of energy levels. *Proc. R. Soc. A*, 137:696, 1932.

[150] E. P. Glasbrenner and W. P. Schleich. The landau-zener formula made simple. *J. Phys. B: At. Mol. Opt. Phys.*, 56:104001, 2023.

[151] Markus Aspelmeyer, Tobias J Kippenberg, and Florian Marquardt. Cavity optomechanics. *Rev. Mod. Phys.*, 86(4):1391, 2014.

[152] Hewlett Packard / Agilent. Application note 57-1: Fundamentals of rf and microwave noise figure measurements. Technical report, The Hewlett Packard Archive, 1983. Revised July 1983.

[153] JM Raimond, P Goy, M Gross, C Fabre, and S Haroche. Collective absorption of blackbody radiation by rydberg atoms in a cavity: an experiment on bose statistics and brownian motion. *Phys. Rev. Lett.*, 49(2):117, 1982.

[154] Laurent Escotte, Robert Plana, and Jacques Graffeuil. Evaluation of noise parameter extraction methods. *IEEE transactions on microwave theory and techniques*, 41(3):382–387, 1993.

[155] H. Wu, X. Xie, W. Ng, S. Mehanna, Y. Li, M. Attwood, and M. Oxborrow. Room-temperature quasi-continuous-wave pentacene maser pumped by an invasive ce:yag luminescent concentrator. *Phys. Rev. Applied*, 14:064017, 2020.

[156] A. J. Ardizzi, A. Y. Choi, B. Gabritchidze, J. Kooi, K. A. Cleary, A. C. Readhead, and A. J. Minnich. Self-heating of cryogenic high electron-mobility transistor amplifiers and the limits of microwave noise performance. *J. Appl. Phys.*, 132:084501, 2022.

[157] A. J. Ardizzi. *Self-Heating of HEMT Low-Noise Amplifiers in Liquid Cryogenic Environments and the Limits of Microwave Noise Performance*. PhD thesis, Caltech, 2022.

[158] Y. Zeng, J. Stenarson, P. Sobis, N. Wadefalk, and J. Grahn. Sub-mw cryogenic inp hemt lna for qubit readout. *IEEE Trans. Microwave Theory and Tech.*, 72:1606, 2024.

[159] Shkelzen Cakaj, Bexhet Kamo, Indrit Enesi, and Olimpjon Shurdi. Antenna noise temperature for low earth orbiting satellite ground stations at l and s band. *Europe*, 5:6, 2011.

[160] James S. Hyde. Trends in epr technology. In *Biomedical EPR, Part B: Methodology, Instrumentation, and Dynamics*, pages 409–428. Springer, 2005.

[161] Kuan-Cheng Chen, Alberto Collauto, Ciarán J. Rogers, Shang Yu, Mark Oxborrow, and Max Julian David Attwood. Unlocking the potential of photoexcited molecular electron spins for room temperature quantum information processing. *Materials for Quantum Technology*, 2024.

[162] Kathrin Henschel, Johannes Majer, Jörg Schmiedmayer, and Helmut Ritsch. Cavity qed with an ultracold ensemble on a chip: Prospects for strong magnetic coupling at finite temperatures. *Phys. Rev. A*, 82(3):033810, 2010.

[163] Sébastien Pezzagna and Jan Meijer. Quantum computer based on color centers in diamond. *Applied Physics Reviews*, 8(1):011308, 2021.

[164] John Clarke and Frank K Wilhelm. Superconducting quantum bits. *Nature*, 453(7198):1031–1042, 2008.

[165] Yulin Chi, Jieshan Huang, Zhanchuan Zhang, Jun Mao, Zinan Zhou, Xiaojiong Chen, Chonghao Zhai, Jueming Bao, Tianxiang Dai, Huihong Yuan, et al. A programmable qudit-based quantum processor. *Nature communications*, 13(1):1166, 2022.

[166] R Maurand, X Jehl, D Kotekar-Patil, A Corna, H Bohuslavskyi, R Laviéville, L Hutin, S Barraud, M Vinet, M Sanquer, et al. A cmos silicon spin qubit. *Nature communications*, 7(1):13575, 2016.

[167] Jonathan Y Huang, Rocky Y Su, Wee Han Lim, MengKe Feng, Barnaby van Straaten, Brandon Severin, Will Gilbert, Nard Dumoulin Stuyck, Tuomo Tanttu, Santiago Serrano, et al. High-fidelity spin qubit operation and algorithmic initialization above 1 k. *Nature*, 627(8005):772–777, 2024.

[168] Alexandre M Souza, Gonzalo A Álvarez, and Dieter Suter. Robust dynamical decoupling. *Philosophical Transactions of the Royal Society A: Mathematical, Physical and Engineering Sciences*, 370(1976):4748–4769, 2012.

[169] Matteo Atzori, Stefano Benci, Elena Morra, Lorenzo Tesi, Mario Chiesa, Renato Torre, Lorenzo Sorace, and Roberta Sessoli. Structural effects on the spin dynamics of potential molecular qubits. *Inorganic chemistry*, 57(2):731–740, 2018.

[170] SL Bayliss, P Deb, DW Laorenza, M Onizhuk, G Galli, DE Freedman, and DD Awschalom. Enhancing spin coherence in optically addressable molecular qubits through host-matrix control. *Physical Review X*, 12(3):031028, 2022.

[171] M Jeremy Amdur, Kathleen R Mullin, Michael J Waters, Danilo Puggioni, Michael K Wojnar, Mingqiang Gu, Lei Sun, Paul H Oyala, James M Rondinelli, and Danna E Freedman. Chemical control of spin–lattice relaxation to discover a room temperature molecular qubit. *Chemical Science*, 13(23):7034–7045, 2022.

[172] DN Basov, RD Averitt, and D Hsieh. Towards properties on demand in quantum materials. *Nature materials*, 16(11):1077–1088, 2017.

[173] Md Mobarak Hossain Polash, Alex I. Smirnov, and Daryoosh Vashaee. Electron spin resonance in emerging spin-driven applications: Fundamentals and future perspectives. *Applied Physics Reviews*, 10(4):041301, dec 2023.

[174] AO Sushkov, N Chisholm, I Lovchinsky, M Kubo, PK Lo, SD Bennett, David Hunger, Alexey Akimov, Ronald Lee Walsworth, H Park, et al. All-optical sensing of a single-molecule electron spin. *Nano letters*, 14(11):6443–6448, 2014.

[175] Y. Kubo, I. Diniz, A. Dewes, V. Jacques, A. Dréau, J.-F. Roch, A. Auffeves, D. Vion,

D. Esteve, and P. Bertet. Storage and retrieval of a microwave field in a spin ensemble. *Physical Review A*, 85(1):012333, jan 2012.

[176] Nathalie P De Leon, Kohei M Itoh, Dohun Kim, Karan K Mehta, Tracy E Northup, Hanhee Paik, BS Palmer, Nitin Samarth, Sorawis Sangtawesin, and David W Steuerman. Materials challenges and opportunities for quantum computing hardware. *Science*, 372(6539):eabb2823, 2021.

[177] Sruti Mondal, Tanmoy Pain, Kasturi Sahu, and Sanjib Kar. Large-Scale Green Synthesis of Porphyrins. *ACS Omega*, 6(35):22922–22936, sep 2021.

[178] Stefan Stoll and Arthur Schweiger. Easyspin, a comprehensive software package for spectral simulation and analysis in epr. *Journal of magnetic resonance*, 178(1):42–55, 2006.

[179] Ioannis Simenas, Arno Schönfeld, Adam Kopta, Michael J. Hickey, and David P. Mulvihill. A sensitivity leap for x-band epr using a probehead with a cryogenic preamplifier. *Journal of Magnetic Resonance*, 322(3):106876, jan 2021.

[180] Gerd Kothe, Michail Lukaschek, Tomoaki Yago, Gerhard Link, Konstantin L. Ivanov, and Tien-Sung Lin. Initializing 214 Pure 14-Qubit Entangled Nuclear Spin States in a Hyperpolarized Molecular Solid. *The Journal of Physical Chemistry Letters*, 12(14):3647–3654, apr 2021.

[181] Jonathan D. Breeze, Enrico Salvadori, Juna Sathian, Neil McN. Alford, and Christopher W. M. Kay. Room-temperature cavity quantum electrodynamics with strongly coupled Dicke states. *npj Quantum Information*, 3(1):1–4, 2017.

[182] Sergei A. Dzuba, E. S. Salnikov, and L. V. Kulik. CW EPR, echo-detected EPR, and field-step ELDOR study of molecular motions of nitroxides ino-terphenyl glass: Dynamical transition, dynamical heterogeneity and β-relaxation. *Applied Magnetic Resonance*, 30(3-4):637–650, jun 2006.

[183] Sergei A. Dzuba. Probing Small-Angle Molecular Motions with EPR Spectroscopy: Dynamical Transition and Molecular Packing in Disordered Solids. *Magnetochemistry*, 8(2):19, jan 2022.

[184] Léo Delage-Laurin, Ravi Shankar Palani, Natalie Golota, Michael Mardini, Yifu Ouyang, Kong Ooi Tan, Timothy M. Swager, and Robert G. Griffin. Overhauser Dynamic Nuclear Polarization with Selectively Deuterated BDPA Radicals. *Journal of the American Chemical Society*, 143(48):20281–20290, dec 2021.

[185] Chung Jui Yu, Stephen Von Kugelgen, Matthew D. Krzyaniak, Woojung Ji, William R. Dichtel, Michael R. Wasielewski, and Danna E. Freedman. Spin and Phonon Design in Modular Arrays of Molecular Qubits. *Chemistry of Materials*, 32(23):10200–10206, 2020.

[186] Claudio Bonizzoni, Maksut Maksutoglu, Alberto Ghirri, Johan van Tol, Bulat Rameev, and Marco Affronte. Coupling Sub-nanoliter BDPA Organic Radical Spin Ensembles with YBCO Inverse Anapole Resonators. *Applied Magnetic Resonance*, 54(1):143–164, 2023.

[187] Chung-Jui Yu, Matthew D Krzyaniak, Majed S Fataftah, Michael R Wasielewski, and Danna E Freedman. A concentrated array of copper porphyrin candidate qubits. *Chemical science*, 10(6):1702–1708, 2019.

[188] Alexander K Oanta, Kelsey A Collins, Austin M Evans, Saied Md Pratik, Lyndon A Hall, Michael J Strauss, Seth R Marder, Deanna M D'Alessandro, Tijana Rajh, Danna E Freedman, et al. Electronic spin qubit candidates arrayed within layered two-dimensional polymers. *Journal of the American Chemical Society*, 145(1):689–696, 2022.

[189] Daniel W Laorenza, Arailym Kairalapova, Sam L Bayliss, Tamar Goldzak, Samuel M Greene, Leah R Weiss, Pratiti Deb, Peter J Mintun, Kelsey A Collins, David D Awschalom, et al. Tunable cr4+ molecular color centers. *Journal of the American Chemical Society*, 143(50):21350–21363, 2021.

[190] Ainhoa Urtizberea, Eva Natividad, Pablo J Alonso, Laura Pérez-Martínez, Miguel A Andrés, Ignacio Gascón, Ignacio Gimeno, Fernando Luis, and Olivier Roubeau. Vanadyl spin qubit 2d arrays and their integration on superconducting resonators. *Materials Horizons*, 7(3):885–897, 2020.

[191] Matteo Atzori, Lorenzo Tesi, Elena Morra, Mario Chiesa, Lorenzo Sorace, and Roberta Sessoli. Room-temperature quantum coherence and rabi oscillations in vanadyl phthalo-

cyanine: toward multifunctional molecular spin qubits. *Journal of the American Chemical Society*, 138(7):2154–2157, 2016.

[192] Claudio Bonizzoni, Alberto Ghirri, Fabio Santanni, and Marco Affronte. Quantum sensing of magnetic fields with molecular spins. *npj Quantum Information*, 10(1):41, apr 2024.

[193] Wern Ng, Xiaotian Xu, Max Attwood, Hao Wu, Zhu Meng, Xi Chen, and Mark Oxborrow. Move Aside Pentacene: Diazapentacene-Doped para -Terphenyl, a Zero-Field Room-Temperature Maser with Strong Coupling for Cavity Quantum Electrodynamics. *Advanced Materials*, 35(22):2300441, jun 2023.

[194] Samuel Lenz, Bastian Kern, Martin Schneider, and Joris van Slageren. Measurement of quantum coherence in thin films of molecular quantum bits without post-processing. *Chemical Communications*, 55(50):7163–7166, 2019.

[195] Samuel Lenz, David Hunger, and Joris van Slageren. Strong coupling between resonators and spin ensembles in the presence of exchange couplings. *Chemical Communications*, 56(84):12837–12840, 2020.

[196] Samuel Lenz, Dennis König, David Hunger, and Joris Slageren. Room-Temperature Quantum Memories Based on Molecular Electron Spin Ensembles. *Advanced Materials*, 33(30):2101673, jul 2021.

[197] Eufemio Moreno-Pineda, Daniel O. T. A. Martins, and Floriana Tuna. *Molecules as qubits, qudits and quantum gates*, volume 27. Royal Society of Chemistry, 2020.

[198] Aharon Blank and Haim Levanon. Interaction between Polarized Triplets and Stable Radicals in Liquid Solutions. *The Journal of Physical Chemistry A*, 105(20):4799–4807, may 2001.

[199] Aharon Blank and Haim Levanon. Applications of photoinduced electron spin polarization at room temperature to microwave technology. *Applied Physics Letters*, 79(11):1694–1696, 2001.

[200] Christopher W. M. Kay. The Electronic Structure of the Photoexcited Triplet State of Free-Base (Tetraphenyl)porphyrin by Time-Resolved Electron-Nuclear Double Resonance and Density Functional Theory. *Journal of the American Chemical Society*, 125(45):13861–13867, nov 2003.

[201] Reiya Yabuki, Koki Nishimura, Tomoyuki Hamachi, Naoto Matsumoto, and Nobuhiro Yanai. Generation and Transfer of Triplet Electron Spin Polarization at the Solid–Liquid Interface. *The Journal of Physical Chemistry Letters*, 14(20):4754–4759, may 2023.

[202] Haleh Hashemi Haeri, Philipp Spindler, Jörn Plackmeyer, and Thomas Prisner. Double quantum coherence ESR spectroscopy and quantum chemical calculations on a BDPA biradical. *Physical Chemistry Chemical Physics*, 18(42):29164–29169, 2016.

[203] Marcel Levien, Maik Reinhard, Markus Hiller, Igor Tkach, Marina Bennati, and Tomas Orlando. Spin density localization and accessibility of organic radicals affect liquid-state DNP efficiency. *Physical Chemistry Chemical Physics*, 23(8):4480–4485, 2021.

[204] Yuanxin Li, Asif Equbal, Tarnuma Tabassum, and Songi Han. 1 H Thermal Mixing Dynamic Nuclear Polarization with BDPA as Polarizing Agents. *The Journal of Physical Chemistry Letters*, 11(21):9195–9202, nov 2020.

[205] Elizabeth R. Canarie, Samuel M. Jahn, and Stefan Stoll. Quantitative Structure-Based Prediction of Electron Spin Decoherence in Organic Radicals. *The Journal of Physical Chemistry Letters*, 11(9):3396–3400, may 2020.

[206] Michael J. Graham, Joseph M. Zadrozny, Majed S. Fataftah, and Danna E. Freedman. Forging Solid-State Qubit Design Principles in a Molecular Furnace. *Chemistry of Materials*, 29(5):1885–1897, 2017.

[207] A. Gaita-Ariño, F. Luis, S. Hill, and E. Coronado. Molecular spins for quantum computation. *Nature Chemistry*, 11(4):301–309, apr 2019.

[208] Gang-Qin Liu and Xin-Yu Pan. Quantum information processing with nitrogen–vacancy centers in diamond. *Chinese Physics B*, 27(2):020304, feb 2018.

[209] Huijin Park, Junghyun Lee, Sangwook Han, Sangwon Oh, and Hosung Seo. Decoherence of nitrogen-vacancy spin ensembles in a nitrogen electron-nuclear spin bath in diamond. *npj Quantum Information*, 8(1):95, aug 2022.

[210] Roland Nagy, Matthias Niethammer, Matthias Widmann, Yu-Chen Chen, Péter Udvarhelyi, Cristian Bonato, Jawad Ul Hassan, Robin Karhu, Ivan G. Ivanov, Nguyen Tien Son, Jeronimo R. Maze, Takeshi Ohshima, Öney O. Soykal, Ádám Gali, Sang-Yun Lee, Florian Kaiser, and Jörg Wrachtrup. High-fidelity spin and optical control of single silicon-vacancy centres in silicon carbide. *Nature Communications*, 10(1):1954, apr 2019.

[211] Hannah L. Stern, Qiushi Gu, John Jarman, Simone Eizagirre Barker, Noah Mendelson, Dipankar Chugh, Sam Schott, Hoe H. Tan, Henning Sirringhaus, Igor Aharonovich, and Mete Atatüre. Room-temperature optically detected magnetic resonance of single defects in hexagonal boron nitride. *Nature Communications*, 13(1):1–9, 2022.

[212] Nai-Jie Guo, Song Li, Wei Liu, Yuan-Ze Yang, Xiao-Dong Zeng, Shang Yu, Yu Meng, Zhi-Peng Li, Zhao-An Wang, Lin-Ke Xie, Rong-Chun Ge, Jun-Feng Wang, Qiang Li, Jin-Shi Xu, Yi-Tao Wang, Jian-Shun Tang, Adam Gali, Chuan-Feng Li, and Guang-Can Guo. Coherent control of an ultrabright single spin in hexagonal boron nitride at room temperature. *Nature Communications*, 14(1):2893, may 2023.

[213] Hannah L Stern, Carmem M. Gilardoni, Qiushi Gu, Simone Eizagirre Barker, Oliver F J Powell, Xiaoxi Deng, Stephanie A Fraser, Louis Follet, Chi Li, Andrew J Ramsay, Hark Hoe Tan, Igor Aharonovich, and Mete Atatüre. A quantum coherent spin in hexagonal boron nitride at ambient conditions. *Nature Materials*, may 2024.

[214] Daan M. Arroo, Neil Mcn Alford, and Jonathan D Breeze. Perspective on room-temperature solid-state masers. *Applied Physics Letters*, 119(14):140502, oct 2021.

[215] Hao Wu, Shamil Mirkhanov, Wern Ng, and Mark Oxborrow. Bench-Top Cooling of a Microwave Mode Using an Optically Pumped Spin Refrigerator. *Physical Review Letters*, 127(5):053604, jul 2021.

[216] Wern Ng, Hao Wu, and Mark Oxborrow. Quasi-continuous cooling of a microwave mode on a benchtop using hyperpolarized NV-diamond. *Applied Physics Letters*, 119(23):234001, dec 2021.

[217] Aharon Blank, Alexander Sherman, Boaz Koren, and Oleg Zgadzai. An anti-maser for mode cooling of a microwave cavity. *Journal of Applied Physics*, 134(21), dec 2023.

[218] R. Casalini, S. S. Bair, and C. M. Roland. Density scaling and decoupling in o -terphenyl, salol, and dibutyphthalate. *The Journal of Chemical Physics*, 145(6):064502, aug 2016.

[219] Mirjam Schröder, Daniel Rauber, Clemens Matt, and Christopher W. M. Kay. Pentacene in 1,3,5-Tri(1-naphtyl)benzene: A Novel Standard for Transient EPR Spectroscopy at Room Temperature. *Applied Magnetic Resonance*, 53(7-9):1043–1052, sep 2022.

[220] Max Attwood, Xiaotian Xu, Michael Newns, Zhu Meng, Rebecca A Ingle, Hao Wu, Xi Chen, Weidong Xu, Wern Ng, Temitope T Abiola, Vasilios G Stavros, and Mark Oxborrow. N-Heteroacenes as an Organic Gain Medium for Room-Temperature Masers. *Chemistry of Materials*, 35(11):4498–4509, jun 2023.

[221] Reiya Yabuki, Koki Nishimura, Tomoyuki Hamachi, Naoto Matsumoto, and Nobuhiro Yanai. Generation and transfer of triplet electron spin polarization at the solid–liquid interface. *The Journal of Physical Chemistry Letters*, 14:4754–4759, 2023.

[222] Bahadur Sk, Rana Tsuru, Kikuya Hayashi, and Shuzo Hirata. Selective triplet–singlet förster-resonance energy transfer for bright red afterglow emission. *Advanced Functional Materials*, 33(11):2211604, 2023.

[223] Martin Gouterman and Gamal-Eddin Khalil. Porphyrin free base phosphorescence. *Journal of Molecular Spectroscopy*, 53(1):88–100, oct 1974.

[224] Aharon Blank and Haim Levanon. Optimal magnetization in liquids, generated by triplet—doublet interaction. *Molecular Physics*, 100(9):1477–1488, may 2002.

[225] Claudia E Avalos, Sabine Richert, Etienne Socie, Ganesan Karthikeyan, Gilles Casano, Gabriele Stevanato, Dominik J Kubicki, Jacques E Moser, Christiane R Timmel, Moreno

Lelli, et al. Enhanced intersystem crossing and transient electron spin polarization in a photoexcited pentacene–trityl radical. *The Journal of Physical Chemistry A*, 124(29):6068–6075, 2020.

[226] Haochuan Mao, Ryan M Young, Matthew D Krzyaniak, and Michael R Wasielewski. Optical initialization of molecular qubit spin states using weak exchange coupling to photogenerated fullerene triplet states. *The Journal of Physical Chemistry B*, 126(49):10519–10527, 2022.

[227] Michael T. Colvin et al. Ultrafast intersystem crossing and spin dynamics of zinc mesotetraphenylporphyrin covalently bound to stable radicals. *The Journal of Physical Chemistry A*, 115(26):7538–7549, 2011.

[228] Noah E. Horwitz, Brian T. Phelan, Jordan N. Nelson, Matthew D. Krzyaniak, and Michael R. Wasielewski. Picosecond Control of Photogenerated Radical Pair Lifetimes Using a Stable Third Radical. *Journal of Physical Chemistry A*, 120(18):2841–2853, 2016.

[229] Theresia Quintes, Maximilian Mayländer, and Sabine Richert. Properties and applications of photoexcited chromophore–radical systems. *Nature Reviews Chemistry*, 7(2):75–90, jan 2023.

[230] Aimei Zhou, Zhecheng Sun, and Lei Sun. Stable organic radical qubits and their applications in quantum information science. *The Innovation*, 5(5):100662, sep 2024.

[231] Muhandis Shiddiq, Dorsa Komijani, Yan Duan, Alejandro Gaita-Ariño, Eugenio Coronado, and Stephen Hill. Enhancing coherence in molecular spin qubits via atomic clock transitions. *Nature*, 531(7594):348–351, 2016.

[232] Alejandro Gaita-Ariño, Fernando Luis, Stephen Hill, and Eugenio Coronado. Molecular spins for quantum computation. *Nature chemistry*, 11(4):301–309, 2019.

[233] Adrian Mena, Sarah K Mann, Angus Cowley-Semple, Emma Bryan, Sandrine Heutz, Dane R McCamey, Max Attwood, and Sam L Bayliss. Room-temperature optically detected coherent control of molecular spins. *Physical Review Letters*, 133(12):120801, 2024.

[234] Eugenio Coronado. Molecular magnetism: from chemical design to spin control in molecules, materials and devices. *Nature Reviews Materials*, 5(2):87–104, 2020.

[235] Tran-Chin Yang, David J Sloop, SI Weissman, and Tien-Sung Lin. Zero-field magnetic resonance of the photo-excited triplet state of pentacene at room temperature. *The Journal of Chemical Physics*, 113(24):11194–11201, 2000.

[236] Daniel W Laorenza and Danna E Freedman. Could the quantum internet be comprised of molecular spins with tunable optical interfaces? *Journal of the American Chemical Society*, 144(48):21810–21825, 2022.

[237] Yiwen Chu, Prashanta Kharel, William H Renninger, Luke D Burkhart, Luigi Frunzio, Peter T Rakich, and Robert J Schoelkopf. Quantum acoustics with superconducting qubits. *Science*, 358(6360):199–202, 2017.

[238] Martin V Gustafsson, Thomas Aref, Anton Frisk Kockum, Maria K Ekström, Göran Johansson, and Per Delsing. Propagating phonons coupled to an artificial atom. *Science*, 346(6206):207–211, 2014.

[239] Smarak Maity, Linbo Shao, Stefan Bogdanović, Srujan Meesala, Young-Ik Sohn, Neil Sinclair, Benjamin Pingault, Michelle Chalupnik, Cleaven Chia, Lu Zheng, et al. Coherent acoustic control of a single silicon vacancy spin in diamond. *Nature communications*, 11(1):193, 2020.

[240] ER MacQuarrie, TA Gosavi, AM Moehle, NR Jungwirth, SA Bhave, and GD Fuchs. Coherent control of a nitrogen-vacancy center spin ensemble with a diamond mechanical resonator. *Optica*, 2(3):233–238, 2015.

[241] HY Chen, SA Bhave, and GD Fuchs. Acoustically driving the single-quantum spin transition of diamond nitrogen-vacancy centers. *Physical Review Applied*, 13(5):054068, 2020.

[242] D Andrew Golter, Thein Oo, Mayra Amezcua, Ignas Lekavicius, Kevin A Stewart, and Hailin Wang. Coupling a surface acoustic wave to an electron spin in diamond via a dark state. *Physical Review X*, 6(4):041060, 2016.

[243] Martin JA Schuetz, Johannes Knoerzer, Geza Giedke, Lieven MK Vandersypen, Mikhail D Lukin, and J Ignacio Cirac. Acoustic traps and lattices for electrons in semiconductors. *Physical Review X*, 7(4):041019, 2017.

[244] Tomáš Neuman, Matt Eichenfield, Matthew E Trusheim, Lisa Hackett, Prineha Narang, and Dirk Englund. A phononic interface between a superconducting quantum processor and quantum networked spin memories. *npj Quantum Information*, 7(1):121, 2021.

[245] Samuel J Whiteley, Gary Wolfowicz, Christopher P Anderson, Alexandre Bourassa, He Ma, Meng Ye, Gerwin Koolstra, Kevin J Satzinger, Martin V Holt, F Joseph Heremans, et al. Spin–phonon interactions in silicon carbide addressed by gaussian acoustics. *Nature Physics*, 15(5):490–495, 2019.

[246] Young-Ik Sohn, Srujan Meesala, Benjamin Pingault, Haig A Atikian, Jeffrey Holzgrafe, Mustafa Gündoğan, Camille Stavrakas, Megan J Stanley, Alp Sipahigil, Joonhee Choi, et al. Controlling the coherence of a diamond spin qubit through its strain environment. *Nature communications*, 9(1):2012, 2018.

[247] Alberto Hernández-Mínguez, Alexander V Poshakinskiy, Michael Hollenbach, Paulo V Santos, and Georgy V Astakhov. Acoustically induced coherent spin trapping. *Science Advances*, 7(44):eabj5030, 2021.

[248] Andrea Albino, Stefano Benci, Lorenzo Tesi, Matteo Atzori, Renato Torre, Stefano Sanvito, Roberta Sessoli, and Alessandro Lunghi. First-principles investigation of spin–phonon coupling in vanadium-based molecular spin quantum bits. *Inorganic chemistry*, 58(15):10260–10268, 2019.

[249] Daphné Lubert-Perquel, Enrico Salvadori, Matthew Dyson, Paul N Stavrinou, Riccardo Montis, Hiroki Nagashima, Yasuhiro Kobori, Sandrine Heutz, and Christopher WM Kay. Identifying triplet pathways in dilute pentacene films. *Nature communications*, 9(1):4222, 2018.

[250] Kaipu Wang, Hao Wu, Bo Zhang, Xuri Yao, Jiakai Zhang, Mark Oxborrow, and Qing

Zhao. Tailoring coherent microwave emission from a solid-state hybrid system for room-temperature microwave quantum electronics. *Advanced Science*, page 2401904, 2024.

[251] Linbo Shao, Smarak Maity, Lu Zheng, Lue Wu, Amirhassan Shams-Ansari, Young-Ik Sohn, Eric Puma, MN Gadalla, Mian Zhang, Cheng Wang, et al. Phononic band structure engineering for high-q gigahertz surface acoustic wave resonators on lithium niobate. *Physical Review Applied*, 12(1):014022, 2019.

[252] Xiaotian Xu, Michael Newns, and Mark Oxborrow. Simulating the magnetic fields generated by piezoelectric devices using fem software: Beyond the quasistatic approximation. *Journal of Applied Physics*, 132(20), 2022.

[253] Péter Udvarhelyi, Tristan Clua-Provost, Alrik Durand, Jiahan Li, James H Edgar, Bernard Gil, Guillaume Cassabois, Vincent Jacques, and Adam Gali. A planar defect spin sensor in a two-dimensional material susceptible to strain and electric fields. *npj Computational Materials*, 9(1):150, 2023.

[254] Jonathan R Dietz, Boyang Jiang, Aaron M Day, Sunil A Bhave, and Evelyn L Hu. Spin-acoustic control of silicon vacancies in 4h silicon carbide. *Nature Electronics*, 6(10):739–745, 2023.

[255] Aimei Zhou, Zhecheng Sun, and Lei Sun. Stable organic radical qubits and their applications in quantum information science. *The Innovation*, 2024.

[256] Ian D Robertson and Stepan Lucyszyn. *RFIC and MMIC Design and Technology*. IET, 2001.

[257] Thomas H Lee and Thomas H Lee. *Planar microwave engineering: a practical guide to theory, measurement, and circuits*, volume 1. Cambridge university press, 2004.

[258] Daniel White. *Ultra Low Noise Amplifiers for Future Radio Astronomy Observatories*. PhD thesis, University of Manchester, 2020.

[259] PM Smith, K Nichols, W Kong, L MtPleasant, D Pritchards, R Lender, J Fisher, R Actis, D Dugas, D Meharry, et al. Advances in inp hemt technology for high frequency appli-

cations. In *Conference Proceedings. 2001 International Conference on Indium Phosphide and Related Materials. 13th IPRM (Cat. No. 01CH37198)*, pages 9–14. IEEE, 2001.

[260] Clay S Turner. Johnson-nyquist noise. *url: http://www. claysturner. com/dsp/Johnson-NyquistNoise*, 2012.

[261] OM Bulashenko and VA Kochelap. Johnson-nyquist noise for a 2d electron gas in a narrow channel. *Journal of Physics: Condensed Matter*, 5(39):L469, 1993.

[262] GH Hanson and A Van der Ziel. Shot noise in transistors. *Proceedings of the IRE*, 45(11):1538–1542, 1957.

[263] Marian W Pospieszalski. Modeling of noise parameters of mesfets and modfets and their frequency and temperature dependence. *IEEE transactions on microwave theory and techniques*, 37(9):1340–1350, 1989.

[264] Wern Ng, Hao Wu, and Mark Oxborrow. Continuous cooling of a microwave mode on a benchtop using hyperpolarized nv^- diamond. *arXiv preprint arXiv:2110.12105*, 2021.

[265] Christopher L Bremer and Daniel T Kaplan. Markov chain monte carlo estimation of nonlinear dynamics from time series. *Physica D: Nonlinear Phenomena*, 160(1-2):116–126, 2001.

[266] Ingrid Stenger, Alexandre Frigout, Denis Tondelier, Bernard Geffroy, Razvigor Ossikovski, and Yvan Bonnassieux. Polarized micro-raman spectroscopy study of pentacene thin films. *Applied Physics Letters*, 94(13), 2009.

[267] Lisanne Sellies, Raffael Spachtholz, Sonja Bleher, Jakob Eckrich, Philipp Scheuerer, and Jascha Repp. Single-molecule electron spin resonance by means of atomic force microscopy. *Nature*, 624(7990):64–68, 2023.

[268] F Albert Cotton. *Chemical applications of group theory*. John Wiley & Sons, 1991.

[269] Umer Hassan and Muhammad Sabieh Anwar. Reducing noise by repetition: introduction to signal averaging. *European Journal of Physics*, 31(3):453, 2010.

[270] Theodore H. Maiman et al. Stimulated optical radiation in ruby. *Nature*, 187(4736):493–494, 1960.

[271] Ernst Weissbrodt. *Active Electronic Loads for Radiometric Calibration*. PhD thesis, University of Stuttgart, 2017.

[272] Hewlett Packard / Agilent. Application note 57-1: Fundamentals of rf and microwave noise figure measurements. Technical report, The Hewlett Packard Archive, July 1983. Revised in July 1983.

[273] Joseph Weber. Amplification of microwave radiation by substances not in thermal equilibrium. *Transactions of the IRE Professional Group on Electron Devices*, 2(3):1–4, 1953.

[274] K Shimoda, TC Wang, and CH Townes. Further aspects of the theory of the maser. *Physical Review*, 102(5):1308, 1956.

[275] John D Prestage, Robert L Tjoelker, and Lute Maleki. Atomic clocks and variations of the fine structure constant. *Physical review letters*, 74(18):3511, 1995.

[276] Nicolaas Bloembergen. Proposal for a new type solid state maser. *Physical review*, 104(2):324, 1956.

[277] MS Reid, RC Clauss, DA Bathker, and Ch T Stelzried. Low-noise microwave receiving systems in a worldwide network of large antennas. *Proceedings of the IEEE*, 61(9):1330–1335, 1973.

[278] Jacques Vanier. The active hydrogen maser: state of the art and forecast. *Metrologia*, 18(4):173, 1982.

[279] RC Clauss, JS Shell, and MS Reid. Low-noise systems in the deep space network. *Jet Propulsion Laboratory California Institute of Technology*, 2008.

[280] Edward M Purcell and Robert V Pound. A nuclear spin system at negative temperature. *Physical Review*, 81(2):279, 1951.

[281] Albert Einstein. Zur quantentheorie der strahlung. *Phys. Z.*, 18:124, 1917.

[282] Albert Einstein. Über einem die erzeugung und verwandlung des lichtes betreffenden heuristischen gesichtspunkt. *Annalen der physik*, 4, 1905.

[283] Wolfgang Zinth, Alfred Laubereau, and Wolfgang Kaiser. The long journey to the laser and its rapid development after 1960. *The European Physical Journal H*, 36(2):153–181, 2011.

[284] Max Planck. On the law of the energy distribution in the normal spectrum. *Ann. Phys*, 4(553):1–11, 1901.

[285] BR Nag. High electron mobility transistor (hemt). *Physics of Quantum Well Devices*, pages 173–187, 2000.

[286] J De Jong and C MacLean. The zero-field splitting of cyano-substituted benzenes in their lowest excited triplet states. *Journal of Magnetic Resonance (1969)*, 11(3):373–380, 1973.

[287] Colin Thomson. Zero-field splittings in aromatic hydrocarbons. *Molecular Physics*, 11(2):197–203, 1966.

[288] Colin Thomson. Electron spin resonance studies of the triplet state. *Quarterly Reviews, Chemical Society*, 22(1):45–74, 1968.

[289] Colin Thomson. Zero-field splittings in aromatic triplet states. *Theoretica Chimica Acta*, 11(2):165–166, 1968.

[290] Rugang Geng, Timothy Tyler Daugherty, Kevin Do, Hoang Mai Luong, and Tho Duc Nguyen. A review on organic spintronic materials and devices: I. magnetic field effect on organic light emitting diodes. *Journal of Science: Advanced Materials and Devices*, 1(2):128–140, 2016.

[291] Colin Thomson. Esr studies of triplet states in plastics: effect of temperature on the spectra. *The Journal of Chemical Physics*, 41(1):1–6, 1964.

[292] Jonathan Breeze, Ke-Jie Tan, Benjamin Richards, Juna Sathian, Mark Oxborrow, and Neil McN Alford. Enhanced magnetic purcell effect in room-temperature masers. *Nature communications*, 6(1):1–6, 2015.

[293] Hao Wu, Xiangyu Xie, Wern Ng, Seif Mehanna, Yingxu Li, Max Attwood, and Mark Oxborrow. Room-temperature quasi-continuous-wave pentacene maser pumped by an invasive ce: Yag luminescent concentrator. *Physical Review Applied*, 14(6):064017, 2020.

[294] Mirjam Schröder, Daniel Rauber, Clemens Matt, and Christopher WM Kay. Pentacene in 1, 3, 5-tri (1-naphtyl) benzene: A novel standard for transient epr spectroscopy at room temperature. *Applied Magnetic Resonance*, pages 1–10, 2021.

[295] Stefan Weber. *Transient EPR*, pages 255–270. American Cancer Society, 2017.

[296] AW Hornig and James S Hyde. Paramagnetic resonance in triplet naphthalene at liquid helium temperatures. *Molecular Physics*, 6(1):33–41, 1963.

[297] H Schuch, F Seiff, R Furrer, K Möbius, and KP Dinse. Direkte bestimmung des absoluten vorzeichens des triplett-nullfeld-parameters d mit hochauflösender optischer detektion von esr/direct determination of the absolute sign of the triplet zero field parameter d by high resolution optical detection of esr. *Zeitschrift für Naturforschung A*, 29(11):1543–1547, 1974.

[298] Marion C Thurnauer and James R Norris. Magnetophotoselection applied to the triplet state observed by epr in photosynthetic bacteria. *Biochemical and biophysical research communications*, 73(2):501–506, 1976.

[299] APS Supplemental Material, 2024. See Supplemental Material for details of experimental method, theory of cavity-pre-cooling, and noise analysis, http://link.aps.org/supplemental/.../PhysRevApplied....

[300] R Furrer, P Fujara, C Lange, D Stehlik, HM Vieth, and W Vollmann. Transient esr nutation signals in excited aromatic triplet states. *Chemical Physics Letters*, 75(2):332–339, 1980.

[301] Patrick Bertrand. *Electron Paramagnetic Resonance Spectroscopy*. Springer, 2020.

[302] MS De Groot, IAM Hesselmann, and JH Van der Waals. Phosphorescence and spin polarization: A preliminary report. *Molecular Physics*, 12(3):259–264, 1967.

[303] Clyde A Hutchison Jr and Billy W Mangum. Paramagnetic resonance absorption in naphthalene in its phosphorescent state. *The Journal of Chemical Physics*, 34(3):908–922, 1961.

[304] Liang Jin, Matthias Pfender, Nabeel Aslam, Philipp Neumann, Sen Yang, Jörg Wrachtrup, and Ren-Bao Liu. Proposal for a room-temperature diamond maser. *Nature Communications*, 6(1):8251, 2015.

[305] Alexander Sherman, Oleg Zgadzai, Boaz Koren, Idan Peretz, Eyal Laster, and Aharon Blank. Diamond-based microwave quantum amplifier. *Science Advances*, 8(49):eade6527, 2022.

[306] Sergey Bravyi, Andrew W Cross, Jay M Gambetta, Dmitri Maslov, Patrick Rall, and Theodore J Yoder. High-threshold and low-overhead fault-tolerant quantum memory. *Nature*, 627(8005):778–782, 2024.

[307] CM Knaut, A Suleymanzade, Y-C Wei, DR Assumpcao, P-J Stas, YQ Huan, B Machielse, EN Knall, M Sutula, G Baranes, et al. Entanglement of nanophotonic quantum memory nodes in a telecom network. *Nature*, 629(8012):573–578, 2024.

[308] Angela Sara Cacciapuoti, Marcello Caleffi, Francesco Tafuri, Francesco Saverio Cataliotti, Stefano Gherardini, and Giuseppe Bianchi. Quantum internet: Networking challenges in distributed quantum computing. *IEEE Network*, 34(1):137–143, 2019.

[309] Jian-Long Liu, Xi-Yu Luo, Yong Yu, Chao-Yang Wang, Bin Wang, Yi Hu, Jun Li, Ming-Yang Zheng, Bo Yao, Zi Yan, et al. Creation of memory–memory entanglement in a metropolitan quantum network. *Nature*, 629(8012):579–585, 2024.

[310] Jake McGuire, Haralampos N Miras, James P Donahue, Emma Richards, and Stephen Sproules. Ligand radicals as modular organic electron spin qubits. *Chemistry–A European Journal*, 24(66):17598–17605, 2018.

[311] Gavin W Morley, Marc Warner, A Marshall Stoneham, P Thornton Greenland, Johan Van Tol, Christopher WM Kay, and Gabriel Aeppli. The initialization and manipulation

of quantum information stored in silicon by bismuth dopants. *Nature materials*, 9(9):725–729, 2010.

[312] Marc Warner, Salahud Din, Igor S Tupitsyn, Gavin W Morley, A Marshall Stoneham, Jules A Gardener, Zhenlin Wu, Andrew J Fisher, Sandrine Heutz, Christopher WM Kay, et al. Potential for spin-based information processing in a thin-film molecular semiconductor. *Nature*, 503(7477):504–508, 2013.

[313] Selena J Lockyer, Alessandro Chiesa, Grigore A Timco, Eric JL McInnes, Tom S Bennett, Inigo J Vitorica-Yrezebal, Stefano Carretta, and Richard EP Winpenny. Targeting molecular quantum memory with embedded error correction. *Chemical science*, 12(26):9104–9113, 2021.

[314] Daniele Cuomo, Marcello Caleffi, and Angela Sara Cacciapuoti. Towards a distributed quantum computing ecosystem. *IET Quantum Communication*, 1(1):3–8, 2020.

[315] William J Munro, Nicolo'Lo Piparo, Josephine Dias, Michael Hanks, and Kae Nemoto. Designing tomorrow's quantum internet. *AVS Quantum Science*, 4(2), 2022.

[316] Mahdi Chehimi and Walid Saad. Physics-informed quantum communication networks: A vision toward the quantum internet. *IEEE network*, 36(5):32–38, 2022.

[317] Claudio Bonizzoni, Alberto Ghirri, Fabio Santanni, Matteo Atzori, Lorenzo Sorace, Roberta Sessoli, and Marco Affronte. Storage and retrieval of microwave pulses with molecular spin ensembles. *npj Quantum Information*, 6(1):68, 2020.

[318] Mateo Casariego, Emmanuel Zambrini Cruzeiro, Stefano Gherardini, Tasio Gonzalez-Raya, Rui André, Gonçalo Frazão, Giacomo Catto, Mikko Möttönen, Debopam Datta, Klaara Viisanen, et al. Propagating quantum microwaves: towards applications in communication and sensing. *Quantum Science and Technology*, 8(2):023001, 2023.

[319] P Rabl, D DeMille, John M Doyle, Mikhail D Lukin, RJ Schoelkopf, and P Zoller. Hybrid quantum processors: molecular ensembles as quantum memory for solid state circuits. *Physical review letters*, 97(3):033003, 2006.

[320] Min Jiang, Yushu Qin, Xin Wang, Yuanhong Wang, Haowen Su, Xinhua Peng, and Dmitry Budker. Floquet spin amplification. *Physical Review Letters*, 128(23):233201, 2022.

[321] D Ziemkiewicz and S Zielińska-Raczyńska. Solid-state pulsed microwave emitter based on rydberg excitons. *Optics Express*, 27(12):16983–16994, 2019.

[322] Daan M Arroo, Neil McN Alford, and Jonathan D Breeze. Perspective on room-temperature solid-state masers. *Applied Physics Letters*, 119(14), 2021.

[323] Jonathan D Breeze, Enrico Salvadori, Juna Sathian, Neil McN Alford, and Christopher WM Kay. Continuous-wave room-temperature diamond maser. *Nature*, 555(7697):493–496, 2018.

[324] Andreas Gottscholl, Maximilian Wagenhöfer, Manuel Klimmer, Selina Scherbel, Christian Kasper, Valentin Baianov, Georgy V Astakhov, Vladimir Dyakonov, and Andreas Sperlich. Superradiance of spin defects in silicon carbide for maser applications. *Frontiers in Photonics*, 3:886354, 2022.

[325] Justin T Hou, Pengxiang Zhang, and Luqiao Liu. Proposal for a spin-torque-oscillator maser enabled by microwave photon-spin coupling. *Physical Review Applied*, 16(3):034034, 2021.

[326] Bimu Yao, YS Gui, JW Rao, YH Zhang, Wei Lu, and C-M Hu. Coherent microwave emission of gain-driven polaritons. *Physical Review Letters*, 130(14):146702, 2023.

[327] Mark Oxborrow, Jonathan D Breeze, and Neil M Alford. Room-temperature solid-state maser. *Nature*, 488(7411):353–356, 2012.

[328] Wern Ng, Xiaotian Xu, Max Attwood, Hao Wu, Zhu Meng, Xi Chen, and Mark Oxborrow. Move aside pentacene: Diazapentacene-doped para-terphenyl, a zero-field room-temperature maser with strong coupling for cavity quantum electrodynamics. *Advanced Materials*, 35(22):2300441, 2023.

[329] Mark Oxborrow. Maser assembly. Patent WO EP US JP GB EP3557703A1, 10 2019. Priority date: 2012-08-17, Filed: 2013-08-15.

[330] Hao Wu, Wern Ng, Shamil Mirkhanov, Arman Amirzhan, Supamas Nitnara, and Mark Oxborrow. Unraveling the room-temperature spin dynamics of photoexcited pentacene in its lowest triplet state at zero field. *The Journal of Physical Chemistry C*, 123(39):24275–24279, 2019.

[331] Hao Wu, Shamil Mirkhanov, Wern Ng, and Mark Oxborrow. Bench-top cooling of a microwave mode using an optically pumped spin refrigerator. *Physical Review Letters*, 127(5):053604, 2021.

[332] Donald P Fahey, Kurt Jacobs, Matthew J Turner, Hyeongrak Choi, Jonathan E Hoffman, Dirk Englund, and Matthew E Trusheim. Steady-state microwave mode cooling with a diamond n-v ensemble. *Physical Review Applied*, 20(1):014033, 2023.

[333] Aharon Blank and Haim Levanon. Applications of photoinduced electron spin polarization at room temperature to microwave technology. *Applied Physics Letters*, 79(11):1694–1696, 2001.

[334] AI Shushin. Radical–triplet pair mechanism of electron spin polarization. detailed theoretical treatment. *The Journal of Physical Chemistry A*, 118(48):11355–11363, 2014.

[335] Nathan Hinkley, Jeff A Sherman, Nathaniel B Phillips, Macro Schioppo, Nathan D Lemke, Kyle Beloy, Marco Pizzocaro, Christopher W Oates, and Andrew D Ludlow. An atomic clock with 10–18 instability. *Science*, 341(6151):1215–1218, 2013.

[336] Aharon Blank and Haim Levanon. Optimal magnetization in liquids, generated by triplet—doublet interaction. *Molecular Physics*, 100(9):1477–1488, 2002.

[337] Akio Kawai and Kazuhiko Shibuya. Electron spin dynamics in a pair interaction between radical and electronically-excited molecule as studied by a time-resolved esr method. *Journal of Photochemistry and Photobiology C: Photochemistry Reviews*, 7(2-3):89–103, 2006.

[338] Aharon Blank and Haim Levanon. Toward maser action at room temperature by triplet-radical interaction and its application to microwave technology. *RIKEN REVIEW*, 44:128, 2002.

[339] Alan D Adler, Frederick R Longo, John D Finarelli, Joel Goldmacher, Jacques Assour, and Leonard Korsakoff. A simplified synthesis for meso-tetraphenylporphine. *The Journal of Organic Chemistry*, 32(2):476–476, 1967.

[340] Sucharita Mandal and Snorri Th Sigurdsson. On the limited stability of bdpa radicals. *Chemistry–A European Journal*, 26(33):7486–7491, 2020.

[341] Olesya Haze, Bjorn Corzilius, Albert A Smith, Robert G Griffin, and Timothy M Swager. Water-soluble narrow-line radicals for dynamic nuclear polarization. *Journal of the American Chemical Society*, 134(35):14287–14290, 2012.

[342] Aharon Blank and Haim Levanon. Interaction between polarized triplets and stable radicals in liquid solutions. *The Journal of Physical Chemistry A*, 105(20):4799–4807, 2001.

[343] S Reindl and Alfons Penzkofer. Higher excited-state triplet-singlet intersystem crossing of some organic dyes. *Chemical physics*, 211(1-3):431–439, 1996.

[344] Nagao Azuma, Takehiro Ozawa, and Jun Yamauchi. Molecular and crystal structures of complexes of stable free radical bdpa with benzene and acetone. *Bulletin of the Chemical Society of Japan*, 67(1):31–38, 1994.

[345] David T Breslin and Marye Anne Fox. Characterization of the excited-state reactivity of a persistent aryl-substituted allyl free radical. *The Journal of Physical Chemistry*, 97(50):13341–13347, 1993.

[346] Koichi Kikuchi, Yutaka Kurabayashi, Hiroshi Kokubun, Youkoh Kaizu, and Hiroshi Kobayashi. Triplet yields of some tetraphenylporphyrins and octaethylporphyrins. *Journal of Photochemistry and Photobiology A: Chemistry*, 45(2):261–263, 1988.

[347] Masahiko Taniguchi, Jonathan S Lindsey, David F Bocian, and Dewey Holten. Comprehensive review of photophysical parameters (ε, ϕf, τs) of tetraphenylporphyrin (h2tpp) and zinc tetraphenylporphyrin (zntpp)–critical benchmark molecules in photochemistry and photosynthesis. *Journal of Photochemistry and Photobiology C: photochemistry reviews*, 46:100401, 2021.

[348] Mataz Alcoutlabi and Gregory B McKenna. Effects of confinement on material behaviour at the nanometre size scale. *Journal of Physics: Condensed Matter*, 17(15):R461, 2005.

[349] Mirjam Schröder, Daniel Rauber, Clemens Matt, and Christopher WM Kay. Pentacene in 1, 3, 5-tri (1-naphtyl) benzene: a novel standard for transient epr spectroscopy at room temperature. *Applied Magnetic Resonance*, 53(7-9):1043–1052, 2022.

[350] Max Attwood, Xiaotian Xu, Michael Newns, Zhu Meng, Rebecca A Ingle, Hao Wu, Xi Chen, Weidong Xu, Wern Ng, Temitope T Abiola, et al. N-heteroacenes as an organic gain medium for room-temperature masers. *Chemistry of Materials*, 2023.

[351] Hao Wu, Shuo Yang, Mark Oxborrow, Min Jiang, Qing Zhao, Dmitry Budker, Bo Zhang, and Jiangfeng Du. Enhanced quantum sensing with room-temperature solid-state masers. *Science Advances*, 8(48):eade1613, 2022.

[352] Samuel Lenz, Dennis König, David Hunger, and Joris van Slageren. Room-temperature quantum memories based on molecular electron spin ensembles. *Advanced Materials*, 33(30):2101673, 2021.

[353] S. Lenz et al. Quantitative prediction of nuclear-spin-diffusion-limited coherence times of molecular quantum bits based on copper (ii). *Chemical Communications*, 53(32):4477–4480, 2017.

[354] Arzhang Ardavan, Olivier Rival, John JL Morton, Stephen J Blundell, Alexei M Tyryshkin, Grigore A Timco, and Richard EP Winpenny. Will spin-relaxation times in molecular magnets permit quantum information processing? *Physical review letters*, 98(5):057201, 2007.

[355] NV Prokof'Ev and PCE Stamp. Theory of the spin bath. *Reports on Progress in Physics*, 63(4):669, 2000.

[356] WM Witzel and S Das Sarma. Concatenated dynamical decoupling in a solid-state spin bath. *Physical Review B*, 76(24):241303, 2007.

[357] Rogerio de Sousa and S Das Sarma. Theory of nuclear-induced spectral diffusion: Spin decoherence of phosphorus donors in si and gaas quantum dots. *Physical Review B*, 68(11):115322, 2003.

[358] Semen Aleksandrovich Al'tshuler and Boris Mikhailovich Kozyrev. *Electron paramagnetic resonance*. Academic Press, 2013.

[359] Jan M Binder, Alexander Stark, Nikolas Tomek, Jochen Scheuer, Florian Frank, Kay D Jahnke, Christoph Müller, Simon Schmitt, Mathias H Metsch, Thomas Unden, et al. Qudi: A modular python suite for experiment control and data processing. *SoftwareX*, 6:85–90, 2017.